# On the dynamic pressure response of the brain during blunt head injury: modelling and analysis of the human injury potential of short duration impact

Submitted by
*Christopher William Pearce*
to the University of Exeter as a thesis for the degree of
Doctor of Philosophy in Engineering, June 2013



I certify that all material in this thesis which is not my own work has been identified and that no material has previously been submitted and approved for the award of a degree by this or any other University.

Signature: ……..

# Abstract

Impact induced injury to the human head is a major cause of death and disability; this has driven considerable research in this field. Despite this, the methods by which the brain is damaged following non-penetrative (blunt) impact, where the skull remains intact, are not well understood. The mechanisms which give rise to brain trauma as a result of blunt head impact are frequently explored using indirect methods, such as finite element simulation. Finite element models are often created manually, but the complex anatomy of the head and its internal structures makes the manual creation of a model with a high level of geometric accuracy intractable. Generally, approximate models are created, thereby introducing large simplifications and user subjectivity.

Previous work purports that blunt head impacts of short duration give rise to large dynamic transients of both positive and negative pressure in the brain. Here, three finite element models of the human head, of increasing biofidelity, were employed to investigate this phenomenon. A novel approach to generating finite element models of arbitrary complexity directly from three-dimensional image data was exploited in the development of these models, and eventually a highly realistic model of the whole head and neck was constructed and validated against a widely used experimental benchmark.

The head models were subjected to a variety of simulated impacts, ranging from comparatively long duration to very short duration collisions. The dynamic intracranial pressure response, characterised by large transients of both positive and negative pressure in the brain, was observed following short duration impacts in all three of the models used in this study. The dynamic intracranial response was also recorded following short duration impacts of high energy, involving large impact forces, which were deemed to be realistic representations of actual impact scenarios. With the aid of an approximate analytical solution, analysis of the simulations revealed that the dynamic response is caused by localised skull deflection, which induces flexural waves in the skull. The implications of these magnified pressures are discussed, with particular regard to the potential for intracranial cavitation.

## Acknowledgments

I would like to thank my supervisor Dr. Philippe Young, without whom this work would not have been possible, and who's expertise, guidance, and friendship have been invaluable. I would also like to acknowledge the University of Exeter for the opportunity to undertake this research, and for providing me with financial support. Many thanks go to Dr. Christopher Morfey and Dr. Emma Forsey (née Johnson) who, along with Dr. Young, conducted the original research on which this work is based.

Special thanks go to Simpleware Ltd., that generously provided the technical resources and facilities which I have used throughout. I would like to thank Dr. Ross Cotton, Dr. Viet Bui Xuan, Dr. Rebecca Bryan, and Sumit Paranjape, who gave me technical help and with whom I have had valuable discussions about aspects of this research. I am most grateful to all my friends at Simpleware, who have provided indispensible support in both an academic and personal sense; I apologise profusely that I cannot mention you all here. I would like also to acknowledge Arup Group Ltd. and Dr. Brian Walker, who generously supplied several of the tools and training that I relied on during this work. I am very grateful to Liliana Cowlam for the original simulation from which a portion of this research was developed, and for her kind assistance and encouragement.

My parents have, as always, been unconditionally supportive during the highs and lows of this journey, thank you. Last but not least, I would like to thank Sophy ~ your love and patience has been integral to every page written, and without your sincere encouragement this work would have been neither started nor finished.


## Disclaimer

This work is concerned with the biomechanics of head impact: it should be understood that the scope of the thesis is limited to investigation of the primary biomechanical event, and any discussion related to the predicted severity of injuries stemming from impacts simulated in this study is based solely on these mechanical considerations. It has been shown that primary head injuries, such as those caused by impact, can lead to secondary injuries as a consequence of disrupted biological processes (see Section 1.3.2 for further information). These secondary injuries may significantly affect the clinical outcome of a head injury sufferer and are not taken into account here.

# Table of Contents

# List of Figures

# List of Tables

# Chapter 1: Head impact – Introduction

## 1.1 Epidemiology of head injury

It is difficult to estimate the prevalence of head injury incidences: the degree of trauma can vary so greatly that complications arise defining what is, and is not, classified as a head injury. Although injury to the head is technically a very broad category, the phrase "head injury" is often not used simply as an umbrella term, but may informally refer to what can be the most debilitating outcome of such an incident, namely damage to the brain - this is sometimes called "traumatic brain injury" (TBI). Specifically TBI is defined as injury which is *intracranial*, i.e. it involves the brain or other contents of the cranium, and *mechanical*, thus distinguishing it from injury by disease. Every year over one million people attend accident and emergency departments in the UK with a head injury. Mechanically induced trauma to the body is the leading cause of death in people under 40, and head injury accounts for approximately 50% of deaths in this group (Department of Health, 2005). Of those that survive a head injury, many continue to suffer and require care; research conducted in the UK found that slightly less than 50% of subjects studied after having sustained severe concussion had persistent problems, or had become unemployable (Hardy, Khalil, & King, 1994). Many of the people affected are young, which causes a high prevalence of disability in the population. There are an estimated 135,000 people in the UK dependent on care after suffering brain injury (Watkins & Thomas, 2003). In the United States roughly 1.7 million people sustain TBI per year, and of these 52,000 die; for the year 2000 alone the direct medical cost and indirect cost through loss of productivity resulting from this high TBI rate was estimated at $60 billion (US Centre for Disease Control and Prevention, 2010a).

In the United States falls are the single most common cause of TBI annually (35.2% of cases), followed by motor vehicle collisions (17.3%), general accidental impact including sporting injuries (16.5%), and violence (10%). However motor vehicle collisions result in the largest percentage of TBI-related deaths (31.8%) (US Centre for Disease Control and Prevention, 2010b). This distribution is typical of many developed nations. In combat, explosive blasts have recently become a major cause of injury to the brain. Some 14-20% of surviving casualties have TBI, and the number of incidences has risen so fast that TBI is often called the "signature wound" of the recent Iraq and Afghanistan conflicts (US Department of Veterans Affairs, n.d.).

Trauma to the brain is characterised by high mortality and long-term disability rates, leading to high socio-economic costs for patients, families and governments. This has led to a large amount of research into the behaviour of the head during impact, the natural protective functions of the various structures of the head, and the injury mechanisms which occur when these are not sufficient.

## 1.2 Anatomy of the head

The human head is a highly complex system of complementary organs. It includes the brain, the centre of the nervous system, one of our most vital organs and arguably the most well protected. Various structures attempt to mitigate injury to the brain when the head is subject to physical insult. Overall the head can be said to consist approximately of a weight-bearing and protective skeletal structure, the skull, with a large central cavity which houses the brain. The following is an outline of the macrostructures of the major features of the head system, namely the skull and cranial contents. The microstructure and composition of brain tissue, cranial bone, cerebrospinal fluid, and the scalp layer are investigated further in Section 2.3.2.

### *1.2.1 The skull and neck*

The skull can be divided into two regions, the *viscerocranium* (or "facial bones") and the *neurocranium* (also known as the "braincase" or "cranial vault"). Although classifications sometimes vary, the skull can be said to consist of twenty-two bones, fourteen of which define the facial anatomy from the forehead to the lower jaw. The brain and spinal cord together are known as the central nervous system (CNS), and are protected by the cranial vault and the *vertebral column* respectively. The cranial vault is composed of eight separate bones; these are, in order of approximate anterior to posterior location, the *frontal bone*, *ethmoid*, *sphenoid*, two *parietal bones* (one for each side, left and right), two *temporal bones* (also one for each side), and the *occipital bone* (Claessens, 1994). Except for the *mandible*, all bones which comprise the skull are joined by sutures which form as a person develops. Before the articulations between the various bones have ossified, some degree of flexibility and movement is possible. Consequently paediatric biomechanical studies concerning the head must be conducted separately (Roth, Raul, & Willinger, 2009). In adults these bones are joined in such a way that they do not form local weaknesses in the skull (Claessens, 1994).

The braincase forms an unbroken shell around the brain except for a few small openings at its base for arteries, veins, and nerves. The largest of these holes, the *foramen magnum*, is an

opening to accommodate the *brain stem* which forms the transition from brain to spinal cord (Claessens, 1994). The cranial bone itself exists in two phases which together form a sandwich panel structure; this is explored further in Section 2.3.2. The cranial vault is covered by the scalp: a thick protective layer of skin and muscle tissue.



*Figure 1.1: Sagittal section view of the skull: bones of separate embryonic origin are distinguished, and sutures are visible. (Van De Graaff & Fox, 1995)*

The skull and head are supported by the neck, and specifically the seven cervical vertebrae that form the core of the neck. The *vertebral arch* of each of these bones encloses a length of the spinal cord, shielding it from external forces. The body of each vertebrae is separated from the next by a series of *intervertebral discs* made primarily of cartilage. These discs are reasonably compliant allowing flexibility in the neck and spinal column.

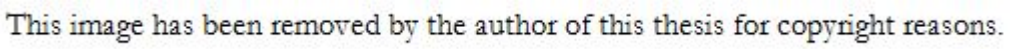


*Figure 1.2: A radiograph of the cervical spine. The base of the skull can be seen supported by the vertebrae of the neck. Dense bone material appears as white or light grey; the darker regions interspersing the vertebrae reveal the locations of the intervertebral discs. (Van De Graaff & Fox, 1995)*

### *1.2.2 The brain and other structures within the cranial vault*

The brain of the average human adult contributes around 1.5 kg to the weight of the head, which is approximately 4.5 kg in total (Claessens, 1994). Although the brain is a highly intricate, continuous structure it can be grossly divided into three major regions: the brain stem, *cerebrum*, and *cerebellum*. The brain stem joins the spinal cord to the base of the brain. One of its roles is to regulate autonomic functions vital for survival such as respiration, digestion, and circulation.

The cerebrum is the most highly developed region of the human brain and is associated with higher mental functions. It is situated above the brain stem, and occupies the majority of the cranial vault, accounting for 80% of the mass of the brain (Van De Graaff & Fox, 1995). Its size and proximity to the inner surface of the skull make the cerebrum the structure of the brain most vulnerable to mechanical injury. The CNS is composed of tissues known as grey matter and white matter. Grey matter consists mainly of neuron cell bodies, while white matter consists of axonal fibres which communicate electrical signals between regions of the nervous system. A large proportion of the grey matter in the brain is located in the *cerebral cortex*, the outermost layer of the cerebrum approximately 1.5-3.5 mm thick (Goldsmith, 1972). It is here that processing of information takes place, giving the cortex a key role in reasoning, intelligence, sensory interpretation and voluntary motor activities. The cerebral cortex is convoluted (intricately folded) into many *gyri* (ridges) and *sulci* (furrows) to increase its surface area, allowing for a greater number of

axonal connections to be made. The largest of these furrows lies on the midsagittal plane and divides the cerebrum into two separate *cerebral hemispheres* which meet only at a central bridge of axons, the *corpus callosum*. These two hemispheres can each be further subdivided into regions known as *lobes* by way of the large sulci which define their perimeter. The lobes are named after the bones of the skull which they lie beneath. The lobes have been found to correspond to different brain functions, and so damage to various regions of the cerebrum will induce different pathological manifestations depending on location.



*Figure 1.3: Sagittal view of the brain: the major lobes of the cerebrum are distinguished. The brain stem and cerebellum are also visible. (Van De Graaff & Fox, 1995)*

The functions associated with the lobes of the cerebrum are summarised below.

- Frontal: verbal communication, personality, voluntary control of skeletal muscles, and higher cognitive processes such as planning and problem solving.
- Temporal: interpretation of auditory information, and memory of auditory and visual input.
- Parietal: understanding sensory information such as speech, or interpreting shapes and textures.

- Occipital: interpreting visual information, focusing the eye, and correlation of visual input with past visual experiences.
- Insula: while not well understood it is believed to be involved with memory and awareness. This lobe is located deep within the cerebrum and not visible from its exterior.

The final major region of the brain, the cerebellum, is located in the posterior of the cranial cavity, beneath the occipital lobes. Its primary function is to modify impulses for voluntary movement originating at the cerebral cortex, aiding coordination of the skeletal muscles and balance. Like the cerebrum, the cerebellum is also divided into two hemispheres. These are joined by the *vermis*, a white matter structure similar to the corpus callosum.

The brain and spinal cord are covered by three membranes called the *meninges*, which together form an impermeable layer and have circulatory and protective functions. The thickest of these membranes is the *dura*: a layer of tough, fibrous tissue which lines the inside of the cranial vault. Flaps of dura mater known as the *falx cerebri* and *falx cerebelli* also extend inwards to form vertical partitions which separate the two hemispheres of the cerebrum and the two hemispheres of the cerebellum respectively. A horizontal partition between the lower anterior surface of the cerebrum and the upper surface of the cerebellum is also formed by a layer of dura mater known as the *tentorium cerebelli*. The next membrane inwards, the *arachnoid*, is a delicate web of fibers loosely connecting the dura to the third tissue layer, the *pia mater*. This final membrane is another delicate layer of tissue which closely covers the brain and spinal cord, containing many small blood vessels (Claessens, 1994; Goldsmith, 1972). A section view of the head (Figure 1.4) reveals many of these structures. The *subarachnoid space*, located between the arachnoid and pia mater, is a region completely filled with a watery fluid called the *cerebrospinal fluid* (CSF). The brain, having about the same density, is buoyant in this fluid allowing it to be suspended so that it does not rest on the bottom of the skull. The CSF has a mechanical protective function, acting as a buffer between the brain and the interior of the skull. The CSF also aids the metabolism of the CNS: it provides nutrients, and as it is reabsorbed into the bloodstream it carries with it any metabolic waste produced by the brain or spinal cord. The CSF continually flows through this subarachnoid space around the brain and spinal cord, and also through cavities and channels in the brain known as the *ventricles*. All these locations of CSF are connected, and reabsorption or production of CSF allows the pressure to be regulated.

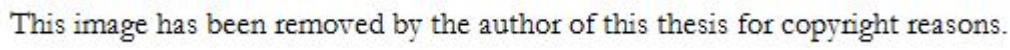


*Figure 1.4: Coronal section view of the head. The tissue layers which surround the brain can be seen, from the exterior to interior these are : the scalp, skull, dura mater, arachnoid, subarachnoid space (filled with cerebrospinal fluid), and pia mater. (Van De Graaff & Fox, 1995)*

The brain receives and expels blood through a complex network of large and small arteries and veins. A large proportion of arterial blood is directed by the arteries of the neck into the cranial cavity through the foramen magnum. These arteries then branch out multiple times to supply the many smaller vessels which permeate the brain. The arteries within the cranial vault are connected in a self-intersecting network which reduces the risk of "ischemia" (reduced blood supply, starvation of oxygen) if a portion of the vascular system becomes non-functional. The "blood-brain barrier" is a series of specialised cells which line the capillaries supplying the brain and shield it from infection by permitting only small essential molecules (nutrients, hormones) to pass. The majority of venous blood drainage occurs through a system of venous sinuses which lie embedded in the dura mater.

## 1.3 Head impact injury

Mechanical injury to the human body occur when biological tissues are deformed beyond their recoverable limit. As a result, anatomical structures may be damaged or their function impaired. The size and location of the head make it vulnerable to a multitude of potentially dangerous loading patterns. In our modern society high-speed travel, various ball sports and contact sports, and advances in weaponry have further widened the range of potential

physical insults that the head might be subjected to. By definition, TBI is caused by external, mechanical means. This allows the distinction to be made between three broad categories of loading which may cause TBI: "crushing" where the head is compressed between two surfaces, "impact" involving sudden contact with an external body, or non-contact "inertial" type loading (typically where accelerations are transmitted to the head through the neck, caused by sudden motion of the body) (Stålhammar, 1986). These latter two loading conditions are the most common (Hardy et al., 1994). The current study is concerned with impact loading. This mechanism is typified by the short duration of the loads involved, the shortest of the three categories stated above. As a rough guide, impact to the head by a hard object such as a concrete floor or a falling stone may last around 1-3 ms, while a typical collision of the head with the interior dashboard of a vehicle could be expected to last between 5-15 ms, and a blow by a fist lasts about 20-30 ms (Stålhammar, 1986).

### *1.3.1 Impact mechanics and dynamic considerations*

Impact occurs when two objects collide. The initial instant when the two surfaces of these objects meet is known as *incidence*. Were the objects to continue their motion uninhibited there would be interpenetration or interference between the two surfaces, but this is resisted by the interface pressure which occurs at the area of contact. During the contact period this pressure in the contact area causes local deformation of the objects involved, leading to a resultant force of action or reaction that acts in opposing directions on the two colliding objects. At incidence this contact force is zero, but it immediately begins to increase with increasing indentation and so reduces the speed at which the objects approach each other (Stronge, 2000).

At some instant in the contact period the contact force will reach its maximum, at which time the velocity of approach between the two objects is effectively zero. What occurs after this point depends on the degree of "elasticity" or "inelasticity" of the collision. In a perfectly elastic collision, the kinetic energy of the bodies before the impact is conserved through elastic deformation of the contact surfaces. This energy is recoverable, such that the contact force which accumulates at the area of contact between the two bodies eventually forces them to rebound with a mutual velocity of separation equal to their initial mutual velocity of approach. In a perfectly inelastic collision, none of the initial kinetic energy is conserved and the bodies rebound with a velocity of separation equal to zero. In practice, perfectly elastic or perfectly inelastic collisions are extremes that do not occur. The degree of elasticity or inelasticity of an impact can be approximately summarised by a

parameter called the "coefficient of restitution" $e$, which is defined as the magnitude of the mutual velocity of separation over the magnitude of the mutual velocity of approach of the two bodies. Thus the coefficient of restitution has limits $0 \leq e \leq 1$, determined by a perfectly inelastic or perfectly elastic impact respectively. Practically, in any collision an amount of energy will be dissipated and so the mutual velocity of separation will always be less than the velocity of approach. Other than any heat or sound resulting from the collision, which in many cases can be assumed negligible, energy will be dissipated during impact by any plastic deformation that occurs, fracture, and by elastic stress waves generated in the two bodies which "radiate" strain energy away from the contact site (K. L. Johnson, 2003).

Stress waves initiate at the contact area and propagate through the objects, eventually encompassing their entire volume. At the boundaries between various materials and parts in composite structures these waves will be both transmitted and reflected (Stålhammar, 1986). There are two possible "bulk wave" motions in three-dimensional elastic media, these are:

- *dilatational* (or pressure) waves in which regions of the material fluctuate in volume, transmitting a pulse of either compressive or tensile stress without any shear deformation,
- and *distortional* (or shear) waves in which regions of the material distort, transmitting a pulse of shear stress without any local change in volume (K. L. Johnson, 2003).



*Figure 1.5: Diagram of (a) dilatational and (b) distortional strains in a cubic sample of material. (Bradshaw & Morfey, 2001)*

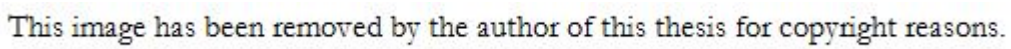


*Figure 1.6: Diagram illustrating the communication of (a) dilatational and (b) distortional waves. The impulses are transmitted across the page, through a rectangular solid with a regular grid marked on its surface. (Shearer, 2009)*

The speed that these waves propagate is dependent on the mechanical characteristics of the material. The dilatational and distortional wave speeds, $c_p$ and $c_s$ respectively, are given by:

$$c_p = \left(\frac{2G(1-\nu)}{\rho(1-2\nu)}\right)^{1/2} \qquad [1.1]$$

$$c_s = \left(\frac{G}{\rho}\right)^{1/2} \qquad [1.2]$$

where $G$ is the shear modulus (Pa), $\nu$ is the Poisson's ratio, and $\rho$ is the density of the material (kg/m$^3$) (K. L. Johnson, 2003).

After the colliding bodies have separated, the remaining stress waves will continue to propagate through the bodies leaving them in a state of vibration (K. L. Johnson, 2003). In any real world system which is in a state of vibration, friction and other resistances will dissipate energy, thus introducing an amount of "damping". The effect of damping is primarily evident in the reduction of the amplitude of vibration over time (Thomson, 1993).

### *1.3.2 Brain injuries*

Depending on the material characteristics, stresses, and time-frame of an impact, various disturbances called "contact phenomena" will exist around the contact site. This will involve local deformations (temporary or permanent) inherent with impact cases, and may also include: perforation where a thin material is pierced entirely by a sharp impactor, cracking or fracture of the material (with or without perforation), or other failure modes

such as shattering (Goldsmith, 1972). In this respect TBI cases are generally classified as being either *blunt* or *penetrating:* where the cranial vault has remained intact, or has been breached, respectively. Penetrating injuries absorb energy primarily near the point of impact, while blunt injuries potentially spread the absorption of energy over the head. Trauma to the brain occurs in penetrating injuries if the brain is exposed and interacts directly with the external object. In these cases the injury mechanism and extent of trauma to the brain is, while devastating, relatively distinct and obvious. The trauma locations and mechanisms resulting from blunt (or "closed") head impact are not well understood and cannot be well predicted, and thus research offers greater opportunity for mitigating this shortfall. Blunt injuries are also the more common (Santiago, Oh, Dash, Holcomb, & Wade, 2012).

Amongst TBI cases a mechanical distinction can be made as to whether the brain injuries involved are *diffuse* or *focal*. Diffuse injury refers to distributed large-scale mechanical damage to neural and axonal tissue, and the minute blood vessels which infiltrate the brain. It also includes damage resulting in diffuse brain swelling. Diffuse injuries are commonly associated with inertial loading and have been linked to motor vehicle accidents (Marik, Varon, & Trask, 2002). Focal injuries occur in localised regions of the brain subject to large stresses, violent contact with the interior surface of the cranium, or tangential motion of the brain relative to the cranium (Bandak, 1996). Focal injuries typically result from impact to the head. Generally rotational acceleration of the head is considered to have the potential to produce either focal or diffuse lesions, whilst translational acceleration tends to cause focal injury (Zhang, Yang, & King, 2001). Common primary injuries associated with non-penetrating TBI include:

- *Diffuse Axonal Injury* (DAI): is a distribution of lesions in the axonal network (white matter) of the brain. It is thought to be caused primarily by the presence of large shear stresses in the tissue (Marik et al., 2002), and has been linked to rotational acceleration of the head (Ommaya, Thibault, & Bandak, 1994). DAI can be difficult to detect as it is often only evident microscopically, although its presence can be identified by staining and diffusion-weighted magnetic resonance imaging (dMRI). DAI has a high mortality rate, and survivors have a high morbidity, often not improving beyond a persistent coma (Marik et al., 2002). There is an overlap between focal injuries and DAI, and in practice both focal and diffuse lesions often coexist (Marik et al., 2002).

- *Intracerebral Haematomas (ICH):* are due to rupture of blood vessels in or around the brain, and the seepage of this blood into neural tissue (Goldsmith, 1972). These focal injuries will produce functional losses in the affected lobes (Cifu & Caruso, 2010). Intracerebral haematoma lesions tend to be large and are often associated with moderate to severe head injuries. Many intracerebral haematomas are delayed, developing 24 hours or more after the incident (Marik et al., 2002).
- *Cerebral contusion:* or "bruising" of the brain, is a focal lesion caused by multiple small intracerebral haemorrhages, i.e. leakage of smaller blood vessels into the brain (Goldsmith, 1972). Both cerebral contusions and intracerebral haematomas commonly develop beneath the point of the impact (known as the "coup") and at the diametrically opposite pole (the "contrecoup"). Furthermore, it has been noted that the frontal and temporal lobes appear particularly susceptible to contusions, but the mechanism which causes these contusions and the reason for their prominence in these locations is not fully understood (Bandak, 1996; Dawson, Hirsch, Lucas, & Sebek, 1980). Alternatively, another category of contusion-type lesions can develop from rotational accelerations which may cause the cortex to slide along the interior surface of the skull; these have been termed "gliding contusions" (Marik et al., 2002).
- *Subdural Haematomas (SDH):* While there is a broad spectrum of SDH, acute cases occur in approximately 30% of severe head injuries (Marik et al., 2002). An SDH is an area of localised bleeding between the dura mater and the arachnoid, caused by rupture of one of the many blood vessels contained within the dura. In an SDH, blood begins to fill a localised region of the subdural space and so compresses the neural tissue beneath it (Claessens, 1994), however in minor cases, a thin film of blood may develop that does not cause any symptoms and may resolve itself without treatment. SDH is often associated with impact (Marik et al., 2002), or can occur as a result of motion of the brain relative to the skull which may tear bridging veins connected to the subdural sinuses (Bandak, 1996); severe brain motion may give rise to both SDH and DAI, and these conditions can be considered to be related. When an SDH is evident this signals, in the majority of cases, that the force of the impact was communicated to the brain itself. Therefore, frequently a cerebral contusion exists beneath an SDH. In roughly 80% of cases with an SDH, it is this underlying brain injury that determines the patient's outcome (Marik et al., 2002). SDH are also associated with coup-contrecoup injuries (Cifu & Caruso, 2010).

These primary injuries occur immediately at the time of the TBI incident, due to the resulting stresses and strains in the head. Secondary brain injuries may develop after the incident, and are due to the physiological response to the initial trauma. It has been postulated that after a brain injury a number of biochemical substances are released which may damage neural tissue, including tissue that was unharmed by the initial trauma (Marik et al., 2002). Secondary brain injuries can also occur as haemorrhaging and *cerebral oedema* (an accumulation of fluid in the brain) cause an increase in the amount of matter contained within the skull. The body can initially compensate for this by reducing the amount of blood and CSF circulating in the cranial vault. However, if the contents of this finite volume increases further, the pressure inside the cranium (known as *intracranial pressure*) rises sharply due to the rigid nature of the skull and the largely incompressible nature of biological fluids and neural tissue (Goldsmith, 1972; Marik et al., 2002). Furthermore, intracranial pressure autoregulation may be compromised following severe TBI, which could compound the problem (Jenkins et al., 1989; Marik et al., 2002). Intracranial pressure is a gauge pressure, measured in millimetres of mercury (mmHg) relative to atmospheric pressure. For an adult lying down intracranial pressure should be between 7 to 15 mmHg, and in a vertical position this becomes negative, commonly around -10 mmHg (Steiner & Andrews, 2006). Raised intracranial pressure is defined as a reading of greater than 20 mmHg (2.66 kPa) for 5 minutes or more (Marik et al., 2002), and has been associated with a poor clinical outcome. High intracranial pressure can crush neural tissue, or lead to large pressure gradients which may induce herniation of the brain. Raised intracranial pressure may cause ischemia in neural tissue by decreasing the pressure gradient necessary for blood perfusion to the brain (Steiner & Andrews, 2006), with posttraumatic ischemic lesions present in up to 80% of fatal head injury cases (Marik et al., 2002).

### *1.3.3 Proposed mechanisms of coup-contrecoup injury*

There has been considerable speculation on the mechanics which produce the stresses and strains capable of inducing primary brain injuries such as those described above. In particular coup-contrecoup injuries have been the subject of much investigation, due in part to the counter-intuitive nature of this effect and its common occurrence. This well documented "coup-contrecoup phenomenon" describes the presence of lesions, frequently contusions, in localised regions not only beneath the point of impact, but also directly opposite (Goldsmith, 1972). Several theories have been put forward to explain the formation of coup-contrecoup injuries; any mechanism proposed must be able to account for the peculiar distribution of trauma.

In 1967, Thomas, Roberts, & Gurdjian observed the existence of pressure gradients in a gel representation of the human brain contained within a dry cadaveric skull when subject to impact. These pressures varied linearly throughout the brain, along the axis in which the strike was applied, from a positive pressure under the site of impact (the coup), to a negative pressure at the contrecoup, passing through zero in the centre of the brain. The existence of this linear pressure gradient response of the brain, producing both positive and negative pressures, had been hypothesised long before it was observed by Thomas et al., and has been found many times since in cadaver (Nahum, Smith, & Ward, 1977), non-biological (Kenner & Goldsmith, 1972, 1973; Stålhammar, 1975), mathematical (Engin, 1969; Misra & Chakravarty, 1985) and numerical models (Huang et al., 2000; Khalil & Hubbard, 1977; Willinger, Kang, & Diaw, 1999), to name just a few examples. Traditionally the subject of brain injury has been the concern of medical professionals. Essentially however impact to the head is a dynamic mechanical problem, and therefore has also been the focus of much engineering research. There are in the literature broadly three main independent theories on the development of coup-contrecoup injuries, these are: the positive pressure, negative pressure, and shear stress theories[1]. The high complexity of the head, and the fact that these theories cannot be verified directly on humans *in vivo*, has resulted in a difficulty gathering evidence to support or cast doubt on any particular hypothesis. Therefore, no single theory has yet been broadly accepted across the research community, and the phenomenon remains poorly understood despite being known to science for at least 200 years (Drew & Drew, 2004).

**Positive pressure:** A relatively simple explanation which is popular in medical textbooks is that impact or inertial loading will result in a coup injury due to violent contact of the brain with the inner surface of the skull and dura. This will in turn cause the brain to rebound within the cranium, propelling it towards the opposite side of the skull where it is again traumatised (Cifu & Caruso, 2010). This theory (sometimes called "ricocheting") alone

[1] The term "pressure" refers to the mean of the principle stress components in local regions of the material. It is necessary to note here that a distinction is made between transient pressures in the brain occurring as a result of the dynamics of impact, and the global pressure that would otherwise exist in the cranial cavity, mentioned previously, which is autoregulated between 15 and -10 mmHg. The coup-contrecoup theories which involve pressure suggest the former of these cause primary brain injuries. The latter will be affected if an injury is severe enough to disrupt the pressure autoregulation, causing a rise in the global cranial pressure ("intracranial hypertension") which may cause secondary injuries (Marik et al., 2002).

would predict a greater degree of trauma at the coup than at the contrecoup, due to a reduction in the relative velocity of the brain after its first (coup) collision with the skull. Therefore it fails to address the issue highlighted by Drew & Drew (2004) which is that, in terms of severity, the contrecoup injury tends to be equal to or greater than the coup injury. To address this issue Drew & Drew postulate that the slightly higher density of CSF compared to the brain will cause the CSF to displace towards the impact site, forcing the brain in the opposite direction. As the brain makes contact with the inner surface of the skull this would produce a contrecoup injury preceding any coup injury.

Alternatively, Lindenberg (1960) suggested that as the head accelerates towards the ground during a fall, the cranial contents will become compressed against the inner surface of the trailing edge of the skull, causing a local region of positive pressure at the contrecoup existing pre-impact. In line with this, Edberg et al. (1963) observed negative pressures at the coup and positive pressures at the contrecoup during pre-impact acceleration of plastic skull models filled with gel. During impact however these pressure gradients were reversed, with positive pressures at the coup, and negative at the contrecoup. These findings agree with the work by Thomas et al. (1967) and others, discussed above. Clearly as the head is accelerated as a result of a fall or impact, a pressure gradient will develop across the contents of the cranium, with positive pressure at the trailing side of the head (coup), and vice versa at the leading side (contrecoup). Proponents of the positive pressure theory contend that damage to the brain occurs in these regions of positive pressure, so accounting for coup injuries when the head is impacted, and contrecoup injuries during a fall (Hardy et al., 1994). Local regions of the brain may be subjected to compressive stresses beyond their recoverable limit, causing functional disturbances, cell death, and possibly rupture of blood vessels. However, Lindenberg (1960) and Dawson et al. (1980) also hypothesised that these accelerations result in a thinning of the CSF layer in the areas of positive pressure, as the brains greater inertia causes it to displace towards the skull's trailing edge more than the CSF. The CSF layer acts as a cushioning barrier, and its removal would further increase the likelihood of focal lesions under sites of positive pressure as the brain may make violent contact with the rigid and uneven inner surface of the skull and dura.

A preliminary concern with these proposed injury mechanisms, which rely on differential movement and shifting of the brain and CSF, is that there is direct disagreement between Lindenberg (1960) and Dawson et al. (1980) with Drew & Drew (2004) regarding whether the brain is of greater or lesser density than the surrounding fluid. Also of concern would

be to what extent this mechanism affects the velocity of the brain, given that the difference in density between the CSF and brain tissue is, whether higher or lower, certainly relatively small (a value of 4% was used by Drew & Drew). Finally, these proposed mechanisms do not take into account the fact that the short time-frames inherent in impact effectively establish "no flow conditions", i.e. in general the CSF will be unable to flow to, or away from, the contact site and will remain a cushioning barrier between the brain and skull. A further confounding factor, as acknowledged by Dawson et al. (1980) and others, is that impacts to certain areas of the head appear to be far less inclined to generate contrecoup injuries: for example, contrecoup injury is rarely observed following impact to the frontal bone. Therefore, it is possible that the coup-contrecoup phenomenon is influenced by local skull anatomy.

**Negative pressure:** It has long been known that many materials are generally weaker in tension than they are in compression, therefore it has been suggested that these negative pressures may damage neural tissue. The primary aspect of the negative pressure hypothesis is "cavitation", which has been deemed the most likely method by which negative pressures may cause tissue damage (Hardy et al., 1994). This theory proposes that areas of negative pressure (i.e. subatmospheric pressure) may exceed the cohesive strength of the fluid-like brain tissue, CSF, or cranial blood, causing them to tear apart, forming tiny cavities. The cavities will immediately collapse when pressure again rises above a critical value. This subsequent violent collapse of the cavities may cause focal lesions, which would provide a causative relation between the negative pressures known to occur at the contrecoup site post-impact and contrecoup injuries.

Ward, Montgomery, & Clark (1948) and Gross (1958) may have been among the first to study this effect, known as cavitation or fluid vaporisation, in relation to brain trauma and contrecoup injuries. Ward et al. observed transient negative pressures in animal heads subject to impact. They also highlighted studies that demonstrate large positive pressures applied to animals and animal neurons *in situ* without injurious effect, arguing that "negative pressures appear to be the ready source of damage to living tissue". In many respects brain tissue can be said to behave like water: both materials have similar densities, high bulk moduli, and low shear moduli. Recognising this, Gross studied the impact of water-filled flasks, and observed negative pressures and cavitation. In some instances the collapse of the cavities was forceful enough to break the glass apparatus. The cavitation theory has since become the most popular explanation for the coup-contrecoup phenomenon (Drew & Drew, 2004), and has been studied by Stålhammar (1975), Lubock

& Goldsmith (1980), Bandak (1996), Nusholtz, Glascoe, & Wylie (1996), and Wardlaw & Goeller (2010) among others.

In other fields cavitation has long been known to be capable of severe structural damage. The classic example is that of hydraulic propellers: in certain conditions cavities may form in the fluid at the low pressure sides of propeller blades, and their violent collapse can, over time, eat away at the metal, causing significant and costly wear (Gross, 1958). Collapse of these cavities is believed to cause local transients of pressure of the order of 1 to 3 GPa, this is therefore a possible mechanism of tissue damage to the brain (Gross, 1958; Johnsen, Colonius, & Cleveland, 2009). In less severe injuries such as concussion, Gross suggested cavitation may explain temporary functional disturbance of the cerebral lobes without overt structural changes by way of the high potential electrical discharges thought to be associated with cavity collapse. This effect is well documented in other fields involving cavitation, and is called "sonoluminescence": the name derives from the fact that when certain fluids are caused to undergo cavitation they begin to emit light (Gross, 1958). Work by Flint & Suslick (1991) however, provides strong evidence that the luminescent effect of cavitation is not, as previously thought, due to an electrical discharge, but is in fact a thermal process. They measured the spectrum of light emitted from cavitation induced in silicone oil, and determined the temperature reached in the collapsing bubbles was around 5075 K. This suggests cavitation may additionally cause thermal damage to neural tissue.

Dawson et al. (1980) argue that evidence for cavitation in biological systems is scarce. This is likely due to the difficulty in monitoring cavitation in high energy, short duration, dynamic processes such as impact on *in vivo* specimens. However *in vivo* formation of "bubbles" (cavities) of dissolved gases coming out of solution is, in other fields, a well known phenomenon – a primary example is decompression sickness (informally: "the bends") which occurs when the body is subjected to a rapid reduction in ambient pressure. Decompression sickness can be fatal, and bubbles have been known to form in all areas of the body, including sometimes the brain and spinal cord (Pelosi et al., 1981). In other contexts, *in vivo* cavitation has been observed problematically in cases such as artificial heart valves, and has been produced intentionally, usually by ultrasound, for therapeutic applications such as the disintegration of kidney and gall stones (Brennen, 2003; Pishchalnikov et al., 2003). Furthermore, cavitation of the *synovial fluid* has been shown to be the source of the audible release during joint manipulation (e.g. "cracking" one's knuckles) (Cramer et al., 2011).

The magnitude of negative pressure required to form cavities is dependent on: (1) the ambient pressure, (2) the vapour pressure of the fluid, and (3) the cohesive strength of the fluid (Gross, 1958). The majority of fluids which have not been degassed in a laboratory have little or no cohesive strength due to the presence of gas nuclei and other contaminants. Therefore, if zero cohesive strength is assumed, the fluid can be thought of as being held together by the external atmospheric pressure. At a pressure of -1 atm (-101.325 kPa) this pressure is removed, and cavities will immediately develop as a result of the vapour pressure of the fluid (Gross, 1958; Thomas et al., 1967). However, degassed fluids can sustain negative pressures far greater than -1 atm (Lubock & Goldsmith, 1980). While investigating potentially deleterious effects of diagnostic ultrasound, Holland & Apfel (1990) observed that the cavitation threshold of degassed saline solution does not change when nucleation sites were added to the solution by infusing it with whole blood. The maximum negative pressure during the rarefaction phase of the ultrasound cycle required to produce cavitation in the saline-blood solution was -20.2 atm (-2.04 MPa). The duration of the negative pressures is believed to affect the ability of these bubbles to form and grow. While a threshold for cavitation in brain tissue still needs to be determined, it is highly unlikely that the threshold for cranial fluids (blood or CSF) will be lower than this value of -20.2 atm, since it represents the lowest pressure required for cavitation in degassed solution. In Holland & Apfel's experiments the ultrasound pulses were of the order of only tens of microseconds, therefore the cavitation threshold for longer duration negative pressure transients, such as those during impact, may be of considerably smaller magnitude. Also, Ward et al. (1948) argue that cavitation in the brain may be relatively easily accomplished due to "the saturation of the fluid phase of the brain by oxygen and, particularly, carbon dioxide" – conditions which are difficult to recreate in models.

Finally, in regard to these brain injury theories concerning pressure, the influence of the foramen magnum must be considered. It was noted in (Thomas et al., 1967) that the pressure gradients which forms in the brain as a result of impact are different depending on whether the foramen magnum is sealed with a rigid or elastic covering. The elastic covering allows local deformation to take place, analogous to a small amount of flow of material through the foramen. This was observed to shift the zero-point of the pressure gradient towards the rear of the skull, such that it lies over the foramen magnum. Gross (1958) suggested this effect may explain the apparent resistance of the brain to contrecoup injury from frontal blows resulting from automobile accidents. In these cases it is reasonable to assume the head is inclined slightly forwards, which therefore positions the foramen magnum closer to the contrecoup location in regard to a horizontal frontal impact. Gross

proposed that contrecoup negative pressure would cause inflow of material and CSF through the foramen magnum, which in turn would mitigate the magnitude of the negative pressure peak.



*Figure 1.7: Diagram depicting inflow through the foramen magnum attenuating negative pressures for an inclined head. (Gross, 1958)*

Any flow of material through the foramen will depend strongly on the duration of the negative pressure peak. As head impacts often last only a few milliseconds, it is reasonable to assume the transient pressures in the brain exist for similarly short periods. More work needs to be done to further our understanding of this possible damage mitigating effect.

**Shear stress:** The positive and negative pressures integral to the above theories are caused by translational acceleration of the head, as a result of impact or inertial loading. It is reasonable to assume that in most impact or inertial head injury incidents the head is also subjected to some degree of rotational acceleration, due to the neck attachment. Combined translational and rotational accelerations will also be imparted to the head if the axis of impact does not run through the head's centre of gravity (Unterharnscheidt & Higgins, 1969). Holbourn (1943, 1945) argued that the near incompressibility (high bulk modulus) of the brain and CSF would render compressive or tensile stresses non-injurious in the majority of cases, while the low shear modulus of these materials makes them susceptible to damage from waves of shear stress generated when the head is rapidly rotated.

While shear stresses in the brain are often thought to be the cause of distributed lesions such as DAI (Hardy et al., 1994; Marik et al., 2002), Holbourn (1943, 1945) suggests they may also be the cause of focal coup-contrecoup injuries. His experiments on paraffin-wax models of the skull filled with gelatin indicated that the uneven ridges of the inner geometry of the skull generate localised concentrations of shear stress at sites which approximate frequently observed coup-contrecoup injury locations. However, some authors raise the point that this theory is unable to account for contrecoup lesions occurring at locations other than the fixed sites where these shear stress concentrations are

predicted (Dawson et al., 1980; Drew & Drew, 2004), or that in some instances concentrations of shearing stress are predicted by Holbourn in regions where contrecoup injuries rarely occur (Yanagida, Fujiwara, & Mizoi, 1989).

Combinations of these theories have also been formed. Work by Gurdjian (1975), Ommaya et al. (1971, 1994), and Yanagida et al. (1989) stress the importance of considering both translational and rotational effects in order to build a complete picture of brain injury, and coup-contrecoup injuries. Holbourn (1943, 1945) and Gurdjian (1975), among others, also underscore the importance of the type of impact involved. Impacts to the head by a missile (a ball, brick, stone etc.) are of high energy, but relatively low momentum, and in these cases it is likely that translational effects will predominate. Under other conditions the head may impact a stationary object, such as the pavement, or a wall – in these circumstances the collision is generally of low energy, but the large masses involved will impart considerable rotational acceleration.

### *1.3.4 Severity coefficients and the Head Injury Criterion (HIC)*

It is clearly of benefit to have a standardised method capable of estimating the severity of a head injury based on external data. This allows the human injury potential of forces measured by non-biological models, e.g. "crash test dummies", to be predicted. Commonly a mathematical expression is used to arrive at a quantity which describes the injury potential of a particular mechanical disturbance (Bandak, 1996). An early example of this is the Gadd Severity Index (GSI) proposed by Gadd (1966). The GSI takes the form of a weighted integral of the acceleration experienced by the head with respect to the duration of an impact. In this way, the GSI was able to improve upon an existing injury criterion given by the Wayne State Tolerance Curve (WSTC), by taking the waveform of the impact into account (Gadd, 1966). The original WSTC estimates the human tolerance to different accelerations based on a limited number of cadaver drop test experiments, and has been deemed by some to be poorly representative of actual tolerances (Cory, Jones, & James, 2001; Versace, 1971).

The Head Injury Criterion (HIC) is the most popular of these severity coefficients, having been widely adopted since its development, initiated by Versace in 1971: the HIC is a modified version of the GSI, which considers a time-window within the injury producing acceleration waveform that is adjusted to maximise the resulting value (Versace, 1971). The primary use of the HIC is to assess motor vehicle accidents, with for example, acceptable HIC scores specified in the US Department of Transportation Safety Standard 208 (Federal

Motor Carrier Safety Administration, 2013). However, some authors suggest the HIC is oversimplified, and a poor predictor of head injury severity. Of note is Goldsmith's 1981 essay, wherein he expresses concerns echoed by others in the field that a single-parameter criterion such as the HIC, determined only by rigid-body linear acceleration of the head, is an unsatisfactory description of head injury in regard to assessing safety – particularly as the influence of angular accelerations, and stress waves through the brain, are not yet fully understood (Goldsmith, 1981). Other severity criteria have been suggested, such as the Head Impact Power (HIP) proposed by Newman et al. (2000) which is based on translational and rotational accelerations of the standard Hybrid III headform, or criteria based on threshold values of strain, pressure, and brain motion as predicted by certain proposed finite element head models (Marjoux et al., 2008; Ward et al., 1980). Despite criticism of the HIC, these alternatives have not been embraced by regulatory bodies. These controversies illustrate that the determination of a satisfactory predictive injury index is a complex problem that remains in debate.

## 1.4 Head impact modelling

The following section outlines the key experimental methods used in blunt head injury research, with particular focus on the development and current status of relevant finite element models. Several modelling techniques have been used in this field. A wide variety of work has been conducted using animals as human analogues. Previously, non-human primates were frequently used (important works include: Gurdjian, 1975; Ommaya & Hirsch, 1971; Ommaya et al., 1967; Unterharnscheidt & Higgins, 1969), while currently it is more common to use small mammals, primarily rodents (Kane et al., 2012; Kharatishvili et al., 2009; McIntosh et al., 1989; Stålhammar, 1975). The animals are subjected to various known mechanical actions, and the physiological responses noted or neuropathological changes examined post-mortem. The use of animals allows *in vivo* experiments to be conducted with the applied forces at a dangerous or fatal level, which is the range of primary interest when investigating the mechanical tolerances of the brain. Disadvantages associated with animal testing involve the need for scaling to human size, different grey to white matter ratios between humans and the animals studied, differences in craniospinal angle, possible influences of anaesthesia, and differences in physiological responses (Goldsmith, 1972; Morales et al., 2005). *In vivo* experiments have been performed on humans by subjecting volunteers to high accelerations on propelled sleds, but clearly the brain behaviour monitored could only be within a limited non-injurious range (Ewing & Thomas, 1972).

*In vivo* methods are valuable given that it is believed the mechanical response of the head may change significantly post-mortem, and the necessary storage and preparation of the cadavers may also have an influence on the tissue material properties (Meulman, 1996). Nonetheless, there is a large body of work involving human cadavers. These *ex vivo* models provide the advantage of allowing large head injury producing forces to be applied to genuine human anatomy, beyond safe limits which would otherwise have to be adhered to. Researchers frequently validate the accuracy and realism of their inorganic or numerical head injury models by comparison to several well known cadaveric experiments. These key benchmark papers include Nahum et al's (1977) and Trosseille et al's (1992) works on the pressure response of the brain, and Hardy et al's (2001) study of brain motion, all involving cadavers subject to impact. However, measurement of results during the above methods can be an issue, as invasive placement of accelerometers, pressure gauges, and other equipment can cause tissue damage. Animal and cadaveric testing can also raise ethical concerns (O'Connor, Smyth, & Gilchrist, 2011).

Another approach is to apply experiments to an inorganic model of the anatomy in question; these models can be physical, analytical, or numerical. Biological systems such as the head are incredibly complex, and so difficulties arise when attempting to construct inorganic models with accurate geometry or similar material properties. Therefore, inorganic models can be said to be most beneficial qualitatively – investigating the mechanisms of brain injury ("pathogenesis"), rather than for determining quantifiable tolerance limits of the brain (Goldsmith, 1972). Inorganic models are frequently designed with the measurement of particular parameters in mind, and hence the measurement of target parameters such as acceleration, pressure, or strain are more straightforward than in organic models. Also inorganic models are often capable of repeated use, and so are ideal for large parametric studies. Physical models have long been used in the field of head injury research. A representative body of work has been conducted by Goldsmith and colleagues, on physical models of the head subject to impact. This valuable research involves models that range in complexity from fluid-filled aluminium or acrylic spherical shells (Kenner & Goldsmith, 1972, 1973), to head-neck systems which incorporate articulated neck attachments (Kabo & Goldsmith, 1983; Landkof, Goldsmith, & Sackman, 1976; Lubock & Goldsmith, 1980).

Analytical models can be cumbersome, and therefore these representations of the head tend to comprise relatively simple geometries and material properties. However, the advantage of these mathematically derived models is that the influence of individual

parameters can be easily investigated with regard to the overall response. Early analytical modelling work was done by Anzelius (1943), who developed expressions which describe the response of a rigid spherical shell filled with inviscid fluid, which represented the skull and brain respectively. Pressures within this fluid could be deduced for a "non-contact" impact, where the sphere is brought suddenly to rest from a constant velocity. Güttinger (1950) used a similar analytical method, representing the head as a fluid-filled spherical shell, but accelerations were applied to the system initially at rest by means of a time-dependent velocity increase. These models predict brain compression at the coup and brain rarefaction at the contrecoup, as later observed by Thomas et al. (1967) and others. Both of these models assume a rigid skull which Engin and colleagues suggested is an unsatisfactory simplification since it results in an infinite wave speed through this medium, and the influence of skull deformation on the intracranial pressure is neglected (Engin & Wang, 1970; Engin, 1969). To overcome these limitations an analytical representation of an elastic spherical shell filled with inviscid fluid was developed (Engin & Liu, 1970; Engin, 1969); head impact was simulated by applying a force-time history to the shell's surface. A slight modification to Engin et al's analytical model was used by Kenner & Goldsmith (1972, 1973) and was found to show reasonable agreement to the response of their physical models of comparable geometry. Since this work not much literature has been released concerning analytical models of head impact – over the last 20 years or so numerical methods, in particular the finite element method (FEM or FE), have become the predominant modelling techniques in this field.

### *1.4.1 Finite element method*

The finite element method is a computational modelling technique. The geometry of the physical system to be investigated is represented computationally, if three-dimensional the simulated geometry will have a volume; this is then divided into a number of discrete smaller volumes. These smaller volumes are known as *elements*, and the array of elements which together make up the description of the entire finite element model is known as a *mesh*. The elements are assigned relevant material properties, such as density and stiffness. When the finite element model is subjected to a simulated experiment, such as impact loading, the partial differential equations (PDEs) required to compute the solution are solved for each integration point, within each element – thus cumulatively describing the solution of the entire system. The finite element method is an approximate technique, its accuracy is not only dependent on the ability to precisely recreate the geometry and material properties in question, but also on the number and distribution of integration

points within the model. In this respect, the accuracy of the finite element method is analogous to the accuracy of a digital camera's pixelated image: the greater the number of elements within a model (or pixels in an image), the more accurate the resulting solution. This method is in principle capable of handling highly complex geometries and material properties, allows limitless repeatability of experiments, and easy monitoring of field effects, not relying on discrete measuring points (e.g. strain gauges) used in physical tests (Sauren & Claessens, 1993). The increase in availability of computer power has produced a growing amount of finite element research in many areas, including the investigation of TBI.

Kenner & Goldsmith (1972) investigated the efficacy of the finite element method in predicting the impact response of an empty spherical shell in comparison to physical and analytical models of the same event; this is one of the earliest applications of the finite element method to the field of head injury. Khalil & Hubbard (1977) studied the response of the head as represented by three finite element models of relatively simple geometry. The head was modelled as a fluid-filled sphere, or an ellipsoid which more closely represented the geometry of the cranial cavity. These models contained distinct linear elastic outer layers which represented the scalp and skull. An important addition was the inclusion of inviscid fluid occupying the central cavity, which was assigned properties similar to water in order to represent the brain. Early finite element models such as these were restricted to simple geometries and materials, but these have quickly risen in complexity, resulting in many elaborate biofidelic representations of the head. As such a wealth of literature exists on the subject of finite element head models, including thorough reviews by Sauren & Claessens (1993), Voo et al. (1996), Raul et al. (2008), and Deck & Willinger (2009).

When investigating TBI particular attention to detail must be given to the geometry of the brain and its surrounding structures, the material properties of these, their *contact conditions* and their *boundary conditions* (which determine how structures within the finite element model interact and are constrained, respectively). Increasing the complexity of the material properties and contacts can significantly raise the computational resources required to reach a solution. Therefore, a common topic in finite element literature is the identification of which simplifying assumptions (be they simplified geometry, materials, or boundary/contact conditions) can be made without appreciably affecting the brain's response (Horgan & Gilchrist, 2004; Khalil & Hubbard, 1977; Kuijpers et al., 1996; Wahi & Merchant, 1977; Wittek & Omori, 2003), usually by means of parametric studies.

Furthermore, the geometry of most finite element models is generated by Computer Aided Design (CAD) methods, which rely on the manual creation of the model's geometry via user input. It is therefore unfeasible to fully recreate the anatomical subtleties of the head using this method, i.e. an amount of geometric approximation will always be necessary; smaller structures tend to be omitted, and larger structures may be considerably simplified. One of the most sophisticated head models created solely by manual CAD methods is presented in (Zong, Lee, & Lu, 2006). Here the head and neck are represented by eight distinct structures, presented in Figure 1.8 (a-j), with the entire model visible in Figure 1.8 (k). Zong et al. include the two components of the central nervous system (brain and spinal cord), the brain's major protective structures (skull and CSF) and the major components of the neck (vertebrae and discs). The anatomy of these structures is based on published geometric data, and is approximate but reasonable. The skull, for example, is reminiscent of a motorbike helmet – it represents to a recognisable degree the inner and outer contours of the skull, but is still considerably simplified. The skull is also constructed as a composite of three layers, in an attempt to recreate the response of the complex microstructure of cranial bone. While this model still represents considerable geometric simplification of the real anatomy, it demonstrates a substantial increase in realism over spherical and ellipsoidal head models found in many physical and finite element experiments.



*Figure 1.8: Zong et al's head model: internal structures and entire model. (Zong et al., 2006)*

Although this model succeeds in capturing the major features of the head, there are several drawbacks to the user driven CAD method: the creation of complex models is time consuming, and requires geometric simplification and subjectivity in terms of user input.

### *1.4.2 Image-based meshing*

Image-based meshing is a novel finite element technique which can avoid or reduce many of these deficiencies. While image-based meshing exists in different forms, the basic

premise is to convert an image of the object in question directly into a finite element mesh. This is often done on an automated or semi-automated basis, increasing the accuracy of the model by minimising user input (and possible user error). The speed and robustness of the process makes it feasible to include more structures within a model compared to traditional CAD models, and it has intrinsically high geometric accuracy. These advantages make image-based meshing particularly suited to the study of biological systems. The geometric fidelity of the model is restricted mainly by the resolution of the original image, but can also be influenced by noise, poor contrast between materials, and motion artefacts (Young et al., 2008).

One of the earliest uses of this approach of interest to TBI investigation was by Mehta et al. (1997), who created an image-based computational model of the human skull. 14 two-dimensional image "slices" were selected from three-dimensional computed tomography (CT) scan data of a cadaveric skull. These slices depicted parallel section views throughout the head. On each of these slices the skull was manually highlighted using an image processing tool. Mehta et al. then used a code to automatically convert these highlighted outlines into CAD coordinate and spline data, from which a model could be constructed. Similarly the Université Louis Pasteur (ULP) head model, presented in (Willinger et al., 1999), is based on 18 slices of an *in vivo* magnetic resonance imaging (MRI) scan, but was completed using manual CAD methods. However, the ULP model is far more complex, consisting of skull, scalp, meninges, the major components of the brain, and includes a Lagrangian formulation to represent the CSF layer. This model has been validated against cadaveric experiments by Nahum et al. (1977) and Trosseille et al. (1992) (Willinger et al., 1999), and has been applied to legal medicine studies (Raul et al., 2006). Since early pioneering efforts such as these the technology has developed dramatically.

The most recent method is to first obtain a three-dimensional image of the object (e.g. the head) by means of volumetric scanning techniques, typically CT or MRI. MRI tends to be used for *in vivo* investigations as it provides good contrast between soft biological tissues, and repeated CT scans can be harmful. Data from these volumetric scans is in the form of a regular Cartesian grid, i.e. an array of "voxels" (three-dimensional pixels). Each voxel has a greyscale value which indicates the image signal strength at that location. Structures ("volumes of interest" or VOIs) can be distinguished within the scanned volume by differences in greyscale value; this process is known as "segmentation". Segmentation can be performed by a variety of methods, such as manually selecting voxels, or automated grouping together of voxels which are within a certain greyscale threshold. The next stage

is to define the exterior surfaces of these VOIs. By far the most popular approaches for the extraction of these surfaces are based on the marching cubes algorithm, which considers the centre points of each voxel to be vertices in a grid. The algorithm proceeds through the scanned volume processing groups of adjacent vertices in this grid (eight vertices at a time, therefore a "cube"), determining which vertices in each group can be considered inside or outside the VOI. In this way the algorithm is able to determine the most suitable way each "cube" can be bisected by a series of conforming triangular surface patches, therefore generating the exterior surface of each VOI. This approach can be improved by accounting for the "partial volume effect": at the surface of a scanned object, the exterior surface of that object may only partially occupy the voxel in that area – in this case the greyscale value will reflect the fraction of the voxel occupied by that object. Taking this into account, if the marching cube surface patches are allowed to intersect at appropriate points between the grid vertices (based on the greyscale value of each voxel), rather than intersecting only at the vertices themselves, it is possible to obtain markedly smoother and more faithful surfaces (i.e. "sub-voxel" accuracy) (Young et al., 2008). With the exterior of the VOIs defined by discretised surfaces they can then be meshed using traditional mesh generation algorithms.

Image-based meshing using a high degree of automation, as described above, is still an emerging technology; many of the most recent models still rely on an appreciable amount of user input. Nevertheless image-based meshing has invariably been utilised, to greater or lesser degree, in the construction of the latest generation of sophisticated finite element head models – some examples include:

- The Kungliga Tekniska Högskolan (KTH) model contains cranial and facial bones, scalp, distinct structures of the brain and spinal cord, meninges, and 11 pairs of bridging veins (Kleiven & Von Holst, 2002; Kleiven, 2006). A CSF layer is included which allows tangential movement of the brain relative to the dura, but includes radial transmission of tension and compression. A simplified neck was also modelled. The mesh has been parameterised, allowing it to be scaled appropriately without compromising mesh quality. The model was based on contours manually extracted from cross-sectional images from the "Visible Human Database" (www.nlm.nih.gov/research/visible/visible_human.html). This model has been validated against cadaveric impact pressure data (Nahum et al., 1977), brain motion data (Hardy et al., 2001), as well as cadaveric impact experiments by Trosseille et al. (1992) (Ho, 2008).

- Horgan & Gilchrist's (2004) University College Dublin Brain Trauma Model (UCDBTM) differentiates both cranial and facial bones, grey and white matter of the brain, CSF, and the vasculature. The model was constructed using skull geometries acquired from CT scans from the Visible Human Database, and was validated against cadaveric impact tests (Trosseille et al., 1992) and brain motion data (Hardy et al., 2001).
- El Sayed et al's (2008) University of Salerno model was constructed from MRI data from "The Whole Brain Atlas" (www.med.harvard.edu/aanlib/home.html). This model includes the skull without facial bones, the CSF layer, and ventricles. The soft tissue region is detailed, with distinctions made between grey matter, white matter, and the corpus callosum and brain stem. The model showed good agreement with the brain's pressure response measured in Nahum et al's (1977) benchmark experiments (El Sayed et al., 2008).
- The model presented in (Chen & Ostoja-Starzewski, 2010) was developed directly from *in vivo* MRI scan data. A custom code was implemented which converted the image voxels into regular cubic hexahedral mesh elements. Laplacian smoothing was then applied directly to the mesh to remove the hexahedral elements' unrealistic jagged edges. The final model differentiates skull, CSF, grey matter and white matter; and was validated against Nahum et al's (1977) results.

One problem involved in the generation of head models is the large degree of variation between individuals. The semi-automated nature of the latest image-based meshing techniques addresses this problem by making the generation of individual patient-specific models tractable. The ability to easily create customised computational models opens up a host of possibilities. A specific finite element model of an individual could aid forensic investigation (Motherway et al., 2009), could aid in surgery planning for that individual, or could be used in the generation of custom headgear. While image-based meshing can aid the geometric accuracy of a head model, the authenticity of the model's response is also dependent on the material properties it is assigned; when concerned with biological systems determining the most suitable material formulations becomes non-trivial.

## 1.5 Related research

Previous work by Young & Morfey, and E. Johnson & Young, has demonstrated using simple models that large transient pressures can occur in the brain as a result of low mass, low velocity head impacts. Young & Morfey (1998) performed a range of parametric

studies on a 2-phase finite element model of the human head in order to explore the sensitivity of the brain's pressure response to changes in material, geometric and loading parameters. The model used was a simple fluid-filled sphere consisting of an outer shell with external radius $R_{sh}$, internal radius $R_f$, and thickness $h$, representing the skull, containing a fluid sphere representing the brain. The skull material was linear elastic with modulus $E_{sh}$, Poisson's ratio $\nu_{sh}$, and density $\rho_{sh}$, while the brain was modelled as an inviscid fluid with bulk modulus $B_f$, and density $\rho_f$. All materials were isotropic and homogeneous. Baseline geometric and material constants appropriate for the human head were taken from Engin's (1969) analytical model[2]. This simplified model was used to reduce the complexity of the system so that critical parameters which have a large effect become more evident (Young & Morfey, 1998).

The finite element mesh was in the form of a 30º wedge, which had symmetry conditions applied such that it behaves as a full sphere. The exterior shell was composed of 24 two-dimensional shell elements, while the interior fluid was modelled by 384 three-dimensional eight noded hexahedral elements. Impact loading was simulated by applying a pressure-time history to a circular cap with a sector half angle of 15º on the exterior of the shell. A Hanning squared function was used, which is a reasonable approximation of impact loading[3] (Young & Morfey, 1998). A sensitivity study was performed, consisting of a range of simulated impacts with varying impact duration $T_p$, while all other parameters, including the peak impact force $F_{max}$, were held constant. As impact duration was lowered Young &

---

[2] These baseline values were:

Skull: $E_{sh}$ = 13.79 GPa, $\nu_{sh}$ = 0.25, $\rho_{sh}$ = 2140 kg/m$^3$

Brain: $B_f$ = 2.18 GPa, $\rho_f$ = 1002 kg/m$^3$

Geometry: $R_{sh}$ = 80.01 mm, $R_f$ = 76.20 mm, $h$ = 3.81 mm

[3] Hanning squared pressure-time history given by:

$$P(t) = \frac{F(t)}{(\pi \cdot R_f^2 \cdot \sin^2\varphi)} \qquad [1.3]$$

$$\text{where } F(t) = F_{max}\left[\frac{1}{2} - \frac{1}{2}\cos\left(2\pi \cdot \frac{t}{T_p}\right)\right]^2 \qquad [1.4]$$

$t$ is time (s), $T_p$ is the duration of the applied load (s), $F_{max}$ is the maximum force in the x-direction (N), $R_f$ is the inner radius of the skull (m), and $\varphi$ is the loading area sector half angle (rad). (Young & Morfey, 1998)

Morfey found that the intracranial response began to deviate from the typical linear pressure gradient through the brain observed by Thomas et al. (1967); i.e. the system's response was no longer "quasi-static".

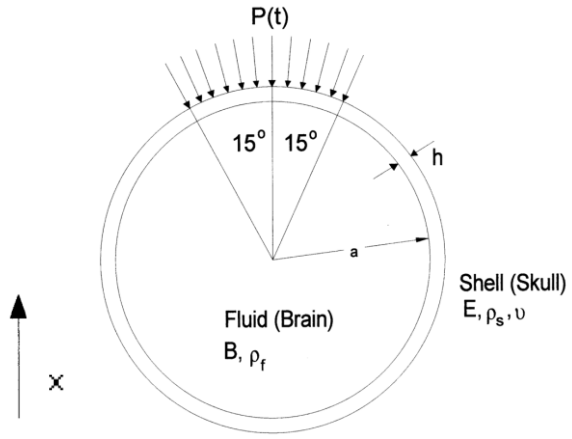


*Figure 1.9: Diagram of Young & Morfey's fluid-filled spherical shell model. (Young & Morfey, 1998)*

The dilatational wave speed for grey and white matter is large such that a pressure pulse can typically traverse the diameter of the cranial cavity 10 times per millisecond (Bradshaw & Morfey, 2001). However the vast majority of blunt head impact experiments are limited to a narrow range of contact durations: typically impacts of 3 to 10 ms. As such, for these comparatively long duration impacts, the pressure in the brain will arrive at hydrostatic equilibrium almost instantaneously (Bradshaw & Morfey, 2001). This response is "quasi-static", namely the pressure behaviour is essentially identical to that of a fluid-filled rigid container under constant acceleration. A linear pressure gradient will exist in the brain, varying from the maximum positive pressure $P_{quasi}$ under the site of impact (coup) to the minimum of negative pressure of equal magnitude $-P_{quasi}$ at the contrecoup. In this case, the pressure is not dependent on the shear or bulk modulus of the tissue, but only on its density (Bradshaw & Morfey, 2001). These peak internal pressures in the brain can be predicted for the quasi-static response quite simply from the expression:

$$P_{quasi} = \frac{r_c \cdot \rho_f \cdot F_{max}}{m} \qquad [1.5]$$

where $r_c$ is the radius of the brain measured from its centre of gravity to its exterior surface at the coup or contrecoup (m), $\rho_f$ is the density of brain tissue (kg/m$^3$), $F_{max}$ is the peak force transmitted by the impact (N), and $m$ is the total mass of the skull and its contents (kg) (Young & Morfey, 1998).

*Figure 1.10: The rigid-body acceleration of a fluid-filled container and the skull, generating a quasi-static pressure response in the fluid and in the brain respectively. (Gross, 1958) Before this phenomenon could be verified experimentally by Thomas et al. (1967) and others, it had been proposed by Gross in 1958.*

This pressure behaviour is prevalent in head impact literature, in which it is uncommon to investigate short duration impacts. A portion of Young & Morfey's results are presented below in Figure 1.11. In agreement with the quasi-static theory, the magnitude of the peak intracranial pressures for medium to long duration impacts (approximately 1 ms and above) was independent of the measured contact duration $T_p$, and solely a function of peak force $F_{max}$. The greatest positive and negative pressures occurred at the coup and at the contrecoup respectively; these rose and fell in correlation with the force-time history of the impact, as was expected.

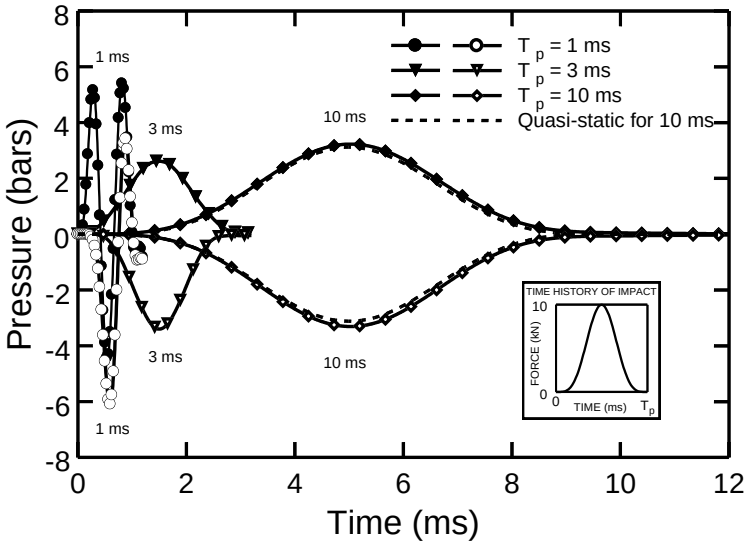


*Figure 1.11: Pressure response in the brain for impacts with $T_p$ = 1, 3, and 10 ms. Solid markers indicate pressures recorded at the coup, hollow markers at the contrecoup. (Young & Morfey, 1998)*

However as impact duration was reduced to 1 ms, the peak pressures observed became significantly greater than predicted by the quasi-static solution, and both positive and

negative pressure transients were generated at the coup and contrecoup, i.e. the response was qualitatively and quantitatively different. As the impact duration was further reduced the magnitudes of the observed pressures continued to rise further above what would be expected for a quasi-static response. Peak intracranial pressures of over 60 bars (6 MPa) and -30 bars (-3 MPa) were recorded at the coup for the shortest impact studied (0.05 ms) – this is in a sense a "magnification" of the respective peak positive and negative pressures by approximately 20 and 10 times the quasi-static pressures (i.e. those in the 3 ms and 10 ms impacts) despite an equal maximum applied force. Similar behaviour is observed at the contrecoup. Young & Morfey proposed that this dynamic response of the head may explain dual coup-contrecoup injuries, by way of the large pressure transients localised in these regions. Furthermore, it was suggested that the formation of negative pressures at the coup and contrecoup during the dynamic response makes cavitation a possible injury mechanism for both of these locations, rather than just at the contrecoup.

The period of the first (n=2) equivoluminal mode of vibration $T_\Omega$ for the fluid-filled shell was calculated using a modification of an exact analytical solution based on full 3D elasticity equations presented in (Jiang, Young, & Dickinson, 1996). The results of the parametric studies could then be collapsed by normalising the impact duration $T_p$ on this period. This non-dimensional ratio was found to be a good predictor of the system's response: a critical value of approximately $T_p$ / $T_\Omega$ = 2 exists, above which the pressure response of the brain will be quasi-static. Lower values predict the onset of dynamic effects accompanied by large positive and negative pressure transients (Young & Morfey, 1998). The exact solution for the period of oscillation of the n=2 equivoluminal mode of a single spherical shell filled with incompressible fluid was shown by Young (2002) to be well approximated by the closed-form explicit expression:

$$T_\Omega = \sqrt{\frac{3\pi(5+\nu_{sh})(m_{sh}+m_f)}{8hE_{sh}}} \qquad [1.6]$$

where $m_{sh}$ + $m_f$ is the mass of the shell and the mass of the fluid (kg) i.e. the total head mass for this 2-phase model. Interestingly, it was shown in (Young, 2002) that the frequency of this n=2 mode is insensitive to the ratio of the density of the shell and fluid – the frequency is negligibly affected by whether the mass of the system is concentrated in the shell or distributed throughout the fluid. Furthermore, the frequency is not affected by the bulk modulus of the fluid, it is identical for a spherical shell *in vacuo* or when filled with incompressible fluid. Young (2002) considers the equivoluminal nature of the n=2 mode (i.e. the independence of this mode on the compressibility of the fluid) to explain why the

dynamic response of the head model is not influenced by the inclusion of a hole in the shell (e.g. simulating the foramen magnum), the main outcome of which would be to allow volume change in the cranial cavity despite being filled with incompressible brain tissue.

Young (2003) developed an analytical description of the case of a fluid-filled sphere subject to impact by an elastic spherical projectile. The model can be applied to the study of blunt head impacts by defining the geometric and linear material constants as equal to those used in Young & Morfey's finite element model.

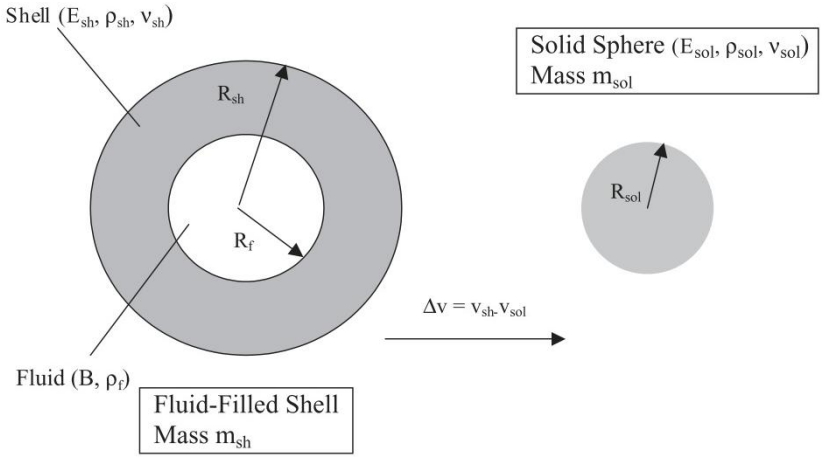


*Figure 1.12: Diagram representing the analytical head impact model. (Young, 2003)*

Dynamic contact problems such as impact are generally approximated analytically by an extension of the classical Hertzian theory of statical elastic contact. This theory is based on the assumptions that: (i) the contact surfaces are frictionless, (ii) the contact surfaces are continuous and non-conforming, (iii) the strains are small, and (iv) each solid can be considered as an elastic half-space (K. L. Johnson, 2003). This theory can be extended to apply to impact. However the resulting description will not be truly dynamic: inertial effects cannot be accounted for and are ignored. This imposes further assumptions: (v) the motion of stress waves is negligible, and (vi) at any instant the total mass of each body is moving with the velocity of its centre of mass (K. L. Johnson, 2003). Young's (2003) analytical model considers both Hertzian contact stiffness $k_H$ and local bending and membrane stiffness $k_{sh}$, for this case respectively given by:

$$k_H = \frac{4}{3} R^{*1/2} E^* \qquad [1.7]$$

$$k_{sh} = 2.3(E_{sh}h^2)/R_{sh}(1-\nu_{sh}^2)^{1/2} \qquad [1.8]$$

The assumptions inherent in these expressions mean they are only valid within certain limits. The expression for Hertzian contact stiffness requires that: (i) the maximum contact area radius $a$ is small compared to the relative radius of curvature $R^*$ (i.e. $a / R^* << 1$), and (ii) $a$ is small compared to the dimensions of each body ($a / h << 1$). The expression for bending and membrane stiffness is valid provided: (iii) if $(4/27(h/R_{sh})^2(1 - \nu_{sh}^2))^{1/4} < 0.4$ then $a / h << 1$, and (iv) if $a/(R_{sh}h)^{1/2}(12(1 - \nu_{sh}^2))^{1/4} < 0.4$ then $a / h$ not $<< 1$ (Young, 2003).

If $R_{sol}$ is the external radius of the spherical impactor, $E_{sol}$ is its elastic modulus, and $m_{sol}$ is its mass, then the relative properties of the head and impactor are given by:

$$R^* = \frac{R_{sh}R_{sol}}{R_{sh}+R_{sol}} \qquad E^* = \frac{E_{sh}E_{sol}}{(1-\nu_{sol}^2)E_{sh}+(1-\nu_{sh}^2)E_{sol}} \qquad m^* = \frac{m \cdot m_{sol}}{m+m_{sol}} \qquad [1.9, 1.10, 1.11]$$

where $m$ is the total mass of the head system (kg), and $R^*$, $E^*$, and $m^*$ are the relative external radii, elastic moduli, and masses respectively (Young, 2003). The two stiffnesses $k_H$ and $k_{sh}$ are considered decoupled and treated in series, which allows approximate expressions to be derived for global impact characteristics such as: impact duration $T_p$, peak impact force $F_{max}$, and the Head Injury Criterion (HIC):

$$T_p = \pi\sqrt{\frac{m^*}{k_{effec}}} \qquad \text{where} \qquad k_{effec} = 1/\left(\frac{1}{k_{sh}} + \frac{1}{k_H^{2/3}F_{max}^{1/3}}\right) \qquad [1.12, 1.13]$$

$$m^*\Delta v^2 = \frac{F_{max}^2}{k_{sh}} + \frac{4}{5}\frac{F_{max}^{5/3}}{k_H^{2/3}} \qquad [1.14] \qquad \text{and}$$

$$HIC = \frac{7.25311}{\pi^{5/2}}\frac{F_{max}}{m}T_p \qquad [1.15]$$

where $\Delta v$ is the mutual approach velocity of the fluid-filled sphere and impactor (m/s). The expressions for $T_\Omega$ [1.6] and $T_p$ [1.12] can be used in combination to determine the non-dimensional ratio $T_p / T_\Omega$ for a given head impact, therefore predicting the nature of the intracranial response (Young, 2003).

E. Johnson (2005) and E. Johnson & Young (2005) investigated the ability of Young's analytical model to predict the onset of dynamic pressure transients in a range of experimental head impacts. Three physical head models were used, each one increasing in realism and complexity over the last – the three models consisted of: a polymer spherical shell, a rapid prototyped model of a skull based on *in vivo* MRI data, and a cadaveric skull, all of which were filled with fluid to represent the brain. In this way the applicability of this analytical model beyond simple fluid-filled sphere representations of the head was also

progressively investigated. Each model was subject to a range of blunt impacts via a pendulum-mass system. Parametric studies were carried out by varying impactor mass and velocity in order to investigate the sensitivity of these systems to the changing parameters. Pressure transducers monitored the fluid pressures at the coup and contrecoup during these impacts. It was found that the analytical model's predictions agreed well with the experimental results, i.e. the $T_p$ / $T_\Omega$ ratio could be used to forecast which experimental impacts deviated from the quasi-static response. Furthermore the dynamic response (and corresponding large intracranial pressure transients) was observed in all three models of increasing complexity, supporting the theory that the dynamic magnification of pressures is also valid for non-spherical geometries (E. Johnson & Young, 2005; E. Johnson, 2005).

## 1.6 Current study

The current research explores the dynamic intracranial response as a possible cause of coup-contrecoup injuries, and the mechanics of this phenomenon. This study is focussed on blunt head impact, and is concerned primarily with the resulting pressures in the brain and intracranial fluids. Furthermore, experiments were performed in such a way as to simplify the problem so that only translational accelerations needed to be considered: attempt was made to minimise any rotational accelerations by keeping the mass of the impactor low where possible, by setting the axis of impact to run through the head's centre of gravity, and by implementing only direct impacts (i.e. where the velocity of the projectile is normal to the head's surface). Impacts were simulated numerically using the finite element method, and Young's (2003) analytical description of head impact was used in parallel to determine the accuracy and limits of this model.

The dynamic intracranial response, first documented by Young & Morfey (1998) and Young (2003) in a simple fluid-filled sphere, was studied further by E. Johnson (2005) who incrementally introduced more realistic geometry and materials to the skull. In the current study further complexities are introduced, such as realistic brain material, a CSF layer, a scalp layer, and the neck. This work progressed in three stages, utilising finite element models of increasing biofidelity.

*Stage 1:* The first model approximated the human head as a fluid-filled sphere. For this initial model, material properties and geometric dimensions were identical to those used in Young & Morfey's (1998) original work, so that the results could be conveniently compared. Unlike Young & Morfey's work however, rather than indirectly modelling impact through the application of a force-time history, here impacts were simulated directly

by modelling collision of the head with a spherical impactor. A parametric study was carried out by subjecting the stationary head model to ten impacts with incrementally varying impactor masses and velocities, in order to be able to study the model's response to impacts with a wide range of contact durations. Young's (2003) analytical model was employed to calculate the masses required for the impactors to achieve a similar peak force $F_{max}$ in all of these impact cases.

*Stage 2:* The second model was of intermediate complexity; it utilised the same simple linear material properties and impactor as the fluid-filled sphere model, but had a modified skull with high geometric accuracy. Image-based meshing techniques were used to replace the spherical shell with realistic skull geometry captured from *in vivo* MRI scan data of an adult human male. A parametric study was carried out in the same manner as in Stage 1: 12 impacts were performed on the rear of the skull, these had varying impactor masses and velocities such that the impacts were of similar peak force, but dissimilar duration. Additional high energy impacts were also performed to study the influence of geometric non-linearities which may result from significantly increased impact forces.

*Stage 3:* The final stage employed a complex high biofidelity model of the whole head and neck. This model was generated using semi-automated image-based meshing techniques, which allowed the brain, spinal cord, CSF layer, skull, scalp, vertebrae and intervertebral discs to be accurately meshed. The model was derived from the same set of MRI data that was used in Stage 2. This scan data had been segmented by Simpleware Ltd. under the auspices of a US Naval Research Laboratory (NRL) contract, and had been used previously to generate a finite element model of the head that was first presented in (Weber & Young, 2003). The Simpleware-NRL head model was modified in this study: the mesh was adapted to include an area of local refinement in order to better capture the contact mechanics at the impact site, and the various structures were assigned updated material properties based on a thorough review of the open literature. Many structures could be satisfactorily modelled by linear elastic materials, but those of particular importance to the impact response were assigned more complex material models: nervous tissue was represented by a viscoelastic model, the CSF was an elastic fluid, and the scalp beneath the impact site was assigned non-linear elastic properties based on *in vitro* tests by Gadd et al. (1970). This represented significant geometric and material advancements over Stages 1 and 2. The biofidelic model was validated against data from Nahum et al's (1977) cadaveric experiments, which is used widely in the literature to verify the accuracy of head models. The size and complexity of this finite element model required greater computational

resources per simulation; therefore, instead of a large parametric study as performed previously, 3 blunt head impacts (excluding the validation) were simulated in the form of individual case studies.

## 1.7 Hypothesis

"Dynamic magnification of peak intracranial pressures occurs in a highly biofidelic head model under realistic impact conditions."

## 1.8 Aims

This study aims to verify whether the dynamic intracranial response (associated with potentially injurious pressures at the coup and contrecoup) is capable of occurring in the real human head under reasonable impact conditions, or whether it is an artefact of the large geometric and material simplifications made in the test cases it has been observed in so far. The research was also focussed on achieving a greater understanding of the mechanics involved in the generation of these large pressure transients.

## 1.9 Objectives

- To develop a fluid-filled sphere finite element model of the human head, based on work by Young & Morfey (1998).
- To develop a finite element model of the human head utilising realistic skull geometry captured from MRI scan data.
- To conduct a thorough literature survey on tissue material properties of the human head in order to modify an existing image-based finite element model of the whole head and neck.
- To validate the efficacy of this newly created biofidelic model at predicting the pressure response of the brain by comparison with Nahum et al's (1977) cadaveric impact data.
- To explore the effect of varying impactor mass and velocity on the contact duration and maximum force of head impacts as simulated in three models of increasing realism.
- To investigate the effect these varying impact characteristics have on the intracranial pressure behaviour of the three head models, and to verify whether the dynamic intracranial response occurs despite the progressive inclusion of realistic geometries and material properties.

- To explore the applicability of Young's (2003) analytical model of a fluid-filled sphere in collision with an elastic spherical projectile to head impact problems, based on the model's predictions of contact duration $T_p$, and maximum force $F_{max}$ compared to the results of the finite element simulations.
- To investigate whether collapsing the results on the non-dimensional ratio $T_p$ / $T_\Omega$ reveals any trends that the intracranial pressure response adheres to, and to what extent these trends are shared between the three head models of increasing realism.
- To probe the mechanism that gives rise to the dynamic intracranial response originally observed by Young & Morfey (1998).

Anzelius, A. (1943). The effect of an impact on a spherical liquid mass. *Acta Pathologica Microbiologia Scandanavia*, *48*, 153–159.

Bandak, F. A. (1996). Biomechanics of impact traumatic brain injury. *NATO Advanced Studies Institute: Crashworthiness of Transportation Systems*, *1*.

Bradshaw, D., & Morfey, C. L. (2001). Pressure and shear responses in brain injury models. *Proceedings of the 17th International Technical Conference on the Enhanced Safety of Vehicles* (pp. 1–10). Amsterdam, The Netherlands.

Brennen, C. (2003). Cavitation in biological and bioengineering contexts. *Proceedings of the 5th International Symposium on Cavitation*. Osaka, Japan.

Chen, Y., & Ostoja-Starzewski, M. (2010). MRI-based finite element modeling of head trauma: spherically focusing shear waves. *Acta Mechanica*, *213*(1-2), 155–167.

Cifu, D. X., & Caruso, D. (2010). *Traumatic Brain Injury*. Demos Medical, New York.

Claessens, M. H. A. (1994). Anatomical description of the human head. *Technical report*. Retrieved from http://alexandria.tue.nl/repository/books/642185.pdf

Cory, C., Jones, M. D., & James, D. (2001). The potential and limitations of utilising head impact injury models to assess the likelihood of significant head injury in infants after a fall. *Forensic Science International*, *123*, 89–106.

Cramer, G. D., Ross, J. K., Raju, P. K., Cambron, J. A., Dexheimer, J. M., Bora, P., McKinnis, R., et al. (2011). Distribution of cavitations as identified with accelerometry during lumbar spinal manipulation. *Journal of Manipulative and Physiological Therapeutics*, *34*(9), 572–83.

Dawson, S. L., Hirsch, C. S., Lucas, F. V., & Sebek, B. A. (1980). The contrecoup phenomenon: Reappraisal of a classic problem. *Human Pathology*, *11*(2), 155–166.

Deck, C., & Willinger, R. (2009). The current state of human head finite element modelling. *Int. J. Vehicle Safety*, *4*(2), 85–112.

Department of Health. (2005). *The national service framework for long term conditions*. *BMJ (Clinical research ed.)* (Vol. 330). doi:10.1136/bmj.330.7503.1280

Drew, L. B., & Drew, W. E. (2004). The contrecoup–coup phenomenon: a new understanding of the mechanism of closed head injury. *Neurocritical Care*, *1*, 385–390.

Edberg, S., Rieker, J., & Angrist, A. (1963). Study of impact pressure and acceleration in plastic skull models. *Laboratory Investigation*, *12*(12), 1305–1311.

El Sayed, T., Mota, A., Fraternali, F., & Ortiz, M. (2008). Biomechanics of traumatic brain injury. *Computer Methods in Applied Mechanics and Engineering*, *197*(51-52), 4692–4701.

Engin, A. E. (1969). The axisymmetric response of a fluid-filled spherical shell to a local radial impulse – a model for head injury. *Journal of Biomechanics*, *2*(3), 325–341.

Engin, A. E., & Liu, Y. K. (1970). Axisymmetric response of a fluid-filled spherical shell in free vibrations. *Journal of Biomechanics*, *3*(1), 11–16.

Engin, A. E., & Wang, H. C. (1970). A mathematical model to determine viscoelastic behavior of in vivo primate brain. *Journal of Biomechanics*, *3*(3), 283–96.

Ewing, C. L., & Thomas, D. J. (1972). *Human Head and Neck Response to Impact Acceleration*. Pensacola, FL. Retrieved from http://oai.dtic.mil/oai/oai?verb=getRecord&metadataPrefix=html&identifier=AD0747988

Federal Motor Carrier Safety Administration. (2013). Standard No. 208; Occupant crash protection. Retrieved April 30, 2013, from http://www.fmcsa.dot.gov/rules-regulations/administration/fmcsr/fmcsrruletext.aspx?reg=r49CFR571.208

Flint, E. B., & Suslick, K. S. (1991). The temperature of cavitation. *Science*, *253*(5026), 1397–9.

Gadd, C. W. (1966). The use of a weighted-impulse criterion for estimating injury hazard. *Proceedings of the 10th STAPP Car Crash Conference* (pp. 164–174).

Gadd, C. W., Nahum, A. M., Schneider, D. C., & Madeira, R. G. (1970). Tolerance and properties of superficial soft tissues in situ. *Proceedings of the 14th STAPP Car Crash Conference* (pp. 356–368).

Goldsmith, W. (1972). Biomechanics of head injury. In Y. C. Fung, N. Perrone, & M. Anliker (Eds.), *Biomechanics: Its Foundations and Objectives*. Prentice-Hall, Englewood Cliffs, NJ.

Goldsmith, W. (1981). Current controversies in the stipulation of head injury criteria. *Journal of Biomechanics*, *14*(12), 883.

Gross, A. G. (1958). A new theory on the dynamics of brain concussion and brain injury. *Journal of Neurosurgery*, *15*, 548–561.

Gurdjian, E. S. (1975). *Impact head injury: mechanistic, clinical, and preventive correlations*. Charles C Thomas.

Güttinger, W. (1950). Der Stoßeffekt auf eine Flüssigkeitskugel als Grundlage einer Physikalischen Theorie der Entstehung von Gehirnverletzungen. *Zeitschrift für Naturforschung*, *5a*, 622–628.

Hardy, W. N., Foster, C., Mason, M., Yang, K. H., & King, A. I. (2001). Investigation of Head Injury Mechanisms Using Neutral Density Technology and High-Speed Biplanar X-ray. *Stapp Car Crash Journal*, *45*, 337–368.

Hardy, W. N., Khalil, T. B., & King, A. I. (1994). Literature review of head injury biomechanics. *International Journal of Impact Engineering*, 561–586.

Ho, J. (2008). *Generation of patient specific finite element head models*. *Thesis*. Royal Institute of Technology, Stockholm. Retrieved from http://ntnu.diva-portal.org/smash/get/diva2:126650/FULLTEXT01

Holbourn, A. H. S. (1943). Mechanics of head injuries. *Lancet*, *2*, 438–441.

Holbourn, A. H. S. (1945). The mechanics of brain injuries. *British Medical Bulletin*, *3*, 147–149.

Holland, C. K., & Apfel, R. E. (1990). Thresholds for transient cavitation produced by pulsed ultrasound in a controlled nuclei environment. *The Journal of the Acoustical Society of America*, 2059–2069.

Horgan, T., & Gilchrist, M. D. (2004). Influence of FE model variability in predicting brain motion and intracranial pressure changes in head impact simulations. *International Journal of Crashworthiness*, *9*(4), 401–418.

Huang, H. M., Lee, M. C., Lee, S. Y., Chiu, W. T., Pan, L. C., & Chen, C. T. (2000). Finite element analysis of brain contusion: an indirect impact study. *Medical & Biological Engineering & Computing*, *38*(3), 253–9.

Jenkins, L. W., Moszynski, K., Lyeth, B. G., Lewelt, W., DeWitt, D. S., Allen, A., Dixon, C. E., et al. (1989). Increased vulnerability of the mildly traumatized rat brain to cerebral ischemia: the use of controlled secondary ischemia as a research tool to identify common or different mechanisms contributing to mechanical and ischemic brain injury. *Brain Research*, *477*(1-2), 211–224.

Jiang, H., Young, P. G., & Dickinson, S. (1996). Natural frequencies of vibration of layered hollow spheres using exact three-dimensional elasticity equations. *Journal of Sound and Vibration*, *195*(1), 155–162.

Johnsen, E., Colonius, T., & Cleveland, R. (2009). Damage potential of the shock-induced collapse of a gas bubble. *Proceedings of the 7th International Symposium on Cavitation*. Michigan, USA.

Johnson, E. (2005). *The response of the human head to blunt impact: experimental validation of an analytical model. Thesis*. University of Exeter. Retrieved from http://ethos.bl.uk/OrderDetails.do?uin=uk.bl.ethos.421650

Johnson, E., & Young, P. G. (2005). On the use of a patient-specific rapid-prototyped model to simulate the response of the human head to impact and comparison with analytical and finite element models. *Journal of Biomechanics*, *38*(1), 39–45.

Johnson, K. L. (2003). *Contact Mechanics* (9th ed.). Cambridge University Press.

Kabo, J., & Goldsmith, W. (1983). Response of a human head-neck model to transient saggital plane loading. *Journal of Biomechanics*, *16*(5), 313–321.

Kane, M. J., Angoa-Pérez, M., Briggs, D. I., Viano, D. C., Kreipke, C. W., & Kuhn, D. M. (2012). A mouse model of human repetitive mild traumatic brain injury. *Journal of Neuroscience Methods*, *203*(1), 41–9.

Kenner, V. H., & Goldsmith, W. (1972). Dynamic loading of a fluid-filled spherical shell. *International Journal of Mechanical Sciences*, *14*(9), 557–568.

Kenner, V. H., & Goldsmith, W. (1973). Impact on a simple physical model of the head. *Journal of Biomechanics*, *6*(I), 1–11.

Khalil, T. B., & Hubbard, R. P. (1977). Parametric study of head response by finite element modeling. *Journal of Biomechanics*, *10*(2), 119–32.

Kharatishvili, I., Sierra, A., Immonen, R. J., Gröhn, O. H. J., & Pitkänen, A. (2009). Quantitative T2 mapping as a potential marker for the initial assessment of the severity of damage after traumatic brain injury in rat. *Experimental Neurology*, *217*(1), 154–64.

Kleiven, S. (2006). Evaluation of head injury criteria using a finite element model validated against experiments on localized brain motion, intracerebral acceleration, and intracranial pressure. *International Journal of Crashworthiness*, *11*(1), 65–79.

Kleiven, S., & Von Holst, H. (2002). Consequences of head size following trauma to the human head. *Journal of Biomechanics*, *35*(2), 153–60.

Kuijpers, A., Claessens, M. H. A., & Sauren, A. (1996). A two-dimensional FEM analysis of the response of the human head to impact: the importance of boundary conditions. *Computer Methods in Biomechanics and Biomedical Engineering*, 207–216.

Landkof, B., Goldsmith, W., & Sackman, J. L. (1976). Impact on a head-neck structure. *Journal of Biomechanics*, *9*, 141–151.

Lindenberg, R., & Freytag, E. (1960). The mechanism of cerebral contusions. *Archives of Pathology*, *69*, 440. Not first source. Paper unavailable, out of print. Information is as stated in (Dawson et al., 1980; Drew & Drew, 2004; Hardy et al., 1994).

Lubock, P., & Goldsmith, W. (1980). Experimental cavitation studies in a model head-neck system. *Journal of Biomechanics*, *13*(12), 1041–1047.

Marik, P., Varon, J., & Trask, T. (2002). Management of Head Trauma. *Chest*, *122*(2), 699–711.

Marjoux, D., Baumgartner, D., Deck, C., & Willinger, R. (2008). Head injury prediction capability of the HIC, HIP, SIMon and ULP criteria. *Accident; Analysis and Prevention*, *40*(3), 1135–48.

McIntosh, T. K., Vink, R., Noble, L., Yamakami, I., Fernyak, S., Soarest, H., & Faden, A. L. (1989). Traumatic brain injury in the rat: characterization of a lateral fluid-percussion model. *Neuroscience*, *28*(1), 233–244.

Mehta, B. V, Rajani, S., & Sinha, G. (1997). Comparison of image processing techniques (magnetic resonance imaging, computed tomography scan and ultrasound) for 3D modeling and analysis of the human bones. *Journal of Digital Imaging*, *10*(3 Suppl 1), 203–6.

Meulman, J. (1996). An experimental investigation to the constitutive behaviour of brain tissue. *Technical report*, *80*(10), 289–302. Retrieved from http://www.narcis.nl/publication/RecordID/oai:library.tue.nl:461975/Language/en

Misra, J., & Chakravarty, S. (1985). Dynamic response of a head-neck system to an impulsive load. *Mathematical Modelling*, *6*(2), 83–96.

Morales, D. M., Marklund, N., Lebold, D., Thompson, H. J., Pitkanen, A., Maxwell, W. L., Longhi, L., et al. (2005). Experimental models of traumatic brain injury: do we really need to build a better mousetrap? *Neuroscience*, *136*(4), 971–89.

Motherway, J., Doorly, M. C., Curtis, M., & Gilchrist, M. D. (2009). Head impact biomechanics simulations: a forensic tool for reconstructing head injury? *Legal medicine*, *11 Suppl 1*, S220–2.

Nahum, A. M., Smith, R., & Ward, C. C. (1977). *Intracranial pressure dynamics during head impact*. *Proceedings of the 21st STAPP Car Crash Conference*. New Orleans, LA, USA.

Newman, J., Barr, C., Beusenberg, M., Fournier, E., Shewchenko, N., Welbourne, E., & Withnall, C. (2000). A new biomechanical assessment of mild traumatic brain injury, II: results and conclusions. *International Research Council on the Biomechanics of Impact (IRCOBI) Conference Proceedings* (pp. 223–233). Retrieved from http://www.smf.org/docs/articles/hic/Newman_NFL.pdf

Nusholtz, G., Glascoe, L., & Wylie, E. (1996). Modeling cavitation during head impact. *NATO/AGARD, Head Impact Conference, Paper 6*.

O'Connor, W. T., Smyth, A., & Gilchrist, M. D. (2011). Animal models of traumatic brain injury : A critical evaluation. *Pharmacology and Therapeutics*, *130*(2), 106–113.

Ommaya, A. K., & Hirsch, A. E. (1971). Tolerances for cerebral concussion from head impact and whiplash in primates. *Journal of Biomechanics*, *4*, 13–21.

Ommaya, A. K., Hirsch, A. E., Yarnell, P., & Harris, E. H. (1967). *Scaling of experimental data on cerebral concussion in sub-human primates to concussion threshold for man*. Washington, D.C. Retrieved from http://www.dtic.mil/dtic/tr/fulltext/u2/666837.pdf

Ommaya, A. K., Thibault, L., & Bandak, F. A. (1994). Mechanisms of impact head injury. *International Journal of Impact Engineering*, *15*(4), 535–560.

Pelosi, G., Proietti, R., Morte, F. Della, Magalini, S. I., & Bondoli, A. (1981). Decompression sickness: a medical emergency. *Resuscitation*, *9*, 201–209.

Pishchalnikov, Y. A., Sapozhnikov, O. A., Bailey, M. R., Williams, J. C., Cleveland, R. O., Colonius, T., Crum, L. A., et al. (2003). Cavitation bubble cluster activity in the breakage of kidney stones by lithotripter shockwaves. *Journal of Endourology*, *17*(7), 435–446.

Raul, J.-S., Baumgartner, D., Willinger, R., & Ludes, B. (2006). Finite element modelling of human head injuries caused by a fall. *International Journal of Legal Medicine*, *120*(4), 212–8.

Raul, J.-S., Deck, C., Willinger, R., & Ludes, B. (2008). Finite-element models of the human head and their applications in forensic practice. *International Journal of Legal Medicine*, *122*(5), 359–66.

Roth, S., Raul, J.-S., & Willinger, R. (2009). Finite element modelling of paediatric head impact: Global validation against experimental data. *Computer Methods and Programs in Biomedicine*, *99*(1), 25–33.

Santiago, L., Oh, B., Dash, P., Holcomb, J., & Wade, C. (2012). A clinical comparison of penetrating and blunt traumatic brain injuries. *Brain Injury*, *26*(2), 107–125.

Sauren, A., & Claessens, M. H. A. (1993). Finite element modeling of head impact: The second decade. *International Research Council on the Biomechanics of Impact (IRCOBI) Conference Proceedings* (pp. 241–254). Eindhoven, Netherlands.

Shearer, P. M. (2009). *Introduction to Seismology* (2nd ed.). Cambridge University Press.

Stålhammar, D. (1975). Experimental brain damage from fluid pressures due to impact acceleration. (Parts 1, 2 and 3). *Acta Neurologica Scandinavica*, *52*(1), 7–55.

Stålhammar, D. (1986). Experimental models of head injury. *Acta Neurochirurgica. Supplementum*, *36*, 33.

Steiner, L. A., & Andrews, P. J. D. (2006). Monitoring the injured brain: ICP and CBF. *British Journal of Anaesthesia*, *97*(1), 26–38. Retrieved from http://bja.oxfordjournals.org/content/97/1/26.full

Stronge, W. J. (2000). *Impact Mechanics* (1st ed.). Cambridge University Press.

Thomas, L. M., Roberts, V. L., & Gurdjian, E. S. (1967). Impact-induced pressure gradients along three orthogonal axes in the human skull. *Journal of Neurosurgery*, *26*, 316–321.

Thomson, W. T. (1993). *Theory of Vibration with Applications* (4th ed.). Chapman & Hall.

Trosseille, X., Tarriere, C., Lavaste, F., Guillon, F., & Domont, A. (1992). Development of a F. E. M. of the Human Head According to a Specific Test Protocol. *Proceedings of the 30th STAPP Car Crash Conference*.

Unterharnscheidt, F., & Higgins, L. S. (1969). Pathomorphology of experimental head injury due to rotational acceleration. *Acta Neuropathologica*, *12*, 200–204.

US Centre for Disease Control and Prevention. (2010a). Get the stats on traumatic brain injury in the United States. Retrieved June 17, 2012, from http://www.cdc.gov/traumaticbraininjury/pdf/BlueBook_factsheet-a.pdf (updated 17th March 2010)

US Centre for Disease Control and Prevention. (2010b). What are the leading causes of TBI? Retrieved June 17, 2012, from http://www.cdc.gov/TraumaticBrainInjury/causes.html

US Department of Veterans Affairs. (n.d.). *Traumatic brain injury: a guide for patients*. Retrieved from http://www.mentalhealth.va.gov/docs/tbi.pdf

Van De Graaff, K. M., & Fox, S. I. (1995). *Concepts of human anatomy and physiology*. McGraw-Hill Education.

Versace, J. (1971). A review of the severity index. *Proceedings of the 15th STAPP Car Crash Conference* (pp. 771–796). Retrieved from http://www.snellfoundation.org/docs/articles/hics

Voo, K., Kumaresan, S., Pintar, F. A., Yoganandan, N., & Sances, A. (1996). Finite-element models of the human head. *Medical & Biological Engineering & Computing*, *34*(5), 375–81.

Wahi, K. K., & Merchant, H. C. (1977). Mechanical response of a head injury model with viscoelastic brain tissue. *Annals of Biomedical Engineering*, *5*(4), 303–21.

Ward, C. C., Chan, M., & Nahum, A. M. (1980). Intracranial Pressure–A Brain Injury Criterion. *Proceedings of the 24th STAPP Car Crash Conference*.

Ward, J. W., Montgomery, L. H., & Clark, S. L. (1948). A mechanism of concussion: A theory. *Science*, *107*, 349–353.

Wardlaw, A., & Goeller, J. (2010). Cavitation as a Possible Traumatic Brain Injury (TBI) Damage Mechanism. *26th Southern Biomedical Engineering Conference SBEC 2010 April 30-May 2, 2010 College Park, Maryland, USA* (p. 34). Springer Verlag.

Watkins, L., & Thomas, D. G. T. (2003). Traumatic injuries of the head. *Oxford Textbook of Medicine (4th ed.)* (pp. 1108–10). Oxford University Press.

Weber, I., & Young, P. G. (2003). Automating the generation of 3D finite element models based on medical imaging data: application to head impact. *3D Modelling Paris, France* (Vol. 44, pp. 23–24).

Willinger, R., Kang, H. S., & Diaw, B. (1999). Three-dimensional human head finite-element model validation against two experimental impacts. *Annals of Biomedical Engineering*, *27*(3), 403–10.

Wittek, A., & Omori, K. (2003). Parametric study of effects of brain-skull boundary conditions and brain material properties on responses of simplified finite element brain model under angular acceleration impulse in sagittal plane. *JSME International Journal Series C*, *46*(4), 1388–1399.

Yanagida, Y., Fujiwara, S., & Mizoi, Y. (1989). Differences in the intracranial pressure caused by a "blow" and/or a "fall" - An experimental study using physical models of the head and neck. *Forensic Science International*, *41*, 135–145.

Young, P. G. (2002). A parametric study on the axisymmetric modes of vibration of multi-layered spherical shells with liquid cores of relevance to head impact modelling. *Journal of Sound and Vibration*, *256*(4), 665–680.

Young, P. G. (2003). An analytical model to predict the response of fluid-filled shells to impact - a model for blunt head impacts. *Journal of Sound and Vibration*, *267*(5), 1107–1126.

Young, P. G., Beresford-West, T., Coward, S., Notarberardino, B., Walker, B., & Abdul-Aziz, A. (2008). An efficient approach to converting three-dimensional image data into highly accurate computational models. *Philosophical Transactions of the Royal Society A: Mathematical, Physical and Engineering Sciences*, *366*(1878), 3155.

Young, P. G., & Morfey, C. L. (1998). Intracranial pressure transients caused by head impacts. *International Research Council on the Biomechanics of Impact (IRCOBI) Conference Proceedings* (pp. 391–403). Göteborg, Sweden.

Zhang, L., Yang, K. H., & King, A. I. (2001). Biomechanics of neurotrauma. *Neurological Research*, *23*, 144–156.

Zong, Z., Lee, H. P., & Lu, C. (2006). A three-dimensional human head finite element model and power flow in a human head subject to impact loading. *Journal of Biomechanics*, *39*(2), 284–92.

# Chapter 2: Methodology

## 2.1 Generation of the fluid-filled sphere model

Three finite element models of the human head were developed in order to explore the intracranial pressure response to a range of blunt head impacts. The investigation was divided into three stages, employing models of low, medium, and high biofidelity. Stage 1 utilised a simple model assuming a spherical head, with constant skull thickness, containing a spherical fluid brain. In this way the first model was equivalent to Young & Morfey's (1998) fluid-filled sphere model of the head, except that here a significantly higher mesh density (approximately 400 times as many elements per unit volume) was used. In addition, unlike Young & Morfey's investigation, in this study impacts were simulated directly by modelling collision of the head with a spherical impactor mass, rather than indirectly modelling impact through the application of an external force-time history. This provided a more realistic impact loading to the model, and also allowed the validity of Young's (2003) analytical model to be explored by comparing the predicted impact characteristics with the finite element results.

Finally, in Young & Morfey's (1998) finite element study the results were presented as corresponding to a baseline maximum force of $F_{max}$ = 10 kN, such that the resulting intracranial pressures were in a meaningful range. In actuality the simulations were performed using a baseline force several orders of magnitude lower than 10 kN, and the pressure results suitably scaled up from the computed values. This ensured that the response observed by Young & Morfey was in the linear range, i.e. the deflection of the skull was small such that the effect of geometric non-linearities remained insignificant. In this study it was decided to use reasonable impactor characteristic masses and velocities, therefore generating intracranial pressures of magnitudes which could be expected to cause injury. This avoids the need to scale the results. In Stage 1 however the maximum force of the impacts was kept reasonably low (the greatest impact $F_{max}$ in Stage 1 is 0.842 kN); it was assumed the system will remain geometrically linear during this range. The effect of possible geometric non-linearities as a result of high energy impacts on the dynamic pressure response was investigated in Stage 2.

Other than validating Young's (2003) analytical model, the purpose of this Stage 1 investigation was to determine whether large dynamic pressure transients observed by Young & Morfey (1998) occur despite the increased sophistication mentioned above.

### 2.1.1 Geometry

Young & Morfey's (1998) finite element head model exploits the symmetry of the system by reducing the spherical geometry to a wedge and applying appropriate boundary conditions. The geometry and dimensions used in this Stage 1 model were identical to Young & Morfey's (1998) model, except that here the model's spherical geometry remains whole. The model could not be reduced to a wedge, due to constraints stipulated by the mesh refinement algorithm, which required that the refined zone not overlap the boundary of the image. The external radius of the spherical skull $R_{sh}$ was 80.01 mm, with an internal radius $R_f$ of 76.20 mm, and therefore a thickness $h$ of 3.81 mm. These are appropriate dimensions for a spherical approximation to the cranial vault and its average thickness used by Young & Morfey (1998), and originally obtained from (Engin, 1969). The central spherical cavity contained a fluid model to represent the brain. A solid spherical impactor was created with external radius $R_{sol}$ of 40 mm, which was used for all impact cases in Stage 1 and Stage 2 of this study. The impactor's geometry was selected based on calculations using Young's (2003) analytical model and was suitable for simulating a head impact by a generic blunt object or, approximately, a flat surface such as the ground[4]. Also, the impactor's radius was such that it helped avoid small contact areas during impact, which can be numerically unstable. The head and impactor models were generated using the ScanIP image processing software, and the +FE mesh generation and +CAD computer aided design software modules (Simpleware Ltd.). Surface models of the required spherical geometries were created in +CAD, positioned, and converted into "image space" (i.e. the geometry was represented by greyscale values within a three-dimensional image, essentially artificially creating data one would obtain from a CT or MRI scan, directly from CAD) so that it could be imported into ScanIP. Boolean operations were applied to subtract the 76.20 mm sphere from the 80.01 mm sphere, resulting in a spherical shell of $h$ = 3.81 mm.

### 2.1.2 Material properties

In order to easily compare the behaviour of the Stage 1 model with Young & Morfey's (1998) model, in the same manner as the geometric constants above, the material

[4] For example, by changing $R_{sol}$ from 40 mm to ∞: the $F_{max}$ and $T_p$ predicted by Young's (2003) analytical model for the first Stage 1 impact case ($V_{sol}$ = 0.2 m/s and $m_{sol}$ = 8 kg) changes by 12% and 13% respectively.

properties used were identical to those in (Engin, 1969). All materials were isotropic and homogeneous, with linear elastic properties. Here the skull has an elastic modulus $\boldsymbol{E_{sh}}$ **of 13.79 GPa**, Poisson's ratio $\boldsymbol{\nu_{sh}}$ **of 0.25**, and density $\boldsymbol{\rho_{sh}}$ **of 2140 kg/m$^3$**. The brain is represented by an "elastic fluid" formulation, which behaves as an inviscid fluid with a bulk modulus $\boldsymbol{B_f}$ **of 2.18 GPa**, and density $\boldsymbol{\rho_f}$ **of 1002 kg/m$^3$**.

A range of impact tests were performed varying the spherical impactor's elastic modulus $E_{sol}$ in order to select a suitable value to be used during all Stage 1 and Stage 2 experiments. An overly stiff impactor was found to produce a small contact area during collision with the head, resulting in poor performance of the simulated contact between these two objects. Furthermore, for numerical stability it is recommended that two objects which have a contact defined between them do not have significantly different stiffnesses, therefore restricting $E_{sol}$ to within about an order of magnitude greater or lesser than $E_{sh}$. A value of $\boldsymbol{E_{sol}}$ **= 0.8 GPa** with Poisson's ratio $\boldsymbol{\nu_{sol}}$ **= 0.25** performed well, and was adopted for all impacts in Stages 1 and 2 unless otherwise stated. In Stages 1 and 2, numerical considerations were given precedence over representative impactor properties, since the desired impact characteristics (the duration and force of the impacts) were to be obtained by varying the velocity of the impactor and its density $\rho_{sol}$. The use of stiffer, and arguably more realistic, impactor properties are probed in the Stage 2 "high energy impacts" (see Section 4.3).

### *2.1.3 Meshing*

Finite element meshes are composed of individual sub-volumes called elements, with nodes at their vertices. First-order tetrahedral (tet) elements are composed of 4 nodes in three-dimensional space, thereby defining a volume with 4 triangular surfaces. First-order hexahedral (hex) elements are composed of 8 nodes, defining a volume with 6 quadrilateral surfaces. The +FE module has two main meshing approaches. The first method converts the voxels which define an object, known as a "volume of interest" (VOI) of a three-dimensional image, directly into hex elements: this has been termed the "voxel method" (Young et al., 2008). The voxels are defined by the Cartesian grid of the original image, and therefore the mesh will be highly regular. Domains generated in this fashion will have unrealistic stepped surfaces. To resolve this issue, voxels on the surfaces of the VOIs can be sub-divided into tetrahedra based on the surface faces calculated by the marching cubes approach; thereby creating a regular mixed hex/tet mesh with a realistic exterior.

Alternatively, all hex elements can be discretised into tetrahedra, creating a regular fully tet mesh also with a realistic exterior (Simpleware Ltd., 2012).

A second meshing approach creates unstructured (i.e. irregular) meshes. The exterior surface of the VOI is extracted using the marching cubes approach; then a Delaunay tetrahedralization algorithm discretises the interior of this VOI by automatically inserting nodes which define tet elements (Young et al., 2008).

An "elastic fluid" is composed of linear elastic solid elements with zero shear resistance. Under small displacements, i.e. no flow, these elements essentially behave as an inviscid fluid. An experiment was performed to identify the most suitable mesh type for use with this elastic fluid formulation, used here to model the brain. A finite element model of a rigid beaker geometry filled with elastic fluid was created in ScanIP, and meshed using all the available methods in the +FE module. This resulted in four models of equal geometry and materials, with different meshes: a regular fully hex mesh, a regular fully tet mesh, a regular mixed hex/tet mesh, and an irregular fully tet mesh. Finite element simulations were performed on these test models: the beakers were subject to large vertical accelerations, and the resultant hydrostatic pressures in the elastic fluid were compared to the analytical solution. As expected, it was found that the regular fully hex and the regular mixed hex/tet meshes performed best, with errors of 0.05% and 0.08% respectively. This is likely due to the fact that in these cases the majority of the fluid is modelled using hex elements. While first-order tet elements are sufficiently accurate for many applications, especially when a high density mesh is used, it is known that, in many cases, employing tet elements stiffens the mesh; this is a kinematic property of simplicial (triangular and tetrahedral) elements which leads to an overly stiff mesh through a process known as "locking" (Benzley et al., 1995). This experiment indicated that first-order tet elements are undesirable in elastic fluid regions, which are particularly sensitive to any artificially added stiffness. The fully hex mesh created using the unmodified voxel method had unrealistic exterior surfaces, therefore all models in Stages 1 to 3 were created using the mixed hex/tet mesh generation method.

A convergence study was performed to determine the optimum global mesh density. The fluid-filled sphere geometry was meshed 7 times, yielding models with increasing mesh density from approximately 4.3k to 1.1M elements. Since mesh refinement was not required for these convergence study cases, the symmetry of the system could be exploited; the models existed in the form of a 90° wedge, with relevant symmetry conditions applied. Geometric and material constants for these test models were equal to the Stage 1 values

above, except that here the spherical skull was set as rigid ($E_{sk}$ = ∞ GPa). Impact was indirectly simulated by subjecting the rigid skull to a radial Hanning squared force-time history [Equation 1.4] with a duration of 5 ms and maximum force of 0.4 kN. In this way, rigid-body acceleration of the head generated repeatable quasi-static pressure behaviour of the brain without any influence of contact phenomena (e.g. skull bending). The ideal solution was, therefore, given by $P_{quasi}$ [Equation 1.5]. The resulting pressures in the brain were recorded for each test model; the error of each model compared to the analytical solution is reported below in Figure 2.1.

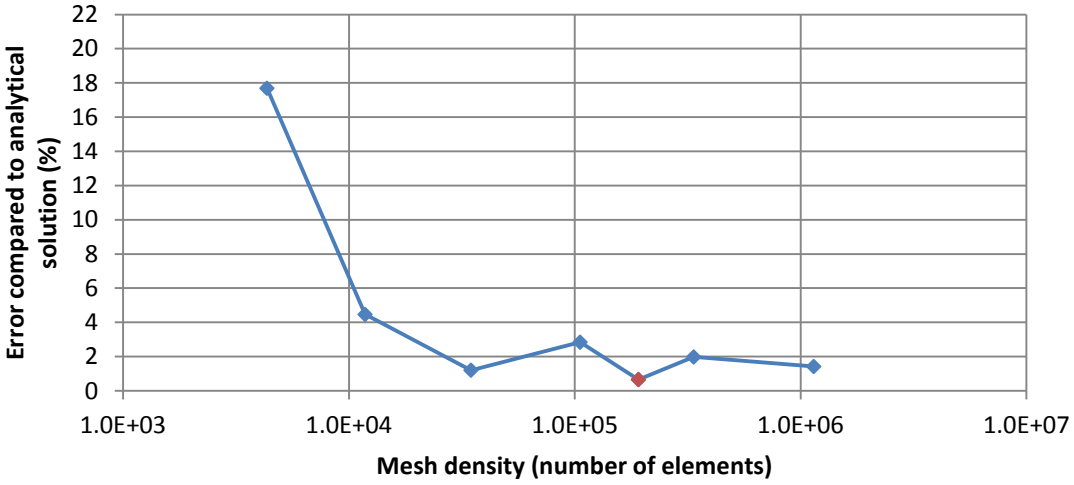


*Figure 2.1: The error in predicted pressures compared to the analytical solution vs. the element count of the 7 convergence study meshes on a logarithmic scale.*

The finite element solution converged as the mesh density was increased above approximately 150k elements; any further increase in mesh density required further computational resources while not appreciably improving the accuracy of the solution. The meshing approach used generates the mesh based on the resolution of the original image data. The optimum mesh (191k elements, marked in red in Figure 2.1) was generated from an image with 2×2×2 mm voxels, resulting in the generated hex elements having an edge length of 2 mm, and being of cubic proportions, which is desirable in critical areas (Oasys Ltd., 2010). It is also important to verify that any solid sections that will be subject to bending have at least 3 elements through their bending section, in order to resist bending correctly (Oasys Ltd., 2010). The chosen mesh satisfied this condition, having a minimum of 3 elements through the thickness of the spherical skull at all points. These mesh characteristics were deemed sufficient to accurately capture the pressure behaviour of the brain and bending of the skull, and so this mesh density (n.b. this image resolution) was used for the Stage 1 and Stage 2 head models.

Initial tests were performed on impacts between solid spheres without fluid cores, but the resulting contact durations of these were found not to agree with those predicted by the Hertzian theory of impact (Johnson, 2003). This classical description of quasi-static contact between two spheres is well established and, provided the characteristics of the impact satisfy certain conditions (see Section 1.5), can be regarded as an accurate solution on which the performance of the finite element contact can be benchmarked. Achieving an accurate description of the contact between the two colliding bodies was critical, as this affects the contact duration and peak force transmitted by the impact. Further tests employing local mesh refinement at the contact site indentified the strong dependence of parameters such as contact duration and peak force on the growth of the contact area. During a collision between objects with curved surfaces, the contact area will initially increase, reach a maximum, and then decrease with time. In finite element analysis the curved surfaces of both objects, and therefore the contact area, are discretised by a number of elements. For blunt head impacts the contact area tends to be small compared to the dimensions of the head, for example the radius of the greatest contact area observed during all Stage 1 impacts was 3.26 mm. Assuming an average element size determined by the global mesh density selected above (2×2×2 mm), a contact area of this size would only contain a maximum of 8 element faces on the surface of each object. It was found that, in order to accurately model the contact, mesh density needed to be increased at the contact site, i.e. a degree of local mesh refinement was required. While the global mesh density was determined by the convergence study, local mesh density requirements at the contact site were investigated using a series of simulated impacts of solid spheres with different degrees of local mesh refinement and validated against the Hertzian theory of impact.

For the geometric and material constants stated above, local mesh refinement resulting in a characteristic element edge length of 0.55 mm at the contact site was found to give accurate results; this is a local increase in mesh density of approximately ($2^3$ / $0.55^3$ =) 48 times the global mesh. This highlights the sensitivity of the contact between objects with high degrees of curvature and relatively small contact areas, such as head models, to the local mesh density at the contact. The accuracy of the contact is an important consideration that should always be verified in these cases.

The "grid mesh refinement" algorithm, which is based on work by Bui Xuan (2008) and has been integrated into the +FE software, allowed a spherical volume with 9 mm radius to be defined at the contact surfaces of the head and impactor models, in which the models were meshed using the required higher density (elements with 0.55 mm edge lengths). The

remainder of the mesh, based on 2 mm spaced elements, gradually reduces element size towards this high density region, creating a smooth transition.

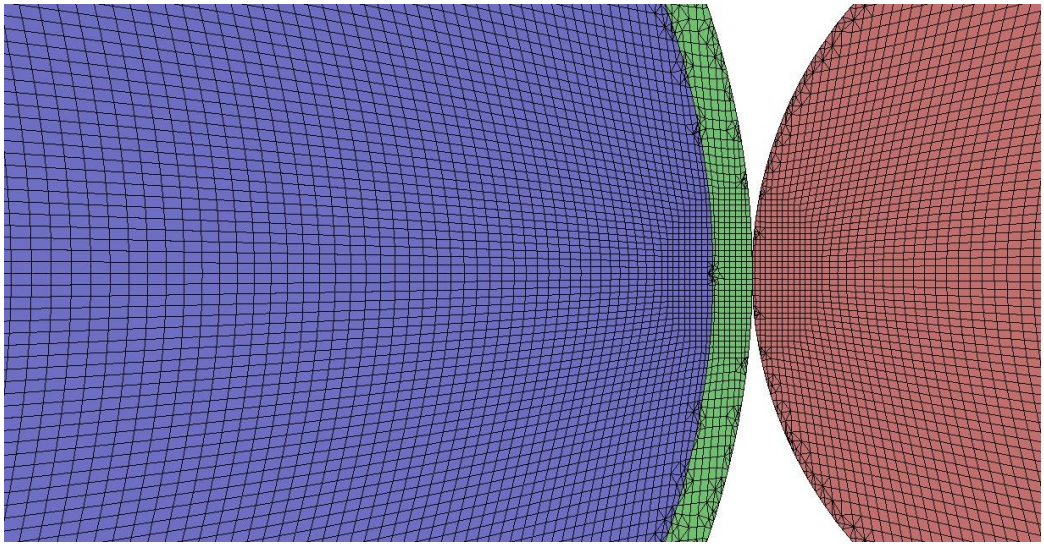

*Figure 2.2: Mid-section of the Stage 1 fluid-filled sphere and impactor meshes, detailed view of the contact area. The blue, green, and red regions represent the brain, skull, and impactor respectively. The smooth transition to an area of high mesh density at the contact is visible.*

Finally, it was necessary to consider the "quality" of the elements in the mesh, since elements with poor quality can cause numerical problems during the simulation process. A commonly used metric for element quality is the "in-out aspect ratio", which is proportional to the ratio of the radius of the inscribing sphere (i.e. the largest sphere which can fit inside the element) to the radius of the circumscribing sphere (i.e. the smallest sphere which can contain the element) (Simpleware Ltd., 2012). An element is said to be of good quality if it is regular with similar edge lengths. The ideal tet element is an equilateral tetrahedron, while the ideal hex element is a cube; the in-out aspect ratio is scaled such that in these cases it yields a value of unity, with the value approaching zero as element quality is reduced. The geometry was meshed several times utilising the mesh optimisation functionality of the +FE software in order to arrive at the best possible quality. The head and impactor models together had a mean in-out aspect ratio of 0.717, which suggests a good quality mesh. It is advisable to keep poor quality elements to a minimum; here the total number of elements with an aspect ratio worse than 0.1 was 7 (which represents 0.0003% of the total mesh). The completed mesh for the Stage 1 fluid-filled sphere head model was composed of just under 1.8M elements, and the spherical impactor was approximately 394k elements.

### *2.1.4 Boundary and contact conditions*

The completed meshes for all models in Stages 1 to 3 of this study were prepared for simulation using the finite element pre-processing software Primer (Oasys Ltd.), and all impacts were simulated using the LS-DYNA explicit finite element code (LSTC Inc.).

The Stage 1 head model was subject only to collinear direct impacts, in order to avoid imparting any rotational accelerations which would increase the complexity of the loading and the number of variables that need to be considered when analysing the brain's response. However, inconsistencies inherent in the finite element mesh may still impart some small degree of rotational acceleration. In order to ensure only translational motion of the model was possible, constraints were applied to two central perpendicular planes which meet along the axis of impact. Nodes which lay on these planes had all degrees of freedom except translational and rotational movement within these planes restricted. The symmetry of both the head model and impactor about these planes means the constraints should not affect the impact response.

In the Stage 1 model two contacts were defined: contact between the brain and skull, and between the skull and impactor. The ideal contact conditions between the brain and skull for this study would allow relative movement of the two contact surfaces, but, since the cranial vault is a closed system without the presence of free gases, would restrict the separation of these surfaces. A contact formulation which allows sliding between surfaces and restricts separation was available. However, this contact formulation restricts the motion of the nodes on the contact surface of each object to within the element faces of the object it is in contact with, i.e. it does not allow relative sliding between contact surfaces greater than the edge lengths of elements which lie on the contact. Also, extensive tests utilising this contact found it to be unstable for this model, probably due to the large mesh size and the fact that one of the objects was an elastic fluid. Instead, contact between the brain and skull was achieved through the use of "shared nodes" on the brain-skull interface, so allowing neither separation nor relative sliding of the two objects (this is hereafter referred to as a "tied" contact). While strictly unrealistic, the implications of this constraint are unlikely to be significant given the absence of any shear resistance in the fluid elements. This contact formulation will cause some degree of unrealistic constraint in the outermost layer of elements representing the brain, but the remainder of the brain region will be able to move in relation to the skull with minimal resistance. This was deemed satisfactory given that it is generally believed that significant relative motion between the brain and skull only occurs in extreme loading conditions (Claessens, 1994).

In finite element analysis contact problems can sometimes occur between objects with dissimilar stiffnesses; in these cases the contact may fail and the objects may interpenetrate. Here the modulus of the skull was more than 17 times greater than the modulus of the impactor, and penetration occurred in the contact between the skull and impactor during preliminary impacts utilising the default contact settings. This problem was resolved by invoking "segment-based contact" (known as "SOFT=2" in LS-DYNA), which can aid contact between dissimilar materials (LSTC Inc and DYNAmore GmbH, 2003).

## 2.2 Generation of the brain and realistic skull model

The Stage 2 head model was of medium complexity. As for the previous model, this model's main components were the brain and skull, however here the spherical shell was replaced with realistic skull geometry extracted from MRI data. This second model utilised the same homogeneous, linear elastic material properties and impactor as the Stage 1 model, so allowing the effect of additional geometric complexity on the pressure response to be studied independently. In this way the Stage 2 investigation explored whether the dynamic pressure response, and associated large pressure transients, occurs despite a realistic (i.e. non-spherical) skull geometry.

The applicability and predictive capability of Young's (2003) analytical model of head impact, based on a simple fluid-filled spherical head, applied to head impacts with more realistic geometry could be investigated. Finally the Stage 2 model also allows the possible pressure release mechanism of the foramen magnum to be explored.

### *2.2.1 Geometry*

The Simpleware-NRL head model, first presented in (Weber & Young, 2003), is a detailed image-based finite element model of the whole head and neck. This model was previously generated from an *in vivo* high resolution T1-weighted MRI scan of a male volunteer, 26 years of age, with no diagnosed conditions and of average height (1.81 m) and build (81 kg). Image-based meshing creates patient-specific models; the volunteer was chosen because of his anatomical similarity (both height and weight within 1.5%) to the American $50^{th}$ percentile male (1.80 m and 82 kg) (NASA, 1995). The in-plane resolution of the scan was 1.03516 mm × 1.03516 mm, with a slice-to-slice separation of 1.04001 mm. The dataset was processed in ScanIP using both manual and semi-automated techniques to distinguish the following 15 regions: the central nervous system (the grey matter, white matter, brainstem, and cerebellum were all differentiated), CSF, ventricular structure, skull,

mandible, cervical vertebrae, intervertebral discs, eyes (eyeballs, optic nerves, and surrounding fatty tissues were all differentiated), cartilaginous structures (nasal cartilage and trachea), and surrounding flesh of the head and neck. When converted into a finite element mesh the completed model had approximately 10M elements.

This MRI scan data was obtained from Simpleware Ltd. and used here to generate the Stage 2 head model. The skull geometry was extracted from this dataset using ScanIP. The skull had both realistic exterior and interior geometries, thus defining a non-spherical cranial cavity in the interior of the skull. In this Stage 2 model the entire volume of the cranial cavity was considered to be occupied by the brain, which was assumed homogeneous and therefore the grey matter, white matter, and cerebellum were not differentiated. As previously, the cranial cavity was filled with a fluid model representing the brain; the fluid must be enclosed, so a deformable thin soft membrane was artificially included over the foramen magnum so that any pressure releasing effects of this feature remain intact.

### *2.2.2 Material properties*

The material properties of the brain and skull in this Stage 2 model were identical to those used in Stage 1 so that the results could be easily compared. The skull was linear elastic, with modulus $E_{sh}$ **of 13.79 GPa**, Poisson's ratio $\nu_{sh}$ **of 0.25**, and density $\rho_{sh}$ **of 2140 kg/m$^3$**. The brain was modelled as an inviscid fluid with bulk modulus $B_f$ **of 2.18 GPa**, and density $\rho_f$ **of 1002 kg/m$^3$**. These values were obtained from (Engin, 1969).

The material properties of the membrane introduced over the foramen magnum were chosen such that this will have a negligible effect on the flow of material in or out of the foramen during impact. The membrane was modelled as an elastic solid with a modulus of **0.2 GPa** (approximately 70 times less stiff than the skull), Poisson's ratio of **0.25**, and density equal to the value chosen for neural tissue, **1002 kg/m$^3$**.

### *2.2.3 Meshing*

The overall dimensions of the model were similar to those of the Stage 1 spherical head model, therefore the convergence study performed in Stage 1 was deemed to still be applicable. This second model was meshed with the same global mesh density settings as previous, which required the original image data used in Stage 2 to be resampled to a 2×2×2 mm voxel size. Mesh refinement was applied in the form of a 9 mm radius zone of high density mesh at the contact site between the skull and impactor, containing elements

with 0.55 mm edge length. As previously, a visual inspection was performed to verify that there were at least 3 elements across the thickness of the skull in order to accurately capture bending stresses; the mesh satisfied this condition, having between 3 and 14 elements across the skull thickness at all points. The geometry was meshed using the mixed hex/tet mesh generation method in the +FE software, resulting in the completed Stage 2 head model having just over 1.8M elements. The spherical impactor was composed of 387k elements. The head and impactor models had good mesh quality, with a mean in-out aspect ratio of 0.697, and only 1 element having an in-out aspect ratio worse than 0.1 (which represents 0.00004% of the total mesh).

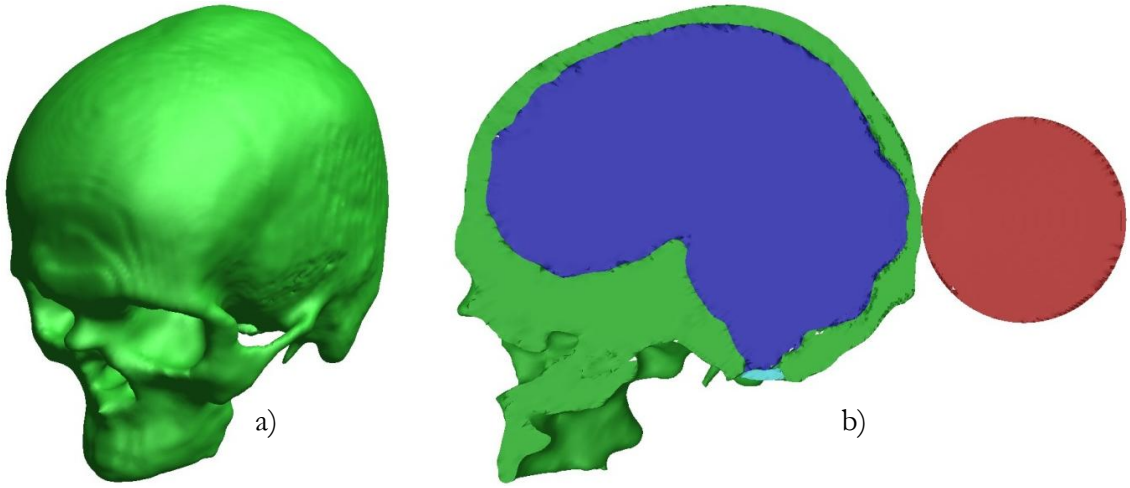


*Figure 2.3: (a) Isometric view of the completed Stage 2 head model. (b) Sagittal section view of the head and impactor models. The blue, light blue, green, and red regions represent the brain, foramen membrane, skull, and impactor respectively.*

### *2.2.4 Boundary and contact conditions*

Similar to the fluid-filled sphere head model, the model in Stage 2 was subject only to collinear direct impacts. In order to help ensure no rotational acceleration was imparted to the head, nodes on the central sagittal plane of the head, about which the head has approximate left/right symmetry, and in which the axis of impact also lay, were constrained. The displacement of these nodes was restricted except for translational and rotational movement within this plane, so restricting global rotation of the model about the vertical axis.

All contacts between the brain, skull, and foramen magnum membrane were modelled as tied. As in Stage 1, special consideration needed to be paid to the contact between the skull and impactor due to their large difference in material properties; a non-standard contact

was required in order to accurately capture the collision between these two objects. Tests were performed using different contact formulations. It was found that the Stage 2 model benefitted from using a standard penalty contact formulation with modified contact stiffness based on stability considerations and timestep size (using the "SOFT=1" option in LS-DYNA) (LSTC Inc and DYNAmore GmbH, 2003). This was found to produce less numerical noise than the segment-based contact used in Stage 1.

## 2.3 Generation of the biofidelic head model

The final model, used in Stage 3, was developed from the same MRI scan data as the model of medium complexity (Stage 2). The Stage 3 model is a complex description of the whole head and neck based on the Simpleware-NRL head model described above (see Section 2.2.1). Geometric features deemed non-relevant to this study were removed, and the accuracy of materials in the model were improved by researching and applying the latest values available in the literature. The purpose of the Stage 3 investigation was to approximate, as close as reasonably possible, the geometric and material parameters of the real human head. In this way it was possible to explore the effect that more realistic brain material, and the inclusion of major structures such as the scalp and neck, would have on the pressure response of the brain. This highly biofidelic model was also used to determine whether, and to what extent, the dynamic pressure response and associated magnification of intracranial pressures occurs despite these alterations, and therefore gives an indication of how likely and how dangerous this injury mechanism may be to humans.

In a similar fashion to Stage 2, here the applicability of Young's (2003) analytical model of head impact, which is based on substantial geometric and material approximations, was investigated in comparison to the predictions of this finite element model based on more complex (e.g. non-spherical) geometry and more complex (e.g. non-linear) materials.

### *2.3.1 Geometry*

The geometry of the Stage 3 biofidelic head model was adapted directly from the Simpleware-NRL head model, with permission. The Simpleware-NRL head model was streamlined to reduce simulation time. Features unlikely to affect the pressure response of the brain (the eyes, optic nerves, nasal cartilage and trachea) were removed by merging these regions with the surrounding flesh. The completed Stage 3 model contained the following features: the central nervous system, CSF, ventricular structure, skull, mandible, cervical vertebrae, intervertebral discs, and flesh of the head and neck.

The Stage 3 model was just over 301 mm tall, measuring from the top of the scalp above the skull cap, to where the neck joins the torso (just above the sternum), approximately 64 mm below the shoulder line. The neck, measured from the bottom of the model to the foramen magnum, makes up just over 150 mm of this height. The Stage 3 model's neck contains the complete cervical section of the vertebral column, including the first 7 vertebrae, and 6 corresponding intervertebral discs.

### *2.3.2 Material properties literature review*

The constitutive material properties of the models of low and medium complexity (Stages 1 and 2), were selected to be equal to those used by Engin (1969). Use of these linear elastic material models was yet a further simplification which allowed easier analysis and comprehension of the mechanisms at work during head injury, and reduced the computational resources needed for simulation. Furthermore, the results could be directly compared to the previous research by Young & Morfey (1998). It was necessary at this point however, to deviate from the simple materials previously used and to apply more complex material models based on results in the literature.

The use of both complex geometry and complex materials will increase the computational resources required to complete a simulation. Therefore, some structures in the Stage 3 model were still assigned linear elastic properties. Major structures deemed of particular importance to the impact response were assigned more complex, realistic constitutive material models in order to accurately capture their behaviour. These were:

- The brain: An accurate material model for the brain was vital, since it was this organ's trauma mechanisms that were to be investigated.
- The CSF: This watery fluid surrounds the brain and is believed to play a valuable damage mitigating role during head impacts.
- The scalp: The Stage 3 model did not differentiate muscles, ligaments, fatty tissue, scalp and skin layers, or other soft tissues which lie outside the cranial cavity. These tissues are difficult to distinguish due to their similar greyscale values, and so were grouped together into a single region of "flesh". This flesh region had the largest volume of all features within the Stage 3 model. Simulation efficiency would be greatly improved if a simple linear elastic material was found to be adequate for this flesh region. However, the "scalp", a layer of flesh beneath the impact site, was differentiated from the rest of this region. The thick compressible scalp layer which surrounds the cranial cavity will have a significant effect on the contact duration

and forces involved during impact. A suitable realistic non-linear material model was required for this area.

The following is a literature survey of head tissue mechanical properties determined experimentally, and of the material formulations used to recreate these properties in relevant finite element models.

#### *2.3.2.1 The brain*

The brain is a highly complex organ, both structurally and constitutively. The brain has been described macroscopically as "somewhat like a gel, although not as stiff" (Goldsmith, 1972). Chemically, it is composed of approximately 78% water, 10-12% lipids, 8% protein, and a small proportion of carbohydrates, inorganic salts, and soluble organic substances (Ommaya, 1968). At a microscopic level, every biological material can be thought of as a mixture of solid and fluid materials due to the composition of cells; thus viscoelastic or multiphasic behaviour should be expected (Claessens, 1994). Biological structures are composites and are known to exhibit mostly non-linear behaviour (Meulman, 1996); furthermore anisotropic behaviour is expected depending on the structure and function of the biological tissue (Claessens, 1994). Thus, variation in observed mechanical properties are expected depending on tissue sample location, cutting angle, and due to natural biological differences between individuals (Christ et al., 2010). Other than the complexity of the system, further factors such as: *in vivo* versus *ex vivo* testing, hours post-mortem, storage and preparation methods of *in vitro* tissue samples, different species being tested, and differences in testing methods result in large variations in reported tissue properties (Melvin et al., 1970; Meulman, 1996; Prange et al., 2000). Careful judgement needs to be applied when selecting which simplifying assumptions can be made when modelling biological tissues such as the brain.

Barber, Brockway, & Higgins (1970) conducted density measurements on brain tissues, and found (with a small exception in part of the *diencephalon*: a region of the forebrain) no significant differences between the density of grey and white matter[5].

Melvin et al. (1970) measured the complex dynamic shear modulus $G^*$ of *in vitro* human brain from autopsy specimens using dynamic mechanical analysis (DMA), in which dynamic shear stress is applied to a viscoelastic material and the resulting strains measured.

[5] Not first source, original paper unavailable. Information is as stated in (Meulman, 1996).

The storage modulus *G'* of *in vivo* rhesus monkey brain tissue was studied using dynamic probe analysis (DPA), and was found to be similar to that of human brain. Slightly higher values of the rhesus monkey brain storage modulus were attributed to the effect of the living state, highlighting mechanical differences between living and dead tissue. The bulk modulus of brain was also measured and found to be approximately equal to that of water (and so incompressible), as expected due to the high water content of the tissue. Ruan, Khalil, & King (1994) investigated the effect of varying certain parameters of a complex finite element head model subject to impact, and suggested, contrary to Melvin et al. (1970), that brain tissue is "not exactly like water, but is a gel-like material with an effective bulk modulus lower than that of water". However, this "effective" lower bulk modulus recommended was in fact to add some compressibility to the brain material to account for the pressure release mechanism of the foramen magnum, which they suggest is required for models which do not include this feature.

In (Claessens, 1994) the structures expected to behave anisotropically due to their fibrous cellular composition are listed as: the meninges, the falx cerebri, the falx cerebelli, the tentorium cerebelli, the corpus callosum and the vermis. Claessens proposes a modelling approach whereby the total contents of the head are modelled as a continuum (using a viscoelastic or multiphasic model), while different structures are differentiated in this continuum by assigning different viscoelastic or multiphasic parameters in these regions.

Christ et al. (2010) used scanning force microscope indentation measurement to determine the elastic moduli of grey and white matter of rat brain tissue samples. It was found that within the linear range (indentation depths of up to 4 μm), the mean moduli of grey and white matter differed noticeably, reported as 454 Pa (with standard deviation ±53 Pa) and 294 Pa (with standard deviation ±74 Pa) respectively. In this study the Hertzian model used to extract the elastic moduli assumes a homogeneous, isotropic material. However, areas of white matter may have high anisotropy due to axonal alignment in the tissue, (Claessens, 1994; Prange et al., 2000). This may explain the larger degree of variation observed in the white matter values, depending on cutting angle.

In (Van Dommelen et al., 2010) properties of grey and white matter were again tested using indentation measurement. Porcine brain tissue samples were used. Grey matter was found to give less variation in results than white matter, indicating that it is more homogeneous and isotropic in nature. Grey matter was again found to have a higher elastic modulus than white matter, on average 34% stiffer. Varying tissue sampling location within the cerebrum

(posterior, superior, anterior) did not produce significant changes in observed mechanical properties.

In (Prange et al., 2000) and (Prange & Margulies, 2002) samples of porcine and human brain were tested up to large strains (50%) using a parallel-plate shear testing device. A modified 1st order Ogden hyperelastic model was fitted to these results, and was validated by predicting well the results of further compression tests of the tissue. Samples were tested from various locations in the brain. As expected, grey matter exhibited the least degree of anisotropy, while white matter tissue from the corpus callosum was most anisotropic. Anisotropy was found to vary according to the neurological architecture in each region. Both fresh porcine and human brain tissue (tested within 5 to 3 hours post-mortem, respectively) were found to be 4-10 times less stiff than much of the previous data available in the literature from autopsy specimens; thus suggesting that time post-mortem had a significant effect on the material properties of the tissue. In these studies human grey matter was found to be approximately 29% stiffer than porcine grey matter, indicating that properties of animal brain tissue cannot be assumed equivalent to human brain tissue; however, the lack of comparative studies in the literature means the degree of variation cannot yet be quantified. Finally, Prange et al. conclude that it is necessary to use a non-linear viscoelastic model to simulate brain tissue when subjected to large strains, rather than linear viscoelastic or elastic models.

Galford & McElhaney (1970) used creep and relaxation experiments on human and monkey brain samples, and determined that brain tissue does not satisfy the "principle of proportionality". This principle states that viscoelastic materials can be characterised as linear when an increase in the excitation during dynamic testing is accompanied by a proportional increase in the response (Meulman, 1996). Galford & McElhaney found that the behaviour of brain tissue deviated from linear viscoelastic theory at high strains (20-40%). Structures may however be damaged at these strains, and hence behave differently. Galford & McElhaney state a linear viscoelastic model of the brain would be sufficient as an approximation. In agreement with this, Meulman (1996) used torsional shear experiments to explore the mechanical behaviour of human brain tissue. It was found that for small strains (up to 1%) linear viscoelastic assumptions of brain tissue behaviour are sufficiently accurate.

Wahi & Merchant (1977) conducted a series of one-dimensional and two-dimensional finite-difference experiments on a simplified fluid-filled elastic skull model. Wahi & Merchant's results showed a significant reduction in intracranial stress (30-40%) if the brain

was modelled viscoelastically as opposed to an inviscid fluid. However, a more recent study by Willinger et al. (1999), using the Université Louis Pasteur (ULP) finite element head model which has been validated against cadaveric experiments, found that viscoelastic properties "do not fundamentally change" the model's response. The authors suggest that during impact scenarios the brain is dominated by short-term elastic behaviour (i.e. high strain rates), whereas viscoelastic (time-dependant) material behaviour has no significant effect during these short durations. This is supported by other research. Notably in work by Kuijpers et al. (1996), a two-dimensional finite element model of a head and neck system was validated against results from cadaveric impacts reported in the literature, and then subjected to parametric impact studies. It was found that linear viscoelastic modelling of the brain did not appreciably alter the response compared to a simple elastic material.

Horgan & Gilchrist (2004) ran a series of impact simulations using a highly detailed image-based finite element model of the head. This baseline model was modified to produce a set of model variations, each with an additional feature such as altered material properties or contact conditions. Impact simulations were applied to all of these individually, and results compared to cadaveric tests in the literature. It was concluded that the complexity modifications investigated (such as: applying different material properties to grey matter, white matter and the ventricles, or addition of a sliding boundary layer between the CSF and meninges) did not significantly affect the results, and did not improve predictive capabilities over the baseline model.

It is clear that the properties of brain tissue vary throughout the organ and its various substructures. However, in line with (Barber et al., 1970), significant density variations have not been reported. Although it is acceptable to assume grey matter as widely homogeneous and isotropic, many authors report fibrous anisotropic regions in the white matter substructures of the brain. Although ideally this would be taken into account in the current Stage 3 model, it would have to rely on a comprehensive source of tissue material properties per structure in the brain, including information such as relative orientation and variation of these properties. There is at present no such resource. Kleiven (2006) and others have homogenised the properties of the grey matter, white matter, cerebellum and spinal cord in their finite element models, "due to lack of published data" for these structures. Here too, in the current Stage 3 model, all features of the central nervous system that have been differentiated in the model (grey matter, white matter, cerebellum, and the brain stem/spinal cord) were assumed homogeneous and isotropic.

The foramen magnum was included in this model, and so the bulk modulus of the brain material does not need to be artificially reduced to add compressibility. In line with Melvin et al. (1970), a bulk modulus equal to that of water was chosen to represent the brain in this model: $\boldsymbol{B_f = 2.19\ GPa}$. As reported in (Barber et al., 1970), the density of brain tissue was set to $\boldsymbol{\rho_f = 1080\ kg/m^3}$, which as expected, is slightly higher than the density of water.

The large variation in experimentally derived material properties means there is still much debate on the issue of which constitutive model to use for the brain. While some authors recommend the use of a non-linear viscoelastic model, others suggest simple linear elastic properties would be sufficient for the short durations associated with impact. In this study, the use of a non-linear viscoelastic model for brain tissue was not preferred, given the lack of a widely agreed set of material constants. Conversely, linear elastic models of the brain had been used previously in Stages 1 and 2: a more complex material model was preferred at this stage, in order to explore the effect this may have on the pressure response. In this project it was decided, in line with Galford & McElhaney (1970), that a linear viscoelastic material model would be sufficiently accurate. The standard linear viscoelastic solid model (or Flügge model) describes shear relaxation behaviour in the form:

$$G(t) = G_\infty + (G_0 - G_\infty)e^{-\beta t} \qquad [2.1]$$

where the shear modulus $G$ is a function of: the long term (infinite) shear modulus $G_\infty$, the short-term shear modulus $G_0$, time $t$, and the decay constant $\beta$ which determines the rate of transition between the short and long duration moduli (Sauren & Claessens, 1993). This constitutive law was chosen as it is an established viscoelastic description suitable for brain tissue modeling, and is widely used in finite element head impact research. There is a large selection of material constants ($G_\infty$, $G_0$, $\beta$) available in the literature. A broad selection of relevant finite element research which represents the brain using this linear viscoelastic model was analysed. Although overall there is a large variation between the constants used, a narrow range of values for these constants have proven more popular and given results that have been validated. Information on the material constants used to model the brain is presented below. Table 2.1 was adapted from the review paper by Sauren & Claessens (1993), while Table 2.2 extends this list by providing information obtained through the author's own literature survey.

| Author | $G_\infty$ (kPa) | $G_0$ (kPa) | $\beta$ ($s^{-1}$) | $\rho$ ($kg/m^3$) | $v$ | $B_f$ (GPa) |
|---|---|---|---|---|---|---|
| Galbraith & Tong (1988), Tong et al. (1989) | 5.512 | 11.02 | 200 | | 0.4995 | |
| Cheng, Rifai, Khatua, & Piziali (1990) | 16.2 | 49.0 | 145 | | 0.5 | |
| Lee (1990) | 2.87 - 18.0 | 26.9 - 110.0 | 50 | 950 | | 1.25 - $5.44 \times 10^{-3}$ |
| DiMasi, Marcus, & Eppinger (1991) | 17.225 | 34.45 | 100 | | | $68.95 \times 10^{-3}$ |

*Table 2.1: Properties of the brain used in finite element analyses, from Sauren and Claessens (1993) ("Table 3: Mechanical properties of tissues in the linear viscoelastic models.")*

| Author | $G_\infty$ (kPa) | $G_0$ (kPa) | $\beta$ ($s^{-1}$) | $\rho$ ($kg/m^3$) | $v$ | $B_f$ (GPa) | Validated against cadaver tests by |
|---|---|---|---|---|---|---|---|
| Kuijpers et al. (1996) | 169.0 | 338.0 | 50 - 10000 | 1040 | 0.48 | | Nahum et al. (1977) |
| Willinger et al. (1999) | 168.0 | 528.0 | 35 | 1140 | | 2.19 | Nahum et al. (1977), Trosseille et al. (1992) |
| Horgan & Gilchrist (2004) | 2.0 ; 4.5 | 10.0 ; 22.5 | 80 | 1060 | | 2.19 | Hardy et al. (2001), Trosseille et al. (1992) |
| Belingardi, Chiandussi, & Gaviglio (2005) | 167.0 | 490.0 | 145 | 1140 | | | Nahum et al. (1977) |
| Suh, Kim, & Oh (2005) | 168.0 | 528.0 | 35 | 1000 | 0.499 | | Nahum et al. (1977) |
| Raul et al. (2006) | 16.7 | 49.0 | 145 | 1040 | | 1.225 | Nahum et al. (1977), Trosseille et al. (1992) |
| Gong, Lee, & Lu (2008) | 168.0 | 528.0 | 35 | 1040 | | 2.19 | Nahum et al. (1977) |
| Pinnoji & Mahajan (2008) | 16.7 | 49.0 | 145 | 1040 | | 1.125 | |
| Chen & Ostoja-Starzewski (2010) | 6.4 ; 7.8 | 34.0 ; 41.0 | 400 | 1040 | | 2.19 | Nahum et al. (1977) |

*Table 2.2: Properties of the brain used in finite element analyses, including information on whether the head model was successfully validated against empirical test data.*

Note that in Table 2.2, Kuijpers et al. (1996) did a parametric study on $\beta$, while Horgan et al. (2004) and Chen et al. (2010) differentiated between grey and white matter by applying stiffer shear modulus values to the brainstem and white matter.

Wittek & Omori (2003) conducted a series of sensitivity studies on a finite element model of a thin slice of brain tissue under angular acceleration. The brain material was approximated as per Equation 2.1, above. Parameters $G_\infty$, $G_0$, and $\beta$ were varied independently to investigate the effect they would have on the brain's response. Intuitively, it was found that increasing $G_\infty$ or $G_0$ would reduce the peak shear strains observed. Increase in $\beta$ was found to increase the peak shear strains, due to the fact that a large $\beta$ causes a fast transition from the short-term modulus to the smaller long term modulus.

As stated previously, in this model the regional anisotropy and variation in properties throughout the brain would not be considered. It was assumed that across the entire structure these small areas of differing directional anisotropy would cumulatively average out, such that it is reasonable to assign the entire structure an isotropic shear modulus equal to that of grey matter. Indeed, the findings of Prange et al. (2000) demonstrate that in shear grey matter is insignificantly (about 4%) stiffer than white matter (Kleiven, 2006).

Due to the fact that such a wide range of shear moduli has been used in the literature, it was decided in this study to select values that were most mitigating to trauma, i.e. that were most resistant to high stresses and strains. This was to underestimate the magnitude of any dynamic intracranial pressure transients which may occur. If these transients were found to have a significant effect despite these material properties, the severity of the trauma estimated in these simulations would provide a lower bound of the severity which could be expected in reality; providing confidence that this phenomenon may cause serious injury and so merit further investigation. In this model, the shear modulus of the brain was described by the values $\boldsymbol{G_\infty = 170.0\ kPa}$, $\boldsymbol{G_0 = 530.0\ kPa}$, and $\boldsymbol{\beta = 35\ s^{-1}}$. These values were chosen to be close to those used by previous finite element head models which performed well when compared to cadaveric experiments.

#### *2.3.2.2 The skull and spine*

At a chemical level, bone material can be seen as a composite of mineral crystalline fibres in a collagen matrix. These mineralised fibres are packed into cylindrical structures called *osteons*, and in turn these osteons are packed together in a similar fashion to fibres in wood. These osteons may be arranged in a preferred orientation to give anisotropic properties preferable for long bone, or may be arranged in a random fashion (Vincent, 1990). The bones of the skull have a sandwich panel structure: a layer of porous *cancellous* bone lies between two layers of compact *cortical* bone. The cancellous region (often called the *diploë* layer) is a foam-like structure, composed of a web of thin bone beams known as *trabeculae* (Gibson & Ashby, 1999). The overall thickness of this sandwich panel structure varies between approximately 9.5 to 13 mm, increasing towards the base of the skull (Goldsmith, 1972).

This complex microstructure, along with factors such as: tissue sample location, testing sample orientation, testing strain rate, the species of donor, and natural differences between individuals, result in large variation in the measured mechanical properties of bone. There is much data relating mechanical properties of bone to its density (Gibson & Ashby, 1999;

Rho et al., 1995; Vincent, 1990), and changes in these properties with age (Wood, 1971; Zioupos & Currey, 1998). Although there is a wealth of literature on the properties of bovine and human long bone (mostly the femur), the current review is focussed mainly on human cranial bone properties.



*Figure 2.4: Diagram of skull bone cross-section. (Van De Graaff & Fox, 1995)*

Research is often done on the mechanical properties of compact or trabecular bone regions individually, not on the behaviour of the sandwich structure as a whole. In (Melvin et al., 1970) cranial bone samples from human autopsy specimens and embalmed skulls were tested. The samples were frozen after removal until ready for testing. As opposed to soft biological tissues, storage of bone samples is less of an issue with regard to affecting mechanical properties. Cortical bone and cancellous bone layers were considered distinct and subjected to different tests. Cortical bone was tested mechanically in tension tangential to the skulls surface. Its elastic behaviour was found to be sensitive to strain rate, giving moduli ranging from 12.4 to 19.9 GPa (1.8 to $2.9 \times 10^6$ psi) for rates of 0.01 to 100 $s^{-1}$, respectively. The diploë layer was tested in shear in this transverse direction and in compression normal to the skull's surface. The diploë layer exhibited greater variability in mechanical properties due to natural biological variance in the trabecular microstructure. Strain rate was found to have an insignificant effect on cancellous bone. As expected, the properties of the diploë layer were observed to be dependent on the density of each sample, however a mean value for the elastic modulus was calculated as 1.38 GPa ($2.0 \times 10^5$ psi).

Wood (1971) subjected human cranial bone to mechanical testing to determine its properties in tension. 120 samples of cortical bone from 30 autopsy subjects were tested over a range of strain rates from 0.005 to 150 $s^{-1}$. It was found that sample location (from parietal, frontal, or temporal bones) had no effect on the mechanical properties. The results

also indicated that sample orientation had no effect, i.e. that cortical bone was tangentially isotropic. A small but "statistically insignificant" decrease in elastic modulus was observed in samples from older donors. It was found that the dynamic properties of cortical bone differ noticeably from its static properties. Wood's (1971) findings for the elastic modulus of cortical cranial bone closely matched those of Melvin et al. (1970), from between 11.5 to 18.2 GPa over a similar range of strain rates. Wood also noted significant variation between human and bovine bone properties reported in other studies, suggesting they cannot be used interchangeably. Finally, Wood proposed that cranial bone appears to have mechanical properties intermediate to the longitudinal and transverse properties of anisotropic long bone. This statement compares well to the wealth of data available on long bones. A relevant example is available in (Saha & Hayes, 1976), where fresh and embalmed human compact bone samples were obtained from femurs and subjected to high strain rate (133 $s^{-1}$) tensile impact tests. Longitudinal and transverse elastic moduli of 14.55 GPa ($2.11x10^6$ psi) and 12.41 GPa ($1.80x10^6$ psi) for fresh femoral bone were found respectively, with small standard deviations, while embalmed specimens produced lower moduli. The mean of the longitudinal and transverse moduli from Saha and Hayes' data is 13.48 GPa, which lies within the range of cranial moduli reported by Wood.

In (Gibson & Ashby, 1999) it is noted that the properties of bone change when dried, as is sometimes done before mechanical testing. Wet bone is reported to have a lower elastic modulus, but higher failure strain. Wet human compact long bone properties are listed as: density between 1800-2000 $kg/m^3$, longitudinal modulus of 17.0 GPa, transverse modulus of 11.5 GPa, with a Poisson's ratio of 0.41. These properties were significantly different from wet bovine compact long bone. The modulus of a solid individual human trabecula is given as 12.0 GPa, but it is stressed that the properties of the cancellous bone layer vary by region and density.

Peterson & Dechow (2003) investigated the properties of cortical bone samples from 15 unembalmed frozen crania using ultrasonic testing. Cortical bone samples were removed from 36 sites on each of the skulls; these sites were distributed throughout the parietal, frontal, temporal, and occipital bones. Facial bone samples, from the *zygoma* (cheek bone), were also tested for comparison. The samples were stored in an ethanol and saline solution, which has been shown to preserve the wet properties of cortical bone. The elastic mechanical properties were tested along the 3 major axes. While elastic properties between all bones were found to vary according to the sampling location, the cranial bones appeared to demonstrate similar behaviour, while the zygoma had a noticeably lower mean elastic

modulus. Results confirmed transverse isotropy (existing tangential to the skull's surface), but also that radial elastic moduli (across the thickness of the samples) were invariably greater than the transverse moduli. The mean elastic moduli for (non-muscle bearing) cortical bone in the major transverse axes were similar, 13.0 & 14.5 GPa, while the mean radial modulus was 19.7 GPa. This normal versus transverse anisotropy is expected from a sandwich panel-like structure. Peterson & Dechow (2003) also performed density measurements. Mean density across all the sample locations was found to be 1803 $kg/m^3$. The zygoma was found to have a significantly lower density than the cranial bones, with a mean value of 1679 $kg/m^3$. Poisson's ratios were also comprehensively measured and recorded across all sample sites in each of the directions tested. Similar to the observed elastic moduli, Poisson's ratio was more dependent on the directional axes that were being tested, as opposed to sample location. The mean Poisson's ratio of (non-muscle bearing) cortical bone across all axes was 0.33 (standard deviation of 0.10). Overall, the results confirm local variation in material properties which, it has been suggested, have adapted to correlate with the stress patterns related to regional mechanical functions. Although different properties were observed between the varying sample locations of the cranium, these were in effect relatively similar when compared to the facial bone.

Although less common, some studies are concerned with the behaviour of both cortical and cancellous bone together. McElhaney et al. (1970) used mechanical testing to determine the quasi-static mechanical properties of whole cranial bone, using samples which contain the entire sandwich structure. Over 200 cranial bone samples were tested from a mixture of embalmed or fresh autopsied human tissue, totalling 57 donors. It was noted that properties of embalmed and autopsy specimens did not significantly differ. Physical properties of rhesus monkey cranial bone were also tested for comparison. Mean parameters of human cranial bone were given as: dry weight density 1412 $kg/m^3$ (0.051 $lb/in^3$, with standard deviation of 0.019 $lb/in^3$), radial compressive elastic modulus 2.4 GPa ($3.5x10^5$ psi, with standard deviation of $2.1x10^5$ psi), tangential compressive elastic modulus 5.6 GPa ($8.1x10^5$ psi, with standard deviation of $4.4x10^5$ psi), and radial and tangential Poisson's ratios of 0.19 (standard deviation of 0.08) and 0.22 (standard deviation of 0.11) in compression respectively. Note that the dry weight density given involved density measurement after heating to ensure all fluid had evaporated, hence this density value is not suitable for representing *in vivo* bone. High variability in diploë layer properties was observed between individuals, which accounts for the large standard deviations in elastic moduli recorded. The observed behaviour confirmed transverse isotropy of the whole

cranial bone samples. Rhesus monkey bone samples yielded lower mean density, and radial and tangential moduli, confirming significant mechanical variation between species.

Hubbard (1971) tested beam-like samples of embalmed cranial bone in three-point bending. The samples contained both layers of compact bone and the diploë, i.e. the entire sandwich structure. The effective elastic modulus of the layered structure was found to range from 8.34 GPa to 9.51 GPa (1.21 to 1.38x$10^6$ psi) for the eight samples tested.

In (Claessens, 1994) it was suggested that when studying fully developed adults, the sutures in the bones do not need to be modelled separately or differentiated, as it has been reported that they have equal bending stiffness, and do not form a weakness. Claessens also argues that the varying thickness of the skull throughout its structure is likely the parameter that will most significantly affect the response of the system – and hence why, although the skull bones have a sandwich panel structure, modelling the skull as isotropic, homogeneous and linear elastic has become widely accepted in the literature.

Strain rate effects have been observed in cortical bone (Melvin et al., 1970; Wood, 1971), but not in cancellous bone (Melvin et al., 1970). To the author's knowledge, rate effects on whole samples (containing both cortical and cancellous regions) have not yet been investigated. The vast majority of finite element head models disregard rate effects in the skull by using a linear elastic material formulation. The importance of these rate effects is expected to be reduced when considering the entire skull sandwich structure, rather than the cortical bone in isolation; therefore a linear elastic material model was selected for the Stage 3 model in this study.

In (Wood, 1971) and (Peterson & Dechow, 2003) variations in the properties of different skull bones were noted, but these were minor. Previous complex finite element models which include the neck and vertebrae have achieved good results by equating the properties of vertebral and cranial bone (Wang et al., 2007; Zong et al., 2006). In reality vertebral bone will have different mechanical properties adapted to suit its function; however, this is expected not to appreciably affect the brain's pressure response, which is primarily under investigation. For the Stage 3 model it was decided that assigning the entire skull, mandible, and cervical vertebrae uniform properties was a reasonable assumption.

The MRI image used in this study did not provide good contrast between the cortical and cancellous bone areas, so the location of these areas was not always clear. In the current model, the layers of cortical bone have not been differentiated from the cancellous region. Hence the skull was modelled as a single homogeneous material, which is common practice

in finite element literature. The existing finite element research which employs homogeneous skull models was examined: in particular the relevant review papers (Deck & Willinger, 2009; Sauren & Claessens, 1993), and some head models which have been proven to perform well (Chen & Ostoja-Starzewski, 2010; Suh et al., 2005; Willinger et al., 1999); from these typical material constants were noted. As detailed in Table 2.2, these models had been validated against cadaveric tests, and so it was assumed that the skull material constants used approximate well the behaviour of the skull's sandwich structure. Young's modulus ranged from 2.4 to 6.5 GPa, with a typical Poisson's ratio of 0.22; this correlates well with properties measured for the whole sandwich structure in work by McElhaney et al. (1970). The density of the homogeneous skull was relatively consistent between models, a typical value being 2070 kg/m$^3$.

While the testing of cortical bone by itself produced high stiffness values similar to those used by Engin (1969), the modulus of the entire structure as measured by McElhaney et al. (1970) and Hubbard (1971) appears noticeably lower. For this study an elastic modulus of **6.5 GPa** was chosen, since it has been shown to perform well in previous finite element models, and lies close to the results reported by McElhaney and Hubbard. Similarly, a Poisson's ratio of **0.22** was selected. The density values commonly used in homogeneous skull models does not appear to agree well with the mechanical tests presented here. A density of 2070 kg/m$^3$ appears reasonable for cortical bone, but is above the density one would expect for a structure containing both cortical and porous cancellous bone. Unfortunately the density measurements of McElhaney et al. (1970) refer to dry weight, which would not be realistic for *in vivo* conditions. A homogeneous skull density intermediate of the cortical and cancellous densities detailed in the research above was deemed a reasonable assumption. A value of **1700 kg/m$^3$** was selected, which is just below the range of wet cortical bone given in (Gibson & Ashby, 1999) and (Peterson & Dechow, 2003), and well within the standard deviation of McElhaney's (1970) density measurements.

Finally, the intervertebral discs need to be considered. The discs are not expected to have a significant effect on the intracranial pressure behaviour for short duration impacts. For long duration impacts however, where the global acceleration of the head plays more of a role, the discs will affect bending of the neck and the resulting rotational forces. Currently, very few finite element head models include a detailed representation of the cervical spine; an exception is the model detailed in (Wang et al., 2007; Zong et al., 2006), where the intervertebral discs are represented by a linear elastic material with a modulus of 7.5845 MPa, Poisson's ratio of 0.35, and density of 1140 kg/m$^3$. These material properties

agree well with the literature. In (Yao et al., 2006) it was determined that a tissue-engineering scaffold for use as a disc restoration implant should have a compressive modulus of between 5-10 MPa in order to accurately represent the behaviour of a healthy disc. In (Rao & Dumas, 1991) the Poisson's ratio of the matrix of the discs composite structure was found to be about 0.45. Finally, a density close to that of water (1000 kg/m$^3$) would be expected due to the material's high water content. Based on these sources, linear elastic material properties for the discs were selected: an elastic modulus of **8.0 MPa**, Poisson's ratio of **0.35**, and density of **1140 kg/m$^3$**.

#### *2.3.2.3 The cerebrospinal fluid*

Cerebrospinal fluid (CSF) is a clear water-like fluid, about 100-150 ml of which circulates about the subarachnoid space and ventricular system of the head (Ommaya, 1968). It contains a small number of cells, and small amounts of protein, glucose, and inorganic salts (Goldsmith, 1972). The brain is surrounded by the CSF, which, other than providing some nutrients to the brain, is thought to have a damping effect minimising brain movement during impact (Claessens, 1994). The CSF layer has the potential to reduce the stresses and strains transferred to the brain, and so it is an important inclusion in this model (Hardy et al., 1994; Ommaya et al., 1994).

The CSF is arguably a less complex material than those previously discussed, and there is less variation in reported material properties. CSF has a high water content, and is expected to have a density roughly equal to that of water. The density of CSF from empirical measurements has been reported by various authors (Claessens, 1994; Goldsmith, 1972; Lubock & Goldsmith, 1980; Meulman, 1996) and is consistently given as about 1006 kg/m$^3$, with very little variation.

In work by Ommaya (1968), CSF is reported to have a low relative viscosity of 1.020-1.027 (compared to 1.000 for water). There appears to be little data on the bulk modulus of the fluid. In physical representations of the head by Ommaya et al. (1994) and Bandak (1996) water was deemed a reasonable approximation of CSF: thus assuming a bulk modulus of 2.19 GPa. Lubock & Goldsmith (1980), on the other hand, used artificial CSF in their physical head model, with a slightly higher bulk modulus of 2.258 GPa.

Ideally the CSF would be modelled as a fluid. The conventional method for numerical analysis of fluid flow is computational fluid dynamics (CFD). However, the dynamic interaction between fluid and solid materials in this case, known as a "fluid-structure interaction problem", would require coupling between CFD and FE codes – these

problems are notoriously computationally expensive and difficult to implement. Finite element head models have incorporated the cerebrospinal fluid layer using various alternate methods. Where it is not possible to model the CSF as a fluid, it is often approximated by a layer of solid elements which are assigned a low elastic modulus (typically in the order of kPa), implying a low shear modulus and hence fluid-like behaviour. These solid elements are then also assigned a Poisson's ratio just below 0.5, so that the material is essentially incompressible. Examples of this practice can be found in literature surveys by Sauren & Claessens (1993) and Deck & Willinger (2009). Another method to represent the cerebrospinal fluid in finite element models is by using an "elastic fluid" material formulation, discussed previously (see Section 2.1.3). Finite element head models which represent the CSF with elastic fluid elements typically set the bulk modulus equal to that of water (El Sayed et al., 2008; Kleiven, 2006).

Other than acting as a buffer, the inclusion of a layer of CSF between the brain and skull plays an important role in reducing the transmission of shear strains. Trosseille et al. (1992), in their finite element head model, observed that the incompressible nature of CSF restricts large perpendicular movement of the brain relative to the skull, while its low shear resistance allows relative transverse motion at this interface. In a series of finite element head impact simulations by Wittek & Omori (2003), it was found that inclusion of the CSF had a major effect on the pressures measured in the brain compared to an interface in which the brain was rigidly tied to the skull. On the other hand it was found that the material properties of CSF (such as viscosity) had minimal effect, which suggests that the subtleties of the interface are less important than the nature of the interface itself. Therefore, it was decided that a linear elastic fluid formulation for CSF would be sufficient for the Stage 3 model.

The author notes that it is common in finite element research for the CSF to be modelled as having a density of 1040 kg/m$^3$. This figure does not agree with the empirical values reported above. The author believes this to be a legacy of early finite element head models, where it was common to assign the CSF properties equal to that of the brain (1040 kg/m$^3$ is a typical density value used for the brain, see Table 2.2). In this project the density of CSF was selected as **1006 kg/m$^3$**.

Ruan et al. (1994) suggested the bulk modulus of CSF be set an order of magnitude lower than that of water, to account for the pressure relieving effect of the ventricular system (a series of channels containing CSF which run through the centre of the brain). This viewpoint was also argued in (Sauren & Claessens, 1993). The ventricular system secretes

cerebrospinal fluid and acts as a channel for flow of CSF before it is absorbed into the bloodstream (Claessens, 1994). Significant strain relief due to these structures was observed in physical models by Ivarsson et al. (2000), and finite element experiments by Belingardi et al. (2005). In this Stage 3 model the ventricular system was differentiated from the surrounding matter, and hence the compressibility of CSF did not need to be artificially reduced; a bulk modulus of **2.19 GPa** was applied, equal to that of water. The ventricular regions and subarachnoid space (between the brain and skull) were both assigned the material properties of CSF.

#### *2.3.2.4 The scalp and flesh*

The scalp is a layer of skin, fat and connective tissue which covers the cranial bones. One of its functions is to act as a cushion against impact (Claessens, 1994). It consists of five tissue layers: (1) skin and hair, (2) a subcutaneous fat connective tissue layer, (3) the *aponeurotic* layer – a fibrous tendon-like membrane, (4) a layer of loose connective tissue, and (5) the *pericranium*, a tough vascular layer. The human scalp is in total about 6 to 12 mm thick. It is said to be highly anisotropic, and can be thought of as a composite of fibres in a matrix of fat (Goldsmith, 1972).

Gadd et al. (1970) conducted a series of drop loading tests on scalp tissue *in situ* on unembalmed human cadavers, and the soft tissue trauma was noted for different impactors and angles. The extent of trauma was observed to depend strongly on the angle of incidence of the impactor. Interestingly however, the orientation of the impactor's edge did not appear to affect the results, despite the anisotropic nature of scalp tissue. Gadd et al. also investigated the mechanical properties of the soft tissue through compression of *in vitro* samples taken from various locations, such as: the frontal scalp, parietal scalp, facial tissue, and soft tissue from the arm. The thickness of soft tissue was found to vary between locations on the head. Also, the scalp was found to be tougher and more resistant to crushing than soft tissue from other areas of the body, where the material was weaker and fatty. The results of these compression tests were presented in the form of hysteresis plots, detailing load vs. displacement of the tissue. Using these plots and the dimensions of the samples and test apparatus given, values of elastic modulus for the parietal scalp (from test 50S of Gadd et al's work) can be derived. The results clearly show a non-linear stiffening of the tissue at high levels of compression (reduction in thickness); this presumably occurs as the structure undergoes significant non-recoverable deformation and densification ("crushing"), so resistance to further deformation is increased. The initial linear elastic modulus of human parietal scalp could be derived from Gadd et al's work as approximately

0.86 MPa – while at approximately 25% compression the modulus was about 3.2 MPa – and at 52% compression, the maximum achieved in Gadd et al's tests, the modulus was about 29.5 MPa.

Raposio & Nordström (1998) tested 20 flaps of *in vivo* scalp tissue from 10 human volunteers during plastic surgery procedures. The outermost layers of scalp tissue were separated below the aponeurotic layer from the connective tissue beneath and tested in tension in-plane. Although soft biological materials are viscoelastic in nature, Raposio & Nordström were able to test the tissue within a short time-frame (approximately 2 seconds per measurement), which they argue negates significant viscoelastic (time-dependant) effects; hence the scalp is treated as linear elastic. The mean observed load per millimeter of extension was given as 117.1 g/mm. This value can be converted into a more convensional elastic modulus by taking into account the dimensions of the tissue given in (Raposio & Nordström, 1998), and the mean thickness of the scalp at the top of the head (which was the location of these tests) as given in (Gadd et al., 1970). A modulus of roughly 0.13 MPa can be derived, which is considerably lower than the results of Gadd et al. (1970) – while this may partially be due to the fact that Raposio & Nordström do not include the tough pericranial layer, contrasting the scalp's resistance to radial compression (reported by Gadd et al.), with the resistance to transverse tension (reported by Raposio & Nordström), serves to highlight the anisotropic nature of this laminar-composite-like material.

The scalp is an important consideration, since it will affect the impact force transferred to the skull. However, there is a surprising paucity of finite element models which include a representation of the scalp, those that do include: the recent versions of the Université Louis Pasteur (ULP) model (Raul et al., 2006), the Kungliga Tekniska Högskolan (KTH) model (Kleiven, 2006), models by Khalil & Hubbard (1977) and Belingardi et al. (2005), and a recent model of paediatric head injury (Roth et al., 2009). These models agree closely on the material constants of the scalp, typically ascribing the structure an elastic modulus of 16.7 MPa, a Poisson's ratio of 0.42, and density of 1200 kg/m$^3$. There is little variation between the properties of the scalp in these models, except in the work by Khalil & Hubbard (1977), where an elastic modulus approximately twice this value was used. Khalil & Hubbard justified this choice by stating, in agreement with the observations in (Gadd et al., 1970), that the scalp will have an increased resistance at large deformations. Therefore, in order to represent this using a linear elastic model, they decided to halve the thickness of the scalp elastic layer (a thickness of 3.18 mm was used), and represent this thinner

"deformed" scalp layer with a greater elastic modulus. Khalil & Hubbard interpreted the findings reported by Gadd et al. (1970) as demonstrating that, at 50% compression, the scalp has a modulus of 34.5 MPa, and so this value was used.

The biofidelic model in this study, the Stage 3 head model, differentiates the flesh and scalp into two regions. The first region represents the flesh of the neck, face, and the majority of the scalp. The second region represents a patch of scalp at the impact site. For the first region, representing the majority of the scalp, it was decided that a linear elastic material approximation would be sufficient. This region was assigned properties equal to those used in the detailed finite element head models mentioned previously: a modulus of **16.7 MPa**, Poisson's ratio of **0.42**, and a density of **1200 kg/m$^3$**. These properties have proven effective at modelling the scalp, and although this was expected to slightly overestimate the stiffness of the other tissues (flesh of face and neck), the effect was assumed negligible.

In this investigation it was critical that the compression behaviour of the scalp at the impact site be represented accurately. As the thin layer of scalp is compressed between the comparatively stiff skull and impactor surfaces, the material crushes and densifies, stiffining significantly. This behaviour was represented by assigning the scalp patch at the impact site a non-linear material formulation (MAT_057 in LS-DYNA), which allows input of a user-defined stress vs. strain curve (LSTC Inc, 2007). Curve fitting was applied to the radial scalp compression data reported in Gadd et al's (1970) research (test 50S). An exponential stress-strain relation [Equation 2.2] was found to represent well Gadd et al's data.

$$\sigma(MPa) = (9 \cdot 10^{20})^{\frac{21\pi}{424}\left(-\varepsilon^{\left(\frac{589\pi}{793}\right)}\right)} - 1 \qquad [2.2]$$

where $\sigma$ is the nominal compressive stress in MPa, and $\varepsilon$ is the nominal strain. The use of this stress-strain relation allowed the compression behaviour of scalp tissue to be estimated beyond the maximum reduction in thickness observed by Gadd et al. The stress-strain relation of the non-linear scalp was defined by Gadd et al's original data between $0 \leq \varepsilon \leq -0.52$, and by Equation 2.2 between $-0.52 < \varepsilon \leq -0.97$. Finally, this non-linear scalp region was assigned a density of **1200 kg/m$^3$**, while Poisson's ratio was effectively zero, since it cannot be applied using this material formulation.

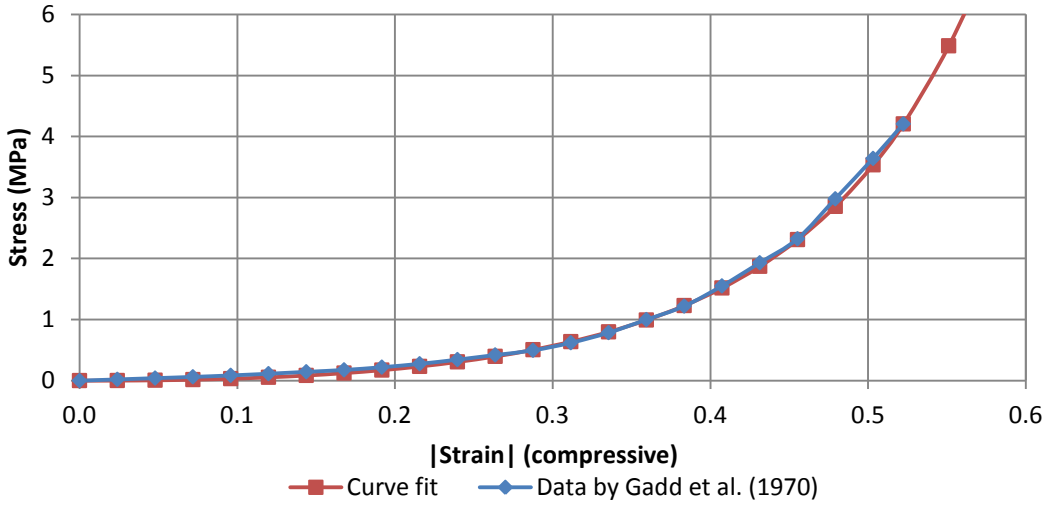


*Figure 2.5: Scalp nominal stress vs. strain in radial compression. Original data by Gadd et al. (1970) up to ε = -0.52 is visible, along with a portion of the exponential curve fit. Good agreement between the original data and the fit can be seen.*

After a comprehensive review of the literature relating to the material properties of the major structures of the head, material models and constants were selected for use in this final head model. Table 2.3 below, summarises these properties.

| Structure | Material formulation | $G_\infty$ (kPa) | $G_0$ (kPa) | $\beta$ ($s^{-1}$) | $B$ (GPa) | $E$ (GPa) | $\nu$ | $\rho$ ($kg/m^3$) |
|---|---|---|---|---|---|---|---|---|
| Grey Matter, White Matter, Cerebellum, Brain Stem | viscoelastic | 170 | 530 | 35 | 2.19 | | | 1080 |
| Skull, Vertebrae | elastic | | | | | 6.5 | 0.22 | 1700 |
| Intervertebral Discs | elastic | | | | | 8.00e-3 | 0.35 | 1140 |
| Cerebrospinal Fluid, Ventricles | elastic fluid | | | | 2.19 | | | 1006 |
| Scalp, Flesh | elastic | | | | | 1.67e-2 | 0.42 | 1200 |
| Scalp at impact site (non-linear) | user defined stress-strain relation | | | | | varies: min. = 8.60e-4, max. = 18.62 | | 1200 |

*Table 2.3: Material properties assigned to all structures represented in the high complexity head model (Stage 3).*

### *2.3.3 Meshing*

In the original Simpleware-NRL head model the MRI image data had been downsampled to a resolution with 1.04×1.04×1.04 mm voxels. Here it has been demonstrated (see Section 2.1.3) that a lower resolution (2×2×2 mm voxels) was suitable for generating a mesh capable of sufficient numerical accuracy for this study. However, a further

consideration of image-based models is that the image resolution is such that it can accurately represent all the necessary small features which have been captured in the original data. In the Stage 3 head model, the image was not downsampled further, but left at 1.04×1.04×1.04 mm, since a lower resolution was found to interfere with the accuracy and connectivity of thin features, in particular the CSF layer. As previously, a high density mesh region with 0.55 mm voxel spacing was applied to the contact site and the model was meshed using the mixed hex/tet method in +FE.

The completed high biofidelity model of the head and neck was composed of just over 13.2M solid elements, and was found to have a minimum of 8 elements across the thickness of the skull. The mean in-out aspect ratio of the mesh was 0.788, and no elements had an aspect ratio lower than 0.1.

### *2.3.4 Boundary and contact conditions*

In the Stage 1 and Stage 2 models the head was unsupported and free to translate along the axis of impact. This assumes therefore, in line with the majority of previous finite element head model research, that the short durations characteristic of impact loading render the constraints imposed by the neck attachment negligible to the local response of the head (Claessens, 1994). Specifically, in work by Willinger et al. (1999) and Suh et al. (2005) it was suggested that the neck constraint has no effect on the mechanics of the head within 6-7 ms after impact. However, Kuijpers et al. (1996) noted that the addition of a neck constraint to their finite element head model subject to impact introduces rotational acceleration and noticeably affects the pressure and shear responses of the brain. This effect is noticeable almost immediately after incidence (within approximately 0.2 ms from the start of impact); the author believes this is due to the fact that Kuijpers et al. (1996) use rigid beams to model the neck, which therefore implies an infinite wave speed through this structure, underestimating the time before it would have an influence on the impact response. In order to investigate and account for the influence of the neck attachment, the Stage 3 head includes the neck as modelled by the first 7 cervical vertebrae, intervertebral discs, and surrounding flesh. The lower boundary of the model is a horizontal planar surface just above the sternum. Fixed constraints were applied to this surface, restricting its 6 degrees of freedom in both translation and rotation. No other constraints were applied to the head in this model.

Contacts between all components of the head were modelled as tied. As mentioned previously, the accuracy of the interface between the brain and skull is generally regarded to

be greatly improved by the inclusion of a layer of elements with zero shear resistance, representing the CSF.

The impactors used in the Stage 3 investigation make contact with the region of non-linear flesh, rather than directly with the skull; therefore the difference in stiffness between the two materials which collide is several orders of magnitude larger than experienced in Stages 1 and 2. Furthermore, just as would occur during a real head impact, this thin layer of flesh (approximately 7 mm in thickness at the contact site) becomes compressed between the comparatively stiff skull and impactor during collision. In this way the flesh experiences significant compressive strains: a maximum of 80.2% reduction in thickness was observed during the Stage 3 investigation (undeformed thickness of 6.88 mm reduced to 1.36 mm). Initial simulations resulted in several errors: the mesh densifies significantly, such that some elements fail by becoming inverted, while at certain regions the contact fails resulting in the flesh and impactor meshes interpenetrating. Impact tests were performed in order to resolve these issues.

The "null shells" method was employed, which is a common technique for dealing with contact problems resulting from the use of dissimilar materials (Oasys Ltd., 2010). A single layer of shell elements was created over the contact surfaces of the flesh and impactor. These shell elements were assigned a "null material" model with zero stiffness, thus not affecting the mechanics of impact. However, this null material allows an elastic modulus to be defined which is used solely for calculation of the contact stiffness. In this way flesh-impactor interaction was modelled indirectly, by defining a contact between the flesh and impactor's null shell coatings.

This flesh-impactor null shell contact formulation was modified: by optimising the contact stiffness for maximum numerical stability (using the "SOFT=1" option in LS-DYNA), by disabling "shooting node logic" ("SNLOG=1"), by artificially increasing the thickness of the contact surface ("SFST=SFMT=2.5"), and by enabling automatic deletion of elements beyond large distortions which require a timestep less than 0.7% of the original simulation timestep ("ERODE=1" and "DTMIN=0.007"). These values were determined through a series of impact tests, examining the effect of various contact modifications on the performance of the model. Together these modifications allowed the contact between the two highly dissimilar materials to function without error. This stable contact, along with a high quality mesh at the contact site, produced a highly deformable and recoverable mesh that was numerically stable, without the need to resort to remeshing or mesh smoothing during the simulation.

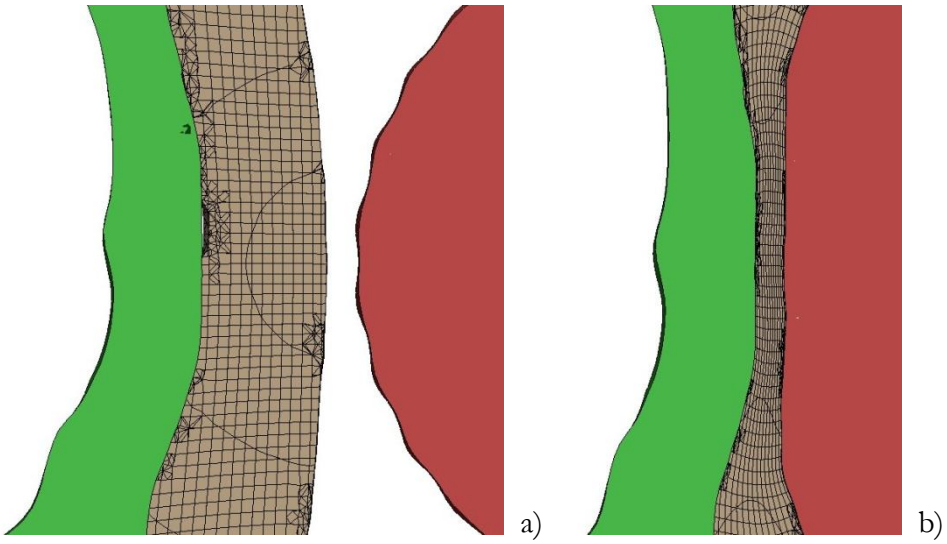


*Figure 2.6: (a) Undeformed, and (b) deformed sagittal section views of the non-linear flesh at the contact site during an impact with a golf ball. The green, beige, and red regions represent the skull, non-linear flesh, and impactor respectively. Element boundaries of the flesh are visible in order to illustrate the degree of densification.*

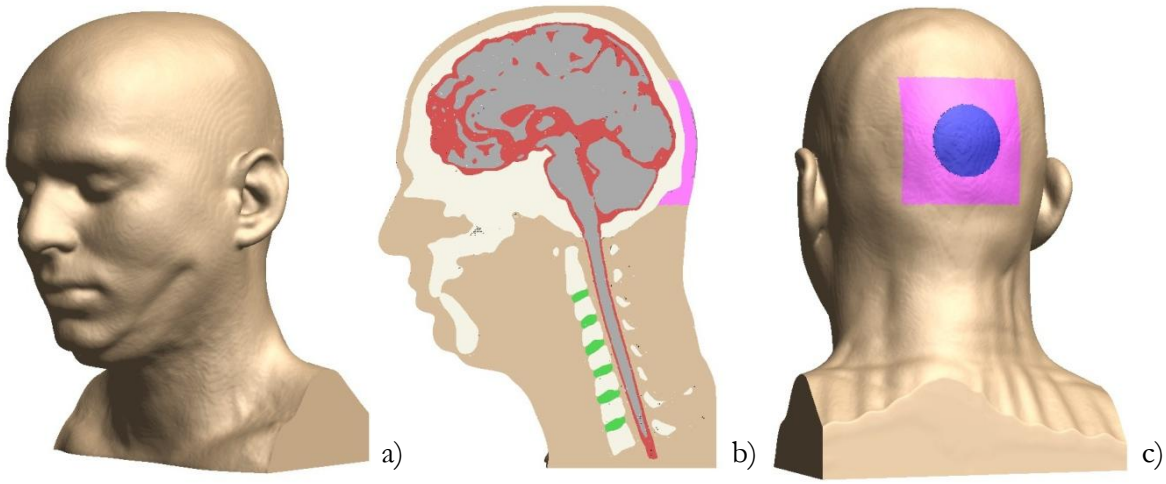


*Figure 2.7: (a) Oblique frontal, (b) sagittal section, and (c) oblique rear views of the completed Stage 3 highly biofidelic head model. Here grey represents the central nervous system, the CSF is red, the skull and other bones are white, the intervertebral discs are green, the linear elastic flesh is beige, the non-linear flesh is magenta, and the null shells coating the impact site are blue.*

## 2.4 Experimental procedure

### *2.4.1 Implicit and explicit time integration*

Generally finite element solvers use one of either implicit or explicit time integration techniques. Which method is most appropriate depends on the time scale of the problem. For problems described by non-linear partial differential equations (PDEs), analytical solutions cannot be derived, and only numerical solutions are available. Both the implicit and explicit numerical analysis methods calculate the solution to the problem in a number of incremental steps, called *timesteps* ($\Delta t$). Here, "implicit" refers to the method of calculating the state of the problem at the next timestep $t + \Delta t$ based on information at time $t + \Delta t$, whereas the "explicit" method determines the state at the next timestep $t + \Delta t$ based on the current timestep $t$ (Harewood & McHugh, 2007).

The implicit method is capable of dividing the simulation time into larger timesteps, therefore fewer timesteps are needed. It is able to do this because each implicit timestep is calculated on an iterative basis and is unconditionally stable. The stiffness matrix of the problem must be assembled and inverted for each timestep, and therefore each timestep is computationally expensive. Implicit analysis is commonly used for static or quasi-static problems. Its long timesteps make it efficient when studying events which occur over a long duration. However, the implicit method is not recommended for high-speed dynamic problems, as the timestep will be too large to capture stress waves through the material, or to accurately capture contacts between objects which may collide. Implicit analysis is also less suited to problems involving many or large non-linearities, as it may have trouble achieving convergence (MSC Software Corporation, 2005).

The explicit method must divide the simulation time into many small timesteps. This is because explicit timesteps are conditionally stable. Each timestep must be below a certain critical duration, which is determined by the size of the smallest element and the wave speed through the material, i.e. the timestep must be smaller than the amount of time required for a stress wave to propagate through the smallest element, in order to prevent the growth of errors. While there are a greater number of timesteps compared to the implicit method, each timestep is computationally inexpensive since no iteration is required. Explicit analysis is more suited to short duration dynamic problems, problems involving contact, and non-linear materials (Oasys Ltd., 2010); therefore in this study an explicit finite element code was used, LS-DYNA (LSTC Inc.).

### *2.4.2 Finite element considerations*

Prior to running any simulations with the completed models, the following points needed to be considered.

#### *2.4.2.1 Hourglassing*

The stresses in elements can be calculated in different ways. In this study all solid elements had stresses calculated at a single integration point in the centre of the element ("ELFORM=1"). This is the default method used in LS-DYNA; these single point elements are generally much more stable and computationally inexpensive compared to fully integrated elements. A disadvantage of this method however, is that under certain loading conditions, single point hexahedral elements may deform according to zero energy deformation modes (Hallquist, 2006). This is called "hourglassing": these non-physical deformation modes produce no stress or strain and therefore deformation is not resisted. Hourglassing can be suppressed by the use of artificial stiffness and viscosity controls within LS-DYNA, designed specifically to counter hourglass modes while adding the minimum amount of additional stiffness to the system. In the Stage 1 and Stage 2 models, the default LS-DYNA viscous hourglass controls were used throughout. It has been reported that the default hourglass stiffening amount is too great for fluids (LSTC Inc and DYNAmore GmbH, 2012; Tutt & Taylor, 2004), therefore in the Stage 3 head model the degree of hourglass stiffening in the CSF region was reduced by an order of magnitude ("QM=0.01").

The degree of hourglassing that occurs in a simulation can be evaluated by tracking the amount of physical energy stored in elements which have undergone hourglassing (the "HGEN=2" option enables this calculation). It is recommended that this "hourglass energy" remain less than 10% of the total energy balance in order for a simulation to remain accurate (Oasys Ltd., 2010). In this study, the amount of hourglass energy was negligible for the majority of impacts. However the large compression of the scalp mesh during the high velocity impacts in the Stage 3 investigation resulted in non-negligible amounts of hourglass energy. The greatest hourglass energy observed was 13.8% of the total energy, however this value was only reached long after the impact was over. In the window of interest (during the contact duration and time immediately after impact) peak hourglass energy was only 8.8%, which was deemed acceptable.

#### *2.4.2.2 Mass scaling*

Pressure waves travel faster through materials which are light and stiff, rather than dense and soft, as described by Equations 1.1 and 1.2. As mentioned above, for the explicit finite element method to remain stable the simulation time must be divided into a number of timesteps, where each timestep is no larger than the shortest time required for a pressure wave to travel across any of the elements in the mesh. The computational resources required for a given simulation depend on the number of timesteps needed, which is determined by the material properties assigned to the model and the size of the smallest elements in the mesh. In this study, the critical timestep is therefore likely to be limited by the smallest elements in the skull, since these elements have been assigned a greater stiffness than the other structures in the model and so have a greater wave speed.

The limiting timestep size can be raised by artificially increasing the material density of the smallest elements in the mesh, such that their wave speed is reduced. This process is known as "mass scaling", and can be useful in reducing the computational resources needed to run large models. This method adds non-physical mass to the system, and therefore must be used moderately to avoid its effects dominating the response. It is commonly recommended that the percentage of added mass not exceed 5% of the total mass of the system (Bala, 2006). In conventional mass scaling, all the eigenfrequencies of the system are affected by these additional inertia forces. In the present research, a modification of the conventional mass scaling technique was used, called "selective mass scaling". This method differs from conventional mass scaling in that only the high frequencies of the system will be affected by any additional mass. The low frequencies (rigid body modes) behave as if no mass has been added, so allowing a greater increase in the critical timestep before the response of the system becomes noticeably affected (LSTC Inc and DYNAmore GmbH, 2010).

No mass scaling was applied to the Stage 1 model; the relative simplicity of this model meant that simulations did not require an unreasonable amount of real time to complete. However, mass scaling was used in Stages 2 and 3, as these models are significantly larger. Before mass scaling was applied an initial test case was run on the Stage 2 model without mass scaling. The Stage 2 simulation without mass scaling required approximately 53 hours per ms of simulation time / number of cores (240 hours to compute 9 ms of simulation time using 2 cores). With selective mass scaling the same impact took 48 hours per ms of simulation time / number of cores. This is a reduction in the amount of real time required to compute the simulation by 9.4%, for a negligible increase in mass of only $6.8\times10^{-7}$ kg

(which represents $6.2\times10^{-6}$ % of the total mass of the system). The output of the mass scaled and non-mass scaled models were compared and no discernible disparity between the results was observed. The maximum mass scaling used during any of the Stage 2 impacts was $3.1\times10^{-3}$ %, and the maximum during the Stage 3 impacts was 0.56%. Hence, in all simulations added mass was well below the recommended limit of 5%. Despite the use of mass scaling, the complex models in Stages 2 and 3 required large amounts of real time to complete. In particular, the various impact experiments performed on the Stage 3 biofidelic head model took between 4 to 47 days to complete (at speeds ranging from 192 to 563 hours per ms of simulation time / number of cores).

### *2.4.3 Running simulations and analysing results*

All impact simulations were run using the MPP ("massively parallel processing") LS-DYNA program version 971, on a single workstation with two Intel Xeon 3.16 GHz CPUs (model number X5460) which have four cores each. The workstation was running Microsoft Windows Server 2003 (SP2) 64-bit, and had 64 GB of RAM.

#### *2.4.3.1 Choice of impact location*

Impact location was an important consideration which needed to be consistent across the models so that they could be easily compared. As mentioned previously, impact location is a factor that can influence whether rotational accelerations are generated in the head. To minimise these, the Stage 1 impacts were collinear, i.e. the centres of gravity of the head model and of the impactor were both intersected by the axis of impact; this is analogous to the impact location used in experiments by Young & Morfey (1998).

In the Stage 2 and Stage 3 models the impacts were collinear with the centre of gravity of the brain, the axis of impact was defined by the intersection of horizontal and midsagittal planes, with the impactor proceeding in a posterior to anterior direction to collide with the rear of the head (on the occipital bone). In this way the Stage 2 and Stage 3 impact locations were identical, with the exception of the scalp layer included between the skull and impactor in Stage 3. Impacts to different regions of the head will modify the intracranial response. In this study the impact location was chosen to reduce the influence of the facial bones: the rear of the head more closely approximates the local geometry of a simple spherical shell, as used in Stage 1.

#### *2.4.3.2 Choice of sampling points*

The results of the finite element simulations were analysed using the D3PLOT graphical post-processor and the T/HIS data plotting software (Oasys Ltd.). D3PLOT allowed the deformations, velocities, pressures, and overall behaviour of the head during impact to be analysed graphically, while T/HIS allowed more detailed XY plotting of parameters such as pressure to be monitored for individual elements within the mesh. In order to enable this more detailed tracking of parameters at individual elements for later analysis in T/HIS, the elements of interest, or "sampling points", needed to be highlighted prior to running the simulations (HISTORY_SOLID in LS-DYNA). This was done sparingly, as a lot of data is generated per sampling point. Several sampling points were placed in regions of particular interest in each model, i.e. at the coup and contrecoup of the brain, and their locations recorded.

#### *2.4.3.3 Filtering*

The main parameter that was analysed was pressure within the brain. In Stage 1, the pressures recorded at sampling points at the coup contained a large amount of noise in the form of high frequency pressure fluctuations. This was almost certainly numerical noise, which is present in any finite element simulation, but may have become exaggerated in Stage 1 due to the exact superposition of nodes on the skull and impactor's contact surfaces. Filtering is often applied to remove high frequency noise which can cloud the underlying results. Commonly a low-pass filter is used, in which case the minimum amount of filtering, i.e. the greatest acceptable cut-off frequency, should be used to avoid distorting the results. Filtering was performed using the guidelines outlined in NASA's "Best practices for crash modeling and simulation" in order to obtain the fundamental pulse (Fasanella & Jackson, 2002). Pressure-time data from sampling points at the coup in Stage 1 were processed in T/HIS using a $2^{nd}$ order Butterworth low-pass filter, with the cut-off frequency set to 10 kHz. No filtering was required in Stages 2 or 3.

Bala, S. (2006). Overview of Mass-Scaling in LS-DYNA. *LS-DYNA and d3VIEW Blog*. Retrieved November 27, 2012, from http://blog2.d3view.com/overview-of-mass-scaling

Bandak, F. A. (1996). Biomechanics of impact traumatic brain injury. *NATO Advanced Studies Institute: Crashworthiness of Transportation Systems*, *1*.

Barber, T., Brockway, J. A., & Higgins, L. S. (1970). The density of tissues in and about the head. *Acta Neurologica Scandinavica*, *46*(1), 85–92.

Belingardi, G., Chiandussi, G., & Gaviglio, I. (2005). Development and validation of a new finite element model of human head. In *Proceedings of the 19th International Technical Conference on the Enhanced Safety of Vehicles* (Vol. 38, pp. 3766–76). Washington, D.C.

Benzley, S., Perry, E., Merkley, K., & Clark, B. (1995). A comparison of all hexagonal and all tetrahedral finite element meshes for elastic and elasto-plastic analysis. In *Proceedings of the 4th International Meshing Roundtable* (pp. 179–191). Sandia National Laboratories, Albuquerque.

Bui Xuan, V. (2008). *Development of a pre-processing environment for 3D image based finite element mesh generation. Thesis*. University of Exeter.

Chen, Y., & Ostoja-Starzewski, M. (2010). MRI-based finite element modeling of head trauma: spherically focusing shear waves. *Acta Mechanica*, *213*(1-2), 155–167.

Cheng, L. Y., Rifai, S., Khatua, T., & Piziali, R. L. (1990). Finite element analysis of diffuse axonal injury. In *Proceedings of the 34th STAPP Car Crash Conference* (pp. 141–154).

Christ, A. F., Franze, K., Gautier, H., Moshayedi, P., Fawcett, J., Franklin, R. J. M., … Guck, J. (2010). Mechanical difference between white and gray matter in the rat cerebellum measured by scanning force microscopy. *Journal of Biomechanics*.

Claessens, M. H. A. (1994). Anatomical description of the human head. *Technical report*. Retrieved from http://alexandria.tue.nl/repository/books/642185.pdf

Deck, C., & Willinger, R. (2009). The current state of human head finite element modelling. *International Journal of Vehicle Safety*, *4*(2), 85–112.

DiMasi, F., Marcus, J., & Eppinger, R. (1991). 3-d anatomic brain model for relating cortical strains to automobile crash loading. In *Proceedings of the 13th International Conference on Experimental Safety Vehicles* (pp. 916–924). Washington, D.C.

El Sayed, T., Mota, A., Fraternali, F., & Ortiz, M. (2008). Biomechanics of traumatic brain injury. *Computer Methods in Applied Mechanics and Engineering*, *197*(51-52), 4692–4701.

Engin, A. E. (1969). The axisymmetric response of a fluid-filled spherical shell to a local radial impulse – a model for head injury. *Journal of Biomechanics*, *2*(3), 325–341.

Fasanella, E. L., & Jackson, K. E. (2002). *Best practices for crash modeling and simulation. NASA technical report*. Retrieved from http://citeseerx.ist.psu.edu/viewdoc/download?doi=10.1.1.6.8863&rep=rep1&type=pdf

Gadd, C. W., Nahum, A. M., Schneider, D. C., & Madeira, R. G. (1970). Tolerance and properties of superficial soft tissues in situ. In *Proceedings of the 14th STAPP Car Crash Conference* (pp. 356–368).

Galbraith, C. G., & Tong, P. (1988). Boundary conditions in head injury finite element modeling. *16th Annual International Workshop on Human Subjects for Biomechanical Research*, 179–193.

Galford, J., & McElhaney, J. H. (1970). A viscoelastic study of scalp, brain, and dura. *Journal of Biomechanics*.

Gibson, L. J., & Ashby, M. F. (1999). Cancellous bone. In *Cellular solids: Structure and Properties - 2nd edition* (pp. 429–452). Cambridge University Press.

Goldsmith, W. (1972). Biomechanics of head injury. In Y. C. Fung, N. Perrone, & M. Anliker (Eds.), *Biomechanics: Its Foundations and Objectives*. Prentice-Hall, Englewood Cliffs, NJ.

Gong, S., Lee, H. P., & Lu, C. (2008). Computational simulation of the human head response to non-contact impact. *Computers & Structures*, *86*(7-8), 758–770.

Hallquist, J. (2006). *LS-DYNA Theory Manual*. Retrieved from http://www.lstc.com/download/manuals

Hardy, W. N., Foster, C., Mason, M., Yang, K. H., & King, A. I. (2001). Investigation of Head Injury Mechanisms Using Neutral Density Technology and High-Speed Biplanar X-ray. *Stapp Car Crash Journal*, *45*, 337–368.

Hardy, W. N., Khalil, T. B., & King, A. I. (1994). Literature review of head injury biomechanics. *International Journal of Impact Engineering*, 561–586.

Harewood, F. J., & McHugh, P. E. (2007). Comparison of the implicit and explicit finite element methods using crystal plasticity. *Computational Materials Science*, *39*(2), 481–494.

Horgan, T., & Gilchrist, M. D. (2004). Influence of FE model variability in predicting brain motion and intracranial pressure changes in head impact simulations. *International Journal of Crashworthiness*, *9*(4), 401–418.

Hubbard, R. P. (1971). Flexure of layered cranial bone. *Journal of Biomechanics*, *4*(4), 251–263.

Ivarsson, J., Viano, D. C., Lövsund, P., & Aldman, B. (2000). Strain relief from the cerebral ventricles during head impact: experimental studies on natural protection of the brain. *Journal of Biomechanics*, *33*(2), 181–9.

Johnson, K. L. (2003). *Contact Mechanics* (9th ed.). Cambridge University Press.

Khalil, T. B., & Hubbard, R. P. (1977). Parametric study of head response by finite element modeling. *Journal of Biomechanics*, *10*(2), 119–32.

Kleiven, S. (2006). Evaluation of head injury criteria using a finite element model validated against experiments on localized brain motion, intracerebral acceleration, and intracranial pressure. *International Journal of Crashworthiness*, *11*(1), 65–79.

Kuijpers, A., Claessens, M. H. A., & Sauren, A. (1996). A two-dimensional FEM analysis of the response of the human head to impact: the importance of boundary conditions. *Computer Methods in Biomechanics and Biomedical Engineering*, 207–216.

Lee, E. S. (1990). *A large-strain, transient-dynamic analysis of head-injury problems by the finite element method. Thesis*. Retrieved from http://smartech.gatech.edu/handle/1853/20753

LSTC Inc. (2007). *LS-DYNA Keyword Users Manual: Volume 1* (Vol. I). Retrieved from http://www.lstc.com/download/manuals

LSTC Inc and DYNAmore GmbH. (2003). Contact: SOFT option. *LS-DYNA Support*. Retrieved November 02, 2012, from http://www.dynasupport.com/howtos/contact/soft-option

LSTC Inc and DYNAmore GmbH. (2010). Selective mass scaling (SMS). *LS-DYNA Support*. Retrieved November 28, 2012, from http://www.dynasupport.com/howtos/general/selective-mass-scaling-sms-2

LSTC Inc and DYNAmore GmbH. (2012). Hourglass. *LS-DYNA Support*. Retrieved November 27, 2012, from http://www.dynasupport.com/howtos/element/hourglass

Lubock, P., & Goldsmith, W. (1980). Experimental cavitation studies in a model head-neck system. *Journal of Biomechanics*, *13*(12), 1041–1047.

McElhaney, J. H., Fogle, J. L., Melvin, J. W., Haynes, R. R., Roberts, V. L., & Alem, N. M. (1970). Mechanical properties of cranial bone. *Journal of Biomechanics*, *3*(5), 495–512.

Melvin, J. W., McElhaney, J. H., & Roberts, V. L. (1970). Development of a Mechanical Model of the Human Head- Determination of Tissue Properties and Synthetic Substitute Materials. In *Proceedings of the 14th STAPP Car Crash Conference* (pp. 221–240).

Meulman, J. (1996). An experimental investigation to the constitutive behaviour of brain tissue. *Technical report*, *80*(10), 289–302. Retrieved from http://www.narcis.nl/publication/RecordID/oai:library.tue.nl:461975/Language/en

MSC Software Corporation. (2005). *Explicit transient dynamic analysis*. *MSC.Dytran Seminar Notes* (pp. 1–14). Retrieved from ftp://ftp.mscsoftware.com.tw/download/training/dytran_basic/chapter_2.ppt

Nahum, A. M., Smith, R., & Ward, C. C. (1977). Intracranial pressure dynamics during head impact. In *Proceedings of the 21st STAPP Car Crash Conference*. New Orleans, LA, USA.

NASA. (1995). Volume 1, Section 3: Anthropometry and biomechanics. *Man-system integration standards*. Retrieved November 05, 2012, from http://msis.jsc.nasa.gov/sections/section03.htm

Oasys Ltd. (2010). *Information provided on the "Introductory training course" 18th to 19th Jan 2010*. *Oasys LS-DYNA training courses*. Solihull, West Midlands, UK.

Ommaya, A. K. (1968). Mechanical properties of tissues of the nervous system. *Journal of Biomechanics*, *1*(2), 127–136.

Ommaya, A. K., Thibault, L., & Bandak, F. A. (1994). Mechanisms of impact head injury. *International Journal of Impact Engineering*, *15*(4), 535–560.

Peterson, J., & Dechow, P. C. (2003). Material properties of the human cranial vault and zygoma. *The anatomical record. Part A, Discoveries in molecular, cellular, and evolutionary biology*, *274A*(1), 785–797.

Pinnoji, P. K., & Mahajan, P. (2008). Two wheeler helmets with ventilation and metal foam. *Defence Science Journal*, *58*(2), 304–311.

Prange, M. T., & Margulies, S. S. (2002). Regional, Directional, and Age-Dependent Properties of the Brain Undergoing Large Deformation. *Journal of Biomechanical Engineering*, *124*(2), 244.

Prange, M. T., Meaney, D. F., & Margulies, S. S. (2000). Defining brain mechanical properties: effects of region, direction, and species. *Stapp Car Crash Journal*, *44*, 205.

Rao, A. A., & Dumas, G. A. (1991). Influence of material properties on the mechanical behaviour of the L5-S1 intervertebral disc in compression: a nonlinear finite element study. *Journal of Biomedical Engineering*, *13*(2), 139–151.

Raposio, E., & Nordström, R. E. A. (1998). Biomechanical properties of scalp flaps and their correlations to reconstructive and aesthetic surgery procedures. *Skin Research and Technology*, *4*(2), 94–98.

Raul, J.-S., Baumgartner, D., Willinger, R., & Ludes, B. (2006). Finite element modelling of human head injuries caused by a fall. *International Journal of Legal Medicine*, *120*(4), 212–8.

Rho, J., Hobatho, M., & Ashman, R. (1995). Relations of mechanical properties to density and CT numbers in human bone. *Medical Engineering & Physics*, *17*(5), 347–355.

Roth, S., Raul, J.-S., & Willinger, R. (2009). Finite element modelling of paediatric head impact: Global validation against experimental data. *Computer Methods and Programs in Biomedicine*, *99*(1), 25–33.

Ruan, J. S., Khalil, T. B., & King, A. I. (1994). Dynamic response of the human head to impact by three-dimensional finite element analysis. *Journal of Biomechanical Engineering*, *116*, 44.

Saha, S., & Hayes, W. (1976). Tensile impact properties of human compact bone. *Journal of Biomechanics*, *9*(4), 243–244.

Sauren, A., & Claessens, M. H. A. (1993). Finite element modeling of head impact: The second decade. In *International Research Council on the Biomechanics of Impact (IRCOBI) Conference Proceedings* (pp. 241–254). Eindhoven, Netherlands.

Simpleware Ltd. (2012). *ScanIP, +FE and +CAD Reference Guide*.

Suh, C., Kim, S., & Oh, S. (2005). Analysis of Traumatic Brain Injury Using a Finite Element Model. *Journal Of Mechanical Science And Technology*, *19*(7), 1424–1431.

Tong, P., DiMasi, F., Carr, G., Eppinger, R., Marcus, J., & Galbraith, C. G. (1989). Finite element modeling of head injury caused by inertial loading. In *Proceedings of the 12th International Conference on Experimental Safety Vehicles* (pp. 617–626).

Trosseille, X., Tarriere, C., Lavaste, F., Guillon, F., & Domont, A. (1992). Development of a F. E. M. of the Human Head According to a Specific Test Protocol. In *Proceedings of the 30th STAPP Car Crash Conference*.

Tutt, B. A., & Taylor, A. P. (2004). The use of LS-DYNA to simulate the water landing characteristics of space vehicles. In *8th International LS-DYNA Users Conference* (pp. 1–14).

Van De Graaff, K. M., & Fox, S. I. (1995). *Concepts of human anatomy and physiology*. McGraw-Hill Education.

Van Dommelen, J. A. W., Van der Sande, T. P. J., Hrapko, M., & Peters, G. W. M. (2010). Mechanical properties of brain tissue by indentation: interregional variation. *Journal of the Mechanical Behavior of Biomedical Materials*, *3*(2), 158–66.

Vincent, J. F. V. (1990). The functional design of bone. In *Structural biomaterials* (pp. 179–196). Princeton University Press.

Wahi, K. K., & Merchant, H. C. (1977). Mechanical response of a head injury model with viscoelastic brain tissue. *Annals of Biomedical Engineering*, *5*(4), 303–21.

Wang, F., Lee, H. P., & Lu, C. (2007). Effects of head size and morphology on dynamic responses to impact loading. *Medical & Biological Engineering & Computing*, *45*(8), 747–57.

Weber, I., & Young, P. G. (2003). Automating the generation of 3D finite element models based on medical imaging data: application to head impact. In *3D Modelling Paris, France* (Vol. 44, pp. 23–24).

Willinger, R., Kang, H. S., & Diaw, B. (1999). Three-dimensional human head finite-element model validation against two experimental impacts. *Annals of Biomedical Engineering*, *27*(3), 403–10.

Wittek, A., & Omori, K. (2003). Parametric study of effects of brain-skull boundary conditions and brain material properties on responses of simplified finite element brain model under angular acceleration impulse in sagittal plane. *JSME International Journal Series C*, *46*(4), 1388–1399.

Wood, J. L. (1971). Dynamic response of human cranial bone. *Journal of Biomechanics*, *4*(1), 1–12.

Yao, J., Turteltaub, S. R., & Ducheyne, P. (2006). A three-dimensional nonlinear finite element analysis of the mechanical behavior of tissue engineered intervertebral discs under complex loads. *Biomaterials*, *27*(3), 377–387.

Young, P. G. (2003). An analytical model to predict the response of fluid-filled shells to impact - a model for blunt head impacts. *Journal of Sound and Vibration*, *267*(5), 1107–1126.

Young, P. G., Beresford-West, T., Coward, S., Notarberardino, B., Walker, B., & Abdul-Aziz, A. (2008). An efficient approach to converting three-dimensional image data into highly accurate computational models. *Philosophical Transactions of the Royal Society A: Mathematical, Physical and Engineering Sciences*, *366*(1878), 3155.

Young, P. G., & Morfey, C. L. (1998). Intracranial pressure transients caused by head impacts. In *International Research Council on the Biomechanics of Impact (IRCOBI) Conference Proceedings* (pp. 391–403). Göteborg, Sweden.

Zioupos, P., & Currey, J. (1998). Changes in the stiffness, strength, and toughness of human cortical bone with age. *Bone*, *22*(1), 57–66.

Zong, Z., Lee, H. P., & Lu, C. (2006). A three-dimensional human head finite element model and power flow in a human head subject to impact loading. *Journal of Biomechanics*, *39*(2), 284–92.

# Chapter 3: Fluid-filled sphere model – Results

## 3.1 Parametric study

The Stage 1 head model was subjected to a parametric study, in the form of a series of ten impact simulations with varying impactor velocities and masses. This allowed the response of the head to be studied over a wide range of contact durations $T_p$.

While the head model was initially at rest, the impactor had an initial velocity $v_{sol}$ which was varied incrementally from 0.2 to 3.8 m/s. For each impact case, the mass of the impactor $m_{sol}$ was calculated such that the kinetic energy $E_k$ of the impactor was constant across the range of impacts. The calculated impactor mass was then implemented by making appropriate changes in the impactor's material density prior to running the simulations. A range of impactor masses from 8.0 to 0.0222 kg was required to maintain constant kinetic energy (at 0.16 J) for the range of velocities stated. In maintaining a constant kinetic energy it was hoped to achieve similar peak impact forces $F_{max}$ in all impact cases, so that the results could be more easily compared.

| Case Number | $v_{sol}$ (m/s) | $m_{sol}$ (kg) |
|---|---|---|
| 1.1 | 0.2 | 8.0000 |
| 1.2 | 0.6 | 0.8889 |
| 1.3 | 1.0 | 0.3200 |
| 1.4 | 1.4 | 0.1633 |
| 1.5 | 1.8 | 0.0988 |
| 1.6 | 2.2 | 0.0661 |
| 1.7 | 2.6 | 0.0473 |
| 1.8 | 3.0 | 0.0356 |
| 1.9 | 3.4 | 0.0277 |
| 1.10 | 3.8 | 0.0222 |

*Table 3.1: Variables of the Stage 1 parametric study.*

## 3.2 Results and comparisons

### *3.2.1 Impact characteristics*

The resulting contact durations $T_p$ and peak impact forces $F_{max}$ were measured for each impact case. The duration that the two colliding bodies were in contact was retrieved from T/HIS: examining the stress reported in the centremost element of the contact area on the head model's surface allowed the times of initiation and cessation of the contact to be

clearly distinguished. The peak impact force was obtained from the velocity-time history of the impactor, which can be reported in T/HIS. This velocity curve was differentiated to obtain the impactor's acceleration-time history during collision. The deceleration curve of the impactor was multiplied by its mass, which gave the force-time history of the impact. From this, the peak value ($F_{max}$) could be recorded for each impact case. $F_{max}$ values recorded were not constant across the range of impacts, but were all within a reasonably tight bracket of 0.753 to 0.842 kN, except for impact Case 1.1, in which a low peak force of 0.406 kN was observed.

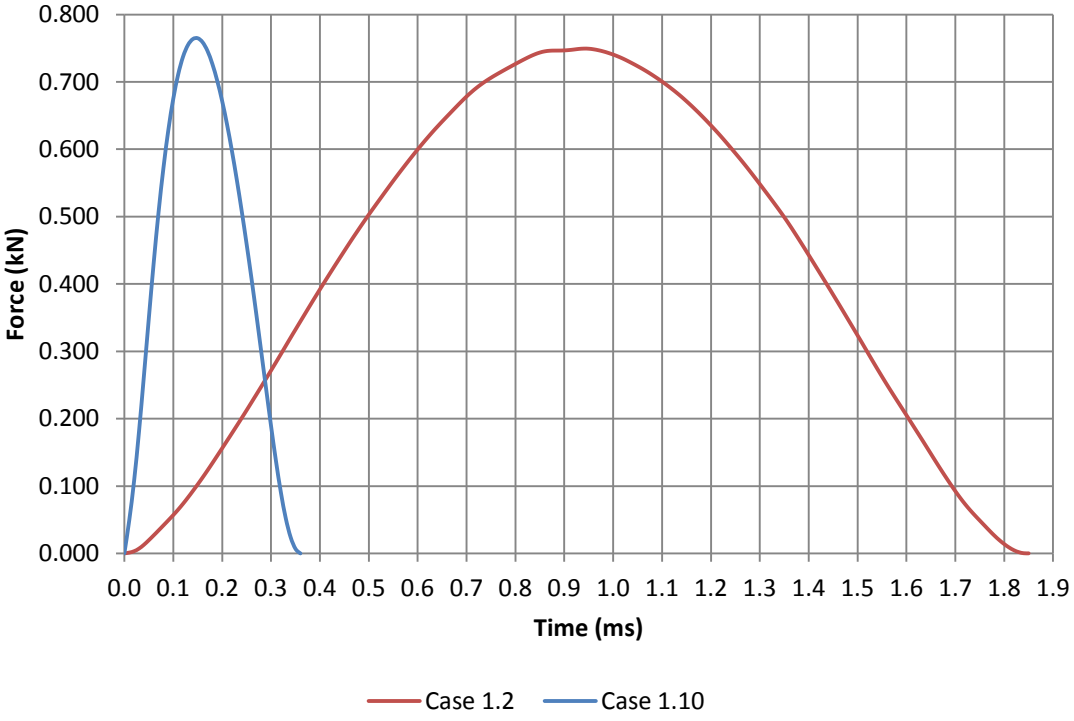


*Figure 3.1: Plots of impact force vs. time for Cases 1.2 and 1.10 illustrate that the force was transmitted to the head model in the form of a smooth sinusoidal "pulse", irrespective of the impact duration $T_p$. Note also that these force-time histories have similar peak values ($F_{max}$) of approximately 0.760 kN.*

The parametric study produced a wide range of contact durations; the impacts observed spanned an order of magnitude, measuring from 3.32 to 0.34 ms. The impact characteristics were recorded and compared to values of contact duration $T_p$ and peak impact force $F_{max}$ as predicted by Young's (2003) analytical model of head impact [Equations 1.12 and 1.14]. The analytical predictions were made using the same dimensions, elastic moduli, material densities, and initial velocities as used in the finite element simulations, and were solved using the iterative solver functionality in Microsoft Excel.

| Case Number | FE $T_p$ (ms) | FE $F_{max}$ (kN) | Analytical $T_p$ (ms) | Analytical $F_{max}$ (kN) | Analytical $T_p$ error (%) | Analytical $F_{max}$ error (%) |
|---|---|---|---|---|---|---|
| 1.1 | 3.317 | 0.406 | 3.364 | 0.381 | 1.42 | -6.33 |
| 1.2 | 1.820 | 0.753 | 1.838 | 0.721 | 0.97 | -4.32 |
| 1.3 | 1.194 | 0.828 | 1.196 | 0.800 | 0.18 | -3.47 |
| 1.4 | 0.872 | 0.842 | 0.876 | 0.826 | 0.50 | -1.97 |
| 1.5 | 0.694 | 0.837 | 0.689 | 0.837 | -0.71 | 0.08 |
| 1.6 | 0.576 | 0.819 | 0.567 | 0.843 | -1.57 | 2.92 |
| 1.7 | 0.493 | 0.797 | 0.481 | 0.847 | -2.43 | 6.19 |
| 1.8 | 0.432 | 0.779 | 0.418 | 0.849 | -3.27 | 9.03 |
| 1.9 | 0.383 | 0.766 | 0.369 | 0.850 | -3.60 | 11.09 |
| 1.10 | 0.344 | 0.763 | 0.331 | 0.852 | -3.82 | 11.59 |

*Table 3.2: Resulting contact durations and peak impact forces in the Stage 1 parametric study. "FE" denotes values measured in the finite element simulations. "Analytical" denotes values predicted by Young's (2003) analytical model.*

Good agreement was observed between the measured and predicted values; this was expected since the Stage 1 finite element model utilises the same simple fluid-filled sphere geometry as Young's analytical description of head impact. In Table 3.2, above, it can be seen that the analytically predicted values of $T_p$ follow closely the contact durations observed in the simulated experiments, with an absolute maximum error of 3.82%. Analytically predicted $F_{max}$ values were also generally close to those observed, although the deviations were slightly larger, with an absolute maximum error of 11.59%. In general the analytical description appeared to perform best for impacts with contact durations between approximately 0.5 to 2 ms, with the predicted values deviating more strongly from those observed as the duration of the impacts decrease.

The vibrational properties of the Stage 1 head model were investigated by performing an eigenvalue analysis in the finite element package Abaqus/CAE (Dassault Systèmes S.A.). The natural modes of any structure depend on the distribution of its mass and stiffness in space, and can therefore be solved using finite element analysis just like other structural problems. Spurious zero modes were observed when attempting to perform the modal analysis on the full Stage 1 head model including the fluid. Young (2002) had shown previously that the first equivoluminal mode of a fluid-filled sphere is independent of whether the mass of the system is distributed throughout the shell and the fluid or just located in the shell, and is not affected by the bulk modulus of the fluid. Therefore, here the modal analysis was performed on the same finite element model as used in the Stage 1

impact simulations, but with the fluid removed, such that the shell was *in vacuo*. The density of the shell was modified such that the total mass of the head system remained constant.

The period of the first (n=2) equivoluminal mode $T_\Omega$ of the fluid-filled sphere head model was extracted from the modal analysis to be used to collapse the results of the parametric study, as done in previous work by Young & Morfey (1998). The $T_\Omega$ value of a fluid-filled sphere with the same dimensions and properties as the Stage 1 model was also calculated using the analytical expression given in (Young, 2002) [Equation 1.6]. The numerical and analytical $T_\Omega$ values were 0.514 and 0.539 ms respectively: the prediction made by Young's simple closed-form explicit expression differed from the numerically predicted $T_\Omega$ value by less than 5% (4.86%).

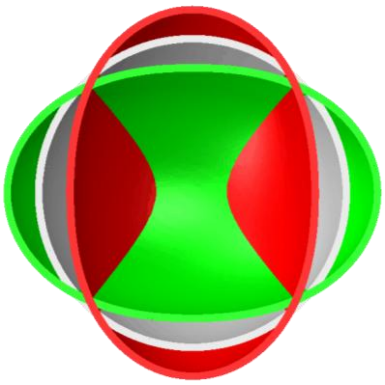

*Figure 3.2: Mid-section view of the Stage 1 model illustrating the first "ovalling" mode of the spherical shell, i.e. the first n=2 equivoluminal mode of vibration. The undeformed geometry is white, while the red and green geometries each represent maximum deformation states that the system oscillates between.*

### *3.2.2 Pressure response*

For each impact, the gross intracranial pressure response was inspected graphically in D3PLOT, while local pressure-time histories at the coup and contrecoup were analysed in T/HIS. The peak positive and negative pressures in the brain invariably occurred at the coup and contrecoup locations, and these values were recorded per impact case.

#### *3.2.2.1 Cases 1.1 and 1.2*

In impact Cases 1.1 and 1.2, with comparatively long contact durations, the fluid representing the brain behaved quasi-statically. This was expected, since the durations of these impacts ($T_p$ of 3.317 and 1.820 ms respectively) were both greater than twice the period of the first equivoluminal mode $T_\Omega$ ($2 \times 0.514 = 1.028$ ms), which has been shown by Young & Morfey (1998) to be a good predictor of the critical impact duration (above

which the system behaves quasi-statically). Impact Cases 1.1 and 1.2 produced similar intracranial behaviour, differing mainly in the magnitude of the pressure peaks observed, due to the different impact forces experienced by these cases. Taking Case 1.1 to be representative of these quasi-static impacts, a typical intracranial pressure response can be seen in Figure 3.3 below, which depicts the local pressures recorded at sampling points located in the coup and contrecoup of the brain.

Quasi-static intracranial pressures occur when the response of the impacted skull is dominated by rigid-body behaviour: a linear pressure gradient develops in the brain, the severity of which corresponds to the acceleration applied to the system. At any instant in the contact period this acceleration is proportional to the impact force, which is transferred as a sinusoidal "pulse", rising and falling over the contact period $T_p$. Therefore, the coup and contrecoup pressure-time histories expected from an ideal quasi-static response are symmetrical about the x-axis, rising to maxima of positive and negative pressure of equal magnitude at the coup and contrecoup respectively (achieved half way through the impact, i.e. at $t = T_p/2$), and then returning to zero as contact ceases ($t = T_p$).

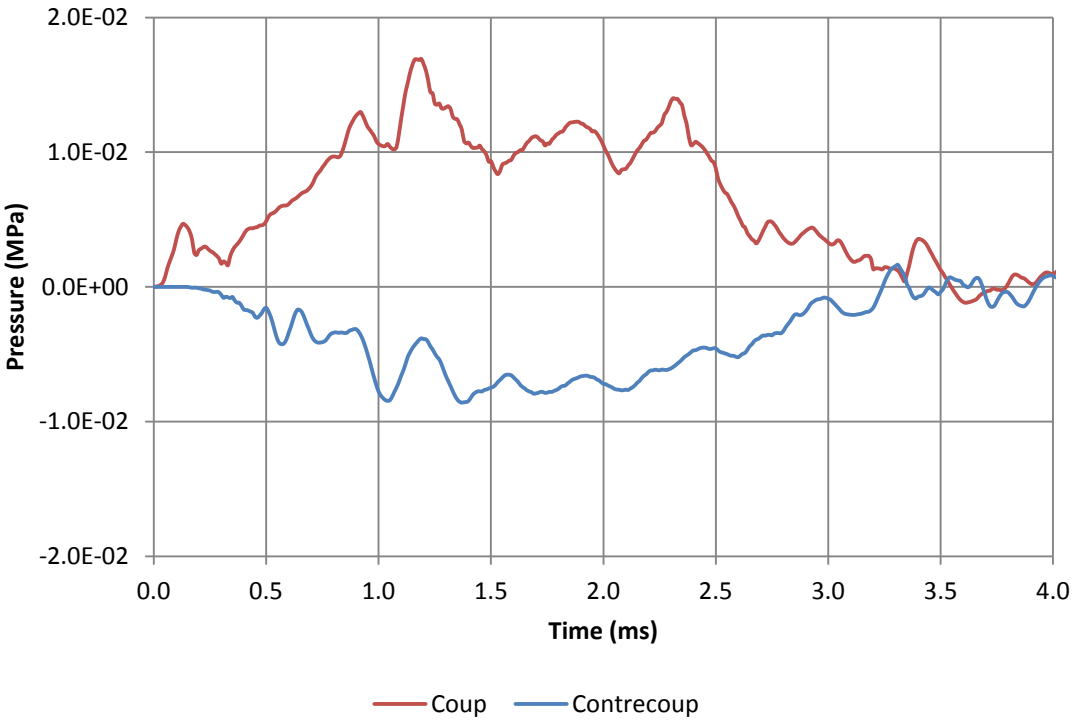


*Figure 3.3: Case 1.1, local pressure-time histories recorded in the brain at the coup and contrecoup.*

In Figure 3.3, the following characteristics typical of a quasi-static response can be seen:

- Peak positive intracranial pressure occurs at the coup, while peak negative intracranial pressure occurs at the contrecoup.
- During the contact period ($0 \leq t \leq 3.317$ ms) no negative pressure is experienced by the coup, and no positive pressure is experienced by the contrecoup.

However:

- The pressure maxima do not occur exactly at $T_p/2$ (1.659 ms).
- Small amounts of negative pressure at the coup, and positive pressure at the contrecoup, are observed after contact has ceased ($t > T_p$).

The two characteristics mentioned directly above would not be expected in the quasi-static response, but occur here due to pressures caused by the excitation of higher order modes and noise superimposed onto these pressure-time histories. (The influence of the natural modes of the system on the intracranial pressure response is investigated further in Section 6.1.2.2.) Also, the magnitudes of the peak positive and negative pressures were not equal. The peak positive pressure at the coup was 1.720e-2 MPa, while the peak negative pressure at the contrecoup was -0.868e-2 MPa.

The peak pressures expected at the coup and contrecoup for a perfectly quasi-static response can be found by substituting the mass and dimensions of the Stage 1 head model, and the peak impact force experienced in Case 1.1, into Equation 1.5. Utilising an $F_{max}$ of 0.406 kN yields $P_{C\ quasi}$ = 1.171e-2 MPa, and $P_{CC\ quasi}$ = -1.167e-2 MPa, where $P_{C\ quasi}$ and $P_{CC\ quasi}$ are the quasi-static pressures at the coup and contrecoup respectively. The sampling point at the coup was placed 5.30 mm away from the brain-skull boundary to avoid the influence of any artificial noise which may occur due to the "tied" contact at this interface. The contrecoup sampling point was 5.52 mm away from the brain-skull boundary, since it was not possible to place a sampling point at an exactly equal distance to that used at the coup, due to differences in mesh density at these locations. The analytically predicted quasi-static pressures are proportional to the sampling points' distance from the brain's centre of gravity, therefore here the values of $P_{C\ quasi}$ and $P_{CC\ quasi}$ were not exactly equal.

The peak coup and contrecoup pressures observed in the finite element simulations differ from these ideal analytically predicted pressures by factors of 1.469 and 0.744 respectively. These differences reflect the considerations mentioned above: the excitation of higher order modes, and noise.

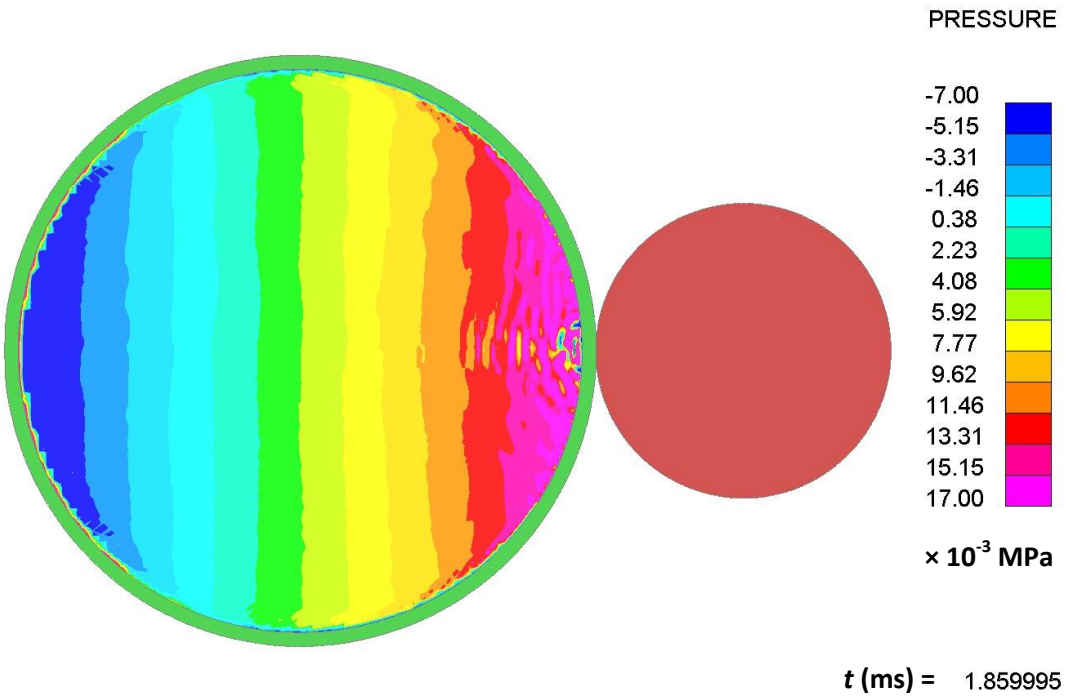


*Figure 3.4: Mid-section view of the Stage 1 model depicting Case 1.1, contours of pressure in the brain at $t$ = 1.860 ms. The solid green and red regions represent the spherical skull and impactor respectively.*

Finally, Figure 3.4 above depicts the contours of pressure observed throughout the brain at 1.860 ms after incidence (approximately half way through the impact). A "banding" pattern can be seen, produced by parallel pressure contours of equal width perpendicular to the axis of impact. This "banding" is caused by a linear pressure gradient throughout the brain, indicative of quasi-static behaviour.

### *3.2.2.2 Cases 1.3, 1.4, and 1.5*

In impact Case 1.3 the resulting contact duration reduced further to 1.194 ms, approaching the critical impact duration as predicted by Young & Morfey (1998) (twice $T_\Omega$ gives 1.028 ms for this model). Cases 1.3, 1.4 ($T_p$ = 0.872 ms), and 1.5 ($T_p$ = 0.694 ms) all have contact durations close to this critical value. The intracranial pressure behaviour observed in these cases appeared to represent the transition between the quasi-static response and the dynamic pressure response reported in (Young & Morfey, 1998). The pressure-time histories still exhibited some characteristics of a quasi-static response, but, as impact duration was further reduced, became increasingly dominated by large pressure transients which fluctuated between both positive and negative pressure.

The local pressures recorded at the coup and contrecoup for Case 1.4 are presented below in Figure 3.5; landmark points on the plot are marked by Roman numerals I to III, which

relate to contours plots I to III depicting pressure throughout the brain at those given times. Examining the pressure-time histories presented in Figure 3.5, some characteristics of the quasi-static response remain visible:

- Peak positive intracranial pressure occurs at the coup, while peak negative intracranial pressure occurs at the contrecoup.
- During the contact period ($0 \leq t \leq 0.872$ ms) no negative pressure is experienced by the coup.

However:

- A positive pressure transient is experienced by the contrecoup from $t = 0.760$ ms until approximately $t = 0.905$ ms. Therefore, positive pressure occurs at the contrecoup within the contact period ($0 \leq t \leq 0.872$ ms).
- The coup and contrecoup pressure-time histories are non-symmetrical, and do not rise and fall in a sinusoidal fashion, i.e. they are no longer proportional to the force-time history of the impact. Also the peak coup and contrecoup pressures do not occur at, or close to, half way through the impact ($t = T_p/2$).
- Finally, peak coup positive pressure and contrecoup negative pressure were recorded as 5.790e-2 MPa and -4.070e-2 MPa respectively. Utilising Equation 1.5 to calculate the maximum quasi-static pressures expected from the same peak impact force as produced in Case 1.4, it was found that the peak pressures observed in the simulated impact differed from $P_{C\ quasi}$ and $P_{CC\ quasi}$ by factors of 2.386 and 1.683 respectively. These factors of difference had increased significantly above those between the simulated and analytical quasi-static solutions.

The contour plots presented in Figure 3.5 provide further insight into the similarities and differences between the intracranial response observed in Case 1.4, and those of quasi-static impacts such as Case 1.1. Contour plots I and III illustrate the localised nature of the high pressure transients. Firstly, in plot I, an initial positive pressure transient is generated at the coup, while other areas of the brain remain unaffected. This is in stark contrast to quasi-static impacts, in which pressures are distributed throughout the brain by means of the linear pressure gradient generated. Secondly, in plot III, transients of positive pressure occur simultaneously at the coup and contrecoup. This, again, is uncharacteristic of a quasi-static response, where coup and contrecoup pressures are typically of opposite sign. Finally however, examining pressure contours roughly half way through the impact in plot II,

evidence of quasi-static behaviour can still be seen, by way of the remnants of a "banding" pattern as caused by a linear pressure gradient due to rigid-body acceleration of the skull.

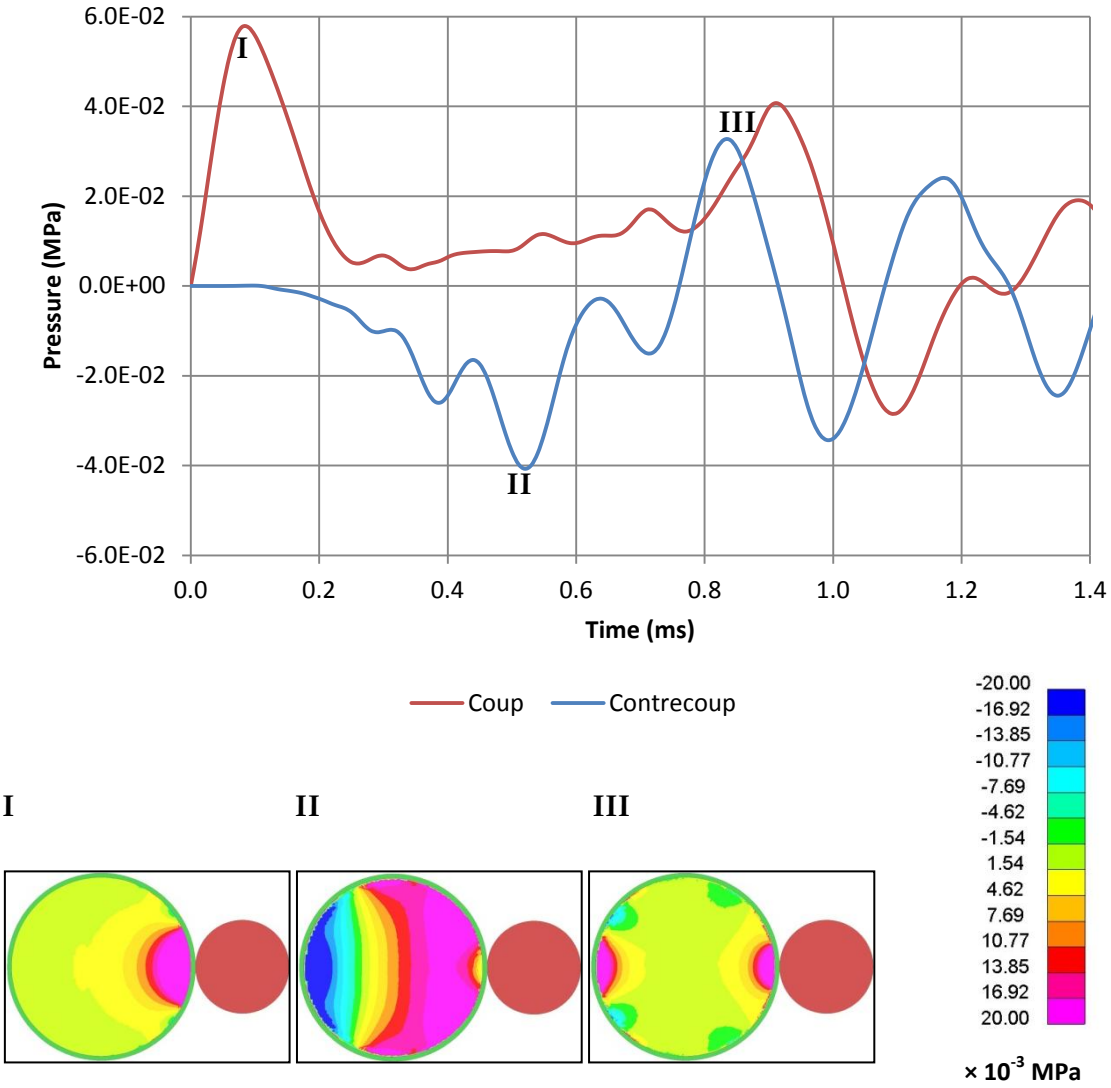


*Figure 3.5: Case 1.4, Top: local pressure-time histories recorded in the brain at the coup and contrecoup. Bottom: contour plots of pressure in the brain at I (t = 0.100 ms), II (t = 0.520 ms), and III (t = 0.860 ms). The solid green and red regions represent the spherical skull and impactor respectively.*

It is clear that in this transitional phase, close to the critical impact duration ($T_p \approx 2 \times T_\Omega$), the mechanism which induces quasi-static intracranial pressure behaviour, namely rigid-body acceleration of the skull, and the mechanism which induces these large pressure transients both occur to some degree.

As impact duration reduces further, in impact Case 1.5, the pressure response of the system does not change much qualitatively, the primary difference being the introduction of negative pressure at the coup during the contact period ($0 \leq t \leq 0.694$ ms): see contour

plot II in Figure 3.6, below. This is therefore the point at which the last remaining recognisable characteristic of a quasi-static type response is lost.

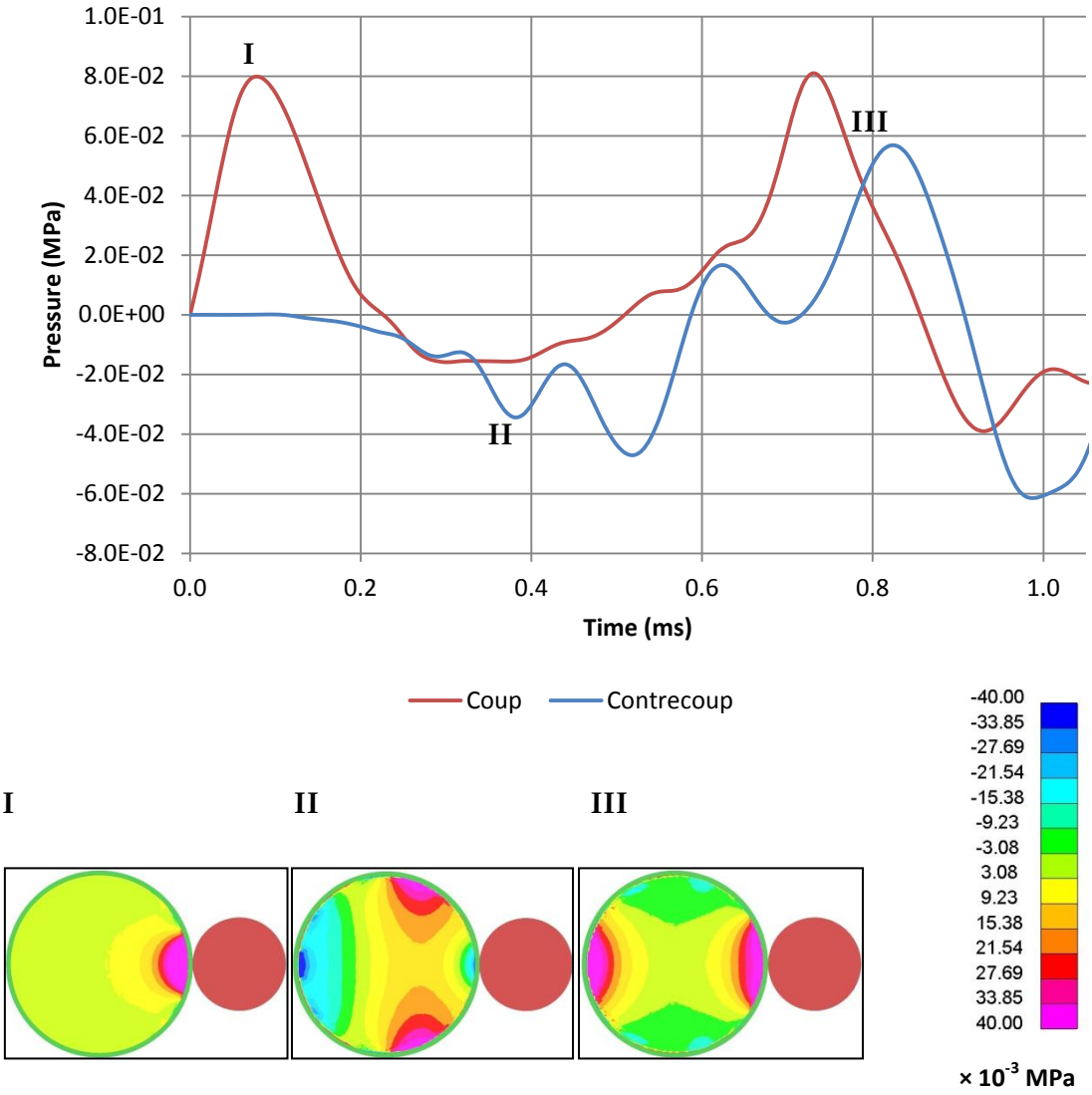


*Figure 3.6: Case 1.5, Top: local pressure-time histories recorded in the brain at the coup and contrecoup. Bottom: contour plots of pressure in the brain at I (t = 0.070 ms), II (t = 0.380 ms), and III (t = 0.800 ms). The solid green and red regions represent the spherical skull and impactor respectively.*

Quantitatively, the magnitude of the peak intracranial pressures continued to rise as $T_p$ was reduced, with the coup and contrecoup pressures observed in Case 1.5 differing from the expected values of $P_{C\,quasi}$ and $P_{CC\,quasi}$ by factors of 3.378 and 2.556 respectively.

### *3.2.2.3 Cases 1.6 to 1.10*

From Case 1.6 onwards the shapes of the pressure-time histories at the coup and contrecoup are broadly similar, differing mainly in the magnitude of the transients observed. Figure 3.7, below, depicts the coup and contrecoup pressure-time histories and

contour plots for Case 1.10, the impact with the shortest contact duration in the Stage 1 parametric study ($T_p$ = 0.344 ms). This description typifies the dynamic response observed in these short duration impacts:

- Shortly after the incidence of impact the brain beneath the coup experiences a large local transient of positive pressure, followed by large negative and positive pressure transients.
- After these three large initial spikes, pressure at the coup undergoes regular fluctuations of smaller magnitude.
- Pressures at the contrecoup remain comparatively low throughout the contact duration, fluctuating in a regular fashion until sometime after $T_p$, when large positive and negative pressure transients then also occur.

All impacts in the parametric study adhered to the trend that the dynamic pressure response produced pressure peaks of increasing magnitude as the contact duration $T_p$ was reduced. The greatest pressure peaks were recorded in Case 1.10, where the coup positive pressure and contrecoup negative pressure peaks were 8.579 and 8.185 times greater than $P_{C\,quasi}$ and $P_{CC\,quasi}$ respectively.

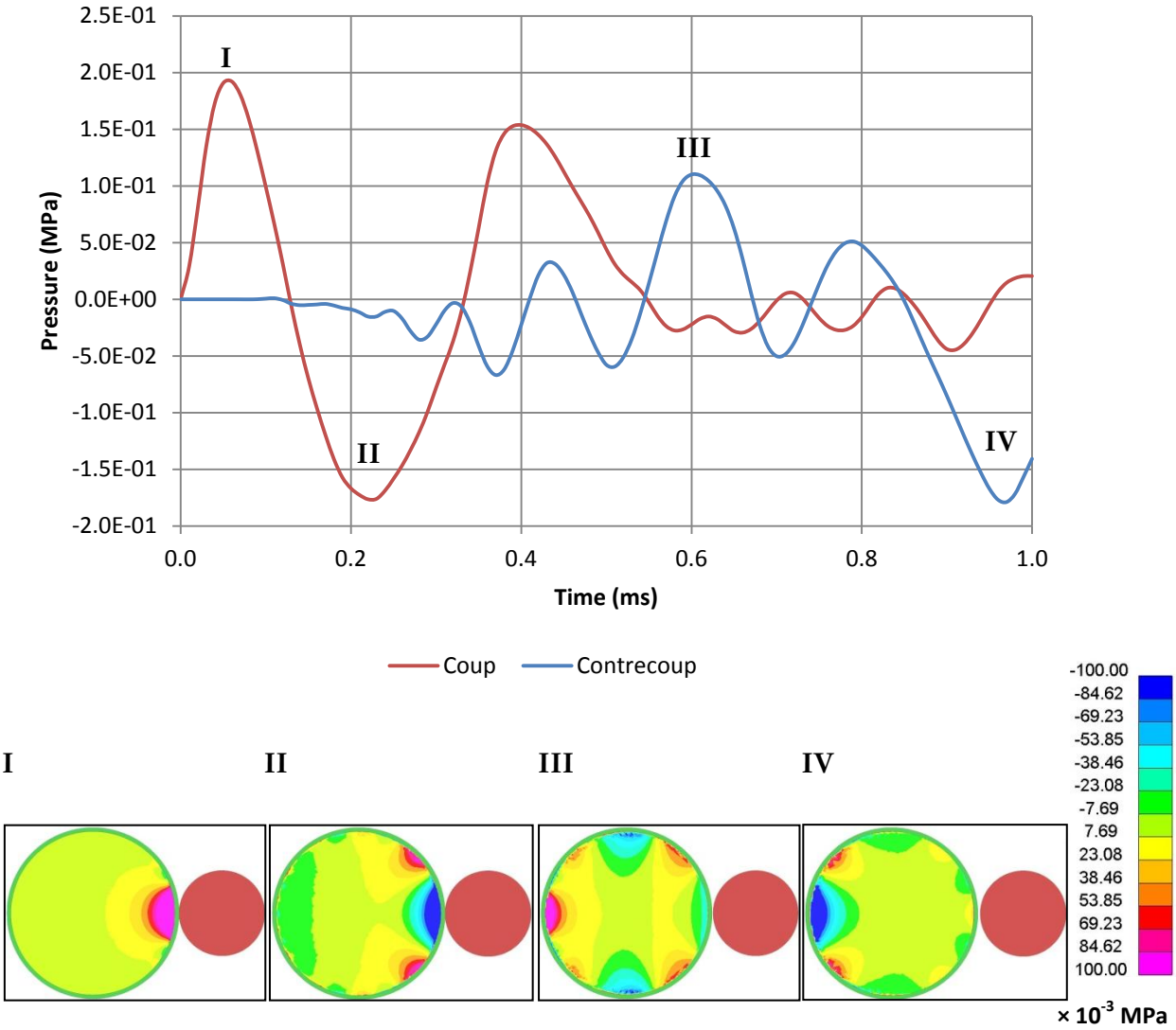


*Figure 3.7: Case 1.10, Top: local pressure-time histories recorded in the brain at the coup and contrecoup. Bottom: contour plots of pressure in the brain at I (t = 0.060 ms), II (t = 0.230 ms), III (t = 0.600 ms), and IV (t = 0.970 ms). The solid green and red regions represent the spherical skull and impactor respectively.*

### *3.2.3 Collapsing the results*

The results of the parametric study were non-dimensionalised in the same fashion as had been done previously in Young & Morfey's (1998) work. The recorded peak intracranial pressures at the coup and contrecoup were normalised over the analytically predicted peak pressures $P_{C\ quasi}$ and $P_{CC\ quasi}$ respectively, i.e. the pressures expected from a quasi-static response, so resulting in a measure of pressure "magnification" (some values of which have been presented already). Impact durations $T_p$ were normalised over the period of oscillation of the first equivoluminal mode of the skull $T_\Omega$. Collapsing the results in this manner reduces the influence of any variation in impact force, and allows qualitative changes in the

pressure response to be analysed more clearly. Table 3.3, below, presents the analytically predicted peak positive ($P_{C\ quasi}$) and peak negative ($P_{CC\ quasi}$) quasi-static pressures, and the peak positive and peak negative pressures recorded at the coup and contrecoup ($P_C$ and $P_{CC}$ respectively, denoted "positive" and "negative") for each impact case. In Table 3.4 the normalised peak pressures at the coup ($P_C$ / $P_{C\ quasi}$) and contrecoup ($P_{CC}$ / $P_{CC\ quasi}$) are presented, along with normalised impact durations ($T_p$ / $T_\Omega$).

| Case Number | Analytical | | FE: Coup | | FE: Contrecoup | |
|---|---|---|---|---|---|---|
| | $P_{C\ quasi}$ (MPa) | $P_{CC\ quasi}$ (MPa) | $P_{C\ positive}$ (MPa) | $P_{C\ negative}$ (MPa) | $P_{CC\ positive}$ (MPa) | $P_{CC\ negative}$ (MPa) |
| 1.1 | 1.171e-2 | -1.167e-2 | 1.720e-2 | -1.870e-3 | 2.255e-3 | -8.680e-3 |
| 1.2 | 2.170e-2 | -2.163e-2 | 3.170e-2 | -1.330e-2 | 1.550e-2 | -2.480e-2 |
| 1.3 | 2.386e-2 | -2.378e-2 | 3.700e-2 | -1.440e-2 | 1.870e-2 | -3.050e-2 |
| 1.4 | 2.426e-2 | -2.419e-2 | 5.790e-2 | -2.852e-2 | 3.270e-2 | -4.070e-2 |
| 1.5 | 2.410e-2 | -2.402e-2 | 8.140e-2 | -3.900e-2 | 5.683e-2 | -6.140e-2 |
| 1.6 | 2.360e-2 | -2.353e-2 | 1.036e-1 | -4.351e-2 | 6.570e-2 | -9.260e-2 |
| 1.7 | 2.297e-2 | -2.290e-2 | 1.245e-1 | -7.260e-2 | 6.690e-2 | -1.560e-1 |
| 1.8 | 2.243e-2 | -2.236e-2 | 1.458e-1 | -1.106e-1 | 7.960e-2 | -1.578e-1 |
| 1.9 | 2.205e-2 | -2.198e-2 | 1.674e-1 | -1.418e-1 | 9.666e-2 | -1.451e-1 |
| 1.10 | 2.198e-2 | -2.191e-2 | 1.886e-1 | -1.760e-1 | 1.104e-1 | -1.794e-1 |

*Table 3.3: Analytically predicted quasi-static peak pressures, and peak pressures observed in the Stage 1 parametric study.*

| Case Number | Normalised | | | | |
|---|---|---|---|---|---|
| | $P_{C\ positive}$ / $P_{C\ quasi}$ | $P_{C\ negative}$ / $P_{C\ quasi}$ | $P_{CC\ positive}$ / $P_{CC\ quasi}$ | $P_{CC\ negative}$ / $P_{CC\ quasi}$ | $T_p$ / $T_\Omega$ |
| 1.1 | 1.469 | -0.160 | 0.193 | -0.744 | 6.451 |
| 1.2 | 1.461 | -0.613 | 0.717 | -1.146 | 3.540 |
| 1.3 | 1.551 | -0.604 | 0.786 | -1.282 | 2.322 |
| 1.4 | 2.386 | -1.175 | 1.352 | -1.683 | 1.696 |
| 1.5 | 3.378 | -1.618 | 2.366 | -2.556 | 1.350 |
| 1.6 | 4.388 | -1.844 | 2.792 | -3.936 | 1.120 |
| 1.7 | 5.418 | -3.161 | 2.922 | -6.813 | 0.959 |
| 1.8 | 6.500 | -4.929 | 3.560 | -7.057 | 0.840 |
| 1.9 | 7.592 | -6.430 | 4.397 | -6.600 | 0.745 |
| 1.10 | 8.579 | -8.007 | 5.038 | -8.185 | 0.669 |

*Table 3.4: Non-dimensional peak positive and negative pressures, and non-dimensional impact durations, of the Stage 1 parametric study.*

The normalised results are presented in Figure 3.8 in terms of non-dimensional coup pressures against the log of non-dimensional impact duration. Similarly, Figure 3.9 displays the normalised results at the contrecoup.

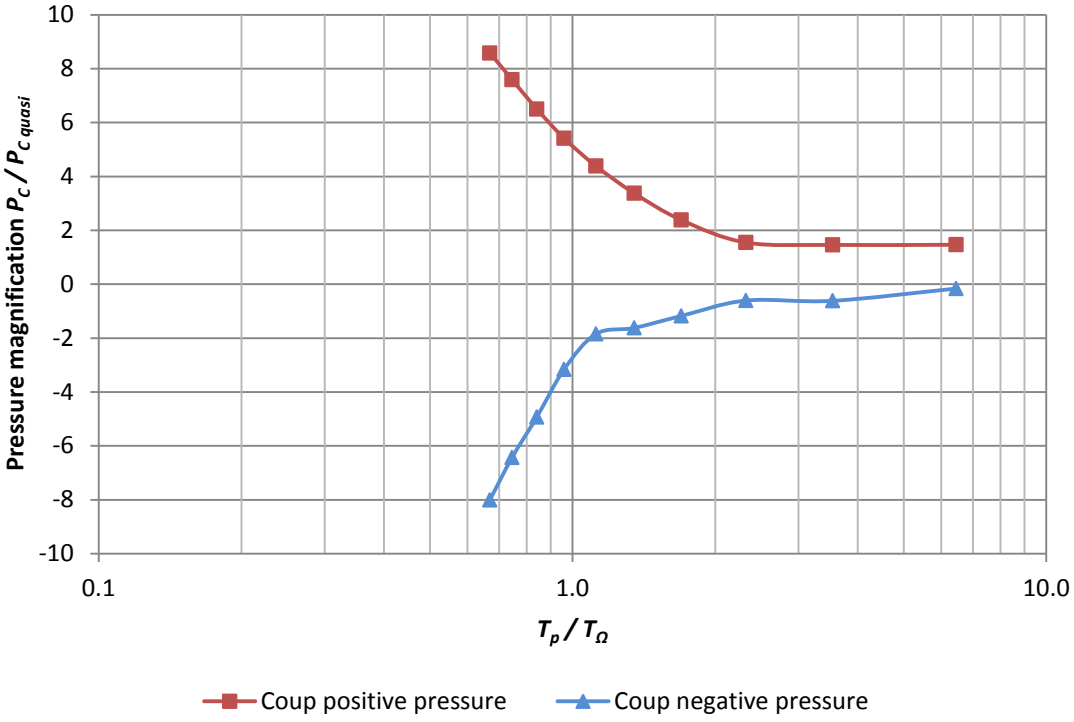


*Figure 3.8: Stage 1 parametric study, normalised peak pressures against $T_p$ / $T_\Omega$ at the coup.*

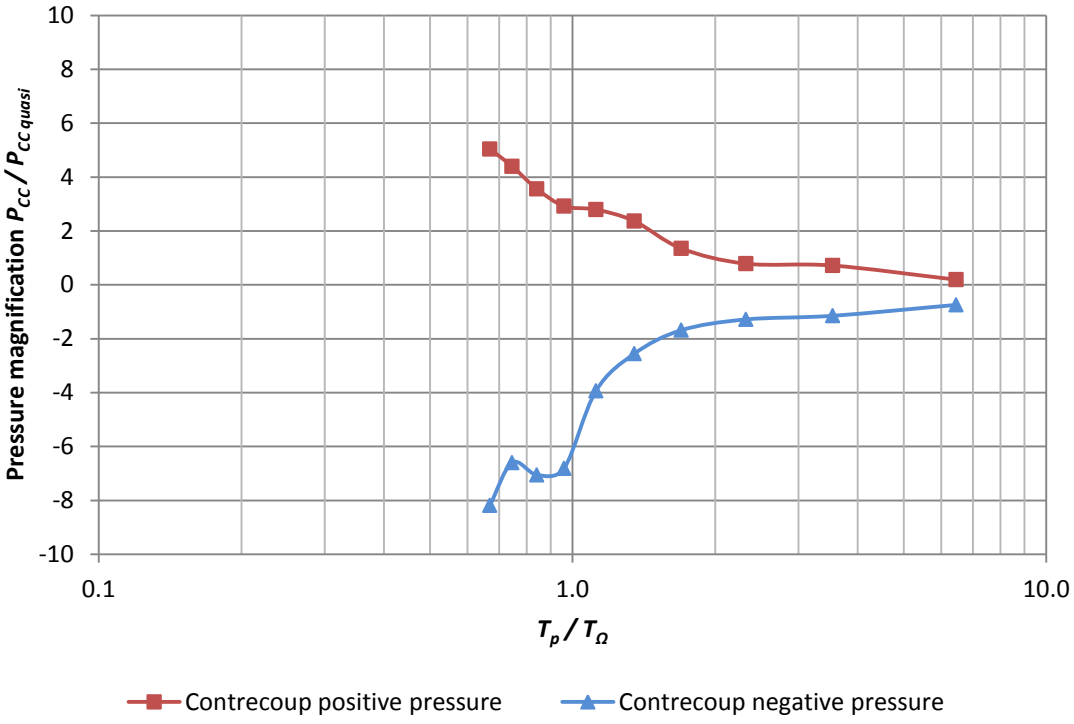


*Figure 3.9: Stage 1 parametric study, normalised peak pressures against $T_p$ / $T_\Omega$ at the contrecoup.*

Examining Figure 3.8 above, it can be seen that initially, when impact duration is large compared to $T_\Omega$ (i.e. $T_p$ / $T_\Omega$ > 2), the "magnification" of the observed coup positive pressures (in regard to the expected quasi-static pressures) remains approximately constant

at a value of around one, while the "magnification" of coup negative pressures remains close to zero. This is because the observed positive pressures were close to those expected, while during the quasi-static response minimal negative pressures were generated at the coup. The reverse can be seen in Figure 3.9, with contrecoup positive pressure magnification initially at a value of approximately zero, and negative pressure magnification close to one.

In both Figures 3.8 and 3.9, all pressure magnification values remain roughly constant as $T_p$ / $T_\Omega$ decreases, until approximately $T_p$ / $T_\Omega$ = 2, below which both positive and negative peak pressures at the coup and contrecoup begin to increase in magnitude dramatically. This suggests that the non-dimensional ratio $T_p$ / $T_\Omega$ is a good predictor of the system's response. The critical value of $T_p$ / $T_\Omega$ = 2 observed in this study is in agreement with the findings of Young & Morfey's (1998) finite element work and Johnson's (2005) physical experiments concerning fluid-filled sphere head models of comparable geometry and properties.

Beyond this critical value (i.e. $T_p$ / $T_\Omega$ < 2) coup and contrecoup pressure magnification rises in magnitude, reflecting the quantitative changes of the pressure transients observed. The coup tended to exhibit a greater degree of magnification of both positive and negative pressures than the contrecoup. Contrecoup negative pressure magnification did not increase in magnitude monotonically, but appeared to fluctuate slightly around $T_p$ / $T_\Omega$ ≈ 0.8 (Cases 1.8 and 1.9): the reason for this is uncertain, but completely smooth plots outlining the behaviour of the system were unlikely given the dynamic nature of the study, and possible interference of the large pressure transients travelling through the fluid.

Finally, while a cavitation threshold for brain tissue and cranial fluids has not yet been established, here a threshold value of -1 atm (-1.013e-1 MPa) was used as a guide in order to determine which impact cases in the current study may be in danger of engendering cavity formation in the brain. The ability of these materials to cavitate is likely to also depend on the duration of the negative pressures sustained, but no data is currently available on this subject. Assuming any transients of pressure below -1 atm to cause intracranial cavitation: Case 1.7 would sustain cavitation at the contrecoup, while in Cases 1.8 to 1.10 cavities would develop at both the coup and contrecoup.

Johnson, E. (2005). *The response of the human head to blunt impact: experimental validation of an analytical model. Thesis*. University of Exeter. Retrieved from http://ethos.bl.uk/OrderDetails.do?uin=uk.bl.ethos.421650

Young, P. G. (2002). A parametric study on the axisymmetric modes of vibration of multi-layered spherical shells with liquid cores of relevance to head impact modelling. *Journal of Sound and Vibration*, *256*(4), 665–680.

Young, P. G. (2003). An analytical model to predict the response of fluid-filled shells to impact - a model for blunt head impacts. *Journal of Sound and Vibration*, *267*(5), 1107–1126.

Young, P. G., & Morfey, C. L. (1998). Intracranial pressure transients caused by head impacts. *International Research Council on the Biomechanics of Impact (IRCOBI) Conference Proceedings* (pp. 391–403). Göteborg, Sweden.

# Chapter 4 - Brain and realistic skull model – Results

## 4.1 Low energy impacts – Parametric study

The Stage 2 investigation consisted of two sets of experiments: initially a parametric study consisting of low energy impacts was performed, followed by an additional study consisting of several high energy impact cases. The parametric study was conducted in the same manner as in Stage 1. A series of 12 impacts were simulated, each with varying impactor characteristics, such that a wide range of contact durations $T_p$ were produced. The impactor's initial velocity $v_{sol}$ was varied between 0.2 and 7.0 m/s, and for each case the impactor's mass $m_{sol}$ was calculated such that the kinetic energy $E_k$ of the impactor remained constant at 0.16 J. Keeping the impactor's kinetic energy constant was an attempt to ensure that all impact cases produced similar values of peak impact force $F_{max}$, so that the results could be easily compared. Also, in maintaining a low kinetic energy it was hoped that all impact cases would remain in the geometrically linear range. The Stage 2 investigation employs the same spherical impactor model as Stage 1; also, the first 10 impact cases utilise identical $v_{sol}$ and $m_{sol}$ values as used in the Stage 1 parametric study, so for these cases the response of the Stage 1 and Stage 2 head models can be directly compared. Two additional impact cases were performed in the Stage 2 parametric study in order to further explore dynamic intracranial pressures arising from short duration impacts.

| Case Number | $v_{sol}$ (m/s) | $m_{sol}$ (kg) |
|---|---|---|
| 2.1 | 0.2 | 8.0000 |
| 2.2 | 0.6 | 0.8889 |
| 2.3 | 1.0 | 0.3200 |
| 2.4 | 1.4 | 0.1633 |
| 2.5 | 1.8 | 0.0988 |
| 2.6 | 2.2 | 0.0661 |
| 2.7 | 2.6 | 0.0473 |
| 2.8 | 3.0 | 0.0356 |
| 2.9 | 3.4 | 0.0277 |
| 2.10 | 3.8 | 0.0222 |
| 2.11 | 5.4 | 0.0110 |
| 2.12 | 7.0 | 0.0065 |

*Table 4.1: Variables of the Stage 2 low energy parametric study.*

## 4.2 Low energy impacts – Results and comparisons

### *4.2.1 Impact characteristics*

The contact durations $T_p$ and peak impact forces $F_{max}$ resulting from the parametric study were retrieved using T/HIS in the same fashion as in Stage 1. The force-time histories indicated that, in all cases, impact force was transferred to the head model in a smooth sinusoidal "pulse", reaching the peak value $F_{max}$ approximately half way through the impact ($t = T_p/2$). As previously, the recorded $F_{max}$ values were found not to be constant throughout the parametric study. Nevertheless, the peak impact forces observed were reasonably close, within a bracket of 0.873 to 0.978 kN; except for the impact with the longest duration, Case 2.1, which once again had a significantly lower peak force of 0.470 kN. The intracranial response arising from different impact cases could be compared and contrasted qualitatively, while the peak intracranial pressures could be compared in a quantitative manner once they have been non-dimensionalised.

A wide range of contact durations from 3.287 to 0.169 ms were recorded. The impact characteristics observed were compared to predicted values of contact duration $T_p$ and peak impact force $F_{max}$ obtained from Young's (2003) analytical model [Equations 1.12 and 1.14]. The only variables which differed in these calculations compared to those in Stage 1 were $m$, $R_{sh}$, and $h$; which in Stage 1 are defined as: the total mass of the head model, the outer radius of the spherical shell, and the thickness of the spherical shell respectively. Young's (2003) analytical model is based on the assumption of a spherical head: in order to adapt this analytical model such that it could make predictions regarding the non-spherical head used in Stage 2, the variables $R_{sh}$ and $h$ were redefined as: the *local* radius of curvature of the skull at the impact site, and the *local* thickness of the skull at the impact site respectively. Before the analytical predictions could be made, appropriate values of $R_{sh}$ and $h$ needed to be found: using the measurement tools in D3PLOT, $R_{sh}$ was found to be approximately 58.00 mm, and $h$ was approximately 5.54 mm. Despite assuming a spherical head, the analytical model predicted well the impact characteristics observed in the Stage 2 parametric study. In Table 4.2 below, it can be seen that the analytically predicted values of $T_p$ were consistently close to the experimental observations, with an absolute maximum error of 6.30%, while the predicted values of $F_{max}$ deviated on average even less, with an absolute maximum error of 3.43%.

| Case Number | FE $T_p$ (ms) | FE $F_{max}$ (kN) | Analytical $T_p$ (ms) | Analytical $F_{max}$ (kN) | Analytical $T_p$ error (%) | Analytical $F_{max}$ error (%) |
|---|---|---|---|---|---|---|
| 2.1 | 3.287 | 0.470 | 3.205 | 0.462 | -2.48 | -1.73 |
| 2.2 | 1.681 | 0.873 | 1.655 | 0.852 | -1.54 | -2.40 |
| 2.3 | 1.076 | 0.957 | 1.063 | 0.936 | -1.25 | -2.20 |
| 2.4 | 0.786 | 0.975 | 0.775 | 0.964 | -1.38 | -1.20 |
| 2.5 | 0.620 | 0.978 | 0.608 | 0.975 | -1.87 | -0.25 |
| 2.6 | 0.504 | 0.976 | 0.500 | 0.982 | -0.85 | 0.55 |
| 2.7 | 0.432 | 0.977 | 0.424 | 0.985 | -1.81 | 0.89 |
| 2.8 | 0.371 | 0.976 | 0.368 | 0.988 | -0.80 | 1.13 |
| 2.9 | 0.329 | 0.975 | 0.325 | 0.989 | -1.26 | 1.43 |
| 2.10 | 0.295 | 0.974 | 0.291 | 0.990 | -1.20 | 1.71 |
| 2.11 | 0.208 | 0.968 | 0.205 | 0.992 | -1.19 | 2.47 |
| 2.12 | 0.169 | 0.960 | 0.158 | 0.993 | -6.30 | 3.43 |

*Table 4.2: Resulting contact durations and peak impact forces in the Stage 2 parametric study. "FE" denotes values measured in the finite element simulations. "Analytical" denotes values predicted by Young's (2003) analytical model.*

Regardless of the impactor's identical geometry, material properties, masses and velocities in Cases 2.1 to 2.10 compared to Cases 1.1 to 1.10 in the Stage 1 study, the values of peak impact force recorded for these Stage 2 impacts were consistently higher than in the equivalent Stage 1 impacts. An explanation can be found by examining Young's (2003) analytical model of head impact. For the most part this current work makes use of the exact implicit expressions outlined in Young's (2003) paper (detailed in Section 1.5), but approximate explicit expressions for impact characteristics such as $F_{max}$ and $T_p$ are also provided in Young's work. Examining the full explicit expression for peak impact force:

$$F_{max} = \frac{R^{*1/5} E^{*2/5} m^{*3/5} \Delta v^{6/5} E_{sh}^{1/2} h}{\left[\frac{1}{\sqrt{2.3}} R^{*1/5} E^{*2/5} m^{*1/10} \Delta v^{1/5} R_{sh}^{1/2} (1-\nu_{sh}^2)^{1/4} + \frac{\sqrt{3}}{2}\left(\frac{16}{15}\right)^{1/10} E_{sh}^{1/2} h\right]} \qquad [4.1]$$

it can be seen that this peak force is proportional to, among others, the variables $R^*$ and $m^*$, which are the relative external radii at the contact site, and relative masses, of the head and impactor respectively [Equations 1.9 and 1.11] (Young, 2003). The simple fluid-filled sphere head model used in Stage 1 had the same material properties as used in the Stage 2 head model, but the latter's image-based geometry was slightly larger, giving a greater mass: the Stage 2 model's mass was 2.917 kg, as opposed to 2.466 kg for the Stage 1 model. Also, the Stage 2 model had a smaller radius of curvature at the impact site: the local radius of curvature at the impact site on the occipital bone was measured as being approximately 58.00 mm, as opposed to 80.01 mm for the Stage 1 model (defined by the exterior radius of

the spherical shell). These differences in the geometry and masses of these two head models result in differing $F_{max}$ values between the comparable Stage 1 and Stage 2 impacts.

An eigenvalue analysis was performed in the finite element package Abaqus/CAE (Dassault Systèmes S.A.) in order to obtain the period of the first n=2 mode of the head $T_{\Omega}$. As previously, the analysis was performed on the realistic skull geometry only, with the enclosed fluid removed, and with the skull's density modified such that the mass of the head remained constant. The head model in Stage 1 was spherical and so possessed an infinite number of planes of symmetry; the realistic skull model in Stage 2 has only one, being roughly symmetrical about the mid-sagittal plane. Therefore, the Stage 2 model had several unique n=2 modes, with different deformation shapes and frequencies; five such modes were computed by Abaqus.

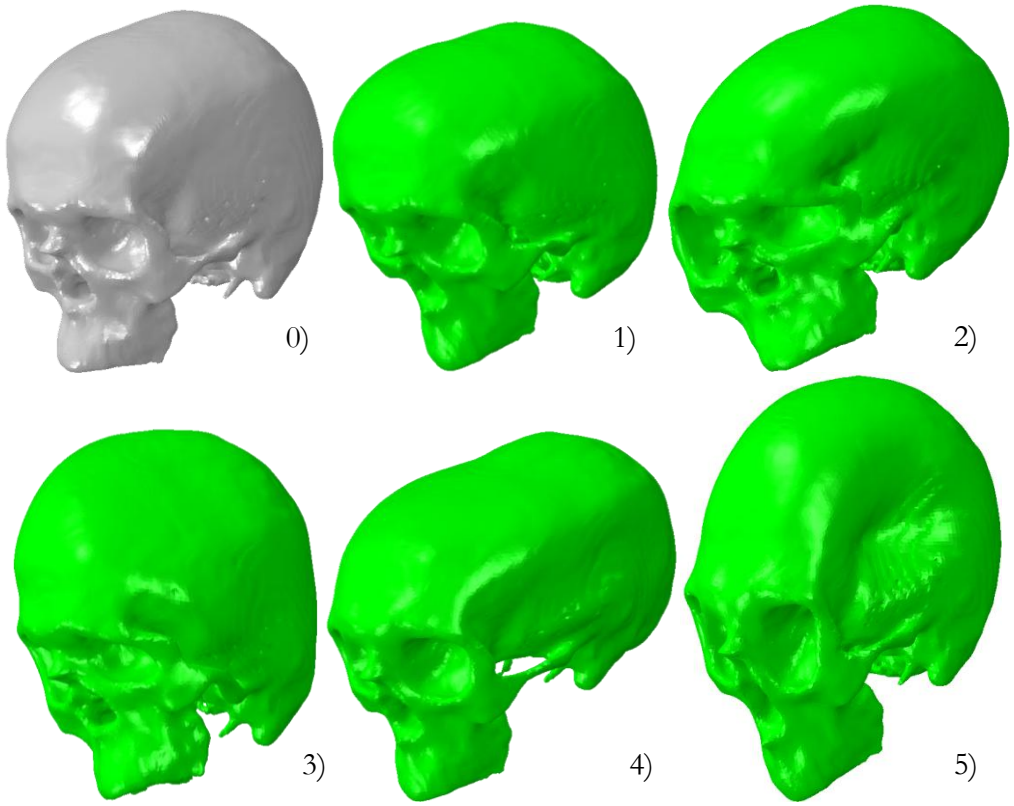


*Figure 4.1: Natural modes of the Stage 2 model: (0) undeformed geometry, (1) to (5) the deformed geometries (highly exaggerated) of the first five non-rigid body modes of the system, i.e. the five n=2 modes.*

At this stage in the investigation, the mechanism which causes the dynamic magnification of intracranial pressures remained uncertain. Nevertheless, in choosing a $T_{\Omega}$ from the five possible n=2 modes, it was decided to select that which was likely to be most relevant to the impacts that were currently under investigation. When a system is subjected to an external load, which, if any, natural modes of the system become excited is determined by

the frequency content of the load, and by the location that it is applied. The fourth n=2 mode (diagram (4) in Figure 4.1, above) was deemed most appropriate to use when non-dimensionalising the Stage 2 results, since the fourth mode oscillates in a longitudinal fashion, with a point of maximum deflection at the site of impact, the coup. Therefore, one would expect this mode to dominate when, as here, the head is subjected to a horizontal load at the rear of the skull. This longitudinal n=2 mode had a period $T_\Omega$ of 0.437 ms. This period of oscillation was shorter than the Stage 1 model's period, since in this realistic skull model the skull thickness $h$ was, on average, greater so resulting in a stiffer cranial vault.

Young's (2002) simple closed-form expression for $T_\Omega$ [Equation 1.6] was used to predict the period of oscillation of the n=2 mode for a fluid-filled sphere with the same dimensions and properties as the Stage 2 model. Since the Stage 1 and Stage 2 head models utilise equal material properties, the only parameters which differed in this calculation were the mass of the head $m$, and the thickness of the skull $h$. The analytically predicted $T_\Omega$ value was 0.486 ms. Despite the analytical model assuming spherical geometry while the Stage 2 model was in fact based on the realistic geometry of a human skull, the analytical model performs surprisingly well, overestimating the period of oscillation by only 11.21% compared to the numerically computed value.

### *4.2.2 Pressure response*

The intracranial pressure response resulting from each impact case was analysed using D3PLOT and T/HIS. As in Stage 1, the peak positive and negative intracranial pressures invariably arose at the coup and contrecoup. In the Stage 2 investigation it was decided to update the method by which pressure is monitored at the coup. The sampling points used to record pressure at the coup and contrecoup effectively provide an average of the pressure across the volume of any element in which recording of pressure-time histories has been engaged (by defining the element as a "HISTORY_SOLID" in LS-DYNA). Due to the mesh refinement required at the coup, large differences in element size existed between the coup and contrecoup of the brain, such that, in the Stage 2 model, the contrecoup pressure-time histories are effectively monitoring the average pressure over a length of 4.08 mm along the impact axis, the centre of which is 4.66 mm from the brain-skull boundary, but elements at the coup have a characteristic length of only 0.55 mm. The severity of any lesions caused by pressure transients in the brain are likely to be affected by the amount of the brain that experiences these transients: if only a tiny portion of the brain is affected, then the resulting injury could be expected to be less severe than if a large portion is affected. To provide more insight into the pressure behaviour at the coup, in the

Stage 2 investigation, two separate pressure-time histories were captured at this location per impact: referred to as "pressure at a point" and "pressure over a patch" respectively. The first pressure-time histories were captured over a small area (0.55 mm length along the impact axis); the centre of this length was only 0.68 mm from the brain-skull boundary at the coup, and so this represented the pressure transients with the greatest magnitude, but these values of pressure only occurred over an extremely localised area of the brain (i.e. at a "point"). The second pressure-time histories were obtained by averaging the output of four sampling points which lay between 0.68 and 6.90 mm from the brain-skull boundary (an average of 3.99 mm away), allowing the pressure to be monitored over a larger area, 6.93 mm in length. Unless otherwise stated, the pressure-time histories presented graphically below are those captured using this second method ("pressure over a patch"), as these pressures over a larger area were deemed more meaningful.

#### *4.2.2.1 Cases 2.1 and 2.2*

As in the previous parametric study, in the longest duration impacts (Cases 2.1 and 2.2) a quasi-static intracranial response was observed. The contact durations of these cases ($T_p$ of 3.287 and 1.681 ms respectively) were both greater than twice the period of the n=2 mode $T_\Omega$ (2 × 0.437 = 0.874 ms), i.e. above the critical impact duration proposed by Young & Morfey (1998) for a spherical head.

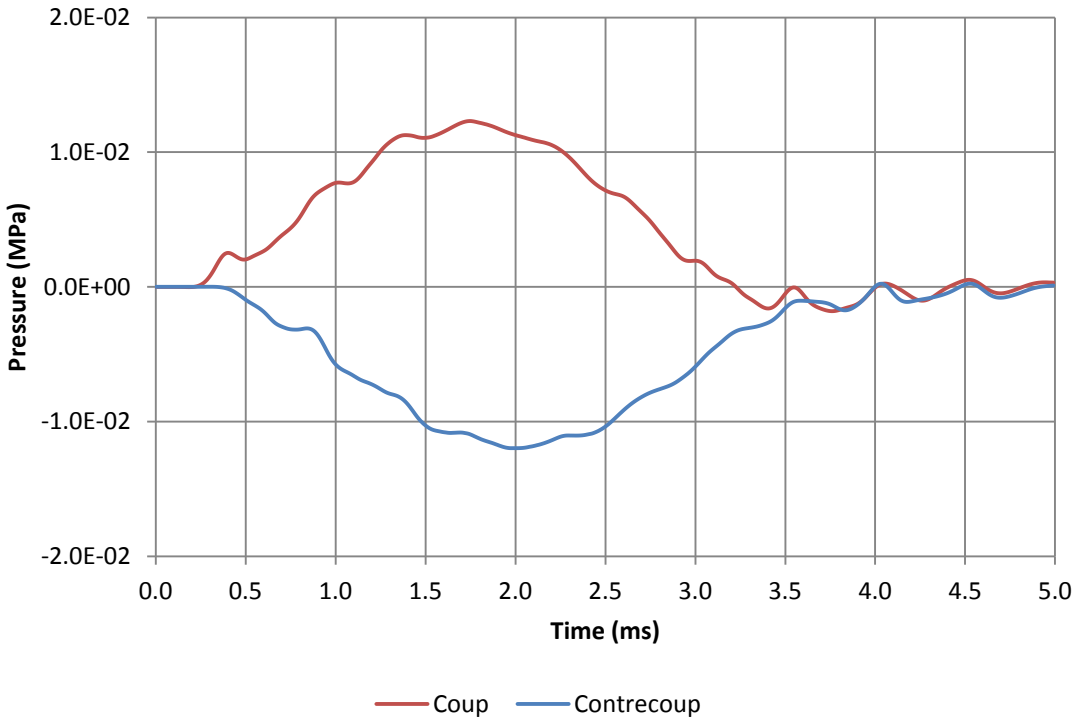


*Figure 4.2: Case 2.1, local pressure-time histories recorded in the brain at the coup and contrecoup.*

The local pressure-time histories recorded at the coup and contrecoup in Case 2.1 are presented in Figure 4.2 above. This response was typical of the quasi-static impacts observed. In both Cases 2.1 and 2.2:

- Coup and contrecoup pressure-time histories are roughly symmetrical and rise and fall in a smooth sinusoidal fashion, i.e. they follow the force-time history of the impact.
- Peak positive intracranial pressure occurs at the coup, while peak negative intracranial pressure occurs at the contrecoup. These pressure maxima do not occur exactly at $T_p/2$ (1.644 ms), but very close to this time.
- During the contact period ($0 \leq t \leq 3.287$ ms) no negative pressure is experienced at the coup, and no positive pressure is experienced at the contrecoup.

All of the above characteristics are indicative of a quasi-static response and can be observed in Figure 4.2. After the contact duration had passed ($t > T_p$), a regular oscillation of pressures at the coup and contrecoup can be seen. This behaviour produced low magnitude transients of positive and negative pressure occurring at both the coup and contrecoup, and was likely caused by the system being left in a state of vibration after impact. This was investigated further in Section 6.1.2.2.

The peak recorded positive pressure at the coup and negative pressure at the contrecoup was 1.230e-2 and -1.197e-2 MPa respectively. Substituting the properties of the Stage 2 model and the parameters of impact Case 2.1 into Equation 1.5, the peak pressures expected at the coup and contrecoup for a perfectly quasi-static response were found to be $P_{C\ quasi}$ = 1.154e-2 and $P_{CC\ quasi}$ = -1.284e-2 MPa respectively. The peak coup and contrecoup pressures observed in the simulated impact differed from these analytically predicted values by factors of 1.066 and 0.932. These factors of difference are closer to unity than those obtained from the equivalent Stage 1 impact (Case 1.1), indicating that here the response is closer to the perfectly quasi-static solution. This is likely due to the absence of noise in the Stage 2 and Stage 3 investigations discussed previously, compared to the Stage 1 study where a small amount of noise was generated at the impact site. Examining Equation 1.5, it can be seen that the magnitude of the peak quasi-static pressures is independent of any geometric dimensions other than the distance from the centre of gravity of the fluid region; the quasi-static response does not depend on the geometry of the head model, and applies equally to any arbitrary container filled with inviscid fluid.

Figure 4.3, below, depicts the contours of pressure observed throughout the brain approximately half way through the impact, at 1.650 ms after incidence. The quasi-static response is again evidenced by the presence of parallel pressure contours (a "banding" pattern), indicating a linear pressure gradient throughout the brain. The light green contour representing pressure of 0 MPa passes through the brain's centre of gravity, indicated by a crosshairs symbol in Figure 4.3: this is as would be expected if no foramen magnum opening was present. The foramen was found by Thomas et al. (1967) to shift the zero-point of pressure such that it lies above it, but appears here to have a negligible effect. The soft membrane covering the foramen had deformed only slightly, representing a negligible flow of material through the foramen caused by the positive pressure residing in the brain above it. This may be due to the duration of the impact being only a couple of milliseconds (3.287 ms in this case), which may not be sufficient for any significant flow through the foramen to occur.

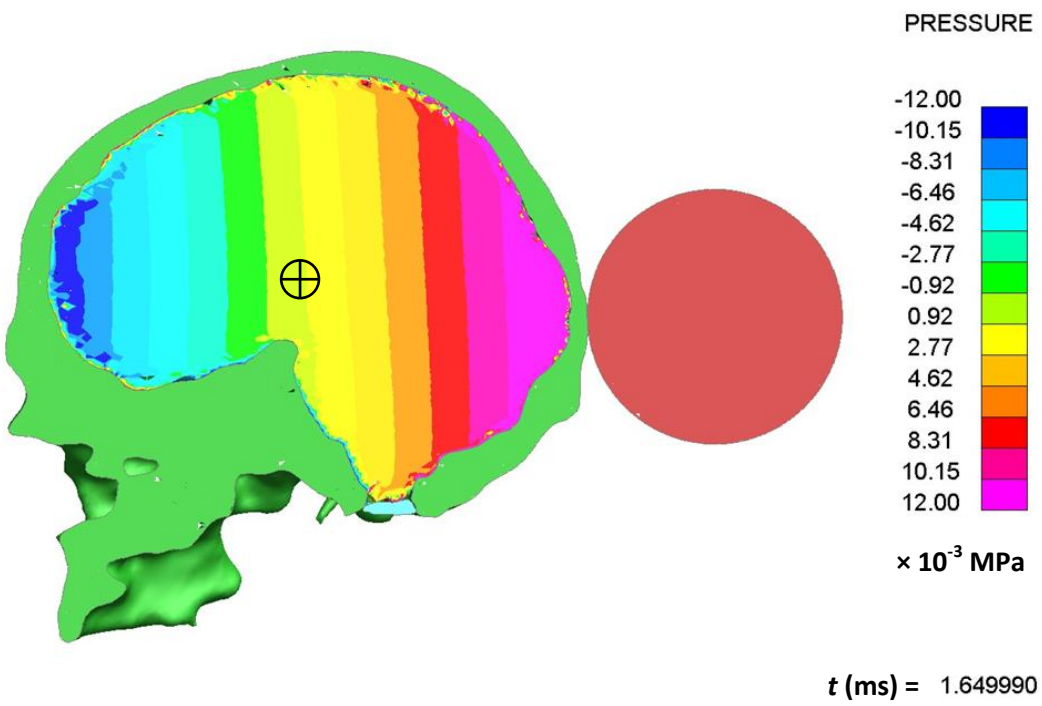


*Figure 4.3: Mid-section view of the Stage 2 model depicting Case 2.1, contours of pressure in the brain at t = 1.650 ms. The solid green, light blue, and red regions represent the realistic skull, foramen magnum, and impactor respectively. The crosshairs symbol indicates the location of the brain's centre of gravity.*

#### *4.2.2.2 Cases 2.3 and 2.4*

The intracranial pressure behaviour observed in impact Cases 2.3 and 2.4 represented the transition from the quasi-static to the dynamic pressure response as observed in Stage 1, and therefore the recorded pressure-time histories were a superposition of typical

quasi-static and dynamic pressure-time histories, containing characteristics of both. In Case 2.3 the contact duration decreased to 1.076 ms, and so was beginning to approach the critical impact duration given by twice $T_{\Omega}$ (0.874 ms).

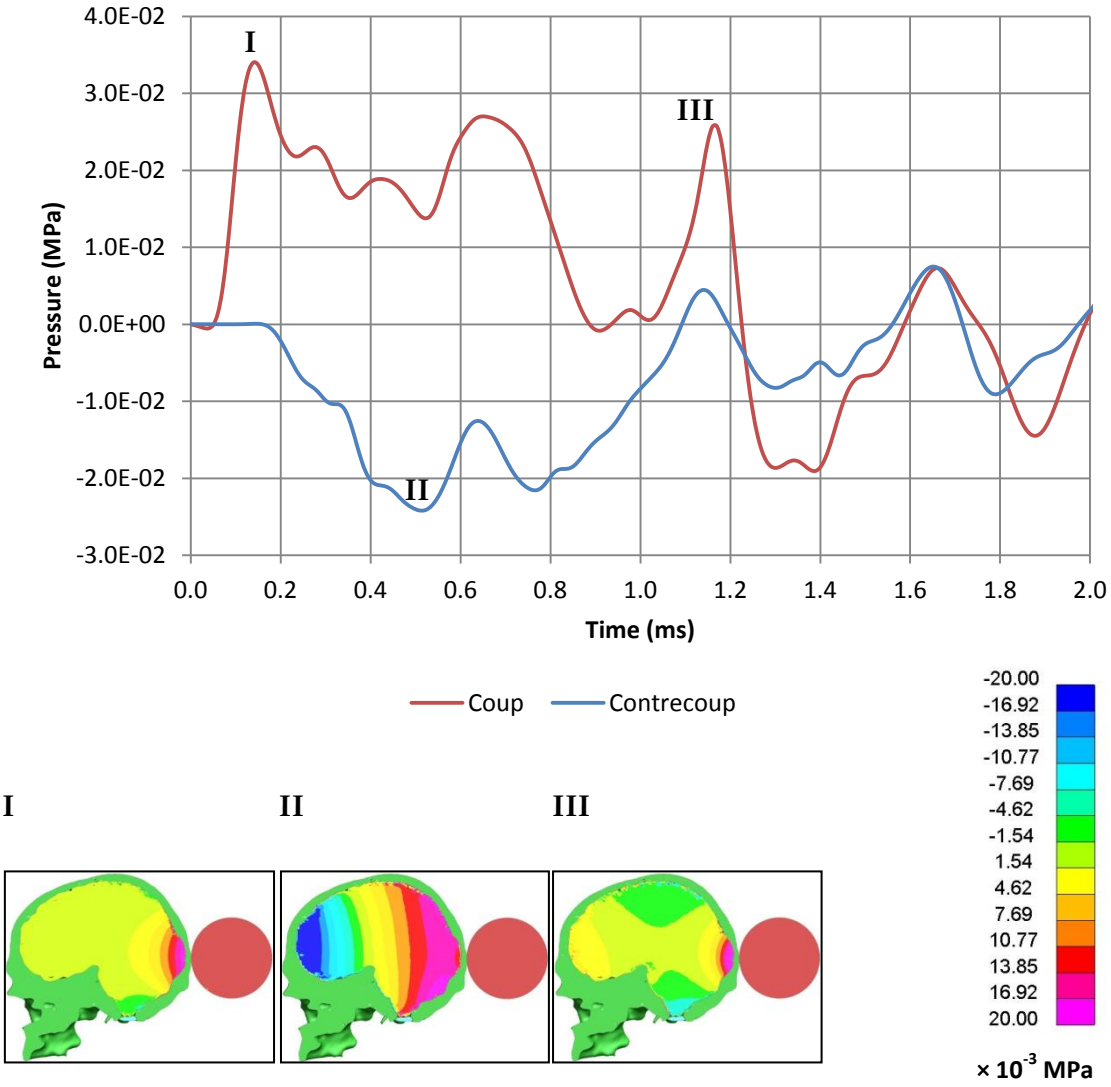


*Figure 4.4: Case 2.3, Top: local pressure-time histories recorded in the brain at the coup and contrecoup. Bottom: contour plots of pressure in the brain at I (t = 0.160 ms), II (t = 0.500 ms), and III (t = 1.140 ms). The solid green, light blue, and red regions represent the realistic skull, foramen magnum, and impactor respectively.*

Figure 4.4, above, presents the local pressures recorded at the coup and contrecoup for Case 2.3; the following characteristics typical of a quasi-static response can be seen:

- Peak positive intracranial pressure occurs at the coup, while peak negative intracranial pressure occurs at the contrecoup.
- During the contact period ($0 \leq t \leq 1.076$ ms) no positive pressure is experienced by the contrecoup.

However:

- During the contact period ($0 \leq t \leq 1.076$ ms) a small amount of negative pressure is experienced by the coup.
- The coup and contrecoup pressure-time histories are non-symmetrical, and do not rise and fall in a sinusoidal fashion. Also the peak coup pressure does not occur at, or close to, half way through the impact ($t = T_p/2$).
- The peak coup and contrecoup pressures were recorded as 3.420e-2 and -2.435e-2 MPa respectively. When compared to the predicted quasi-static peak pressures $P_{C\ quasi}$ and $P_{CC\ quasi}$, it was found that these recorded pressures differed from the analytical quasi-static values by factors of 1.433 and 0.931 respectively.

Furthermore, while contour plot II provided in Figure 4.4 depicts a clear "banding" pattern throughout the brain, indicative of rigid-body acceleration of the head, contour plots I and III reveal localised pressure transients in the brain which are atypical of quasi-static behaviour. Examining contour plots I and III in Figure 4.4, regions of positive pressure are visible at the coup, while the contrecoup and midbrain remain unaffected.

In Case 2.4 the resulting impact duration decreases further to 0.786 ms, which is now less than the critical impact duration predicted by twice $T_\Omega$ (0.874 ms). The coup and contrecoup pressure-time histories recorded in impact Case 2.4 are presented below in Figure 4.5. Examining these pressure-time histories it can be seen that, while in Case 2.4 the peak positive pressure still occurs at the coup and the peak negative pressure still occurs at the contrecoup, for the first time in this parametric study the coup and contrecoup experience both positive and negative pressure transients during the contact period ($0 \leq t \leq 0.786$ ms).

Contour plots of pressure provided in Figure 4.5 were chosen to correspond to approximately the same landmarks in the pressure-time histories as those recorded for impact Case 2.3 (Figure 4.4). The lack of a clear "banding" pattern spanning the length of the brain in contour plot II (Figure 4.5) illustrates how Case 2.4 deviates further from the quasi-static response compared to Case 2.3, as the intracranial pressure behaviour becomes less dominated by rigid-body acceleration of the head and more influenced by dynamic effects. Here peak recorded pressures at the coup and contrecoup were 5.510e-2 and -3.087e-2 MPa respectively, which were greater than the peak pressures expected from a perfectly quasi-static impact by factors of 2.266 and 1.158.

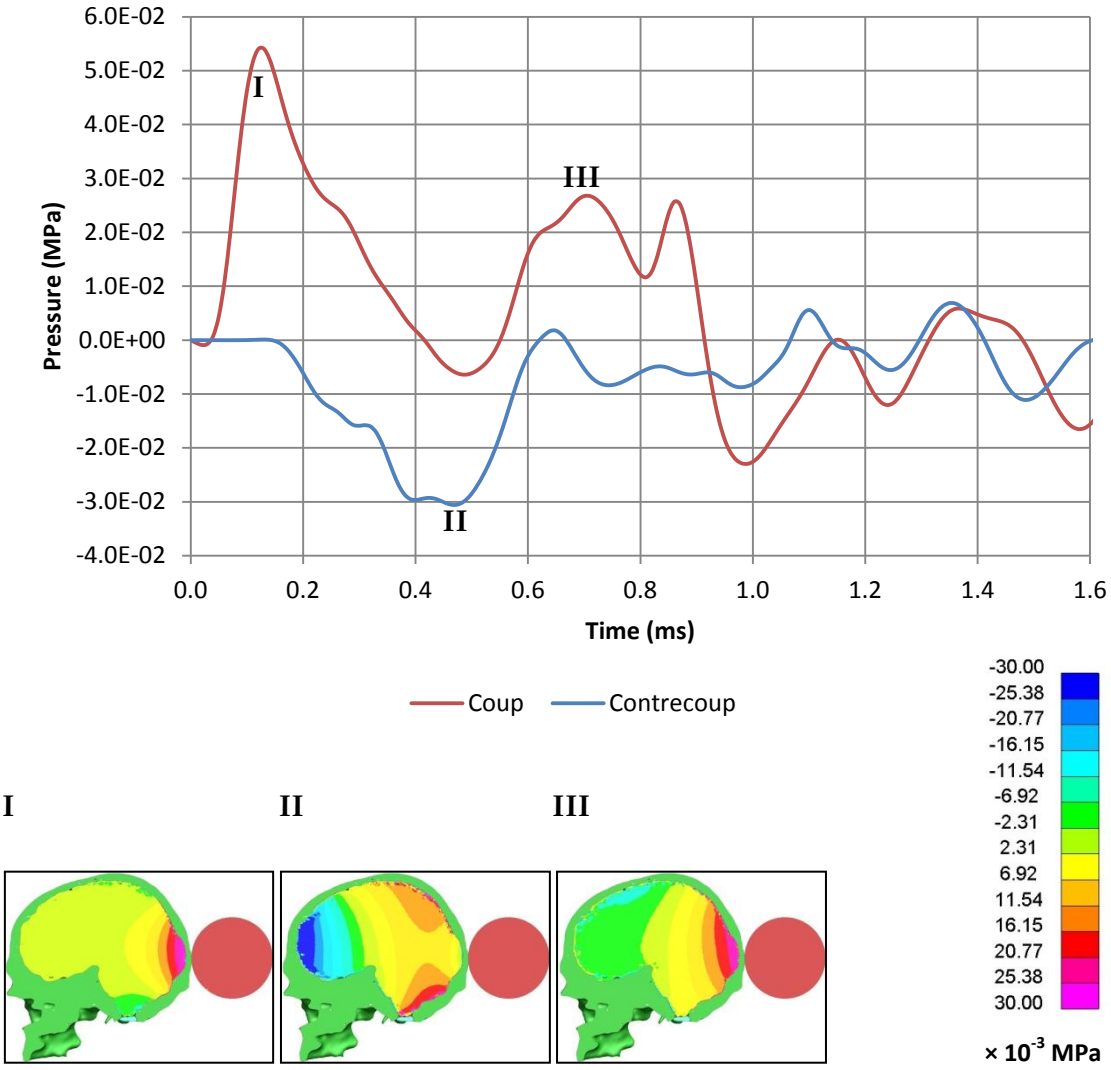


*Figure 4.5: Case 2.4, Top: local pressure-time histories recorded in the brain at the coup and contrecoup. Bottom: contour plots of pressure in the brain at I (t = 0.160 ms), II (t = 0.480 ms), and III (t = 0.680 ms). The solid green, light blue, and red regions represent the realistic skull, foramen magnum, and impactor respectively.*

#### *4.2.2.3 Cases 2.5 to 2.8*

Advancing through the parametric study the impact durations continued to decrease and, as in the Stage 1 investigation, this resulted in a progressive increase in the magnitude of the pressure transients generated in the brain, despite a (roughly) constant impact force for each case. In Cases 2.5 to 2.8 however, during which the duration of the resulting impacts ($T_p$ between 0.620 and 0.371 ms) was close to the period of the longitudinal n=2 mode $T_\Omega$ (0.437 ms), a slightly different intracranial pressure behaviour was observed compared to any which were identified in Stage 1. The peak coup and contrecoup pressures captured in impact Case 2.5 are presented below in Figure 4.6.

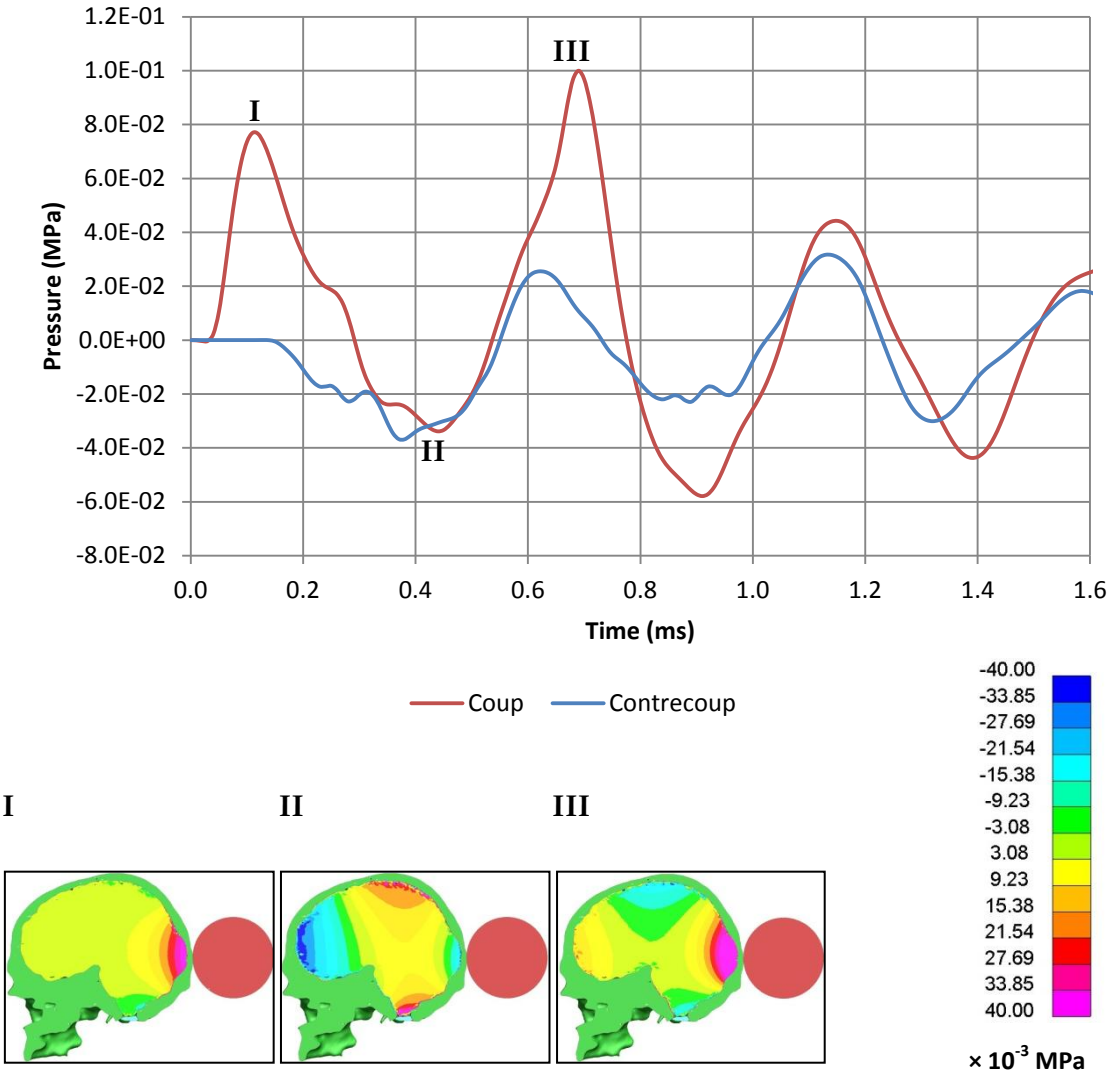


*Figure 4.6: Case 2.5, Top: local pressure-time histories recorded in the brain at the coup and contrecoup. Bottom: contour plots of pressure in the brain at I ($t$ = 0.140 ms), II ($t$ = 0.420 ms), and III ($t$ = 0.680 ms). The solid green, light blue, and red regions represent the realistic skull, foramen magnum, and impactor respectively.*

It can be seen in Figure 4.6 that both during impact ($t \leq 0.620$ ms), and after impact ($t > 0.620$ ms), the coup and contrecoup pressures resulting from Case 2.5 oscillate in sync with each other with a regular period of approximately 0.450 ms, which is close to $T_{\Omega}$. Therefore, the likely explanation for the oscillatory nature of the pressure-time histories recorded in Cases 2.5 to 2.8 is that these impacts excite the skull's longitudinal n=2 mode, and as the skull vibrates it produces alternating transients of positive and negative pressure beneath its two poles of maximum deflection, i.e. at the coup and contrecoup. It is, however, unclear why this oscillatory pressure behaviour was not observed as distinct from the dynamic pressure magnification response witnessed in the Stage 1 investigation, and by Young & Morfey (1998). The dynamic pressure magnification response has previously been

defined (see Section 3.2.2.3) as being characterised by three large alternating pressure spikes (positive, then negative, then positive) occurring first at the coup, and later at the contrecoup, which are distinct from any underlying pressure fluctuations: this differs from the oscillating pressure-time histories depicted in Figure 4.6, as the coup and contrecoup pressure transients during a typical dynamic pressure magnification response are not in sync.

#### *4.2.2.4 Cases 2.9 to 2.12*

The remaining impacts, Cases 2.9 to 2.12 ($T_p$ between 0.329 and 0.169 ms), had contact durations significantly less than the critical impact duration given by twice $T_\Omega$ (0.874 ms). The pressure-time histories recorded for these cases did not differ qualitatively, but were distinguished mainly by the increasing magnitude of the peak intracranial pressures as contact duration was reduced. These cases exhibited large transients of positive and negative pressure occurring at the coup and contrecoup. The impacts produced intracranial pressure behaviour that appeared qualitatively distinct from both the quasi-static response and the oscillatory response described above. The coup and contrecoup pressures recorded for Case 2.10 ($T_p$ = 0.295 ms) can be seen below in Figure 4.7. Despite utilising starkly different skull and brain geometries compared to the simple fluid-filled sphere representation of the head, the short duration impacts in this Stage 2 parametric study exhibited to a remarkable degree the same large pressure transients characteristic of the dynamic pressure magnification response observed in Stage 1 and in Young & Morfey's (1998) investigation. Examining Figure 4.7, the following distinguishing features of this response can be recognised:

- Immediately after incidence the brain beneath the coup experiences three large spikes of pressure, which alternate from positive, to negative, to positive. During this time the contrecoup does not experience any large pressure transients.
- After initially only experiencing small pressures, at some time after these large pressure spikes have occurred at the coup, the contrecoup also experiences three similar large pressure transients: these alternate in the same fashion, and appear to fluctuate with the same period, as those at the coup.
- The large pressure spikes at the coup and contrecoup appear to be distinct from any smaller pressure transients occurring simultaneously (which may be caused by remnants of a quasi-static response, or the oscillation of higher order modes of the system).

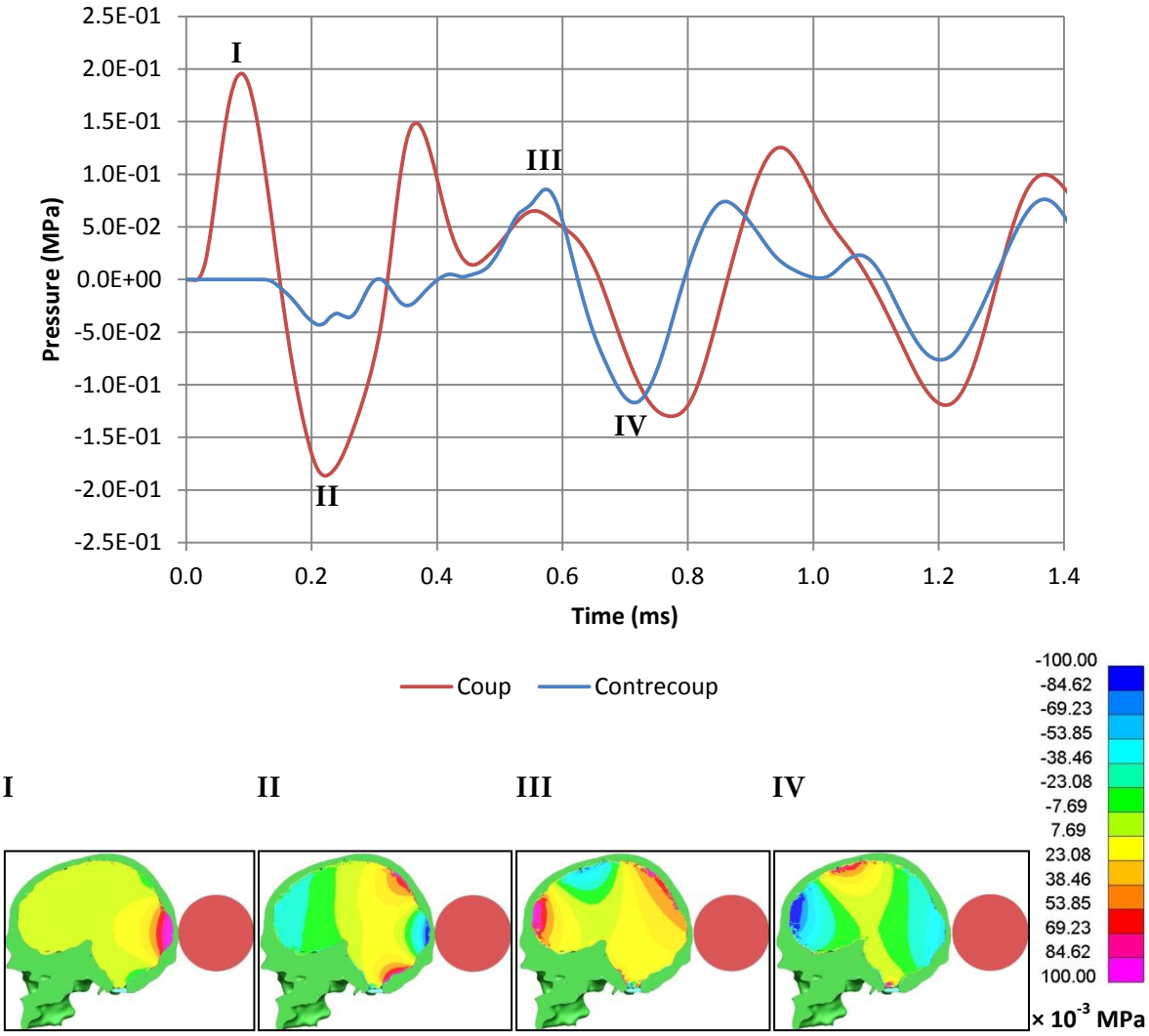


*Figure 4.7: Case 2.10, Top: local pressure-time histories recorded in the brain at the coup and contrecoup. Bottom: contour plots of pressure in the brain at I (t = 0.090 ms), II (t = 0.220 ms), III (t = 0.570 ms), and IV (t = 0.700 ms). The solid green, light blue, and red regions represent the realistic skull, foramen magnum, and impactor respectively.*

In the Stage 1 investigation only two possible intracranial pressure behaviours were identified: if the contact duration was long then a quasi-static response could be expected, whereas short duration impacts resulted in dynamic intracranial pressure magnification and its associated large pressure transients (while medium contact durations resulted in an amalgam of these two behaviours). In the previous section, however, it was described how certain Stage 2 impacts had resulted in oscillating intracranial pressures. It is possible that the Stage 1 simulations did not compute enough time after the impact had ceased for it to become apparent (in cases where $T_p \approx T_\Omega$) that the system was in a state of vibration. This is unlikely however, since when comparing the pressure-time histories resulting from very short duration impacts ($T_p < T_\Omega$) produced in the Stage 1 and Stage 2 investigations (such as Cases 2.10 and 1.10, see Figures 4.7 and 3.7), while large alternating pressure spikes typical of dynamic pressure behaviour can be seen in both of these cases, only in the Stage 2 impact case are large syncopated oscillatory pressures visible. In other words, in Case 2.10 the large pressure spikes typical of a dynamic pressure response are superimposed onto an oscillatory pressure response as described in Section 4.2.2.3. This suggests that some aspect of the geometry of the realistic skull makes it particularly susceptible to the excitation of its longitudinal n=2 natural mode compared to the simple fluid-filled sphere geometry, such that very short duration impacts will cause the skull to vibrate. If this occurs then oscillatory pressures appear superimposed onto any underlying pressure response. A possibility is that the presence of the foramen magnum, which introduces a discontinuity in the skull's exterior, may make it more sympathetic to excitation of this n=2 mode than the continuous spherical shell in Stage 1.

Finally, the pressure response of the shortest duration impact in this low energy parametric study, Case 2.12 ($T_p$ = 0.169 ms), is presented below in Figure 4.8. Here the "pressure at a point", i.e. the coup pressure-time history captured over a small area located close to the brain-skull boundary is shown, in addition to the regular coup and contrecoup histories. As one would expect, it can be seen that the pressure-time histories recorded by this sampling point are qualitatively the same as the standard coup pressures (captured "over a patch"), but the recorded transients are of greater magnitude.

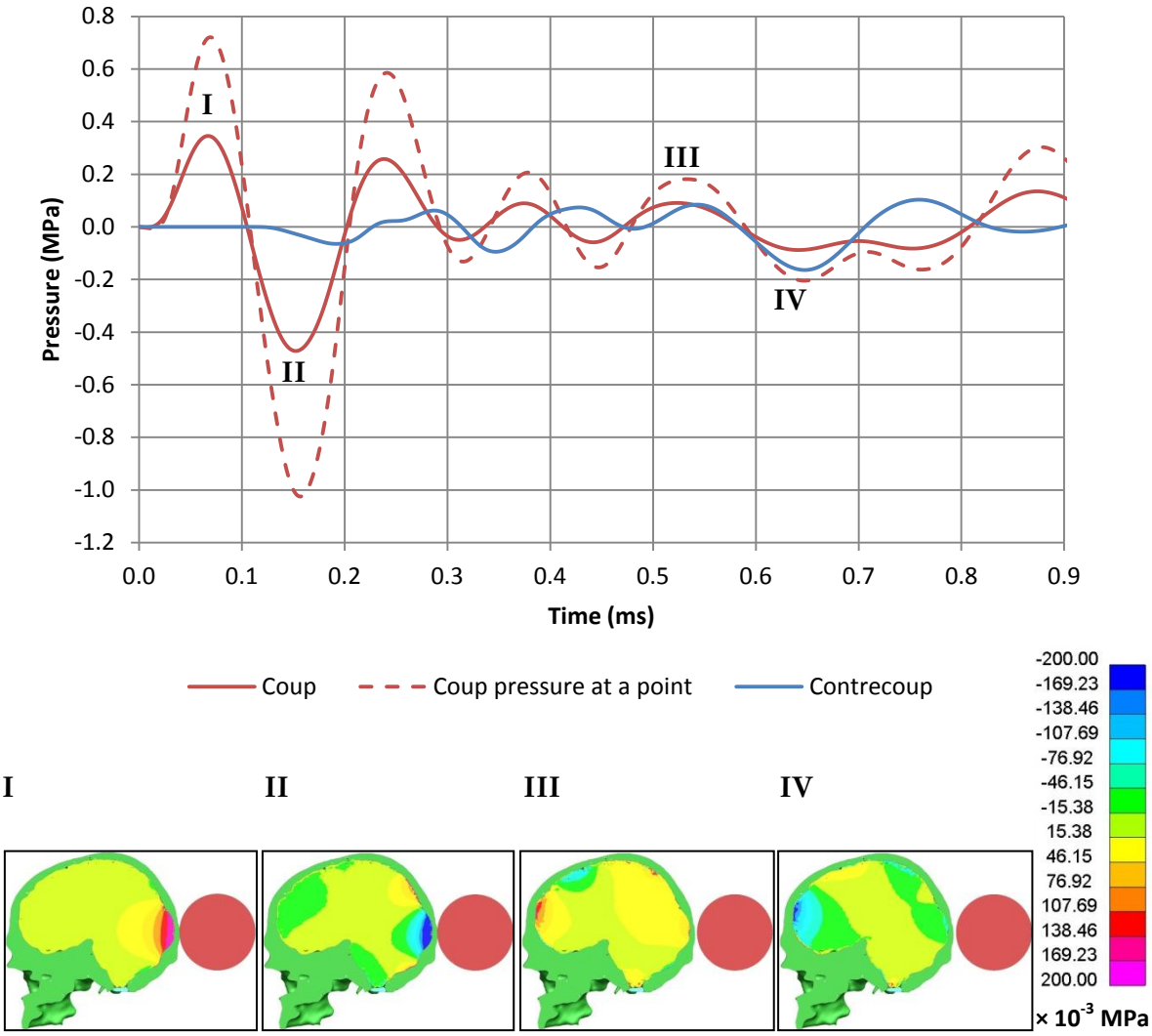


*Figure 4.8: Case 2.12, Top: local pressure-time histories recorded in the brain at the coup and contrecoup; for the coup both pressure histories "over a patch" (Coup) and "pressure at a point" are shown. Bottom: contour plots of pressure in the brain at I (t = 0.070 ms), II (t = 0.140 ms), III (t = 0.520 ms), and IV (t = 0.630 ms). The solid green, light blue, and red regions represent the realistic skull, foramen magnum, and impactor respectively.*

### *4.2.3 Collapsing the results*

The results of the Stage 2 low energy parametric study were non-dimensionalised in order to reduce the influence of variations in impact force, and to highlight trends in the pressure response. The peak pressures that would be expected at the coup and contrecoup locations for a perfectly quasi-static impact, $P_{C\ quasi}$ and $P_{CC\ quasi}$, were calculated using Equation 1.5. An additional quasi-static coup pressure $P_{C\ point\ quasi}$ was also calculated in this manner, based on the position of the "pressure at a point" sampling location. These expected peak quasi-static pressures are given below in Table 4.3. The peak intracranial pressures recorded for

each impact case at: the coup ("over a patch"), coup ("at a point"), and contrecoup, are provided in Table 4.4. These peak intracranial pressures were normalised over their respective analytically predicted peak quasi-static pressures, while impact durations $T_p$ were normalised over the period of the longitudinal n=2 mode $T_\Omega$. These non-dimensional ratios of pressure and time are presented in Table 4.5. Initially in Cases 2.1 and 2.2 coup "pressure at a point" was not monitored, and data pertaining to this sampling location was only available from Case 2.3 onwards.

| Case Number | Analytical | | |
|---|---|---|---|
| | $P_{C\ quasi}$ (MPa) | $P_{C\ point\ quasi}$ (MPa) | $P_{CC\ quasi}$ (MPa) |
| 2.1 | 1.154e-2 | N/A | -1.284e-2 |
| 2.2 | 2.144e-2 | N/A | -2.386e-2 |
| 2.3 | 2.387e-2 | 2.496e-2 | -2.616e-2 |
| 2.4 | 2.432e-2 | 2.543e-2 | -2.665e-2 |
| 2.5 | 2.438e-2 | 2.550e-2 | -2.672e-2 |
| 2.6 | 2.434e-2 | 2.545e-2 | -2.668e-2 |
| 2.7 | 2.435e-2 | 2.546e-2 | -2.668e-2 |
| 2.8 | 2.435e-2 | 2.546e-2 | -2.668e-2 |
| 2.9 | 2.431e-2 | 2.542e-2 | -2.664e-2 |
| 2.10 | 2.427e-2 | 2.538e-2 | -2.660e-2 |
| 2.11 | 2.415e-2 | 2.525e-2 | -2.646e-2 |
| 2.12 | 2.394e-2 | 2.504e-2 | -2.624e-2 |

*Table 4.3: Analytically predicted quasi-static peak pressures for the Stage 2 low energy parametric study.*

| Case Number | FE: Coup | | | | FE: Contrecoup | |
|---|---|---|---|---|---|---|
| | $P_{C\ positive}$ (MPa) | $P_{C\ negative}$ (MPa) | $P_{C\ point\ positive}$ (MPa) | $P_{C\ point\ negative}$ (MPa) | $P_{CC\ positive}$ (MPa) | $P_{CC\ negative}$ (MPa) |
| 2.1 | 1.230e-2 | -1.830e-3 | N/A | N/A | 2.771e-4 | -1.197e-2 |
| 2.2 | 2.540e-2 | -5.830e-3 | N/A | N/A | 1.390e-3 | -2.151e-2 |
| 2.3 | 3.420e-2 | -1.940e-2 | 6.900e-2 | -4.310e-2 | 7.555e-3 | -2.435e-2 |
| 2.4 | 5.510e-2 | -2.290e-2 | 1.117e-1 | -5.195e-2 | 7.048e-3 | -3.087e-2 |
| 2.5 | 1.003e-1 | -5.790e-2 | 2.022e-1 | -1.225e-1 | 3.174e-2 | -3.720e-2 |
| 2.6 | 1.257e-1 | -8.770e-2 | 2.596e-1 | -1.877e-1 | 5.690e-2 | -4.560e-2 |
| 2.7 | 1.253e-1 | -1.130e-1 | 2.553e-1 | -2.316e-1 | 5.800e-2 | -6.892e-2 |
| 2.8 | 1.500e-1 | -1.320e-1 | 3.056e-1 | -2.723e-1 | 6.360e-2 | -8.739e-2 |
| 2.9 | 1.730e-1 | -1.455e-1 | 3.544e-1 | -3.233e-1 | 7.698e-2 | -9.756e-2 |
| 2.10 | 1.960e-1 | -1.860e-1 | 4.010e-1 | -4.134e-1 | 8.583e-2 | -1.170e-1 |
| 2.11 | 2.860e-1 | -3.535e-1 | 5.902e-1 | -7.630e-1 | 1.014e-1 | -1.609e-1 |
| 2.12 | 3.480e-1 | -4.730e-1 | 7.230e-1 | -1.026 | 1.036e-1 | -1.643e-1 |

*Table 4.4: The peak positive and negative pressure values recorded at both coup sampling locations, and at the contrecoup, during the Stage 2 low energy parametric study.*

| Case Number | Normalised | | | | | | |
|---|---|---|---|---|---|---|---|
| | $P_{C\ positive} / P_{C\ quasi}$ | $P_{C\ negative} / P_{C\ quasi}$ | $P_{C\ point\ positive} / P_{C\ point\ quasi}$ | $P_{C\ point\ negative} / P_{C\ point\ quasi}$ | $P_{CC\ positive} / P_{CC\ quasi}$ | $P_{CC\ negative} / P_{CC\ quasi}$ | $T_p / T_\Omega$ |
| 2.1 | 1.066 | -0.159 | N/A | N/A | 0.022 | -0.932 | 7.516 |
| 2.2 | 1.185 | -0.272 | N/A | N/A | 0.058 | -0.901 | 3.845 |
| 2.3 | 1.433 | -0.813 | 2.764 | -1.727 | 0.289 | -0.931 | 2.461 |
| 2.4 | 2.266 | -0.942 | 4.391 | -2.043 | 0.264 | -1.158 | 1.797 |
| 2.5 | 4.114 | -2.375 | 7.932 | -4.806 | 1.188 | -1.392 | 1.417 |
| 2.6 | 5.164 | -3.603 | 10.199 | -7.374 | 2.133 | -1.709 | 1.153 |
| 2.7 | 5.146 | -4.641 | 10.028 | -9.096 | 2.174 | -2.583 | 0.988 |
| 2.8 | 6.161 | -5.422 | 12.004 | -10.697 | 2.384 | -3.276 | 0.849 |
| 2.9 | 7.115 | -5.984 | 13.939 | -12.714 | 2.889 | -3.662 | 0.753 |
| 2.10 | 8.075 | -7.663 | 15.799 | -16.288 | 3.227 | -4.399 | 0.674 |
| 2.11 | 11.845 | -14.640 | 23.375 | -30.219 | 3.832 | -6.081 | 0.475 |
| 2.12 | 14.535 | -19.756 | 28.879 | -40.981 | 3.949 | -6.260 | 0.387 |

*Table 4.5: Non-dimensional peak positive and negative pressures, and non-dimensional impact durations, of the Stage 2 low energy parametric study.*

Figure 4.9, below, displays the normalised results of the Stage 2 low energy parametric study in terms of the non-dimensional peak positive and negative coup pressures against the log of non-dimensional impact duration. Non-dimensional coup pressures captured "at a point" are provided in addition to non-dimensional standard coup pressures ("over a patch"). Likewise, Figure 4.10 depicts the normalised pressures at the contrecoup. In both Figures 4.9 and 4.10, the collapsed results of the Stage 1 investigation are also provided for comparison.

The non-dimensional results presented in Figures 4.9 and 4.10 illustrate the general trend observed: as the duration of the impacts was reduced, the magnitude of the peak pressures arising at the coup and contrecoup increased. Comparing the non-dimensional results at the coup and contrecoup in this Stage 2 investigation with those observed in the simple fluid-filled sphere head model in Stage 1, markedly similar trends of behaviour can be seen, including an approximately equal critical impact duration (of $T_p / T_\Omega = 2$), and similar degrees of pressure "magnification" in response to impacts shorter than this critical duration. These similarities occur despite gross differences in skull and brain geometry between the Stage 1 and Stage 2 models.

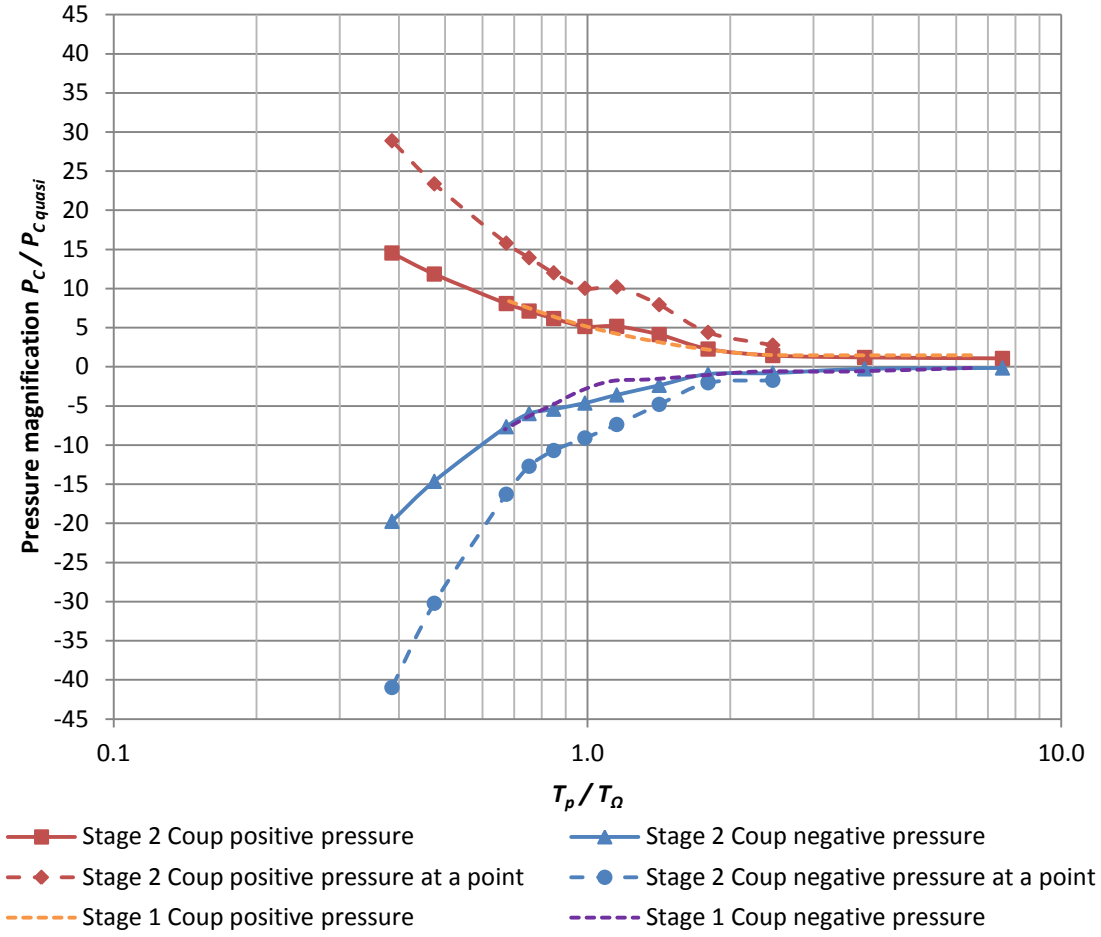


*Figure 4.9: Stage 2 parametric study, normalised peak pressures against $T_p$ / $T_\Omega$ at the coup. Normalised Stage 2 coup "pressure at a point" values and normalised Stage 1 coup pressures are provided for comparison.*

Examining Figure 4.9 reveals that the normalised coup pressures captured "at a point" demonstrate that a greater degree of pressure magnification occurs close to the brain-skull boundary, while the normalised standard coup pressures exhibit a lesser degree of magnification similar to that in the Stage 1 study. Only in Cases 2.11 and 2.12, which had significantly reduced impact durations, do these standard coup pressures reach higher degrees of magnification than observed in Stage 1. At the contrecoup however (see Figure 4.10), below the critical value of approximately $T_p$ / $T_\Omega$ = 2, pressure magnification is significantly lower than that experienced by the Stage 1 model. This reduction in the magnitude of pressure magnification at the frontal side of the cranium (compared to the spherical model) may be due to the presence of the facial bones, which appear to have a mitigating effect. This may be the reason why in the Stage 2 investigation, in impact Cases 2.5 and above (i.e. all impacts with non-dimensional durations less than $T_p$ / $T_\Omega \approx 1.5$), the peak negative pressure generated at the coup was of greater magnitude than any negative

pressure generated at the contrecoup. In the quasi-static response negative pressure is typically generated only at the contrecoup, and even in the dynamic intracranial pressure response caused by short duration impacts in Stage 1, peak negative pressures were always located at the contrecoup.

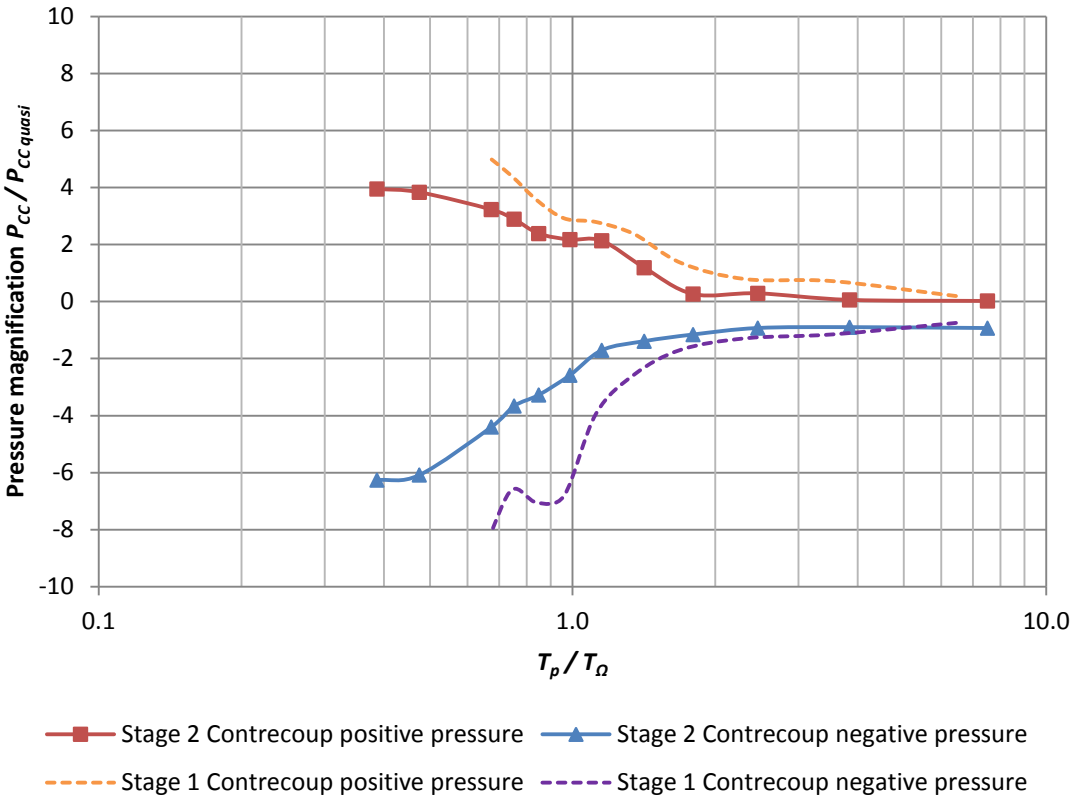


*Figure 4.10: Stage 2 parametric study, normalised peak pressures against $T_p$ / $T_\Omega$ at the contrecoup. Normalised Stage 1 contrecoup pressures are provided for comparison.*

Once again, the peak negative pressures generated in the parametric study were analysed to determine which impacts may cause deleterious cavity formation in the cranial fluids. Assuming, as a guideline, a cavitation threshold of -1 atm (-1.013e-1 MPa), it was found that Cases 2.7 to 2.12 are in danger of cavitation at the coup, while Cases 2.10 to 2.12 are in danger of cavitation at the contrecoup. If it is assumed that any cavitation within the cranial vault is capable of causing serious injury, even if it is only over a very small area located close (0.68 mm) from the brain-skull boundary (and therefore, likely to be in the CSF region rather than in, or directly adjacent to, the brain), then by examining the coup pressures captured "at a point" it can be seen that cavitation may occur in Cases 2.5 to 2.12.

## 4.3 High energy impacts

Following the low energy parametric study, a series of additional impacts were simulated in order to investigate the head model's response to collisions with more realistic parameters, and also to explore the limits of geometric linearity of the model. While not all of these cases were of higher energy than in the parametric study, for convenience they are referred to here as the Stage 2 "high energy impacts". These impacts utilise the same head and impactor models as previous Stage 2 experiments. The impactor velocity and mass parameters of these cases are provided below in Table 4.6, along with the resulting kinetic energy of the impactor $E_k$. Also provided are values of the impactor's elastic modulus $E_{sol}$ which, unlike in the parametric study, was not constant across all simulations, but was varied according to the purpose of the experiments.

| Case Number | $v_{sol}$ (m/s) | $m_{sol}$ (kg) | $E_{sol}$ (GPa) | $E_k$ (J) |
|---|---|---|---|---|
| 2.13 | 10.0 | 0.0222 | 0.80 | 1.11 |
| 2.14 | 100.0 | 0.0222 | 0.80 | 110.80 |
| 2.15 | 3.8 | 0.0222 | 13.79 | 0.16 |
| 2.16 | 3.8 | 0.0222 | 30.00 | 0.16 |
| 2.17 | 3.8 | 0.0222 | 100.00 | 0.16 |
| 2.18 | 5.4 | 100.0000 | 30.00 | 1458.00 |
| 2.19 | 7.0 | 0.3200 | 30.00 | 7.84 |

*Table 4.6: Variables of the Stage 2 high energy impacts.*

## 4.4 High energy impacts – Results and comparisons

### *4.4.1 Impact characteristics*

The resulting contact duration $T_p$ and peak impact force $F_{max}$ for each high energy impact was measured using T/HIS. In these cases it was not attempted to obtain a constant peak impact force across the simulations; as such, the recorded $F_{max}$ values varied over a wide range, from 1.565 to 45.519 kN. Contact durations ranging from 0.145 to 1.393 ms were observed, the majority of which were within a tight bracket close to 0.160 ms. As previously, these recorded impact characteristics were compared to values predicted using Young's (2003) analytical model of collision between a spherical impactor and a fluid-filled spherical head [Equations 1.12 and 1.14], applying the same adaptations as discussed in Section 4.2.1. The contact durations and peak impact forces recorded in these finite element simulations, and corresponding analytically predicted values, are presented below in Table 4.7.

| Case Number | FE $T_p$ (ms) | FE $F_{max}$ (kN) | Analytical $T_p$ (ms) | Analytical $F_{max}$ (kN) | Analytical $T_p$ error (%) | Analytical $F_{max}$ error (%) |
|---|---|---|---|---|---|---|
| 2.13 | 0.245 | 3.080 | 0.250 | 3.019 | 1.90 | -1.97 |
| 2.14 | 0.160 | 45.519 | 0.183 | 40.359 | 14.20 | -11.34 |
| 2.15 | 0.169 | 1.565 | 0.162 | 1.711 | -3.83 | 9.34 |
| 2.16 | 0.154 | 1.673 | 0.153 | 1.799 | -0.72 | 7.52 |
| 2.17 | 0.145 | 1.742 | 0.147 | 1.862 | 1.46 | 6.88 |
| 2.18 | 1.393 | 35.394 | 1.465 | 33.671 | 5.18 | -4.87 |
| 2.19 | 0.485 | 12.377 | 0.488 | 13.427 | 0.57 | 8.48 |

*Table 4.7: Resulting contact durations and peak impact forces in the Stage 2 high energy impacts. "FE" denotes values measured in the finite element simulations. "Analytical" denotes values predicted by Young's (2003) analytical model.*

Once again it can be seen that, in terms of these impact characteristics, the analytical model's predictions are faithful to the simulations despite being based on a simple spherical geometry. However, the analytical predictions deviate more strongly from the experimental values in cases with a large peak impact force: analytical values of both $T_p$ and $F_{max}$ were least accurate for Case 2.14, which was subject to the greatest peak force, resulting in absolute errors of 14.20% and 11.34% respectively.

### *4.4.2 Pressure response*

#### *4.4.2.1 Cases 2.10, 2.13, and 2.14*

The additional impact Cases 2.13 and 2.14, were identical to the short duration impact Case 2.10 from the Stage 2 parametric study, except that here the impactor's initial velocity was raised from the original value (3.8 m/s), first to 10.0 m/s, and then to 100.0 m/s. By increasing the impactor's velocity while keeping its mass and material properties constant throughout these cases, the intention was to produce three impacts with similar contact durations, but with peak impact forces varying over a wide range. These impacts could then be compared in order to verify whether the system was responding in a linear fashion. This was an important consideration, since collapsing the results in order to remove the influence of variations in peak impact force across a range of simulated impacts, as has been done for each stage of this study, would be meaningless if the system reacted in a non-linear fashion to changes in this variable.

The intracranial pressure-time histories recorded at the coup during Cases 2.10, 2.13, and 2.14 are presented below in Figure 4.11; to facilitate the comparison of these, the pressures

were normalised over the magnitude of the peak impact force $F_{max}$ (0.974, 3.080, and 45.519 kN respectively) which generated each of these disturbances. All the materials in the Stage 2 model were linear, and so the only non-linearities which could be introduced were geometric. The system is within the geometrically linear range if a given change in the input (in this case, the peak impact force $F_{max}$), produces a proportional change in the response; the response of concern here being the intracranial pressure. Were the system to begin responding in a non-linear fashion as the peak impact force rises above some critical value, a noticeably different intracranial pressure response would be expected, with, crucially, the magnitudes of these pressures no longer adhering to this simple linearly proportional relationship with the impact force $F_{max}$. However, it can be seen that the three curves depicted in Figure 4.11 have similar shape and similar peak values. Therefore, while an upper limit has not been determined, it appears that for all impacts with peak impact force up to approximately 45 kN, the Stage 2 head model responds in a linear fashion. None of the simulated impacts in any stage of this investigation exceeded this impact force.

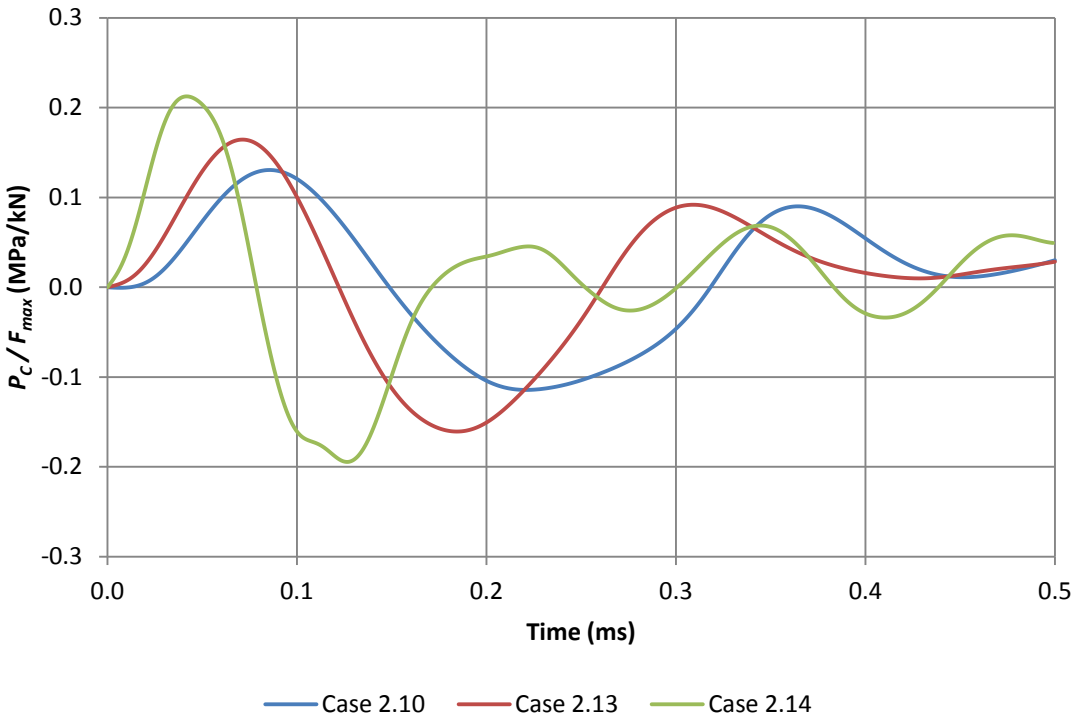


*Figure 4.11: Cases 2.10, 2.13, and 2.14: local pressure-time histories recorded in the brain at the coup, normalised over $F_{max}$.*

Despite the fact that Cases 2.10, 2.13, and 2.14, have significantly different impact forces (roughly a factor of 47 difference across the range), normalising the intracranial pressures in this manner yielded curves which are much alike. While, as mentioned, this points

towards linear behaviour of the system, one nevertheless finds that these normalised transients are not of exactly the same magnitude, but have somewhat different maxima and minima. This is due to the fact that, whilst the magnitudes of the peak intracranial pressures in a perfectly quasi-static regime are dependent on $F_{max}$ (see Equation 1.5), the Stage 1 and Stage 2 parametric studies suggest that, for the dynamic pressure response, the magnitudes of these peak pressures are not only proportional to $F_{max}$, but also dependent on the contact duration $T_p$. In this way, the small differences in contact duration between these cases (the longest and shortest duration impacts differing by less than a factor of 2), has resulted in this comparatively small variation in the peak values of the curves of normalised pressure visible in Figure 4.11.

#### *4.4.2.2 Cases 2.10, 2.15, 2.16, and 2.17*

Once again, Cases 2.15, 2.16, and 2.17 were identical to impact Case 2.10 except for one parameter. Previous impacts in the parametric study utilised a low impactor elastic modulus (0.80 GPa), and therefore the skull (with a modulus of 13.79 GPa) was considerably stiffer than the impactor. In reality the hollow skull is a deformable body, and the majority of objects with which a dangerous collision could be expected are solid, with similar or higher moduli, and so are effectively rigid in comparison. The aim of these three additional cases was to determine a value of the impactor's elastic modulus $E_{sol}$ such that it becomes effectively rigid compared to the skull, to enable further high energy impacts more closely representing real world head injury scenarios. In Cases 2.15 to 2.17 the impactor's modulus was raised, first to 13.79 GPa (equal to that of the skull), then to 30.00 GPa, and lastly to 100.00 GPa, while retaining a constant velocity and mass. These impacts had similar contact durations, the largest of which was produced by Case 2.10 ($T_p$ = 0.295 ms): therefore, these impacts all had durations well beneath the period of the skull's longitudinal n=2 mode $T_\Omega$ and, as expected, resulted in similar dynamic intracranial pressure responses.

By examining Equation 4.1 it can be seen that in Young's (2003) analytical model of head impact, and presumably in the finite element experiments, the peak impact force transferred by the impactor is dependent on $E^*$, the relative elastic modulus of the two colliding bodies [Equation 1.10]. Therefore, the peak impact force could be used as an indirect measure of $E^*$, and monitoring this force across these four impacts (Cases 2.10 to 2.17) would allow a suitable $E_{sol}$ value to be selected. A plot of the peak impact force resulting from these four impacts against the impactor's elastic modulus is presented below in Figure 4.12. It can be seen that the $F_{max}$ relationship converges at around $E_{sol}$ = 30.00 GPa, i.e. it does not increase significantly beyond this point. This indicates that at this value

the impactor was effectively rigid compared to the skull, and a modulus of 30.00 GPa was selected for the impactor in the following realistic case studies, impact Cases 2.18 and 2.19.

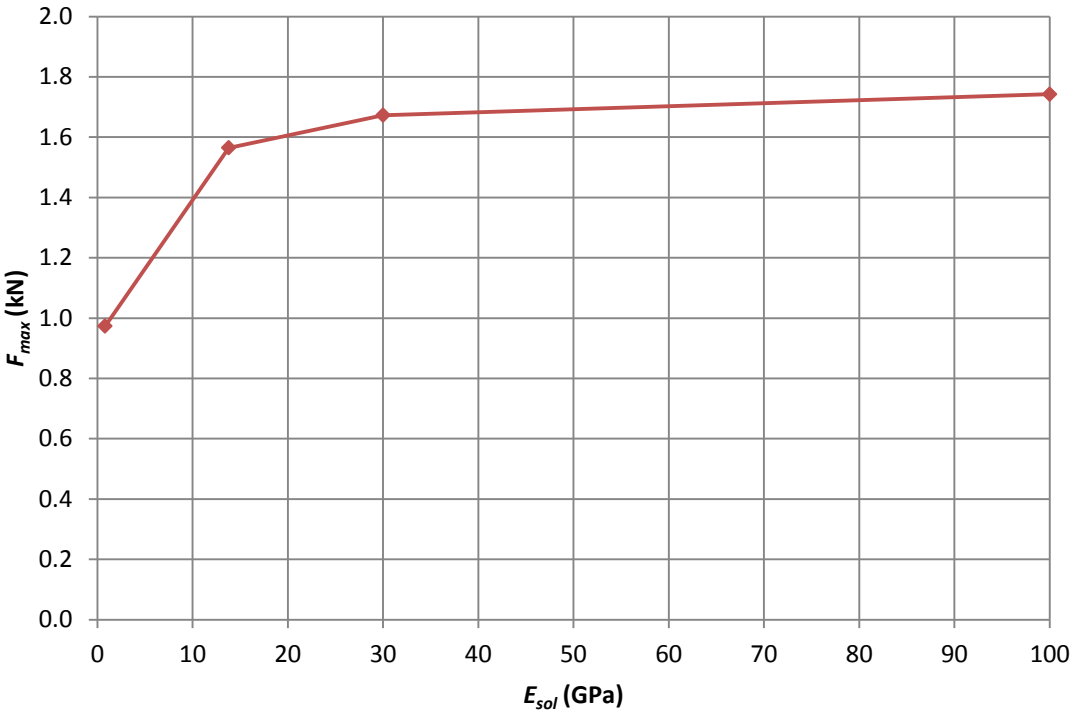


*Figure 4.12: Cases 2.10, 2.15, 2.16, and 2.17: Peak impact force vs. impactor's elastic modulus.*

#### *4.4.2.3 Case 2.18: Fall hitting the ground*

The aim of this high energy impact was to investigate the intracranial response to an impact with more realistic properties, and more damage potential, than those done previously; specifically it was an attempt to simulate the loading that would be achieved were a person to fall and hit the rear of their head against a rigid surface, such as the ground or a wall. While at first they seem like different cases, a moving impactor striking a stationary head, and a moving head striking a stationary impactor, are essentially the same scenario differing only by the frame of reference from which it is analysed.

An immobile object such as the ground or a wall has in effect an infinite mass compared to the head. The impactor was assigned an elastic modulus of 30.00 GPa and a mass of 100 kg, which was assumed to make it both effectively rigid and of infinite mass compared to the Stage 2 head model (which had a total mass of 2.917 kg). An impactor velocity of 5.4 m/s was used (equal to that used in the dynamic low energy Case 2.11): this is in essence the mutual velocity of approach, i.e. the velocity of the head immediately prior to impact in this hypothetical fall. Simple Newtonian models can be used to predict the height

of an unimpeded fall that corresponds to this ultimate velocity (Cory, Jones, & James, 2001); this is achieved surprisingly well as air resistance does not play a significant role in the reduction of fall velocity from below a height of approximately 15 m (Snyder, 1963). A free-fall from 1.49 m would result in an impact velocity of 5.4 m/s. This was deemed an interesting case study, since this distance corresponds roughly to the median height of children 12-13 years of age (Tanner et al., 1966), and so may be relevant to paediatric head injury investigation and forensics. The same impactor model was used as in previous Stage 1 and Stage 2 impacts: this had a radius of curvature $R_{sol}$ of 40 mm, but, as previously discussed, this parameter ($R_{sol}$) has a minor effect on the impact force experienced by the head (see Section 2.11). Furthermore, ground surfaces may be pebbled or uneven, resulting in a non-flat contact surface. Depending on the angle of the subject's body at impact, the impact force acting on the head may be influenced by the mass of the person's body. In this simulation the head is unconstrained, and is therefore treated as decoupled, i.e. negligible additional forces are imparted by the body.

This impact had a contact duration of 1.393 ms, which is greater than the critical impact duration predicted by twice $T_{\Omega}$ (0.874 ms), and therefore a quasi-static response was expected. Examining the coup and contrecoup pressure-time histories given in Figure 4.13 below, it can be seen that, in general, the response represents a typical quasi-static impact: the pressures are roughly symmetrical about the horizontal axis, rise and fall over $T_p$, and reach values of approximately equal magnitude and opposite sign at roughly half way through the impact ($t = T_p/2$). The pressure-time histories and contour plots provided in Figure 4.13 also reveal short transients of high positive pressure localised at the coup: these small peaks occur at the beginning and end of the contact duration. However, for the majority of the impact (see contour plot II), the system behaves essentially quasi-statically.

The simulation provides an insight into the intracranial pressure response that could be expected in a generalised fall scenario: it was shown that a quasi-static response was generated in this context, and likely would be in most medium to long duration impacts such as falls. While approximating a fall (involving a moving head) instead with a collision involving an initially stationary head was deemed sufficiently accurate for this generalised investigation, the above setup is not suitable for obtaining any quantitative data in terms of forces or pressures that could be expected from a real world fall. To be better suited to forensic applications, the finite element setup would have to account for the variations in properties of biological materials with age (particularly the stiffness of the skull), include a

neck constraint to introduce angular acceleration, and include a realistic ground surface with relevant material properties (Cory et al., 2001; Cory & Jones, 2006).

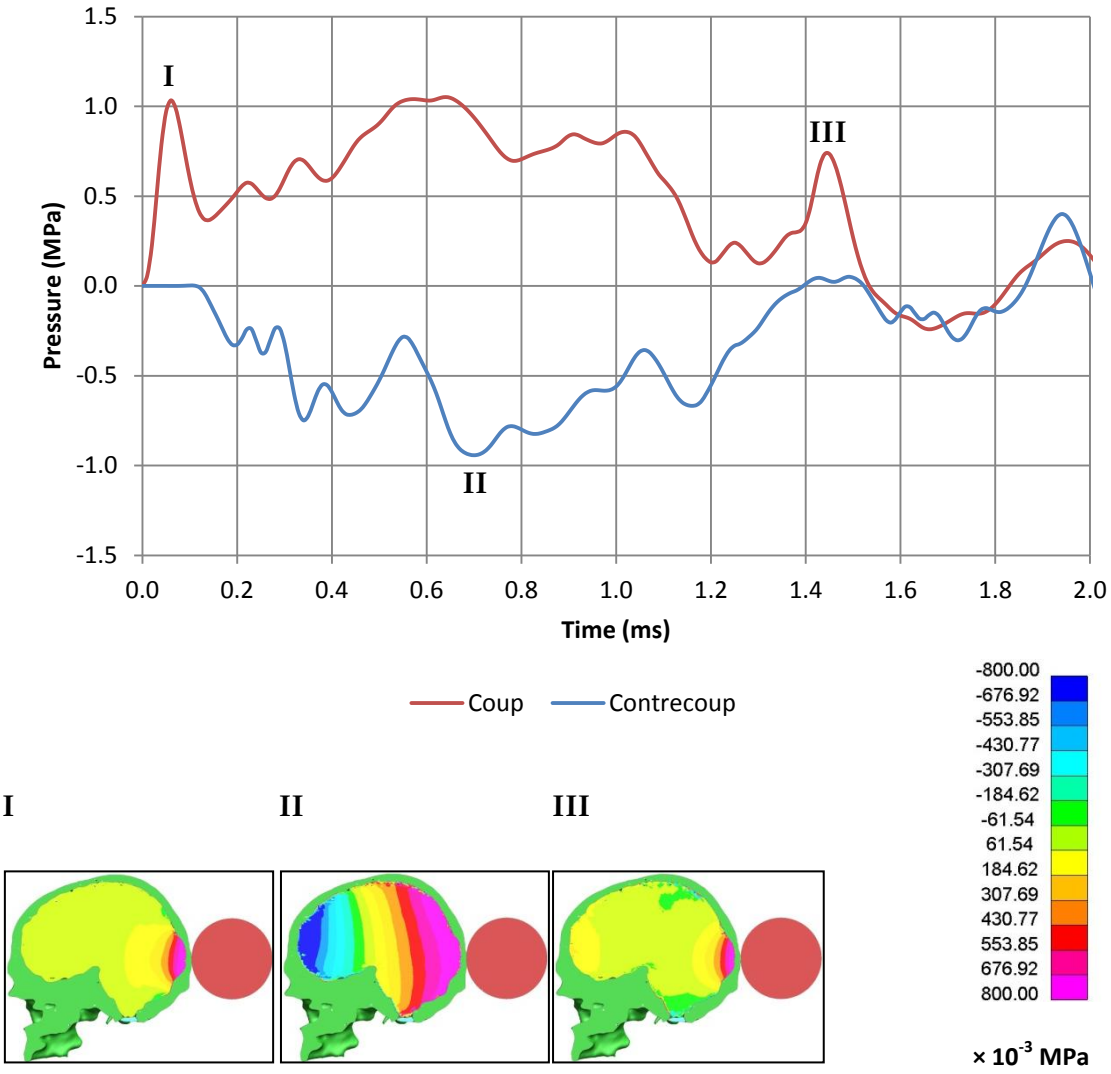


*Figure 4.13: Case 2.18, Top: local pressure-time histories recorded in the brain at the coup and contrecoup. Bottom: contour plots of pressure in the brain at I (t = 0.060 ms), II (t = 0.720 ms), and III (t = 1.440 ms). The solid green, light blue, and red regions represent the realistic skull, foramen magnum, and impactor respectively.*

#### *4.4.2.4 Case 2.19: Rigid light projectile*

As opposed to a collision with a rigid heavy impactor, as in Case 2.18, in the final high energy impact the aim was to study the pressure response resulting from impact by a projectile that was rigid with low mass. The impactor in Case 2.19 had an elastic modulus of 30.00 GPa, a mass of 0.3200 kg (equal to that of Case 2.3), and an initial velocity of 7.0 m/s (equal to the highest velocity in the low energy parametric study, used in Case 2.12). Therefore, the impactor was considered effectively rigid compared to the skull, and,

while lighter than the head model, gave in combination with its velocity a significantly higher kinetic energy than any of the parametric study impacts (approximately 50 times greater). This produced an impact with high peak force (12.377 kN) and low contact duration (0.485 ms) as could be expected from insult to the head by a stone, sports equipment, or other small projectile.

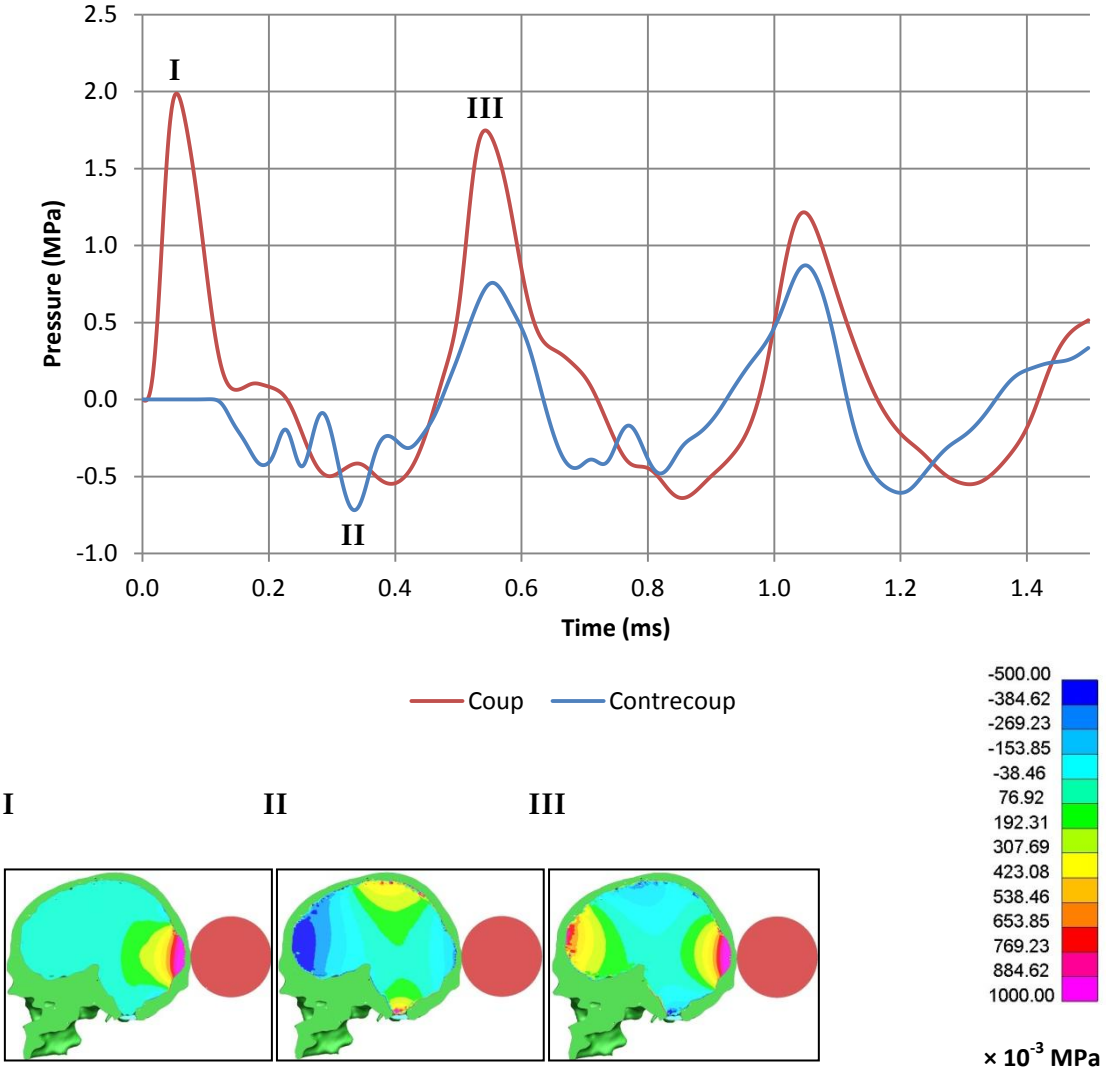


*Figure 4.14: Case 2.19, Top: local pressure-time histories recorded in the brain at the coup and contrecoup. Bottom: contour plots of pressure in the brain at I (t = 0.060 ms), II (t = 0.340 ms), and III (t = 0.540 ms). The solid green, light blue, and red regions represent the realistic skull, foramen magnum, and impactor respectively.*

Coup and contrecoup pressure-time histories and contour plots captured in Case 2.19 are presented above in Figure 4.14. The contact duration was close to the period of the skull's longitudinal n=2 mode $T_{\Omega}$ (0.437 ms), and like Cases 2.5 to 2.8 in the parametric study where this was also true, it can be seen that the coup and contrecoup pressure-time

histories oscillate in sync with each other. The peak recorded positive pressure at the coup and negative pressure at the contrecoup were compared to the peak intracranial pressures expected from an ideal quasi-static response ($P_{C\ quasi}$ and $P_{CC\ quasi}$), predicted using Equation 1.5. These peak recorded pressures at the coup and contrecoup were found to differ from $P_{C\ quasi}$ and $P_{CC\ quasi}$ by factors of 6.462 and 2.141 respectively. An amount of pressure "magnification" was expected based on the results of previous Stage 2 impacts with contact durations below twice $T_{\Omega}$ (0.874 ms), but here the positive pressure transients localised beneath the coup were magnified substantially more than those at the contrecoup. This is illustrated by the large coup positive pressure transients visible in Figure 4.14. These were likely a consequence of the large peak impact force $F_{max}$, which, while this impact was shown to still be in the geometrically linear range, was the third largest of all of the Stage 2 impacts and significantly larger than any of the impact forces experienced by the low energy cases.

### *4.4.3 Collapsing the results*

The results of the Stage 2 high energy impacts were normalised, as before, in order to better illustrate trends in the head model's response. Table 4.8, below, lists the analytically predicted peak positive pressures at the coup (at both sampling locations: pressure "over a patch" and "at a point"), and peak negative pressures at the contrecoup, expected from an ideal quasi-static response [Equation 1.5]. In Table 4.9, the peak positive and negative intracranial pressures recorded during the finite element experiments at these coup and contrecoup locations are provided. In the two cases with the highest peak impact force, Cases 2.14 and 2.18, it was found that the pressure-time histories captured at the small sampling point located close to the brain-skull boundary (coup pressures "at a point") were muddied by large amounts of numerical noise, so these peak pressure values were deemed unrepresentative and were ignored. The recorded coup and contrecoup peak pressures were normalised over the analytically predicted quasi-static peak pressures, providing a measure of pressure "magnification" compared to the quasi-static response. Also, the impact durations were normalised over the period of the longitudinal n=2 mode of the system. These non-dimensional results are presented in Table 4.10.

| Case Number | Analytical | | |
|---|---|---|---|
| | $P_{C\ quasi}$ (MPa) | $P_{C\ point\ quasi}$ (MPa) | $P_{CC\ quasi}$ (MPa) |
| 2.13 | 7.679e-2 | 8.030e-2 | -8.415e-2 |
| 2.14 | 1.118 | N/A | -1.244 |
| 2.15 | 3.901e-2 | 4.080e-2 | -4.276e-2 |
| 2.16 | 4.171e-2 | 4.361e-2 | -4.571e-2 |
| 2.17 | 4.344e-2 | 4.543e-2 | -4.760e-2 |
| 2.18 | 8.690e-1 | N/A | -9.671e-1 |
| 2.19 | 3.086e-1 | 3.227e-1 | -3.382e-1 |

*Table 4.8: Analytically predicted quasi-static peak pressures for the Stage 2 high energy impacts.*

| Case Number | FE: Coup | | | | FE: Contrecoup | |
|---|---|---|---|---|---|---|
| | $P_{C\ positive}$ (MPa) | $P_{C\ negative}$ (MPa) | $P_{C\ point\ positive}$ (MPa) | $P_{C\ point\ negative}$ (MPa) | $P_{CC\ positive}$ (MPa) | $P_{CC\ negative}$ (MPa) |
| 2.13 | 7.700e-1 | -7.810e-1 | 1.547 | -1.686 | 2.840e-1 | -4.640e-1 |
| 2.14 | 9.598 | -8.959 | N/A | N/A | 4.332 | -7.113 |
| 2.15 | 6.620e-1 | -6.780e-1 | 1.410 | -1.446 | 1.680e-1 | -2.720e-1 |
| 2.16 | 7.740e-1 | -7.640e-1 | 1.650 | -1.626 | 1.720e-1 | -2.850e-1 |
| 2.17 | 8.630e-1 | -8.260e-1 | 1.856 | -1.733 | 1.725e-1 | -2.890e-1 |
| 2.18 | 1.072 | -2.666e-1 | N/A | N/A | 4.030e-1 | -9.440e-1 |
| 2.19 | 1.994 | -6.417e-1 | 3.886 | -1.401 | 8.737e-1 | -7.240e-1 |

*Table 4.9: The peak positive and negative pressure values recorded at both coup sampling locations, and at the contrecoup, during the Stage 2 high energy impacts.*

| Case Number | Normalised | | | | | | |
|---|---|---|---|---|---|---|---|
| | $P_{C\ positive} / P_{C\ quasi}$ | $P_{C\ negative} / P_{C\ quasi}$ | $P_{C\ point\ positive} / P_{C\ point\ quasi}$ | $P_{C\ point\ negative} / P_{C\ point\ quasi}$ | $P_{CC\ positive} / P_{CC\ quasi}$ | $P_{CC\ negative} / P_{CC\ quasi}$ | $T_p / T_\Omega$ |
| 2.13 | 10.027 | -10.171 | 19.266 | -20.997 | 3.375 | -5.514 | 0.560 |
| 2.14 | 8.588 | -8.016 | N/A | N/A | 3.483 | -5.719 | 0.367 |
| 2.15 | 16.968 | -17.378 | 34.561 | -35.443 | 3.929 | -6.362 | 0.386 |
| 2.16 | 18.558 | -18.318 | 37.832 | -37.282 | 3.763 | -6.235 | 0.353 |
| 2.17 | 19.866 | -19.015 | 40.858 | -38.151 | 3.624 | -6.071 | 0.332 |
| 2.18 | 1.234 | -0.307 | N/A | N/A | 0.417 | -0.976 | 3.185 |
| 2.19 | 6.462 | -2.079 | 12.042 | -4.341 | 2.583 | -2.141 | 1.109 |

*Table 4.10: Non-dimensional peak positive and negative pressures, and non-dimensional impact durations, of the Stage 2 high energy impacts.*

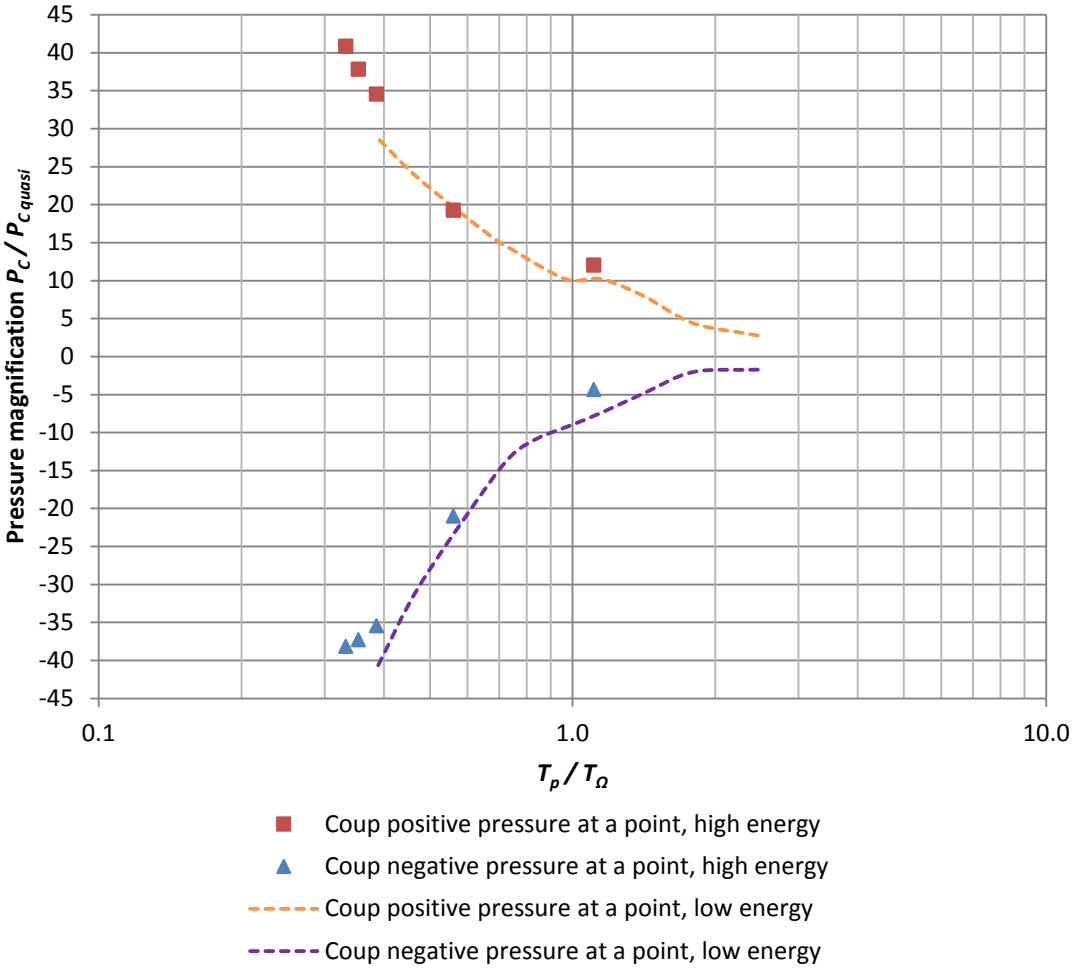


*Figure 4.15: Stage 2 high energy impacts, normalised coup peak pressures recorded "at a point" against $T_p$ / $T_\Omega$. Normalised coup "pressure at a point" values from the Stage 2 low energy parametric study are provided for comparison.*

The non-dimensionalised results at the coup were plotted in Figure 4.15, and those at the contrecoup were plotted in Figure 4.16; in both figures the collapsed results of the Stage 2 low energy parametric study were also shown for comparison. At the coup, the normalised pressures captured at both sampling locations ("over a patch" and "at a point") during the high energy impacts closely followed the trends observed during the Stage 2 low energy impacts at each of these locations respectively. In Figure 4.15, the normalised positive and negative coup pressures resulting from the high energy impact cases are plotted alongside those from the Stage 2 low energy parametric study; for brevity, here only the non-dimensional pressures captured "at a point" are provided. The high energy results are plotted as individual data points, rather than as continuous curves, due to the small number of these cases. In agreement with the low energy parametric study, in Figure 4.15 it can be seen that as the duration of the impacts was reduced, the magnitudes of both positive and negative intracranial pressures rose. The greatest degree of pressure magnification in the

Stage 2 high energy impacts occurred in the peak positive pressure at the coup during Case 2.17, in which pressure recorded "over a patch" was almost 20 (19.866) times greater, and pressure recorded "at a point" was over 40 (40.858) times greater, than the quasi-static pressures predicted analytically. By contrast, the greatest pressure magnification in the Stage 2 low energy study occurred in the peak *negative* pressure at the coup during Case 2.12, where pressure recorded "over a patch" was nearly 20 (19.756) times greater, and pressure recorded "at a point" was over 40 (40.981) times greater, than the analytical quasi-static predictions. Indeed, in Figure 4.15, it can be seen that the short duration high energy impacts consistently resulted in greater peak positive pressures, but smaller peak negative pressures, than the low energy impacts. It appears that the larger peak impact forces in these high energy cases produce pressures which are consistently more positive than those with lower impact forces (as discussed briefly in Section 4.4.2.4), which would be consistent with larger amounts of local skull deflection at the coup.

The contrecoup pressures (Figure 4.16) on the other hand, follow the trends observed during the Stage 2 low energy impacts almost exactly. Similar to the low energy parametric study, the peak pressures at the contrecoup exhibit drastically less pressure magnification than at the coup. Unlike the parametric study however, clusters of data points are visible, because the high energy impact cases were not designed to generate impacts distributed over a wide range of contact durations. In Figures 4.15 and 4.16, it is visible that the critical impact duration, which determines the transition from a quasi-static to a dynamic response, appears to remain roughly constant for both the low and high energy impacts, at a value of $T_p / T_\Omega = 2$.

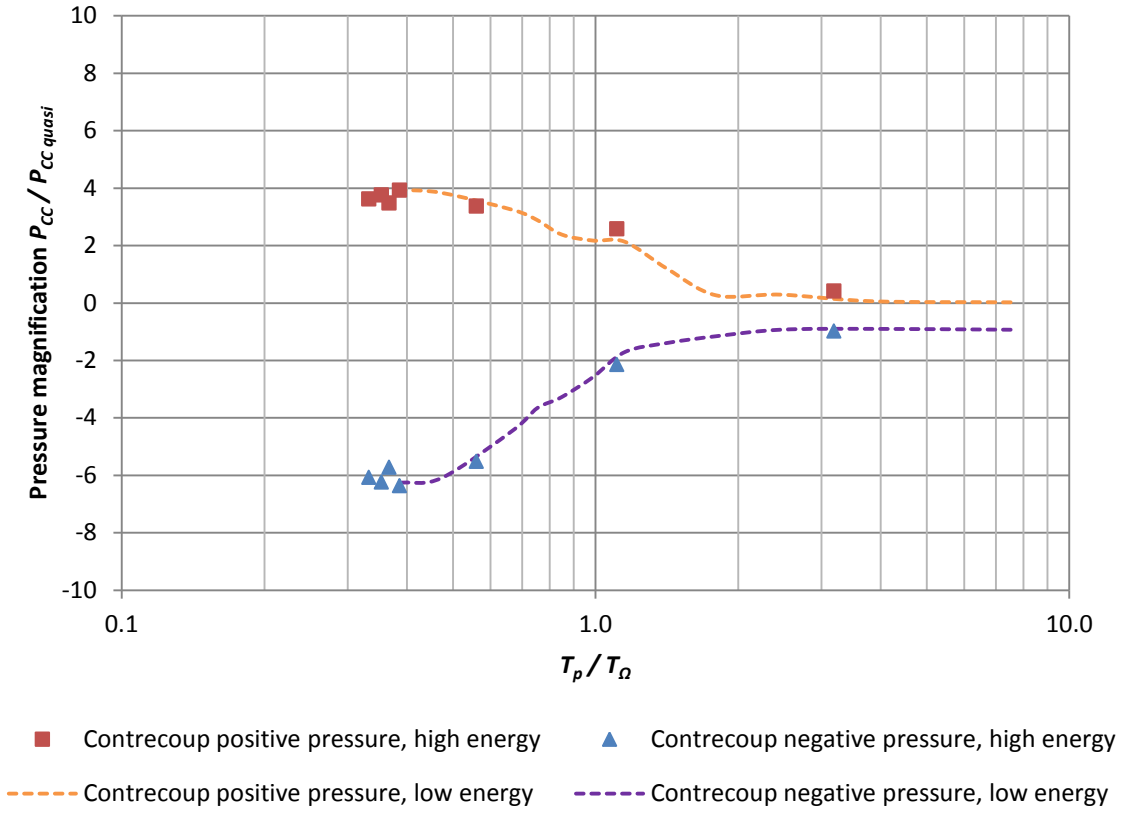


*Figure 4.16: Stage 2 high energy impacts, normalised peak pressures against $T_p$ / $T_\Omega$ at the contrecoup. Normalised contrecoup pressures from the Stage 2 low energy parametric study are provided for comparison.*

Lastly, utilising a guideline cavitation threshold of -1 atm (-1.013e-1 MPa), the peak negative pressure values presented in Table 4.9 reveal that all of the high energy cases may be in danger of sustaining cavitation in the cranial fluids at both the coup and contrecoup, were these actual head injury scenarios.

Cory, C., & Jones, M. D. (2006). Development of a simulation system for performing in situ surface tests to assess the potential severity of head impacts from alleged childhood short falls. *Forensic Science International*, *163*(1-2), 102–14.

Cory, C., Jones, M. D., & James, D. (2001). The potential and limitations of utilising head impact injury models to assess the likelihood of significant head injury in infants after a fall. *Forensic Science International*, *123*, 89–106.

Snyder, R. G. (1963). Human survivability of extreme impacts in free-fall. *34th Annual Aerospace Medical Association*. Los Angeles.

Tanner, J. M., Whitehouse, R. H., & Takaishi, M. (1966). Standards from Birth to Maturity for Height, Weight, Height Velocity, and Weight Velocity: British Children, 1965. *Archives of Disease in Childhood*, 454–471.

Thomas, L. M., Roberts, V. L., & Gurdjian, E. S. (1967). Impact-induced pressure gradients along three orthogonal axes in the human skull. *Journal of Neurosurgery*, *26*, 316–321.

Young, P. G. (2002). A parametric study on the axisymmetric modes of vibration of multi-layered spherical shells with liquid cores of relevance to head impact modelling. *Journal of Sound and Vibration*, *256*(4), 665–680.

Young, P. G. (2003). An analytical model to predict the response of fluid-filled shells to impact - a model for blunt head impacts. *Journal of Sound and Vibration*, *267*(5), 1107–1126.

Young, P. G., & Morfey, C. L. (1998). Intracranial pressure transients caused by head impacts. *International Research Council on the Biomechanics of Impact (IRCOBI) Conference Proceedings* (pp. 391–403). Göteborg, Sweden.

# Chapter 5 – Biofidelic head model – Results

## 5.1 Model validation

At the outset of the Stage 3 investigation, the validity of the completed biofidelic head model was explored by simulating experiment 37 from Nahum et al's (1977) cadaveric impact tests. In Nahum et al's experiment, stationary unembalmed cadaver subjects were subjected to head impacts by rigid masses of constant velocity, and the pressure-time histories were monitored at various locations in the head. The cadavers' cranial vascular and CSF networks were repressurised to *in vivo* levels. The cadavers were seated, and their heads rotated forward such that the Frankfurt anatomical plane (the horizontal plane of the skull) was inclined at 45°. The impacts were delivered to the frontal bone, on the mid-sagittal plane, in the anterior to posterior direction. Of the eight individual cadaver experiments presented in Nahum et al's paper, experiment 37 is frequently employed as a benchmark because it corresponds to the youngest male cadaver subject (42 years of age). The impactor used in Nahum et al's experiment was a steel cylinder of mass 5.59 kg and velocity of 9.4 m/s. Padding materials were introduced between the head and impactor in order to lengthen the duration of the impact.

To ensure accurate reproduction of the experimental loading, in this study the force-time history of the impact recorded in Nahum et al's experiment 37 was applied directly to the Stage 3 finite element model. The load was distributed evenly over a circular area of 1556 $mm^2$ on the scalp above the frontal bone of the head model, and was directed 45° to the horizontal, which is equal to the method used by Chen & Ostoja-Starzewski (2010) in their recreation of Nahum et al's experiment. The force-time history applied is presented below in Figure 5.1, along with a diagram illustrating the location and direction of the distributed load. For this simulation only, the small patch of realistic, but computationally expensive, non-linear scalp was moved from the rear of the head model to sit beneath the new impact location over the frontal bone.

The resulting pressure-time histories were captured at several locations including beneath the impact site on the frontal bone (i.e. the coup), and in the posterior fossa region (between the foramen magnum and the tentorium cerebelli) which was effectively the contrecoup in this case. These coup and contrecoup pressure-time histories for both Nahum et al's cadaveric experiment and the Stage 3 simulation are presented in Figure 5.2.

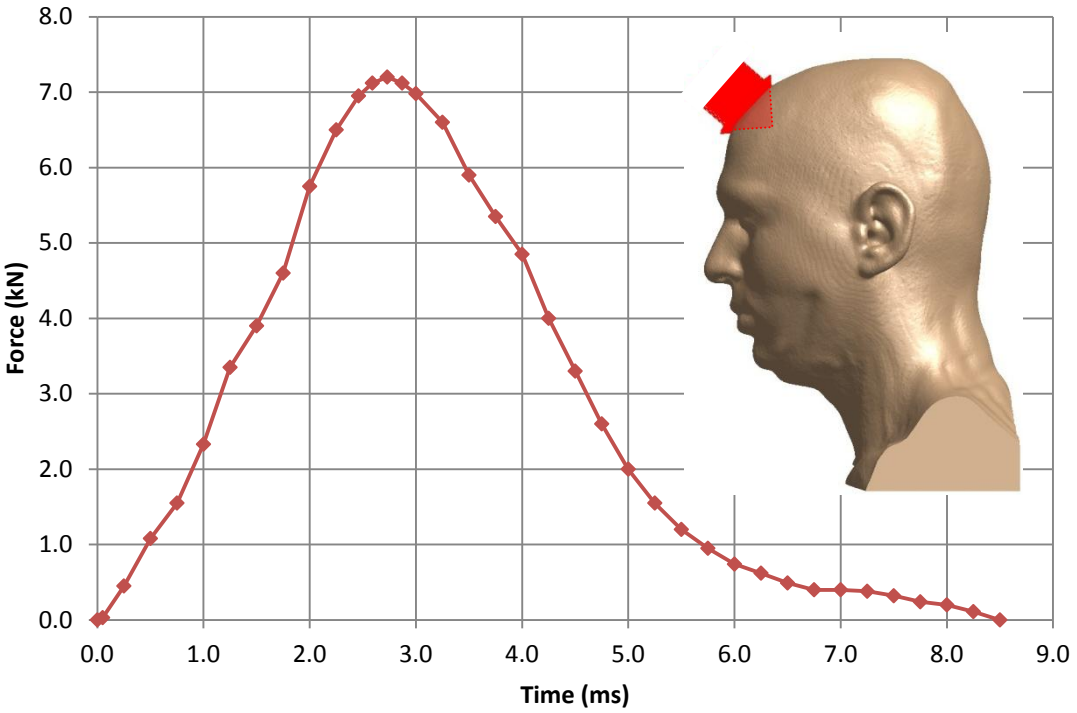


*Figure 5.1: The force-time history, originally from Nahum et al's (1977) cadaver impact experiment 37, applied to the Stage 3 biofidelic head model for validation purposes. Inset diagram: arrow represents the location and direction of the applied load, with the arrow width (approximately 44.5 mm) indicating the diameter of the circular load area.*

Some high frequency noise was evident in the pressure-time histories obtained from the finite element simulation. This was inconsistent with the clean results produced by all other Stage 3 impacts, and was believed to be caused by high frequency content inherent in the load curve due to sudden gradient changes introduced at the discrete data points (visible in Figure 5.1). To remove this noise, in this case only, the pressure-time histories obtained from the biofidelic head model were filtered in T/HIS in a similar manner to that used in Stage 1. In this case a 1$^{st}$ order Butterworth low-pass filter was used, with cut-off at 0.3 kHz.

Examining Figure 5.2, below, it can be seen that the coup pressures recorded in the finite element model show excellent agreement with those from the cadaveric experiment. The large positive pressure transient generated at the coup shared both a similar duration and peak value as Nahum et al's measurements. The pressure-time history recorded at the contrecoup also agreed well with the cadaveric experiment's pressures in terms of curve shape, but for the majority of the impact the simulated pressures were approximately 0.03 to 0.05 MPa larger than the values in Nahum et al's experiment. Both the coup and

contrecoup intracranial pressures predicted by the finite element model deviate more strongly from the experimental values after roughly 4.5 ms, i.e. after the majority of the impact force had been transmitted. From this point onwards, the coup pressures predicted by the finite element model decreased below the cadaveric coup pressures, experiencing negative values from 5.14 ms onwards, whereas the benchmark pressures remained positive. The predicted contrecoup pressures however, in this latter half of the impact, rose in conjunction with the cadaveric pressure-time history, but as mentioned above, overestimated the response.

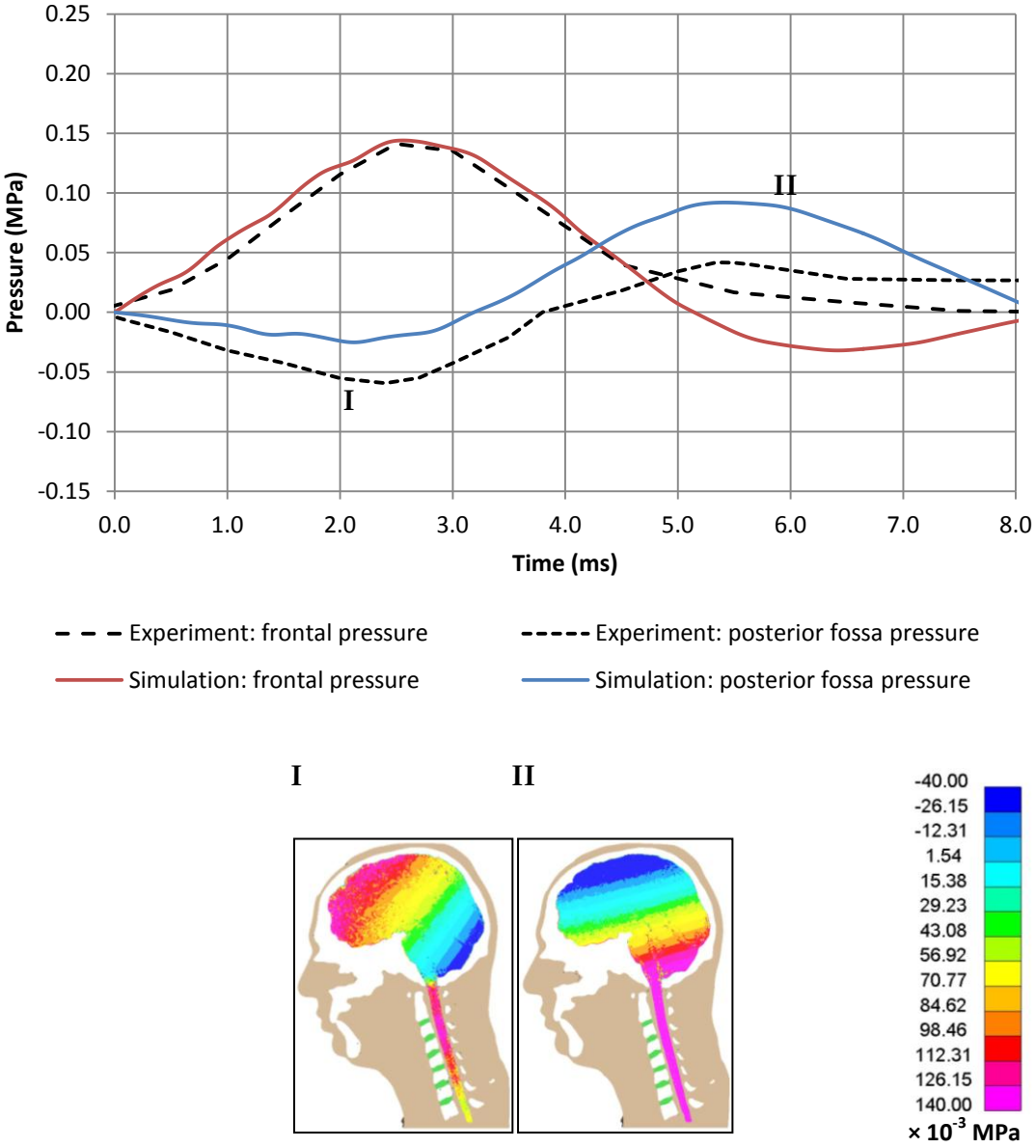


*Figure 5.2: Top: coup (frontal) and contrecoup (posterior fossa) pressure-time histories resulting from the biofidelic head model simulation and from cadaveric experiment number 37 in (Nahum et al., 1977). Bottom: contour plots of pressure in the cranial contents and spinal cord at I (t = 2.080 ms), and II (t = 5.980 ms).*

These differences in pressure response (particularly beyond 4.5 ms) between the finite element model's predictions and Nahum et al's physical measurements were hypothesised to arise mainly from differences in neck-elasticity, affecting the constraints that the head experiences in these two cases. It is well known that the properties of biological materials are changed *ex vivo*, and are also affected by the storage of the cadavers and time since death (Meulman, 1996); hence a considerable reduction in elasticity could be expected. Furthermore, in the finite element model there is an absence of muscles and ligaments, and so the neck's behaviour is dominated by the "flesh" component which was assigned linear elastic behaviour. It is believed that the differences in pressure-response occurring in the latter half of the impact were due to the vertical component of the applied force compressing the elastic neck downwards. Beyond 4.5 ms the input force diminishes, and the vertical force of the compressed neck accelerates the skull upwards, i.e. the direction of the vertical acceleration of the cranium becomes reversed. Examining contour plots I and II in Figure 5.2, linear pressure gradients (or "banding" patterns) can be seen at both instances; in the first image the pressure gradient was induced by the acceleration of the skull due to the applied load, but in the second image (corresponding to 5.980 ms after incidence) the pressure gradient is reversed indicating a reversed acceleration of the skull. The degree to which this elastic behaviour of the neck is inaccurate is unknown since it has here been compared only to the response of a cadaver model, which will itself respond differently from an *in vivo* case. The influence of the finite element model's elastic neck nevertheless negligibly affects the intracranial pressures during the initial stages of impact, and is unlikely to have any discernible effect during short duration impacts in which typically no significant acceleration of the skull occurs. The Stage 3 biofidelic head model was considered to have predicted well the intracranial pressures reported by Nahum et al. (1977), and was deemed a valid tool for the determination of intracranial pressure effects which could be expected from realistic impact scenarios.

## 5.2 Case studies

The computational resources required per simulation rendered a full parametric study of the Stage 3 biofidelic head model impractical, instead three case studies were performed: impact by a golf ball, by a heavy spherical mass, and by a light spherical mass.

The golf ball impactor geometry was generated manually in the CAD software package SolidWorks (Dassault Systèmes S.A.) and was meshed using the +FE software module in ScanIP. The geometry was based on a sphere with radius $R_{sol}$ equal to 21.39 mm, which is

the size of a standard golf ball (Maruoka et al., 2001). The meshing was performed in the same manner as the other models in this study, using the mixed hex/tet mesh generation algorithm. The entire golf ball model was meshed with the same high element density as had been applied to the head's impact site (i.e. using elements with characteristic edge length of 0.55 mm), and a decimation algorithm was used to merge hex elements away from the golf ball's exterior surface (in groups of 2×2×2) so reducing the total element count. This resulted in an impactor model with just under 359k elements in total, which had good element qualities (the mean in-out aspect ratio was 0.765, and no elements had an aspect ratio worse than 0.1). The impactor model was homogeneous and isotropic, and was assigned an elastic modulus $E_{sol}$ of 0.1 GPa, which has been shown to perform well as a homogeneous approximation of the stiffness of a golf ball's core (Roberts et al., 2001). The golf ball model's density $\rho_{sol}$ was set such that the mass of the impactor $m_{sol}$ was equal to 0.0444 kg (44.4 g), which was the mean mass of a group of commercial golf balls studied by Roberts et al. (2001). Finally, in the golf ball impact case, this impactor was assigned an initial velocity $v_{sol}$ of 76.0 m/s, which is just below the maximum allowable velocity a golf ball must not exceed under test conditions (R&A Rules Ltd., 2008).

In addition to using this impactor model to represent a golf ball in the first impact case, this impactor was also used in the two other case studies. In this way, the impactor's size, curvature, and elastic modulus were constant across these three experiments, allowing the intracranial responses to be normalised and compared. However, in the other two case studies the impactor's mass and velocity were varied. In the final case study, impact by a light spherical mass, the mass of the impactor $m_{sol}$ was reduced to 0.0100 kg (10 g), while its initial velocity $v_{sol}$ was maintained equal to the golf ball (76.0 m/s).

In the second case study, impact by a heavy spherical mass, the impactor's mass was set to a large value $m_{sol}$ = 14.0 kg, greater than the mass of the entire Stage 3 head model including the flesh and neck ($m$ = 7.219 kg). In this second case study, the impactor's velocity $v_{sol}$ was calculated in such a way as to attempt to produce an equal peak impact force $F_{max}$ as that which occurred in the original golf ball impact. This would allow these two cases to be easily compared without the need to normalise the results. This had been attempted previously in the Stage 1 and Stage 2 parametric studies by maintaining a constant impactor initial kinetic energy $E_k$ across all impacts, but with a limited degree of success. Here a different parameter was used, which can be derived from the Hertzian theory of elastic impact (and so is subject to the assumptions governing Hertzian contact models: outlined in Section 1.5). Two collinearly colliding spheres have masses $m_1$ and $m_2$, and velocities $v_1$

and $v_2$ respectively. The centres of the spheres approach each other by some displacement $x$ during impact, due to their elastic deformation. The relative velocity of these two bodies is given by (Johnson, 2003):

$$v_2 - v_1 = \frac{dx}{dt} \qquad [5.1]$$

The contact force between these two bodies is (Johnson, 2003):

$$F = m_1 \frac{dv_1}{dt} = -m_2 \frac{dv_2}{dt} \qquad [5.2]$$

From which a relationship between the contact force and the relative velocity of these two spheres ($v_2 - v_1$) can be found (Johnson, 2003):

$$\frac{dv_2}{dt} - \frac{dv_1}{dt} = -\frac{F}{m_2} - \frac{F}{m_1} = -F\left(\frac{1}{m_1} + \frac{1}{m_2}\right) \qquad [5.3]$$

Writing $(1/m_1 + 1/m_2)^{-1}$ as the relative mass of the two bodies $m^*$ [Equation 1.11], and writing $(v_2 - v_1)$ as the mutual approach velocity of these bodies $\Delta v$, and rearranging gives:

$$F = -m^* \frac{d\Delta v}{dt} \qquad [5.4]$$

Integrating the above relationship with respect to the displacement $x$ yields an expression for the kinetic energy of the impact which takes into account the masses and velocities of both objects, rather than just one. In this study, this parameter has been termed the *relative kinetic energy* $E_k^*$:

$$E_k^* = \int F(t) \cdot dx = \frac{1}{2} m^* \frac{x^2}{t^2} + c = \frac{1}{2} m^* \Delta v^2 + c \qquad [5.5]$$

(where $c$ is a constant of integration, which can be omitted.) As opposed to the kinetic energy of the impactor $E_k$ used previously, according to Young's (2003) analytical description of head impact it follows that two separate head impact cases with different masses and velocities, but with equal values of relative kinetic energy $E_k^*$, will result in impacts with identical peak impact force $F_{max}$ (provided the curvature and material parameters of the bodies remain constant). This is because in Young's (2003) analytical model [Equation 1.14] the peak impact force $F_{max}$ is proportional to $m^* \cdot \Delta v^2$, i.e. the same configuration of variables that comprise the definition of $E_k^*$ [Equation 5.5].

The velocity of the heavy spherical impactor was therefore chosen such that this second case study had an equal value of $E_k^*$ as the golf ball impact: given $m_{sol}$ = 14.0 kg, $v_{sol}$ was found to be 7.32 m/s.

| Case Study | $v_{sol}$ (m/s) | $m_{sol}$ (kg) | $E_k$ (J) | $E_k$* (J) |
|---|---|---|---|---|
| Impact by a golf ball | 76.0 | 0.0444 | 128.23 | 127.44 |
| Impact by a heavy spherical mass | 7.32 | 14.0000 | 374.61 | 127.44 |
| Impact by a light spherical mass | 76.0 | 0.0100 | 28.88 | 28.84 |

*Table 5.1: Variables of the Stage 3 impact case studies.*

### *5.2.1 Impact characteristics*

The contact durations $T_p$ and peak impact forces $F_{max}$ were retrieved for each case study using T/HIS. As before, the force-time histories of the impacts were all roughly similar in shape to that of a single sinusoidal "pulse", with the peak $F_{max}$ values occurring at some time close to half way through the impact ($t = T_p/2$).

Just as in Stage 2, before these impact characteristics could be compared to analytically predicted values, certain parameters in Young's (2003) analytical description of head impact were redefined in order to better adapt this model to the Stage 3 investigation. Young's model assumes a spherical head, where $R_{sh}$ and $h$ are defined as the outer radius of the spherical shell, and the constant thickness of the shell respectively. Here the variables $R_{sh}$ and $h$ were redefined as: the local radius of curvature of the scalp at the impact site, and the local thickness of the non-spherical skull at the impact site respectively. Measuring these in D3PLOT, $R_{sh}$ was found to be 111.50 mm, and $h$ was found to be approximately 6.26 mm (which differs slightly from the value used in Stage 2, because this investigation utilises a smaller impactor and so the skull geometry at the impact site was measured over a smaller area). Finally, to represent the soft scalp layer included in the Stage 3 model, when calculating the relative elastic moduli $E^*$ [Equation 1.10] used in the analytical model, the variable representing the impactor's elastic modulus $E_{sol}$ was replaced with the modulus of the linear elastic flesh of the Stage 3 biofidelic head model (16.7 MPa). In this way, in terms of the analytical model, the head was struck by an impactor with stiffness equal to that of flesh, which more accurately represents the arrangement of the Stage 3 finite element experiments than negating the flesh altogether.

In Table 5.2 below, it can be seen that, as expected, the analytically predicted $F_{max}$ values of the golf ball and heavy spherical mass impact case studies were identical. Unfortunately however, Young's (2003) analytical model no longer appears to perform as well in relation to the Stage 3 biofidelic model as it had done in forecasting the impact characteristics of the simpler Stage 1 and Stage 2 models. This is likely due to the major differences

introduced at this stage, namely: the inclusion of flesh and scalp, viscoelastic brain material, and the constraining influence of the neck. Therefore, the peak impact force values recorded in the first and second case study simulations were not equal, but differed by approximately 15%.

In contrast to the Stage 1 and Stage 2 investigations, here the analytical model's predictions of impact duration were poor with an absolute maximum error of 119.13%. The peak impact force predictions were slightly better, but still deviated significantly from the values obtained from the finite element experiments, having an absolute maximum error of 46.43%. Again, these errors were attributed to the large disparity between the assumptions inherent in the analytical model and the geometrically and constitutively complex Stage 3 finite element model.

| Case Study | FE $T_p$ (ms) | FE $F_{max}$ (kN) | Analytical $T_p$ (ms) | Analytical $F_{max}$ (kN) | Analytical $T_p$ error (%) | Analytical $F_{max}$ error (%) |
|---|---|---|---|---|---|---|
| Impact by a golf ball | 0.526 | 22.285 | 0.981 | 11.938 | 86.65 | -46.43 |
| Impact by a heavy spherical mass | 4.653 | 18.851 | 10.196 | 11.938 | 119.13 | -36.67 |
| Impact by a light spherical mass | 0.326 | 6.948 | 0.538 | 4.936 | 64.93 | -28.97 |

*Table 5.2: Resulting contact durations and peak impact forces in the Stage 3 impact case studies. "FE" denotes values measured in the finite element simulations. "Analytical" denotes values predicted by Young's (2003) analytical model.*

An eigenvalue analysis was conducted in Abaqus in order to obtain the period of the longitudinal n=2 mode $T_\Omega$ of the head, i.e. the equivalent period to that which had been used in Stage 2 to normalise the results. The layer of flesh and scalp was not included in the eigenvalue analysis, since being both very soft compared to the skull and reasonably light these materials were expected to have a negligible effect on the free vibration response of the system. The analysis was therefore similar to that conducted in Stages 1 and 2: it was performed on the skull model only, with the brain and CSF removed, but the density of the skull scaled such that its mass was equal to the original mass of the skull and cranial contents combined. As expected, the analysis yielded mode shapes for the Stage 3 model's skull identical to those of the Stage 2 model, depicted in Figure 4.1. The revised elastic modulus of the skull in this biofidelic model however, resulted in the longitudinal n=2 mode having a period $T_\Omega$ of 0.611 ms; this was greater than the equivalent period of the Stage 2 model's skull, which agrees with the fact that the elastic modulus had been reduced.

Also, the period of oscillation of the n=2 mode $T_\Omega$ of a fluid-filled sphere with dimensions and material properties equal to the skull used in the computational free vibration analysis above was predicted using Young's (2002) closed-form expression [Equation 1.6]. The analytically predicted $T_\Omega$ value was 0.641 ms, which was an error of only 4.91% compared to the numerically computed solution.

### *5.2.2 Pressure response*

For each impact case, the resulting intracranial pressure response was explored using D3PLOT and T/HIS. Unlike in the Stage 2 investigation, the biofidelic head model did not require the use of two methods of capturing pressure-time histories at the coup (the "pressure at a point" and "pressure over a patch" sampling locations). The inclusion of the scalp layer placed the region most heavily influenced by the mesh refinement at the impact site further away from the brain. Therefore, the coup and contrecoup sampling locations in the Stage 3 model were of both comparable size and position: the coup pressures were averaged over a length of 0.870 mm along the impact axis, the centre of which was 4.769 mm from the brain-skull boundary, while the contrecoup pressures were captured over a length of 1.040 mm along this axis, with its centre 4.965 mm away from the brain-skull boundary.

While the pressure-time histories presented in this section were captured exclusively in the brain, the graphical contour plots of pressure presented in these Stage 3 cases depict not only pressure contours throughout the brain, but also in the spinal cord and CSF network. The CSF was included in these pressure plots because intracranial cavitation is not expected to be injurious only if it is generated directly in the neural tissue itself, but also if it occurs in the capillaries and CSF which surround and permeate the brain.

#### *5.2.2.1 Impact by a golf ball*

The golf ball impact lasted 0.526 ms (which is less than $T_\Omega$, giving the ratio $T_p$ / $T_\Omega$ = 0.860) and produced a peak force of 22.285 kN. The resulting pressure-time histories captured at the coup and contrecoup are presented below in Figure 5.3, along with the force-time history of the impact. It is clear that the magnitudes of these intracranial pressures are not instantaneously proportional to the force transferred by the impact. At the coup three large pressure transients can be seen beginning immediately after incidence, which alternate from positive, to negative, to positive pressure. This pattern of three large alternating pressure transients was repeated sometime later (from $t \approx 0.700$ ms) at the

contrecoup. Counter-intuitively, at approximately half way through the impact when the transferred force reached its peak ($t$ = 0.250 ms), the intracranial pressure directly beneath the impact site was not at its most positive, but was in fact close to zero. The impact produced peak intracranial pressures of 4.907 and -2.865 MPa at the coup, with peaks of 1.690 and -2.651 MPa at the contrecoup. Comparing the peak positive pressure at the coup and peak negative pressure at the contrecoup with $P_{C\ quasi}$ and $P_{CC\ quasi}$ (the coup and contrecoup pressures expected from the perfectly quasi-static solution) calculated using Equation 1.5, it was found that the recorded pressures differed from these analytically predicted values by factors of 7.976 and 3.528 respectively. These alternating transients and "magnified" peak pressures are characteristic of the dynamic pressure magnification response: reported previously in short duration impacts involving the fluid-filled sphere head model (Section 3.2.2.3), and in the brain and realistic skull model (Section 4.2.2.4).

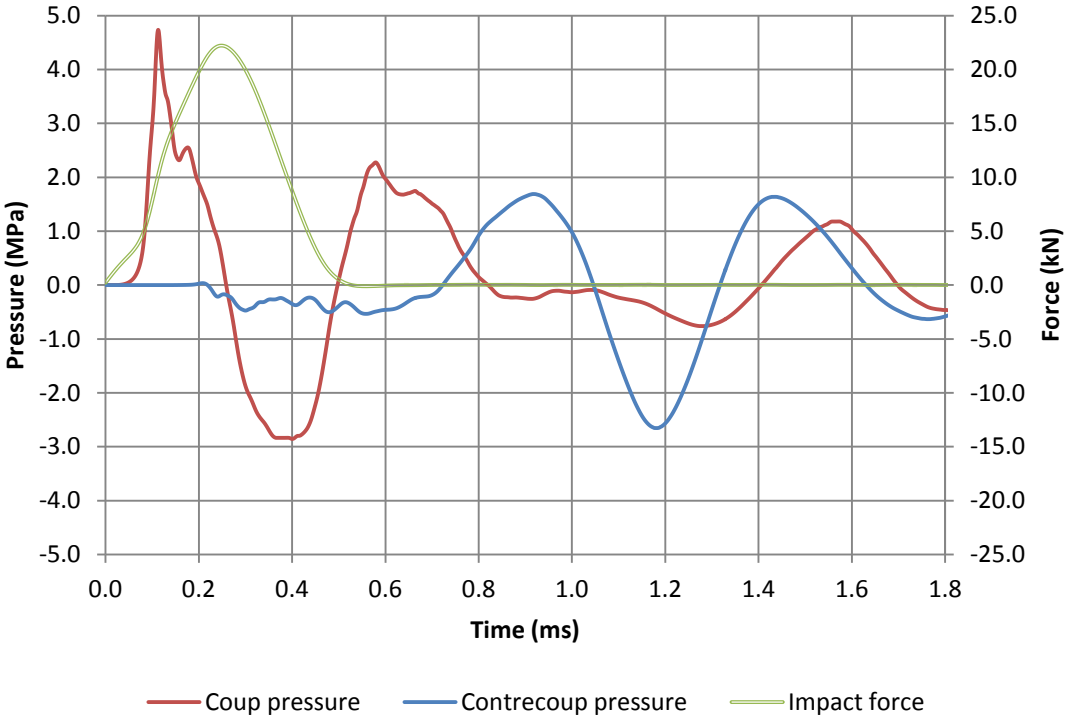


*Figure 5.3: Impact by a golf ball, Stage 3 case study: local pressure-time histories recorded in the brain at the coup and contrecoup, and the force-time history of the impact (plotted with respect to a secondary vertical axis).*

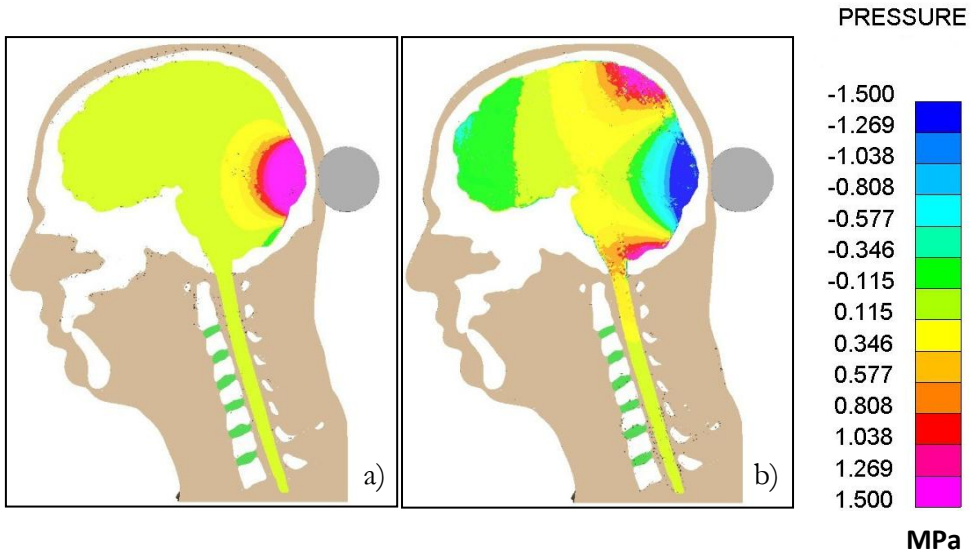


*Figure 5.4: Impact by a golf ball, Stage 3 case study: contour plots of pressure in the cranial contents and spinal cord at (a) t = 0.120 ms, and (b) t = 0.420 ms. Note the large region of fluctuating pressure at the coup.*

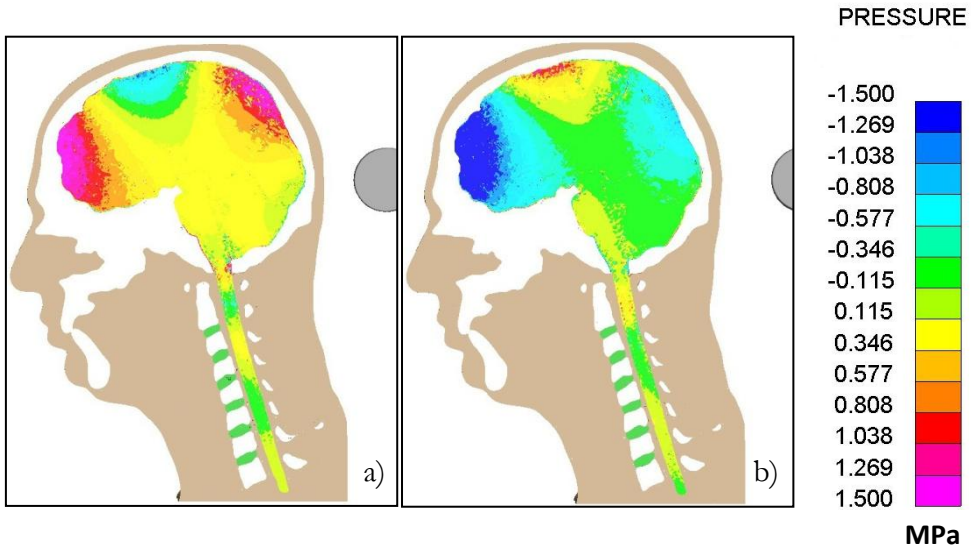


*Figure 5.5: Impact by a golf ball, Stage 3 case study: contour plots of pressure in the cranial contents and spinal cord at (a) t = 0.930 ms, and (b) t = 1.170 ms. Note the large region of fluctuating pressure at the contrecoup.*

The contour plots presented above illustrate the pressure throughout the brain and CSF at various times during and after the golf ball impact. Figure 5.4 serves to highlight the large positive and negative transients experienced by the brain beneath the coup, while Figure 5.5 highlights this same phenomenon with respect to the contrecoup. As with Stages 1 and 2, the peak positive and negative intracranial pressures invariably occurred at the coup and contrecoup locations; however, these were not the only large pressures within the cranial cavity. After the first large positive intracranial pressure transient at the coup had ceased, areas of positive pressure of lower magnitude could be seen radiating away from the coup,

migrating along the outer surface of the cranial cavity. This initial positive pressure transient which occurred at the coup immediately after incidence is visible in Figure 5.4 (a). In Figure 5.4 (b) the brain beneath the coup is now experiencing considerable negative pressure, while the initial positive pressure can be seen radiating away from the impact site, located in this instance in small areas directly above and beneath the coup. As is typical of the dynamic pressure magnification response, fractions of a millisecond later the coup then experiences another large positive pressure transient: it appears that all three of these large pressure transients generated at the coup then radiate outwards, like "ripples" from a central point of disturbance in water, traversing the brain-skull boundary circumferentially towards the contrecoup.

As the cranial cavity can be said to be roughly symmetrical about the anterior to posterior axis, the "ripples" of pressure caused by the initial positive pressure transient at the coup will arrive at the contrecoup at more or less the same time. These are therefore superimposed, resulting in a single transient of positive pressure at the contrecoup of greater magnitude than the "ripple" itself. This appears to occur in response to all three of the large transients generated at the coup, hence resulting in the delayed occurrence of similar fluctuating pressures at the contrecoup. In Figure 5.5 (a) the first large positive pressure transient is visible at the contrecoup, while the "ripples" of negative and then positive pressure can be seen in the superior region of the cranial cavity travelling towards the contrecoup. In Figure 5.5 (b) the negative pressure has arrived at the contrecoup and, due to the superposition mentioned above, this region of "concentrated" pressure is of greater magnitude than the negative pressure "ripple" in the previous diagram. In Figure 5.5 (b) only the final positive pressure transient remains to arrive at the contrecoup and can, as before, be seen traversing the superior region of the cranial cavity, while relatively mild pressures exist elsewhere in the brain.

The golf ball impact case was studied because this object's low mass and high velocity made it a good candidate for inducing the dynamic pressure magnification response as a result of real world impact conditions; whereas the choice of impactor properties in Stages 1 and 2 were designed to explore this phenomenon rather than represent realistic scenarios. It has been shown that the loading resulting from this impact does indeed produce the dynamic intracranial pressure response as observed by Young & Morfey (1998), and this occurs despite the significant increase in complexity and realism introduced by the biofidelic head model.

*5.2.2.2 Impact by a heavy spherical mass*

Impact by a slow moving, heavy mass was simulated in order to elicit a quasi-static response with which the golf ball impact could be easily contrasted. The heavy spherical mass impact lasted 4.653 ms (significantly longer than $T_\Omega$, resulting in $T_p$ / $T_\Omega$ = 7.610) and had a peak impact force $F_{max}$ of 18.851 kN. Once again, as in the Stage 2 high energy impact Case 2.18, collision with a slow and heavy object (in this case approximately twice the mass of the head model) can be considered similar to collision with an immobile object or surface such as the ground. Figure 5.6, below, depicts the pressure-time histories captured at the coup and contrecoup during this case, and the force-time history of the collision. It can be seen that these coup and contrecoup pressure-time histories are roughly symmetrical about the horizontal axis, with no significant negative pressure occurring at the coup, and no significant positive pressure occurring at the contrecoup. The peak pressures at the coup were recorded as 5.550e-1 and -1.270e-1 MPa, with peaks of 1.870e-1 and -4.410e-1 MPa at the contrecoup. These agreed well with the quasi-static solution predicted by Equation 1.5, with the coup positive and contrecoup negative pressures differing from $P_{C\ quasi}$ and $P_{CC\ quasi}$ by factors of only 1.124 and 0.681 respectively. Furthermore, these pressure curves rise and fall in magnitude in conjunction with the force-time history of the impact, i.e. their shapes are more or less equivalent. The preceding characteristics provide evidence that this simulation was successful in eliciting a quasi-static response.

As opposed to the previous impact case, the force-time history curve in Figure 5.6 is not symmetrical about its peak value $F_{max}$, but is more elongated in the latter half of the impact. It is evident that the circumstances affecting the loading and unloading of the head are, in this case, somewhat different. In Figure 5.7, the head is depicted at two instances during and after impact. In Figure 5.7 (a), when the impact force is at its peak, the head model remains essentially upright and close to its undeformed state; whereas in image (b), taken later, it can be seen that the head and neck have been bent forward due to the sustained force supplied by the impactor. While the long contact duration of this impact makes it efficient at inducing global acceleration of the head it also magnifies the influence of the neck constraint, which normally does not play a role in short duration impacts. In Figure 5.7 (b) negative pressure is visible throughout a large portion of the spinal cord: this corresponds to elongation of the neck as the head is pushed forward by the impactor. Hence the elastic neck will be put into a state of tension. This acts to increase the duration that the head and impactor are in contact, by resisting the lateral displacement of the head, resulting in an asymmetrical force-time history. Finally, in Figure 5.7 (a), contours of

pressure throughout the brain reveal a "banding" pattern, typical of the quasi-static response.

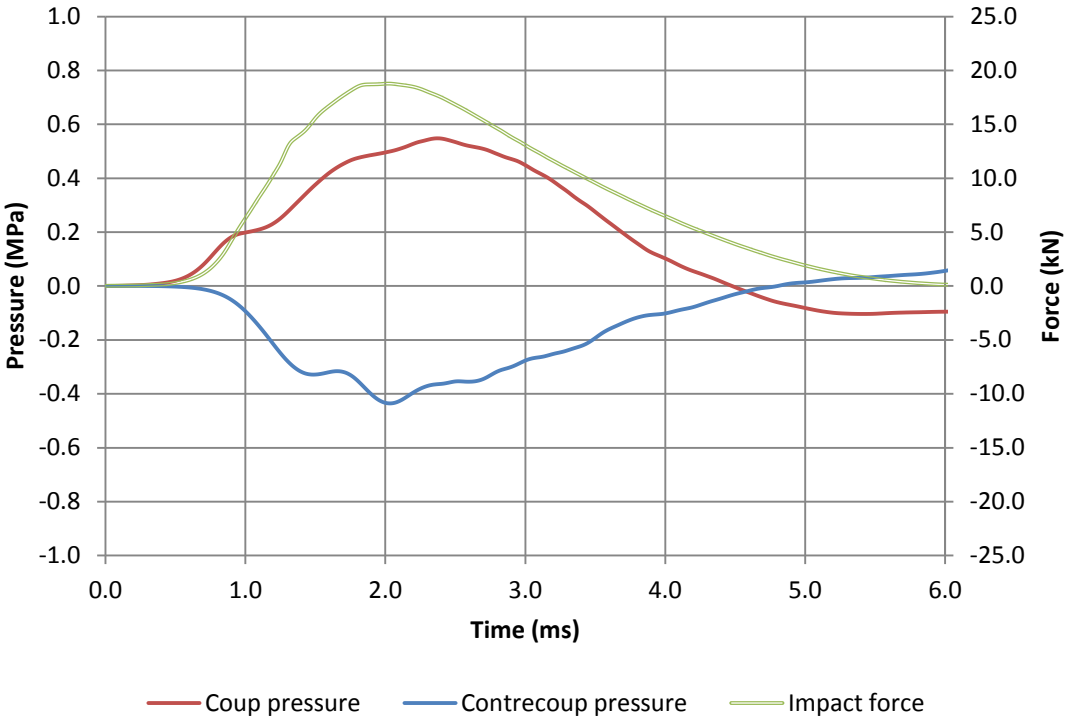


*Figure 5.6: Impact by a heavy spherical mass, Stage 3 case study: local pressure-time histories recorded in the brain at the coup and contrecoup, and the force-time history of the impact (plotted with respect to a secondary vertical axis).*

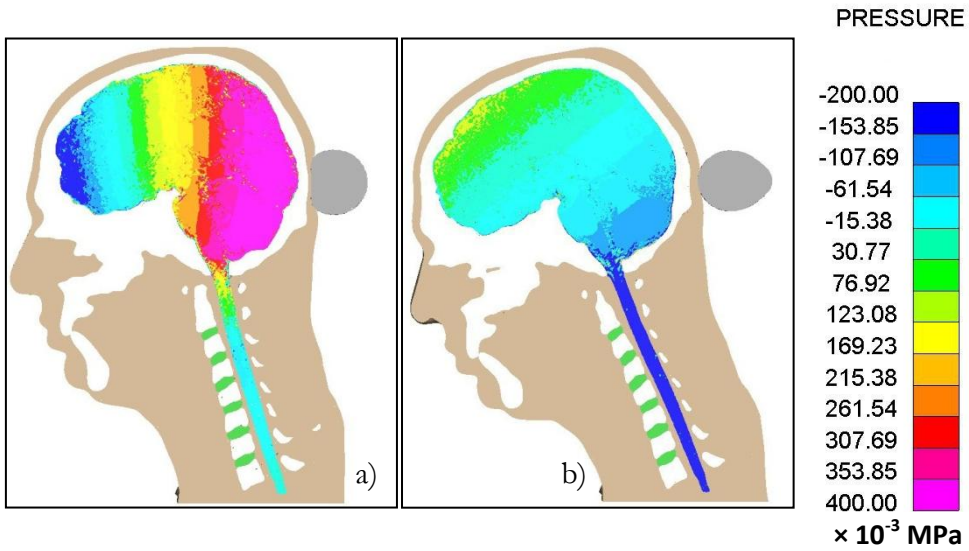


*Figure 5.7: Impact by a heavy spherical mass, Stage 3 case study: contour plots of pressure in the cranial contents and spinal cord at (a) t = 2.000 ms, and (b) t = 6.000 ms. Note the "banding" pattern formed by the pressure contours in (a), and the bending of the neck in (b).*

While the peak impact forces in the golf ball and heavy spherical mass case studies were not equal, these cases can nevertheless be compared without the need to normalise the results. In the heavy spherical mass impact case the peak force $F_{max}$ was approximately 15% less than that of the golf ball impact; yet the coup positive pressure $P_{C\ positive}$ and contrecoup negative pressure $P_{CC\ negative}$ values recorded in the heavy spherical mass impact were roughly 89% and 83% less than the latter case, respectively. The differences in peak force do not account for these drastic quantitative changes observed in intracranial pressure.

#### *5.2.2.3 Impact by a light spherical mass*

In the final Stage 3 impact case, the head was struck by an impactor with the same high velocity as the golf ball, but of reduced mass, in order to induce a strong dynamic pressure magnification effect. This case could be said to represent a non-penetrating head impact by a small projectile such as shrapnel, a stone, or non-lethal ammunition. The resulting collision had a contact duration of 0.326 ms, so giving the ratio $T_p$ / $T_\Omega$ = 0.533. The peak force of this impact was 6.948 kN, which was considerably lower than the peak impact forces recorded in the other two case studies. Figure 5.8, below, presents the pressure-time histories generated at the coup and contrecoup, and the impact's force-time history. As in the golf ball case study, again the recorded intracranial pressure curves do not follow the force-time history of the impact, but are characterised by three large pressure transients of alternating sign, appearing first at the coup and later at the contrecoup after the impact has ceased. The peak positive and negative pressures recorded at the coup were 2.938 and -1.744 MPa, and at the contrecoup these were 7.230e-1 and -1.040 MPa respectively. Comparing these peak coup positive pressure and contrecoup negative pressure values with those expected from a perfectly quasi-static response ($P_{C\ quasi}$ and $P_{CC\ quasi}$) reveals that the pressures generated in this simulation were "magnified", being factors of 15.316 and 4.455 greater than the quasi-static solution respectively. This was the greatest degree of pressure "magnification" that was achieved in the Stage 3 investigation; evidently this case study had succeeded in demonstrating dynamic pressure magnification behaviour in the system.

Examining the dynamic pressure-time histories generated at the coup in response to the two short duration impacts in this investigation (i.e. the golf ball and light spherical mass cases: see Figures 5.3 and 5.8), in both of these cases a small portion of the first large positive pressure transient at the coup can be seen to rise considerably above any of the other positive pressure transients. In Stages 1 and 2, this initial dynamic positive pressure transient tended to be slightly larger in magnitude than any subsequent positive pressures, but the difference in magnitude was far less pronounced than in these Stage 3 cases. In

Figures 5.3 and 5.8, it can be seen that, in both cases, this enlarged initial positive pressure transient appears to correspond to the steepest (highest gradient) portion of the impact's force-time history curve. The comparatively smooth impact force-time histories in Stages 1 and 2 were attributed to the lack of the scalp at the impact location. In Stage 3, the scalp introduced at the impact site undergoes non-linear stiffening as it becomes compressed: this affects the rate at which the force of the impact is transferred to the head, influencing the pressure in the brain beneath this location (at the coup).

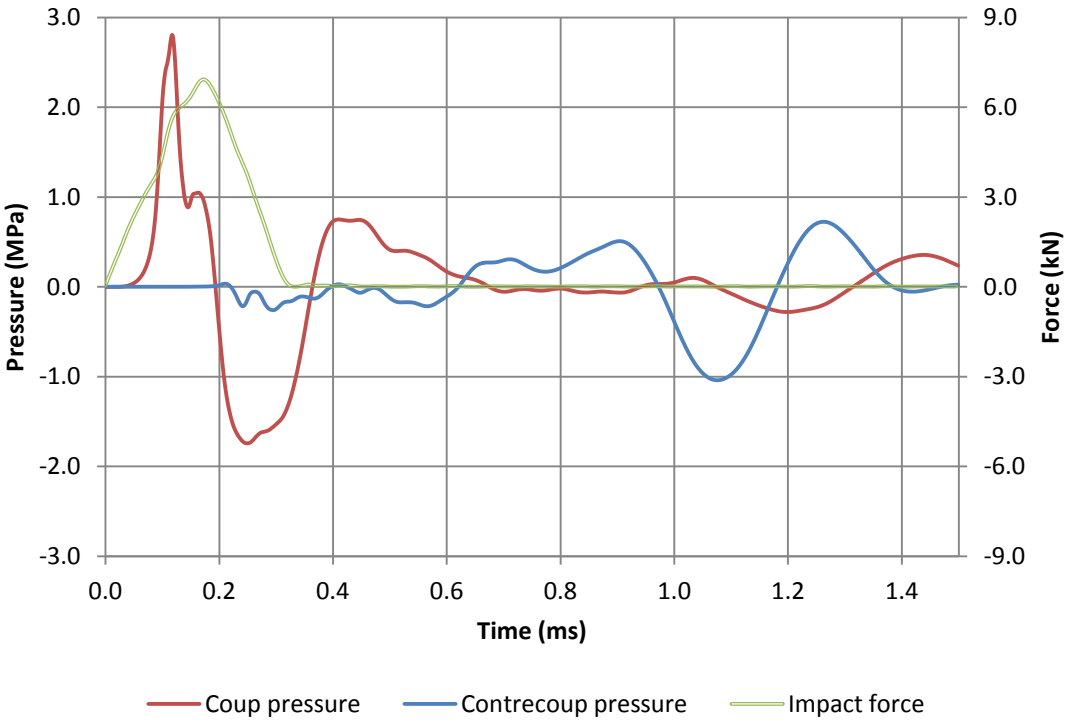


*Figure 5.8: Impact by a light spherical mass, Stage 3 case study: local pressure-time histories recorded in the brain at the coup and contrecoup, and the force-time history of the impact (plotted with respect to a secondary vertical axis).*

Figures 5.9 and 5.10, below, depict contours of pressure in the cranial contents, and contours of acceleration throughout the skull respectively. Both of these images were captured at the same time after impact ($t$ = 0.640 ms): at an instant which lies between the cessation of the three large pressure transients which occur at the coup, and the beginning of the large pressure transients at the contrecoup. In Figure 5.9, the remains of the final large positive pressure transient can still be seen at the coup, while local regions of positive and negative pressure (or "ripples") caused by the preceding pressure transients at the coup are visible radiating away from this location, migrating towards the contrecoup along the brain-skull boundary (as discussed in Section 5.2.2.1). In Figure 5.10, deformation of the

skull was magnified significantly, and contours of acceleration of the bone material have been mapped onto this deformed shape: local areas of the skull that had deviated significantly from the skull's undeformed shape were highlighted by arrows overlaid on both figures.

Comparing Figures 5.9 and 5.10, it can be seen that, beneath areas where the skull had (at this instant) locally deflected "outwards", i.e. locally expanded compared to its undeformed geometry (marked by the red arrows), the brain and CSF were subjected to positive pressure. On the other hand, beneath areas where the skull had locally deflected "inwards" (marked by the blue arrows) the brain and CSF experienced negative pressure. This correlation was not caused by these areas of intracranial pressure inducing local deflections in the skull; the greater stiffness of the skull makes it more inclined to affect the state of the cranial contents, not vice versa (at least not significantly). Rather, as is illustrated by Equation 1.5, the pressure in the cranial contents is a function of the acceleration that it is subjected to. The local deflection at various points throughout the skull, presumably caused as distortional waves radiate through the skull, causes local acceleration in the fluid beneath these points: so resulting in the pressure "ripples" reported at the brain-skull boundary. Therefore, in Figure 5.9, areas of positive intracranial pressure appear under the regions where the skull has locally expanded (red arrows), because here the fluid has been accelerated "outwards", but its inertia causes it to become compressed against the inner surface of the skull. The reverse is true beneath regions where the skull has deflected "inwards" (blue arrows), producing areas of negative pressure in the brain and CSF.

Finally, a comparison can be made between the quasi-static pressure response generated in the previous case study, and the dynamic response resulting from the light spherical mass impact. Again without normalising the results, contrasting these two cases directly underscores the counter-intuitive nature of the dynamic pressure magnification phenomenon. While the peak impact force $F_{max}$ resulting from collision with the light projectile was approximately 63% less than that caused by the heavier projectile, the peak coup positive $P_{C\ positive}$ and contrecoup negative $P_{CC\ negative}$ pressures recorded in the current impact case were 429% and 136% greater than those produced by the heavy spherical mass impact, respectively.

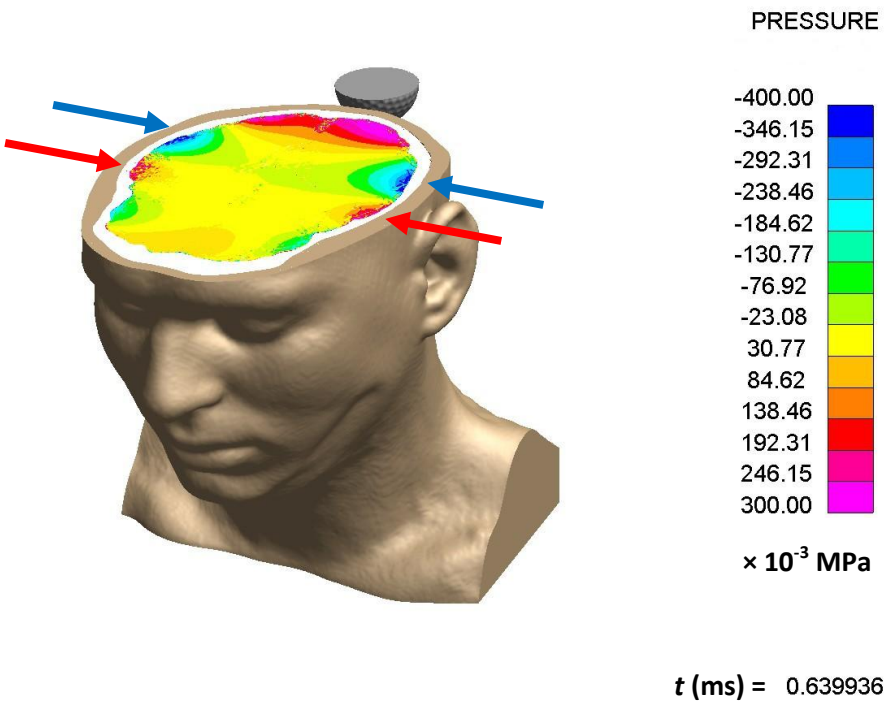


*Figure 5.9: Transverse section view of the Stage 3 model depicting impact by a light spherical mass: contours of pressure in the cranial contents at t = 0.640 ms.*

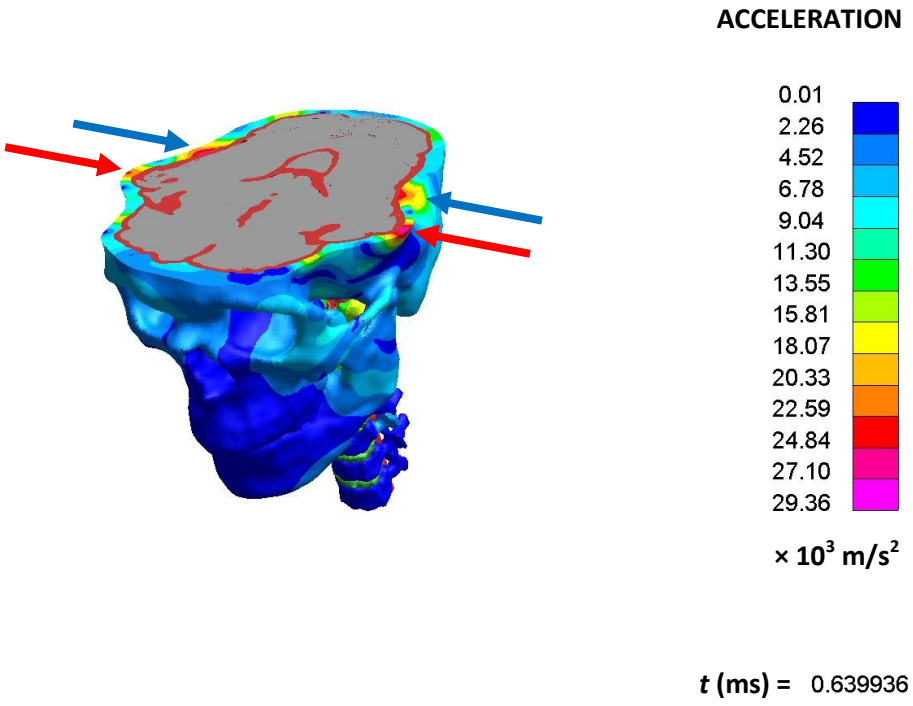


*Figure 5.10: Transverse section view of the Stage 3 model depicting impact by a light spherical mass: contours of acceleration in the skull at t = 0.640 ms. The grey, red, and green regions represent the central nervous system, CSF, and intervertebral discs respectively; the flesh has been made transparent. Local deformation throughout the skull and cranial contents was magnified 100 times.*

### *5.2.3 Collapsing the results*

The peak pressure values obtained from the Stage 3 case studies were non-dimensionalised. In Table 5.3, below, the peak coup ($P_{C\ quasi}$) and contrecoup ($P_{CC\ quasi}$) pressures expected assuming the cranial contents respond according to the perfectly quasi-static solution [Equation 1.5] are presented for each impact case, along with the actual peak pressures recorded during the Stage 3 simulations. The pressure results were collapsed by normalising these recorded peak pressures over the analytically predicted quasi-static pressures (at their respective location: coup or contrecoup), and impact durations $T_p$ were normalised over the skull's longitudinal n=2 mode $T_\Omega$. These non-dimensional measures of pressure "magnification" and impact duration are presented in Table 5.4.

| Case Study | Analytical | | FE: Coup | | FE: Contrecoup | |
|---|---|---|---|---|---|---|
| | $P_{C\ quasi}$ (MPa) | $P_{CC\ quasi}$ (MPa) | $P_{C\ positive}$ (MPa) | $P_{C\ negative}$ (MPa) | $P_{CC\ positive}$ (MPa) | $P_{CC\ negative}$ (MPa) |
| Impact by a golf ball | 6.152e-1 | -7.513e-1 | 4.907 | -2.865 | 1.690 | -2.651 |
| Impact by a heavy spherical mass | 4.938e-1 | -6.472e-1 | 5.550e-1 | -1.270e-1 | 1.870e-1 | -4.410e-1 |
| Impact by a light spherical mass | 1.918e-1 | -2.334e-1 | 2.938 | -1.744 | 7.230e-1 | -1.040 |

*Table 5.3: Analytically predicted quasi-static peak pressures, and peak pressures observed in the Stage 3 impact case studies.*

| Case Study | Normalised | | | | |
|---|---|---|---|---|---|
| | $P_{C\ positive} / P_{C\ quasi}$ | $P_{C\ negative} / P_{C\ quasi}$ | $P_{CC\ positive} / P_{CC\ quasi}$ | $P_{CC\ negative} / P_{CC\ quasi}$ | $T_p / T_\Omega$ |
| Impact by a golf ball | 7.976 | -4.657 | 2.249 | -3.528 | 0.860 |
| Impact by a heavy spherical mass | 1.124 | -0.257 | 0.289 | -0.681 | 7.610 |
| Impact by a light spherical mass | 15.316 | -9.092 | 3.097 | -4.455 | 0.533 |

*Table 5.4: Non-dimensional peak positive and negative pressures, and non-dimensional impact durations, of the Stage 3 impact case studies.*

Figures 5.11 and 5.12, below, graphically display the non-dimensional pressure readings contained in Table 5.4 of the coup and contrecoup respectively. In both of these figures the corresponding non-dimensional pressures obtained during the Stage 2 investigation are also plotted to facilitate the comparison of trends. In Figures 5.11 and 5.12, it can be seen that the short duration cases (the golf ball and light mass impacts) necessarily have a lower $T_p$ / $T_\Omega$ ratio, and as this decreases there is an increase in the amount of pressure

magnification. In other words, during these short duration cases the head system behaves with a tendency to generate transients of intracranial pressure of greater magnitude in response to a given peak impact force. On the other hand, the heavy mass impact case was of comparatively long duration, which produced quasi-static behaviour in the brain and hence peak pressures of lower magnitude. This is illustrated in Figures 5.11 and 5.12 by the data points corresponding to the heavy mass case's normalised positive pressure at the coup and negative pressure at the contrecoup, which both have pressure magnification values close to one, indicating the recorded pressures agree well with the analytically predicted quasi-static pressures [Equation 1.5]. Despite the geometric and material complexities of the biofidelic head model which were not present in the Stage 2 model, Figures 5.11 and 5.12 demonstrate that the normalised results obtained from these three case studies follow closely the trends observed in the Stage 2 investigation.

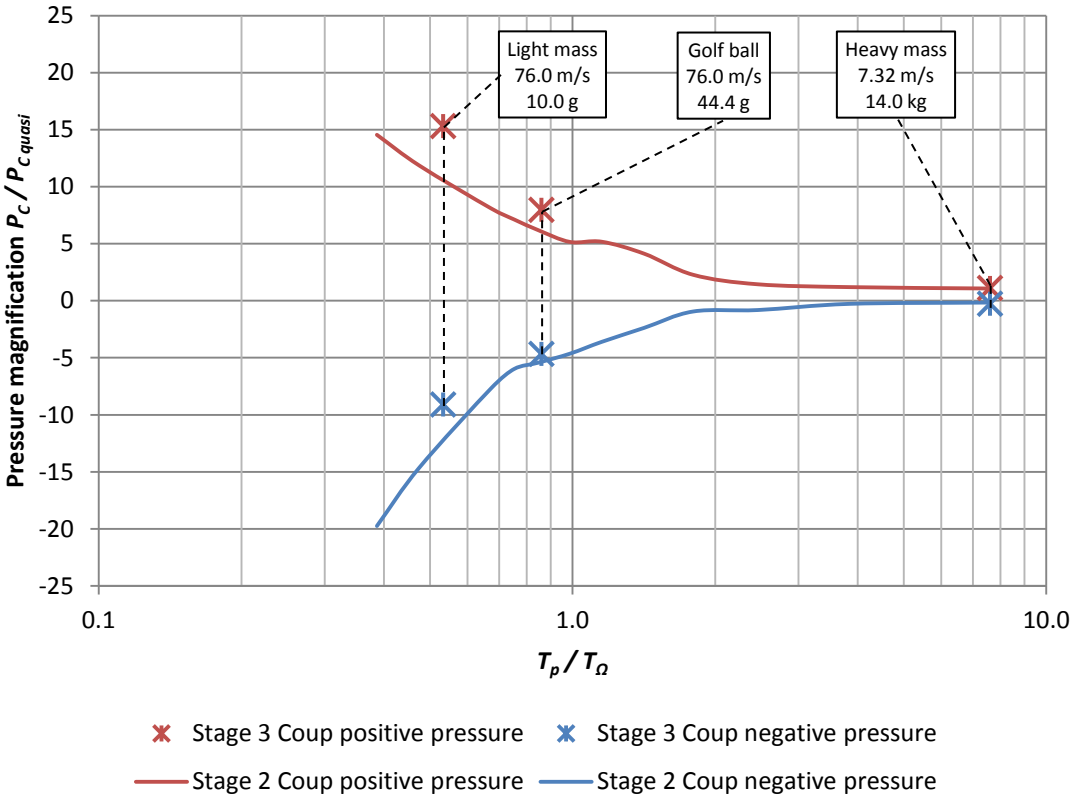


*Figure 5.11: Stage 3 impact case studies, normalised peak pressures against $T_p$ / $T_\Omega$ at the coup. Normalised coup "pressure over a patch" values from the Stage 2 low energy parametric study are provided for comparison.*

The three Stage 3 case studies spanned a wide range of non-dimensional impact durations $T_p$ / $T_\Omega$, resulting in both quasi-static and dynamic pressure behaviour in the brain. Due to the limited number of these impact cases however, it was not possible to determine at what

critical value of $T_p$ / $T_\Omega$ the transition from quasi-static to dynamic intracranial behaviour occurs. Nonetheless, the excellent agreement between the Stage 2 and Stage 3 normalised results suggests a critical value of $T_p$ / $T_\Omega$ = 2, as before.

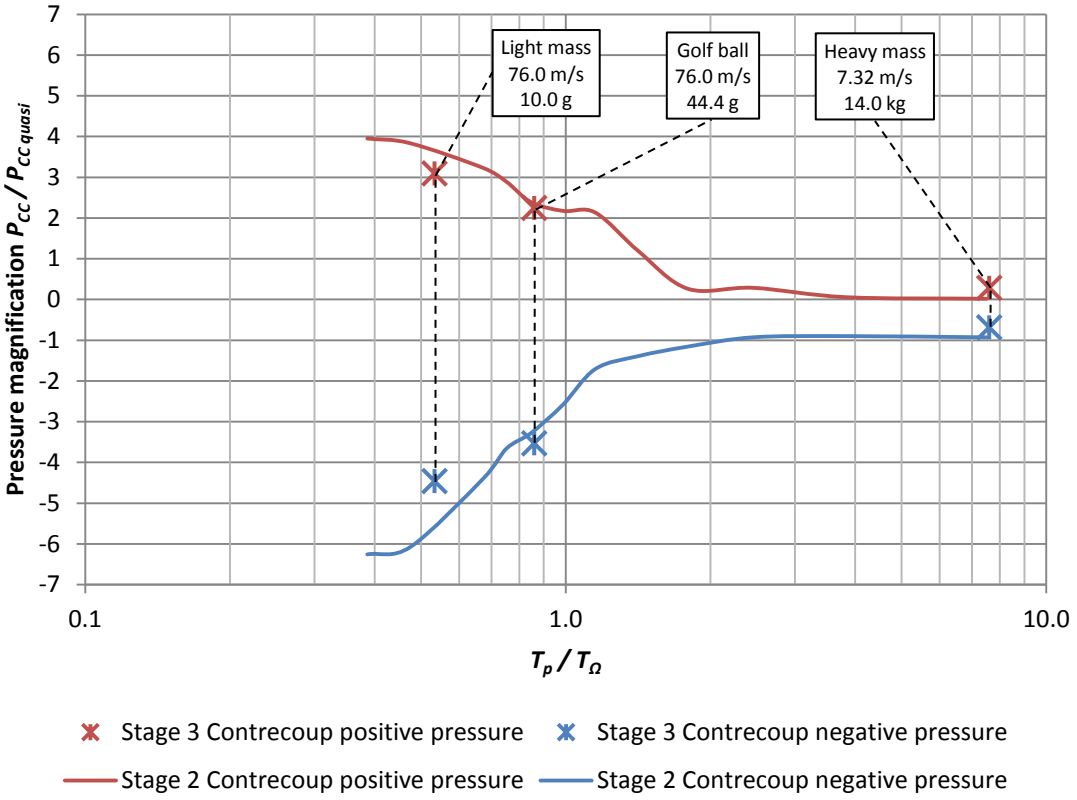


*Figure 5.12: Stage 3 impact case studies, normalised peak pressures against $T_p$ / $T_\Omega$ at the contrecoup. Normalised contrecoup pressures from the Stage 2 low energy parametric study are provided for comparison.*

Figure 5.13, below, presents the non-dimensional peak pressures captured at the coup in a similar fashion as Figure 5.11; however, here data points corresponding to values of the Head Injury Criterion (HIC) achieved during each of the Stage 3 impacts are also provided. These values of impact severity were calculated for each case study using a dedicated function in T/HIS which extracts HIC scores from the acceleration-time history of the head (here the acceleration-time history of the skull was used) (Oasys Ltd., 2009). The HIC values were calculated within a limiting time window of 15 ms, as recommended by the International Standards Organisation (ISO) (Cory, Jones, & James, 2001). The HIC, as originally proposed by Versace (1971), and as calculated by the approximation based on Young's (2003) analytical model of head impact [Equation 1.15], is proportional to the duration that the head experiences acceleration due to impact. Therefore, in Figure 5.13 it can be seen that as the non-dimensional impact duration decreases across these three case studies, the corresponding HIC score also reduces. In decreasing order of duration: the

heavy mass, golf ball, and light mass impacts produced HIC values of 2650, 835, and 52 respectively. Using the most common interpretation of HIC scores these values could, respectively, be said to correspond to a risk of over 99%, a risk of approximately 8%, and a risk of under 1% of life threatening head injury (Mertz, Prasad, & Irwin, 1997). However, as the impact duration decreases below some critical value ($T_p$ / $T_\Omega$ = 2) dynamic pressure magnification begins to occur, i.e. the head system becomes more conducive to generating large transients of positive and negative intracranial pressure, and indeed the peak pressures recorded in the short duration impacts were considerably greater than those captured during the longer heavy mass case. In this way, predictions of the severity of short duration head impacts determined by examining either the peak intracranial pressures or the HIC will be strongly divergent.

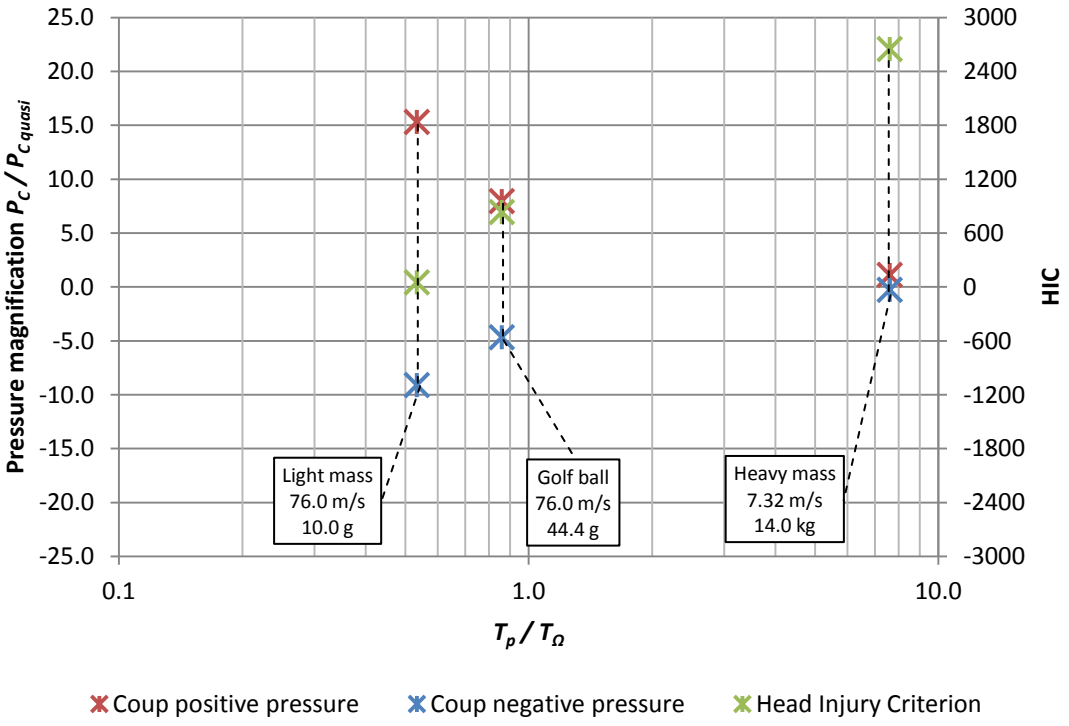


*Figure 5.13: Stage 3 impact case studies, normalised peak pressures at the coup and Head Injury Criterion (HIC) score against $T_p$ / $T_\Omega$ for each impact case. (HIC values are plotted with respect to a secondary vertical axis.)*

Finally, examining the pressures listed in Table 5.3, it is clear that all of the negative pressure transients generated during the Stage 3 investigation exceed -1 atm (-1.013e-1 MPa). If as before this value is used as a guideline for the threshold of cavitation, then cavitation induced injuries could be expected at both the coup and contrecoup in all three of the above case studies.

Chen, Y., & Ostoja-Starzewski, M. (2010). MRI-based finite element modeling of head trauma: spherically focusing shear waves. *Acta Mechanica*, *213*(1-2), 155–167.

Cory, C., Jones, M. D., & James, D. (2001). The potential and limitations of utilising head impact injury models to assess the likelihood of significant head injury in infants after a fall. *Forensic Science International*, *123*, 89–106.

Johnson, K. L. (2003). *Contact Mechanics* (9th ed.). Cambridge University Press.

Maruoka, K., Sakagami, S., Yamada, K., Nakagawa, N., & Sekiguti, Y. (2001). Dynamic impact characteristics of golf ball materials. *Materials and Science in Sports Symposium* (Vol. 7514, pp. 145–149).

Mertz, H. J., Prasad, P., & Irwin, A. L. (1997). Injury risk curves for children and adults in frontal and rear collisions. *Proceedings of the 41st STAPP Car Crash Conference* (pp. 13–30). Retrieved from http://www.snellfoundation.org/docs/articles/hics

Meulman, J. (1996). An experimental investigation to the constitutive behaviour of brain tissue. *Technical report*, *80*(10), 289–302. Retrieved from http://www.narcis.nl/publication/RecordID/oai:library.tue.nl:461975/Language/en

Nahum, A. M., Smith, R., & Ward, C. C. (1977). *Intracranial pressure dynamics during head impact*. *Proceedings of the 21st STAPP Car Crash Conference*. New Orleans, LA, USA.

Oasys Ltd. (2009). *T/HIS Manual, Version 9.4*.

R&A Rules Ltd. (2008). Initial velocity test procedure. Retrieved February 25, 2013, from http://www.randa.org/Equipment/Protocols-and-Procedures/Balls/Initial-Velocity.aspx

Roberts, J., Jones, R., & Rothberg, S. (2001). Measurement of contact time in short duration sports ball impacts: an experimental method and correlation with the perceptions of elite golfers. *Sports Engineering*, *4*, 191–203.

Versace, J. (1971). A review of the severity index. *Proceedings of the 15th STAPP Car Crash Conference* (pp. 771–796). Retrieved from http://www.snellfoundation.org/docs/articles/hics

Young, P. G. (2002). A parametric study on the axisymmetric modes of vibration of multi-layered spherical shells with liquid cores of relevance to head impact modelling. *Journal of Sound and Vibration*, *256*(4), 665–680.

Young, P. G. (2003). An analytical model to predict the response of fluid-filled shells to impact - a model for blunt head impacts. *Journal of Sound and Vibration*, *267*(5), 1107–1126.

Young, P. G., & Morfey, C. L. (1998). Intracranial pressure transients caused by head impacts. *International Research Council on the Biomechanics of Impact (IRCOBI) Conference Proceedings* (pp. 391–403). Göteborg, Sweden.

# Chapter 6 – Discussion

## 6.1 Causative mechanism of dynamic intracranial pressures

In the preceding chapters it has been shown that certain short duration head impacts may produce substantially greater intracranial pressures than a collision of longer duration with equal peak force. During these longer duration collisions a linear pressure gradient is generated throughout the cranial contents, with peak values that show excellent agreement with predictions made assuming hydrostatic equilibrium [Equation 1.5]; this provides cogent evidence that the "quasi-static" intracranial response occurs when an impact force is sustained long enough to overcome the head's inertia and cause global acceleration of the head. In other words, as was first proposed by Gross (1958) and subsequently verified by others, the quasi-static response is caused when the behaviour of the impacted head is dominated by rigid-body acceleration; but what mechanism causes the "dynamic pressure magnification" response? So far the question of the mechanics involved in the generation of these magnified peak intracranial pressures has not been addressed.

### *6.1.1 Examining the frequency domain*

In previous research into the dynamic pressure magnification response of short duration head impacts, such as work by Young & Morfey (1998) and by Johnson & Young (2005), no conclusions were drawn regarding the mechanics of this phenomenon. However, in the current study it was initially theorised that this dynamic intracranial behaviour likely occurs when a sufficient portion of the frequency content of the impact is comparable to the natural frequency of the skull's longitudinal n=2 mode. That is to say, it was thought probable that the dynamic pressure magnification response was due to resonant excitation of the skull; this was for the following reasons:

- It has been demonstrated that the critical impact duration which marks the threshold between the causation of quasi-static or dynamic intracranial pressure behaviour is related to $T_{\Omega}$, the period of the longitudinal n=2 mode of the skull.
- During the dynamic response, peak intracranial pressures are consistently located at the coup and contrecoup, which corresponds to the points of maximum deflection of the skull during excitation of the above mentioned n=2 mode.

- The dynamic pressure magnification response is characterised by regularly fluctuating transients of pressure at the coup and contrecoup, which suggests they may be caused by oscillation of the skull.

The frequency content of the intracranial pressure-time histories captured in the three biofidelic head model case studies (visible in Figures 5.3, 5.6, and 5.8) were processed using the fast Fourier transform (FFT) algorithm in T/HIS. A Fourier transform produces a description of a signal represented by the amounts of sinusoidal components at different frequencies which compose the original signal. The frequency content of the coup pressure-time histories were likely affected by contact phenomena at the impact site and therefore, in order to gain an understanding of the behaviour of the skull during these impacts, only the contrecoup pressure-time histories were analysed. Fourier transforms of the contrecoup pressure-time histories recorded in the Stage 3 impact cases are presented below in Figure 6.1.

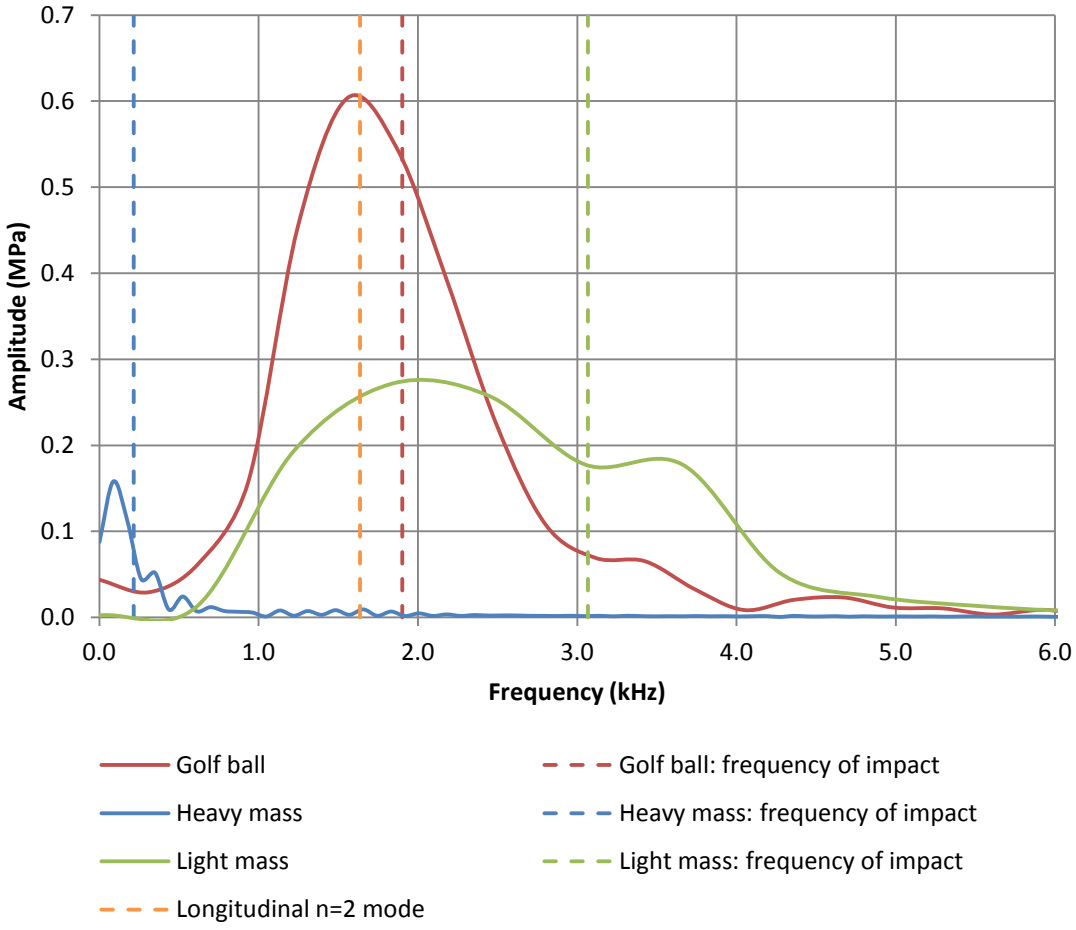


*Figure 6.1: Fourier transforms of the contrecoup pressure-time histories captured during the Stage 3 impact case studies, along with vertical lines indicating the frequencies corresponding to the impact durations in these three cases and the natural frequency of the skull's longitudinal n=2 mode.*

A natural mode of a system will only become excited by an external load if the frequency content of the load is similar to the natural frequency particular to that mode, and if the load is applied to a location that displaces from its undeformed state during vibration of that mode (known as an "anti-node"). This is a consequence of the superposition of waves which can be additive or subtractive, also called *constructive* or *destructive* interference (Rossing & Fletcher, 2004). In Figure 6.1, above, the dashed vertical lines represent the "frequency of impact" for each of the Stage 3 impact cases: these were calculated using the simple expression $f = 1 / T$, where $f$ is the frequency (Hz), and $T$ is the period of oscillation (s) which in this case was assigned the value of impact duration $T_p$. As can be seen in Figures 5.3, 5.6, and 5.8, the force-time histories of the impacts were not perfectly sinusoidal, and thus the frequency content of these force-time histories will be more than just a single frequency: nevertheless, the vertical lines in Figure 6.1 give a rough indication of the frequency content of these impact loads. The natural frequency of the skull's longitudinal n=2 mode ($1 / T_\Omega$), determined by use of a numerical eigenvalue analysis in Section 5.2.1 (with period $T_\Omega$ that was used to normalise the results of the Stage 3 investigation), was also included in Figure 6.1.

The peak amplitudes of the Fourier transforms corresponding to the three impact cases in Figure 6.1 were not equal, because the magnitudes of the original peak pressures varied across these three cases. Even so, the shapes of the Fourier transforms can be compared. As expected, large peaks existed in the frequency spectrum of each case in the immediate vicinity of its corresponding "frequency of impact" derived from impact duration $T_p$. The "frequencies of impact" did not align exactly with these peaks in the frequency response of the head system, presumably because they are only simple approximations of the actual frequency content of the impact loads.

In this system it can be said that the greater the proportion of low frequencies in the frequency spectrum, the greater the amount of rigid-body motion experienced by the head. In Figure 6.1 it can be seen that the Fourier transform obtained from the heavy mass impact case had the majority of its frequency content close to 0 Hz, which was due to this being a long duration, quasi-static impact. The remaining short duration impacts, on the other hand, had far less frequency content close to 0 Hz. Also, both of these spectra (particularly the golf ball case) were dominated by significant frequency content close to the predicted frequency of the longitudinal n=2 mode ($1 / T_\Omega$), indicating the excitation of this mode. Equally, the lack of frequency content in the vicinity of this frequency indicated that this mode was not excited during the heavy mass impact case.

### 6.1.2 Examining the time domain

It has been demonstrated that impact cases which exhibit dynamic magnification of intracranial pressures coincide with those that show excitation of the longitudinal n=2 mode of the skull. However, to answer the question of whether this correlation is in fact causation, the problem must also be considered in the time domain. Analysis of the dynamic intracranial pressures with respect to time reveals two points which appear incompatible with the notion that the dynamic magnification response is caused by resonance of the skull. The first is simply that the intracranial pressures recorded at the coup and contrecoup during a dynamic response are characterised by only three large alternating transients of pressure, which occur while the head and impactor are in contact ($0 \leq t \leq T_p$); whereas, if these transients were indeed a result of resonance of the skull, fluctuating pressures of a similar magnitude could be expected to continue beyond this duration ($t > T_p$).

The second point concerns wave speeds through the head and the fact that impacts which induce the dynamic intracranial response tend to be of very short duration. The vibration of a natural mode of a structure is essentially the formation of a standing wave within that structure, which will persist if the external excitation is maintained at the frequency of the standing wave. The vibration of a natural mode is therefore a steady state response. The natural modes of a structure are determined by its distribution of mass and stiffness in space, so the excitation of a natural mode that involves the entire object cannot occur until such time as stress waves have been able to traverse the entirety of the object and be reflected back to their origin enough times for a standing wave to form.

The dilatational and distortional wave speeds, $c_p$ and $c_s$, are given by Equations 1.1 and 1.2 respectively. Using these expressions it was found that, in the Stage 1 and Stage 2 models the dilatational and distortional stress waves travel through the skull with speeds of $c_p$ = 2781 m/s and $c_s$ = 1605 m/s, while in the Stage 3 model these stress waves have speeds $c_p$ = 2089 m/s and $c_s$ = 1252 m/s. Therefore, in the Stage 2 model for example, the dilatational stress waves will require 0.183 ms to travel once around the skull, from the coup to the contrecoup and back, and the distortional waves require 0.318 ms (utilising the shortest route, which lies approximately on the coronal plane and was measured as 254.85 mm). Consider impact Case 2.12 from Stage 2, one of the shortest impacts investigated in this study with a contact duration $T_p$ of 0.169 ms. This impact case clearly exhibited dynamic pressure magnification in the same fashion as other short duration impacts (see Figure 4.8), yet here the dynamic intracranial pressures occurred before even

the faster dilatational stress waves had been able to traverse the entire skull and return to the coup. It follows that a standing wave could not have been formed within the duration of impact, and consequently that resonance of the skull, when it does arise, is a separate and independent occurrence from the dynamic pressure magnification mechanism.

Subsequently, the analysis and interpretation of the results from the current research was directed towards the identification of an alternative causative mechanism. It was postulated that the large dynamic pressure transients which arise in the brain beneath the impact site may be caused by local contact phenomena: namely, in the case of blunt head impact, due to the small amount of skull deflection which occurs at this location. This was explored initially using the dynamic impact Case 1.10, since the Stage 1 model's simple geometry made it easier to analyse. The velocity-time history of the node which lay directly beneath the centre of the impactor, on the inner surface of the skull (i.e. at the brain-skull boundary of the coup) was exported from D3PLOT, and differentiated in T/HIS to obtain this node's acceleration-time history during impact. This acceleration acted parallel to the axis of impact and was a function of time. Since contact between the skull and impactor occurred over a comparatively small area, the acceleration of this node could be assumed equivalent to the acceleration of the small region of skull at the coup which deflects as a result of impact: this was denoted $a_0$. In Figure 6.2, below, the intracranial pressure-time history captured at the coup for impact Case 1.10, and the local acceleration of the skull beneath the impactor $a_0$ for this case, are plotted together in relation to separate vertical axes[6].

Figure 6.2 depicts the three large alternating transients of intracranial pressure at the coup which are characteristic of the dynamic response: it can be seen that these follow the acceleration-time history $a_0$ closely. There is a slight delay of approximately 0.05 to 0.07 ms between these curves, which is a consequence of the intracranial coup pressure's dependence on the acceleration of the local skull region as a whole, not just its central node[7]. It is evident that the intracranial pressure captured at the coup sampling point is

---

[6] Note that here, and for the following pages (Section 6.1.2.1), all graphs use standard SI units so that they can be more easily related to the calculations that follow.

[7] This delay could be expected to be a "transit time" given by the sampling point's distance from the brain-skull boundary $r$ = 5.30 mm divided by the dilatational wave speed through brain material $c_p$ = 1475 m/s, as calculated using the equivalent to Equation 1.1 for a fluid: $c_p = (B_f / \rho_f)^{1/2}$ (Porges, 1979). However, this gives 0.0036 ms, which is an order of magnitude smaller than the delay visible

strongly influenced by the local acceleration-time history of the skull, being effectively directly proportional to it. This was expected since the problem, involving the unsteady flow of a fluid assumed to be incompressible and inviscid, can be described by Euler's equation of fluid motion (negating the effect of gravity):

$$-\frac{\partial P}{\partial x} = \rho_f a \qquad [6.1]$$

which relates the rate of change of pressure $P$ (Pa) in the fluid with respect to the distance $x$ (m) along a pathline, to the product of fluid density $\rho_f$ (kg/m$^3$) and the local acceleration of a particle of fluid along the pathline $a$ (m/s$^2$) (Crowe, Elger, & Roberson, 2005).

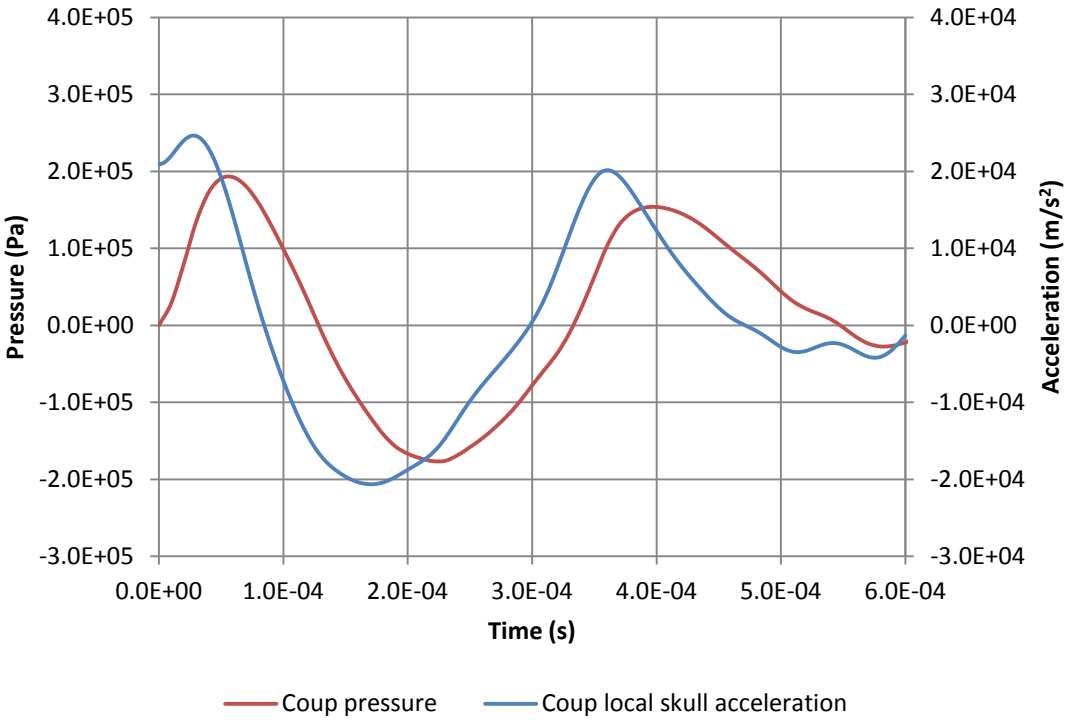


*Figure 6.2: Case 1.10, local pressure-time history recorded in the brain at the coup, and local acceleration $a_0$ of the skull region located at the impact site plotted with respect to a secondary vertical axis.*

---

in Figure 6.2. The delay actually arises from the fact that during impact the contact radius grows, reaching its maximum value $y_C$ at approximately $t = T_p/2$. Therefore, while the magnitude of the acceleration transients experienced by different points in the deflected region of the skull will be similar, the time before those transients are initiated increases as a function of the points' distance from the central node. Assuming a linear growth in contact radius, the average time before the acceleration transients are initiated can be approximated as $T_p/4$, which in this case gives 0.086 ms, similar to the observed delay.

### *6.1.2.1 Analytical description of dynamic coup pressures*

The above evidence seems to verify the proposal that dynamic pressure magnification beneath the coup is caused by skull deflection at this location. With this knowledge, an analytical description of the intracranial pressures which arise at the coup could be derived.

The first step was to arrive at a relationship between acceleration $a_0$ of the deflected region of skull and the pressure $P_R$ in the fluid at some point *R*, where *R* lies on the axis of impact and is a constant distance *r* from the inner surface of the skull. The analytical representation of dynamic pressures at the coup builds upon many of the approximations made and expressions derived in Young's (2003) analytical model of head impact: these are explained at length in Section 1.5 and for the sake of brevity will not be restated. Consider an elastic fluid-filled sphere representing the head, colliding with an elastic spherical mass. In Young's analytical model the Hertzian and membrane/bending components of contact stiffness, $k_H$ and $k_{sh}$, are given by Equations 1.7 and 1.8. Assuming the peak impact force $F_{max}$ is known, Young provides an expression for the total maximum deformation at the contact site $x_C$, where $x_C$ is normal to the contact surface (P. G. Young, 2003):

$$x_C = \frac{F_{max}}{k_{sh}} + \left(\frac{F_{max}}{k_H}\right)^{2/3} \qquad [6.2]$$

This deformation occurs across both the head and impactor. The maximum contact radius between these two bodies $y_C$ can be straightforwardly estimated as the radius of the circular cross-section that would exist in a sphere defined by radius $R^*$ if it were intersected by a plane at a distance $x_C$ beneath the sphere's surface:

$$y_C = \sqrt{R^{*2} - (R^* - x_C)^2} \qquad [6.3]$$

where $R^*$ is the relative external radius of curvature between the two colliding bodies [Equation 1.9]. The growth of the contact area is ignored such that it is approximated by a circle of constant area, defined by the maximum contact radius $y_C$. The intracranial pressure at the coup will be dependent on the local area of the interior surface of the skull which deflects as a result of impact and so disturbs the enclosed fluid. Similar to the contact area on the exterior of the skull, the area of this interior surface is assumed constant and is approximated by a circle of radius $y_0$. If the thickness of the skull *h* is small compared to the contact area defined by $y_C$, the contact area will approximate well the disturbed area on the interior of the skull: i.e. $y_0 \approx y_C$. However, as a result of the force transferred during impact, the elastic skull also experiences deformation removed from the contact site. An expression

describing the deflection $d$ under a distributed load applied radially over a small circular cap on the surface of a partial spherical shell is given in the literature (W. Young & Budynas, 2002):

$$d = \mathcal{A}\frac{F \cdot R_{sh}\sqrt{1-\nu_{sh}^2}}{E_{sh} \cdot h^2} \qquad [6.4]$$

where $F$ is the applied force, $R_{sh}$ is the radius of curvature of the shell, $h$ is its thickness, $E_{sh}$ and $\nu_{sh}$ are the elastic modulus and Poisson's ratio respectively, and $\mathcal{A}$ is a coefficient whose value depends on the dimensions $y_C$ (the radius over which the force is applied), $R_{sh}$, and $h$. Values of $\mathcal{A}$ are tabulated in Roark's Formulas for Stress and Strain and range between 0.286 to 0.433 (W. Young & Budynas, 2002). Substituting the peak impact force $F_{max}$ for $F$, Equation 6.4 gives the maximum deflection $d_{max}$. The maximum value of $y_0$ can then be estimated as the sum of $y_C$ and (using the method applied previously in Equation 6.3) the radius of a circular cross-section at depth $d_{max}$ in a sphere defined by $R_{sh}$:

$$y_0 = y_C + \sqrt{R_{sh}^2 - (R_{sh} - d_{max})^2} \qquad [6.5]$$

This is a gross approximation, but appears to perform well nevertheless.

If $y_0$ is small compared to the radius of curvature $R_f$, then the deflected region of the interior surface of the skull can be thought of as a rigid flat disc with area $\pi y_0^2$. As a result of impact, this disc has time-dependant acceleration $a_0$ in the direction normal to its surface.

Further simplifications can be introduced if the problem is assumed analogous to the steady flow of fluid through a conical pipe. Consider a diverging conical pipe whose radius increases as a function of the distance $r$ along the exterior of the pipe, which has an angle $\theta$ relative to the pipe's central axis. At $r = 0$ a rigid disc with origin $O$ and radius $y_0$ applies a force on the fluid directed along the pipe's central axis. The force $F_0$ acting on an infinitesimally thin layer of fluid of width $\partial x$ adjacent to this disc, is given by Newton's second law:

$$F_0 = ma_0 = a_0\rho_f\pi y_0^2 \cdot \partial x \qquad [6.6]$$

At any distance along the pipe where $r$ is large compared to $y_0$, an imaginary domed surface can be defined whose exterior edge meets (and is approximately normal to) the interior of the pipe. The area of this imaginary surface increases as a function of $r$, and is given by $2\pi r \cdot [r - r \cdot \cos(\theta)]$. The fluid particles which lie on this domed surface will all be an equal

distance $r$ from the origin of the plate $O$. As a result of the force at $r = 0$, the fluid particles which lie on the imaginary surface become accelerated and displace radially away from $O$. The unimpeded movement of these fluid particles is resisted by the presence of the fluid ahead, hence this domed fluid "layer" is subjected to a force $F_R$. By Newton's third law, the reaction $F_R$ distributed across the imaginary surface in the fluid will be equal in magnitude, but opposite in direction to the initial force $F_0$. This reaction takes the form of a local change in pressure $P_R$:

$$\partial P_R = \frac{a_0 \cdot \rho_f \cdot \pi y_0^2 \cdot \partial x}{2\pi r \cdot (r - r\cos\theta)} \qquad [6.7]$$

Since the radius of curvature $R_f$ is large compared to the other dimensions, the conical pipe approaches a flat plate with a circular aperture of radius $y_0$ at the origin $O$. The angle $\theta \rightarrow \pi/2$, so Equation 6.7 becomes:

$$\partial P_R = \frac{a_0 \cdot \rho_f \cdot \pi y_0^2 \cdot \partial x}{2\pi r^2} \rightarrow \frac{\partial P_R}{\partial x} = \rho_f a_0 \frac{y_0^2}{2r^2} \qquad [6.8]$$

The above expression has been rearranged to the familiar form of Euler's equation of fluid motion [Equation 6.1]. The term $2\pi r^2$ in the denominator of Equation 6.8 is equal to half the surface area of a sphere, and is consistent with the assumption made regarding the domed surfaces of equal pressure which exist at any distance $r$ from $O$. The term $a_0 \cdot (y_0^2/2r^2)$ describes the local acceleration of a fluid particle $a_R$ some distance removed from the initial disturbance: a hemi-spherical field of acceleration exists in the fluid, decreasing away from the origin $O$ at a rate proportional to $1/r^2$ (i.e. the common "inverse-square law").

Integrating Equation 6.8 over $x$ gives an expression for the local pressure at some distance $x$ from $O$, where $x$ is along the central axis of the pipe (i.e. the axis of impact). Here $x = r$, so we obtain the local fluid pressure $P_R$:

$$P_R = \rho_f a_0 \frac{y_0^2}{2r^2} x = \rho_f a_0 \frac{y_0^2}{2r} \qquad [6.9]$$

Equation 6.9 is in agreement with the literature in that it states that radiated pressure decreases with the inverse of $r$, rather than $r^2$ like many other natural phenomena (Porges, 1979). In Figure 6.3, below, the intracranial pressure at the coup resulting from impact Case 1.10 is presented, along with the coup pressure predicted by Equation 6.9 utilising the measured local acceleration-time history of the skull (see Figure 6.2). Examining the peak positive pressure values achieved during the recorded and predicted pressure-time histories

it was found that, for this case, the analytical model underestimates intracranial pressure by only 3.66%. The model appears to be effective despite the gross approximations upon which it was based, and the fact that not all of its limits were adhered to[8].

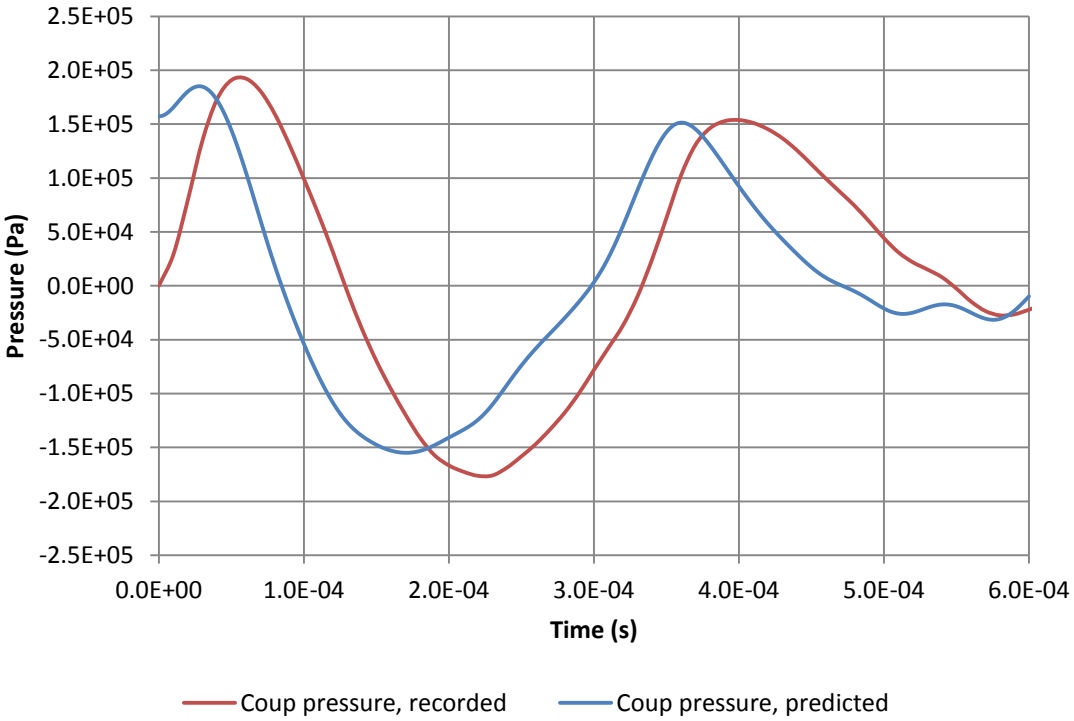


*Figure 6.3: Case 1.10, local pressure-time history recorded in the brain at the coup, and the pressure predicted at this location using Equation 6.9, based on the known local acceleration of the skull $a_0$.*

---

[8] An incompressible and inviscid fluid was assumed: this justifies the use of Euler's equation (Crowe et al., 2005). Furthermore, by assuming steady flow the problem became more tractable by removing the need to consider time derivatives: however, this is only valid if the rate of change of fluid flow, proportional to $\partial a_0/\partial t$, is at all times small compared to the time it takes a particle of fluid to travel the distance $r$. Further assumptions were made regarding the contact area and the area of the interior of the skull which disturbs the fluid: both of these were assumed rigid, flat, and circular, with constant area. This, by definition, introduces the assumption that the acceleration of this region was equal at all points across $y_0$, while in reality it would vary, being greater towards the centre at $O$. It is likely this latter point that resulted in the analytical model's underestimation of intracranial pressure.

Finally, it was assumed that surfaces of equal fluid pressure exist at any distance $r$ from $O$: in effect describing waves propagating with hemi-spherical wavefronts from a point source. This introduces the limit that $r$ must be significantly greater than $y_0$. For Case 1.10 this does not hold true: in fact the calculated $y_0$ was 1.6 times greater than $r$.

The above method allows the estimation of coup intracranial pressures given the local acceleration-time history of the skull beneath the impact site $a_0$ is known. Obtaining detailed knowledge of this localised skull acceleration after a real world head impact has occurred is generally not possible, and even in controlled conditions during physical or cadaveric experiments it remains non-trivial. However, the acceleration-time history $a_0$ can be estimated by an extension to Young's (2003) original analytical model of head impact.

Using Young's analytical model, the characteristics $T_p$ and $F_{max}$, i.e. the total contact duration and peak impact force transferred to the head by a collinear collision with a solid spherical mass, can be predicted by Equations 1.12 and 1.14 given rudimentary knowledge of the head and impactor's material properties, dimensions, and velocities prior to impact. Young states that, for the majority of cases, the actual force-time history of impact can be approximated well by a Hanning force-time history $F(t)$, which is dependent on $T_p$ and $F_{max}$ (P. G. Young, 2003):

$$F(t) = F_{max}\left[\frac{1}{2} - \frac{1}{2}\cos\left(2\pi \cdot \frac{t}{T_p}\right)\right] \qquad [6.10]$$

As long as the local deflection of the skull beneath the impactor remains small, such that the system is geometrically linear, the deflection with respect to time $d(t)$ can be found by substituting $F(t)$ [Equation 6.10] for $F$ in Equation 6.4.

Writing $F(t) \cdot \frac{\mathcal{A} \cdot R_{sh}\sqrt{1-\nu_{sh}^2}}{E_{sh} \cdot h^2}$ as $F(t) \cdot k^{-1}$ one obtains:

$$d(t) = F_{max} \cdot k^{-1}\left[\frac{1}{2} - \frac{1}{2}\cos\left(2\pi \cdot \frac{t}{T_p}\right)\right] \qquad [6.11]$$

where $k$ is the ability of the skull to resist radial deformation at the coup (i.e. its stiffness) and is based on an existing formula describing a partial spherical shell (W. Young & Budynas, 2002). Figure 6.4, below, illustrates the arrangement with a simple diagram: the deflection of the domed shell representing the skull $d(t)$ is positive if in the same direction at the impact force $F(t)$.

Differentiating Equation 6.11 with respect to time gives an expression which describes the velocity-time history of the skull beneath the impact site $v(t)$, and differentiating this once more one arrives at a description of the acceleration-time history $a_0(t)$. These can be written as:

$$\frac{\partial d(t)}{\partial t} = v(t) = \frac{\pi \cdot F_{max} \cdot k^{-1}}{T_p} \sin\left(2\pi \cdot \frac{t}{T_p}\right) \qquad [6.12]$$

$$\frac{\partial v(t)}{\partial t} = a_0(t) = \frac{2\pi^2 \cdot F_{max} \cdot k^{-1}}{{T_p}^2} \cos\left(2\pi \cdot \frac{t}{T_p}\right) \qquad [6.13]$$

Finally, this expression for the acceleration $a_0(t)$ can be substituted into the previously derived Equation 6.9 to obtain an analytical representation of the coup intracranial pressure-time history $P_R(t)$:

$$P_R(t) = \frac{\pi^2 \cdot F_{max} \cdot k^{-1} \cdot \rho_f \cdot y_0^2}{{T_p}^2 \cdot r} \cos\left(2\pi \cdot \frac{t}{T_p}\right) \qquad [6.14]$$

In addition, a slightly modified form of Equation 6.14 attempts to take into account the time delay before these pressures are experienced; this delay is approximated by the inclusion of the phase offset term $-T_p/4$, as mentioned in the footnotes[7].

$$P_R(t) = \frac{\pi^2 \cdot F_{max} \cdot k^{-1} \cdot \rho_f \cdot y_0^2}{{T_p}^2 \cdot r} \cos\left(2\pi \cdot \frac{t - T_p/4}{T_p}\right) \qquad [6.15]$$

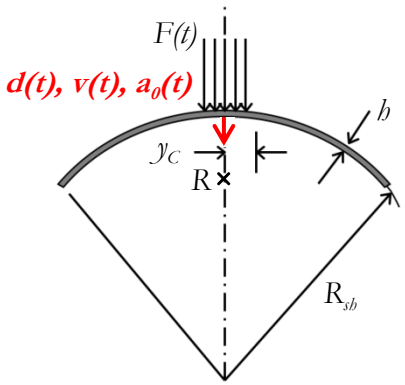


*Figure 6.4: Diagram of the domed shell representing the skull at the coup. The force F(t) acts over a small circular area of radius $y_C$. The resulting deflection, velocity, and acceleration of the skull beneath this force are marked in red.*

The accuracy of the analytical model derived above was explored by attempting to predict the dynamic intracranial pressure transients at the coup resulting from impact Case 1.10. The analytical model requires known values of the impact characteristics $T_p$ and $F_{max}$; these can be calculated using Young's (2003) analytical model, however here "exact" values measured during the original experiment were available and so were used. In Case 1.10, the contact duration $T_p$ was recorded as 3.440e-4 s (0.344 ms) and the peak impact force $F_{max}$ was 763 N (0.763 kN). Assuming a Hanning force-time history, the impact force with respect to time was given by Equation 6.10 and is plotted below in Figure 6.5 (a). Since the

material properties and dimensions of the head and impactor were known, the local deflection, velocity, and acceleration of the skull beneath the impactor could be estimated with Equations 6.11 to 6.13, and are presented in Figure 6.5 (b-d). Lastly, the pressure in the brain at the coup (at $r$ = 5.30 mm away from the interior surface of the skull) was estimated using Equation 6.15, and is plotted in Figure 6.6 alongside the pressure-time history captured at this location during the original finite element experiment.

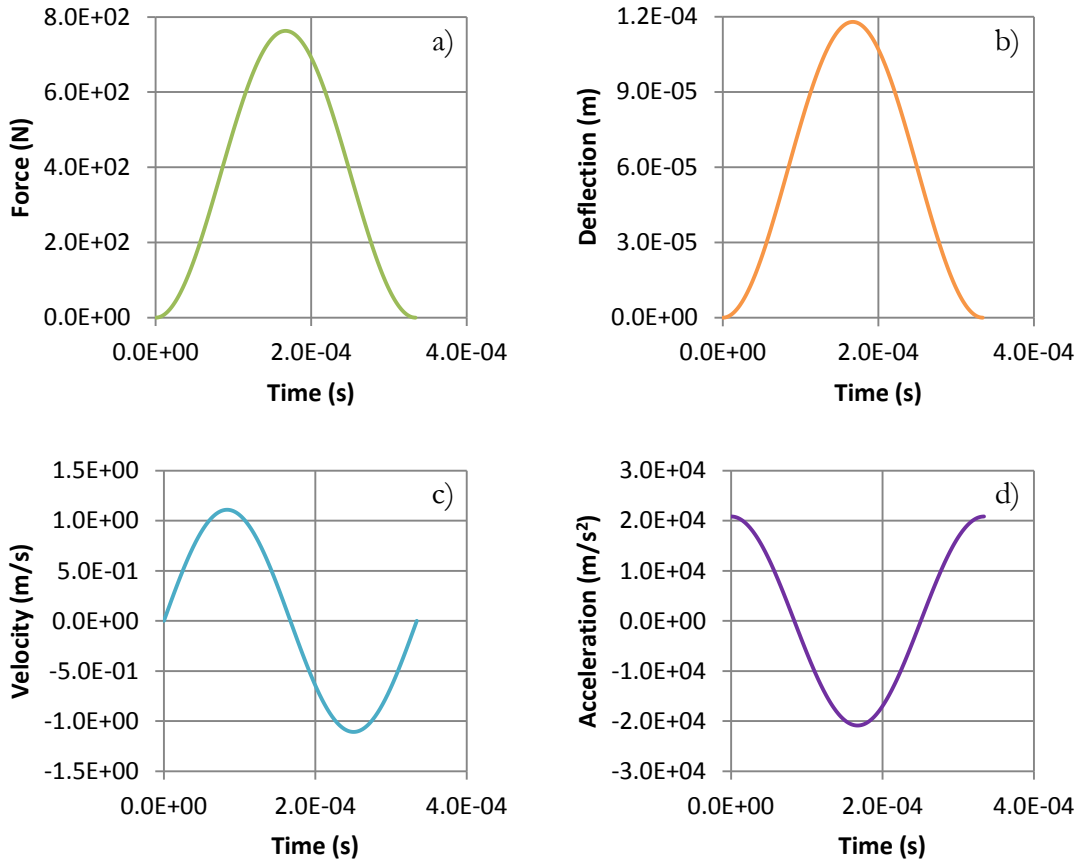


*Figure 6.5: Case 1.10, analytical predictions of: (a) the force-time history of impact F(t), (b) the local deflection of the skull at the impact site d(t), (c) the velocity of this skull region v(t), and (d) the acceleration of this skull region $a_0(t)$.*

Unlike in Figure 6.3, in Figure 6.6 the intracranial pressures predicted at the coup were not derived from a pre-existing knowledge of the local acceleration of the skull beneath the impactor, but were based solely on the impact characteristics $T_p$ and $F_{max}$. Comparing the experimental and analytical pressure transients in this figure, it can be seen that, despite being constructed by many successive approximations, the analytical model is able to predict well the magnitude and duration of these transients. In Figure 6.6, the analytical model underestimates the peak positive intracranial pressure at the coup by 23.14% compared to the experimental data.

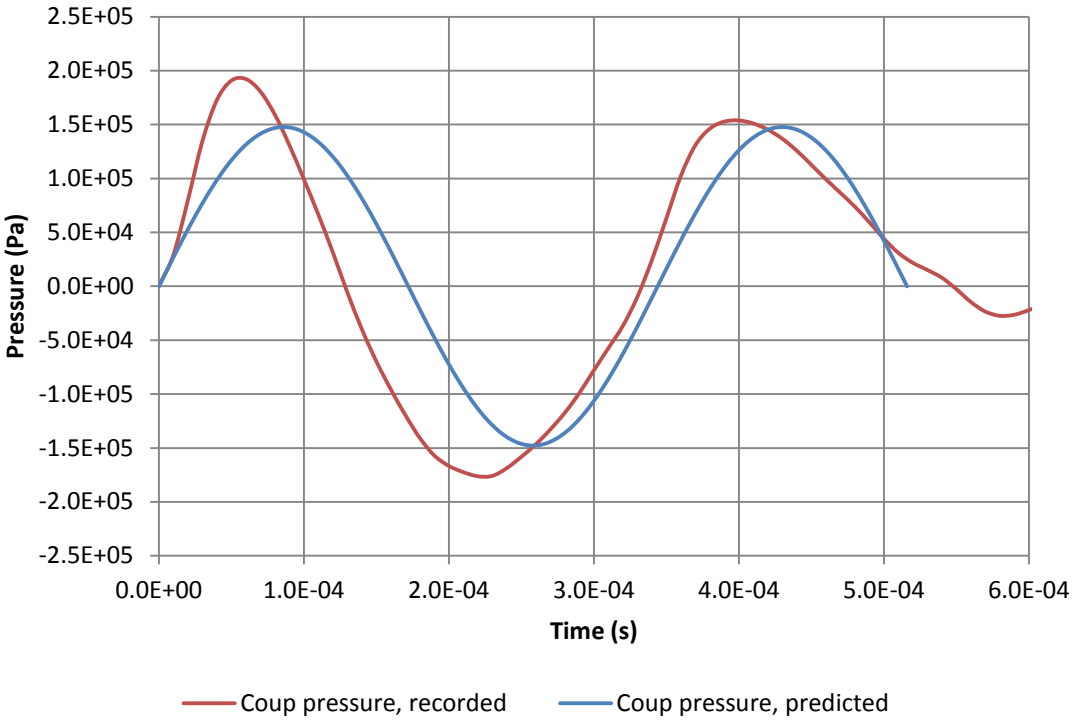


*Figure 6.6: Case 1.10, local pressure-time history recorded in the brain at the coup, and the pressure predicted at this location using Equation 6.15.*

The above procedure was also applied to the shortest duration impact performed on the Stage 3 biofidelic head model: impact by a light spherical mass. Figure 6.7, below, presents the dynamic intracranial pressure transients recorded at the coup during this impact case and those predicted at the same location by Equation 6.15. This prediction is based on the impact characteristics $T_p$ and $F_{max}$, which had been measured experimentally as 3.260e-4 s (0.326 ms) and 6948 N (6.948 kN) respectively. The analytical model assumes that the skull geometry at the impact site can be approximated by a partial spherical shell with radius of curvature $R_{sh}$ and thickness $h$. Just as when Young's (2003) analytical description of head impact was applied to the Stage 3 model (Section 5.2.1), suitable values of $R_{sh}$ and $h$ had to be measured directly from the finite element mesh, since the realistic skull geometry has neither a constant radius or thickness. Here $R_{sh}$ refers to the local radius of the skull at the impact site, not the local radius of the scalp, and was measured as being 58.00 mm, while $h$ was found to be 6.26 mm. Also, in order to represent the effect of the scalp layer, when calculating the relative elastic moduli $E^*$ [Equation 1.10] the impactor's elastic modulus $E_{sol}$ was substituted for the modulus of the linear elastic flesh (16.7 MPa).

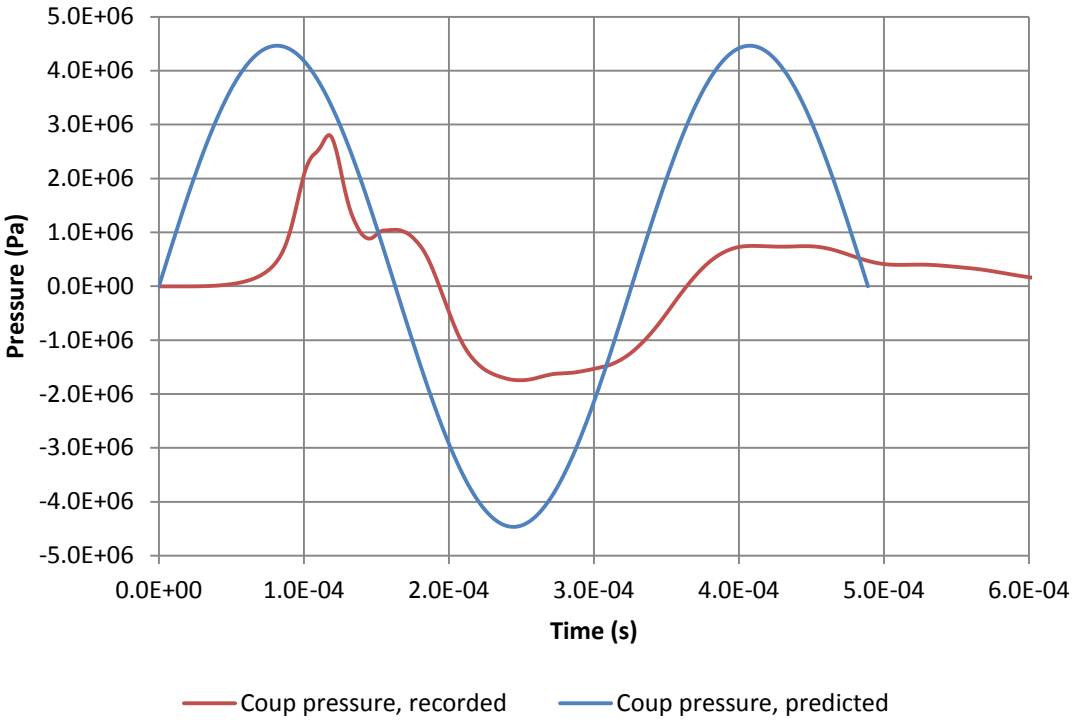


*Figure 6.7: Impact by a light spherical mass, Stage 3 case study: local pressure-time history recorded in the brain at the coup, and the pressure predicted at this location using Equation 6.15.*

In Figure 6.7 it can be seen that, in this case, the analytical model significantly overestimates the dynamic intracranial pressure transients. Examining once again the peak positive pressures, it was found that the predicted value differed from the experimentally observed value by 59.08%. Clearly the analytical model correlates better with experiments involving idealised spherical geometries (such as the Stage 1 model), since the analytical model is itself based on similar idealisations. Nevertheless, the intracranial pressure predictions for this Stage 3 impact case were remarkably similar to the experimental values given the many additional complexities of the biofidelic head model which the analytical model could not take into account (e.g. realistic geometry, viscoelastic brain material, presence of CSF, cushioning non-linear scalp layer, and constraints introduced by the neck).

In summary, a series of simple explicit expressions have been derived which allow the approximate prediction of local fluid pressures that occur as a result of the deflection of the exterior of an elastic fluid-filled container subject to impact. While these may have some relevance to other fields, such as the design of pressure vessels, they were developed and used here in regard to explaining the mechanism by which large, short duration, dynamic pressure transients develop in the brain. In this respect, it is important to note that

the analytical model negates any *global* acceleration of the head, i.e. it assumes that the entire amount of energy transferred by the collision is employed in the development of *local* acceleration of the skull at the impact site. Therefore, the model is only accurate for very short duration (or fixed) head impact cases, which do not induce any significant motion of the head as a whole. Lastly, two important findings arose as a consequence of this derivation:

1. Intracranial pressures which are a result of the deflection of the skull at the impact site are proportional to the acceleration of this skull region. While the peak deflection resulting from different impact scenarios which share a constant value of peak impact force $F_{max}$ will be the same, the *rate* at which the skull travels in order to achieve this deflection is strongly dependant on the impact duration $T_p$. In this way, shorter duration impacts result in a greater magnitude of local skull acceleration. This explains how short duration impacts with $F_{max}$ values equal to those in similar longer duration impacts were able to produce significantly greater intracranial pressures, as was observed many times experimentally in the preceding chapters.
2. The dynamic pressure magnification response has the counter-intuitive tendency of generating negative pressure in the brain beneath the impact site when the deflection of the skull is greatest, i.e. approximately half way through the impact. This is due to the fact that at this instant the velocity of the impactor becomes reversed: its acceleration is negative, away from the centre of the head, causing the adjacent fluid to experience negative pressure. Also in this regard, the fact that the dynamic pressure response is characterised by only three large pressure transients, which have alternating sign, is explained by the pressure's close relationship with the local acceleration of the skull, which rises and falls in the same manner.

#### *6.1.2.2 Analysis of other time dependant phenomena*

The above analysis describes in some detail the generation of dynamic pressure transients at the coup in the brain. However, it has been noted that during the dynamic pressure magnification response similar pressure transients also occur at the contrecoup. In Section 5.2.2.3, the observation that areas of raised intracranial pressure generated at the coup migrate towards the contrecoup in the form of "ripples", which travel along the brain-skull boundary, was discussed. Analysis revealed that these "ripples" of pressure were caused by local deformations (and associated accelerations) formed in the skull by mechanical waves which radiate away from the impact site. The roughly spherical geometry of the head

causes these waves to have similar arrival times at the contrecoup: by means of constructive interference, the "ripples" of smaller pressure are superimposed at the contrecoup to form pressure transients of comparable magnitude to those which had existed at the coup some time earlier. This delay could be obtained by measuring the time between the beginning (or between the crests/troughs) of the corresponding large pressure transients at the coup and at the contrecoup. It was previously believed that distortional waves were the most likely type of wave by which these large pressure transients were communicated to the contrecoup, however the measured time delay did not match the predicted wave speed.

The mechanical waves were visualised in D3PLOT, and once again, the Stage 1 fluid-filled sphere head model was used to simplify the analysis. Short duration impacts in the Stage 1 investigation produced dynamic pressure transients at the contrecoup ranging between 0.698 to 0.766 ms after they were observed at the coup. A typical delay was 0.744 ms, which occurred in the dynamic impact Case 1.10. The distance through the spherical shell from the coup to the contrecoup (half the circumference) was calculated as 245.37 mm; from this the velocity of the mechanical waves which carry the large dynamic disturbances to the contrecoup could be back-inferred as 330 m/s. This differed significantly from the speeds of the dilatational and distortional waves, which were predicted to reach the contrecoup after only 0.088 and 0.153 ms respectively. Velocity vectors on the mid-plane of the spherical shell in Case 1.10, see Figure 6.8 below, serve to illustrate the different mechanical waves travelling through the structure.

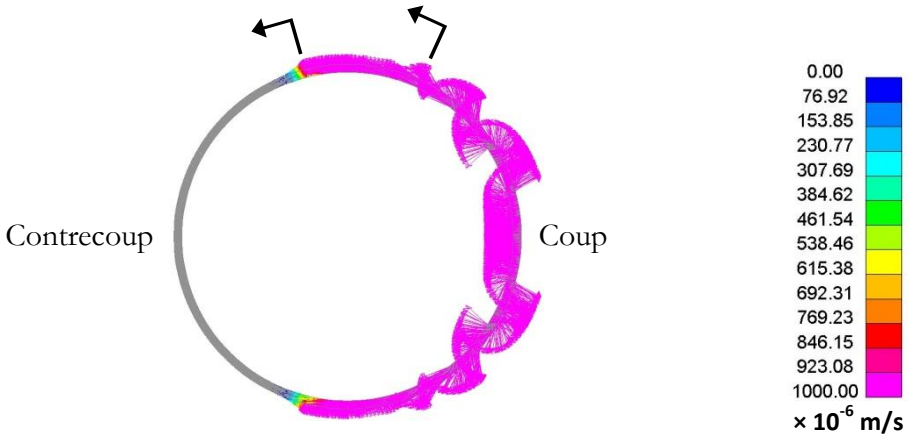


*Figure 6.8: Case 1.10, velocity vectors on the mid-plane of the skull, 0.060 ms after impact. Other features have been blanked. Black arrows indicate the location and direction of the dilatational and distortional wavefronts.*

Three distinct types of mechanical wave were observed. The first were dilatational waves: these travelled fastest, arriving at the contrecoup after approximately 0.080 ms, roughly in

agreement with the arrival time predicted above. The advancing dilatational wavefront can be seen to have travelled the furthest in Figure 6.8, marked by the leftmost arrow. These were followed by distortional waves, which travelled slightly slower, reaching the contrecoup at approximately 0.160 ms. The advancing distortional wavefront is marked by the rightmost arrow. Distortional waves are characterised by the out-of-plane motion of the material, and so were clearly distinguishable from the dilatational waves in which the local deformations within the material are parallel to the motion of the wave itself.

A third type of wave was apparent: these waves were significantly slower than the others, and their arrival time coincided exactly with the beginning of the large dynamic pressure transients at the contrecoup (hence they had an average velocity of 330 m/s, as previously back-inferred). These waves were also distortional in nature, characterised by out-of-plane motion of the material, but had a large amplitude and long wavelength, with crests much further apart than the distortional waves. These waves carried the majority of the energy compared to the other wave types observed. A second velocity vector image captured at a later time, Figure 6.9 (c), is necessary to illustrate this third type of wave.

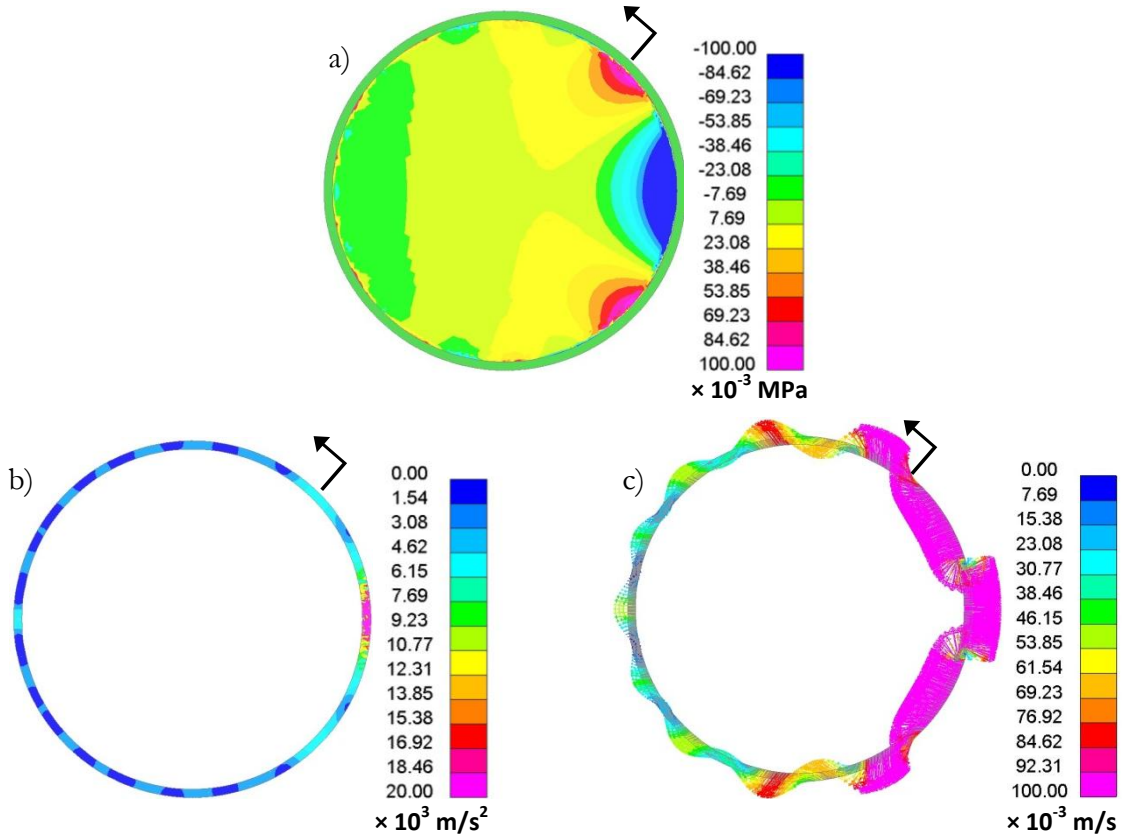


*Figure 6.9: Case 1.10, mid-plane view: (a) contours of pressure in the brain, (b) contours of acceleration in the skull, and (c) velocity vectors in the skull, all captured at 0.230 ms after impact. Black arrows mark the progress of a pressure "ripple".*

The arrow in Figure 6.9 (a) marks the location and direction of a pressure "ripple" travelling towards the contrecoup sometime after impact ($t$ = 0.230 ms). Figure 6.9 (b) depicts the magnitude of the acceleration of the skull material[9], and an arrow in the same location highlights the local acceleration that induces the aforementioned pressure "ripple". Figure 6.9 (c), in turn, depicts the velocity vectors at this instant: waves of the third type can be seen radiating away from the coup, these are of larger amplitude than the rest and are coloured in magenta. An arrow at the same location as before is found to lie above an area where this wave has caused the skull material to undergo a rapid change in velocity, which corresponds to the acceleration depicted previously. Clearly it is this third type of wave which transports the large dynamic pressures from the coup to the contrecoup.

As dilatational and distortional waves travel through a bounded medium, such as a plate of finite thickness $h$, they interfere with each other to produce resonant waves called "Lamb waves" (Shull, 2002). The material motion of these elastic waves can be either symmetric or anti-symmetric about the centre of the plate. There are an infinite number of possible symmetric (S0, S1, S2...) and anti-symmetric (A0, A1, A2...) wave modes, and due to their dispersive nature, these wave modes travel at different speeds depending on the ratio of their wavelength (or frequency $f$) to the plate thickness $h$, as well as the properties of the material (Shull, 2002). These types of waves were originally studied by Lamb in 1917 (Lamb, 1917), but solutions to the characteristic equations developed remained intractable until numerical methods were available. The practical study of Lamb waves relies heavily on "dispersion curves", computed numerically, that relate the frequency of the wave $f$ to its phase velocity $c_{ph}$ in a plate of known material properties and thickness (Rose, 2003). Of these symmetric and anti-symmetric modes, only the two "zero-order modes" exist across all frequencies: these are the "extensional" symmetric wave mode (S0), and the "flexural" anti-symmetric wave mode (A0) (McKnight, 2012).

The speed and motion of the third wave type visible in Figure 6.9 suggests it is a flexural wave. When examined in D3PLOT, individual points in the material appeared to travel in elliptical orbits, which agrees with the material motion of an anti-symmetric Lamb wave (McKnight, 2012) as illustrated by the velocity vector diagram in Figure 6.10 below.

---

[9] Note that in Figure 6.9 (b), the local area of the skull with the greatest acceleration lay beneath the impactor, and was measured to be circular with a radius of approximately 8.35 mm. This agrees well with the equivalent radius $y_0$ from the analytical model derived in Section 6.1.2.1, which was calculated using Equation 6.5 to be 8.91 mm for this case.

*Figure 6.10: Diagram of particle motion through the cross-section of an elastic plate during the propagation of an anti-symmetric Lamb wave. Note the particle motion in the material follows elliptical orbits. (Giurgiutiu, 2000)*

Dispersion curves for a plate with thickness equal to that of the spherical shell used in the Stage 1 head model ($h$ = 3.81 mm), and with equal material properties, were calculated using the Waveform Revealer software application (Laboratory for Adaptive Materials and Smart Structures, 2012). The computed dispersion curves can be seen below in Figure 6.11; these compare well to dispersion curves of bone available in the open literature, such as that used in the study of bovine cortical long bone by Hapsara & Iliescu (2012).

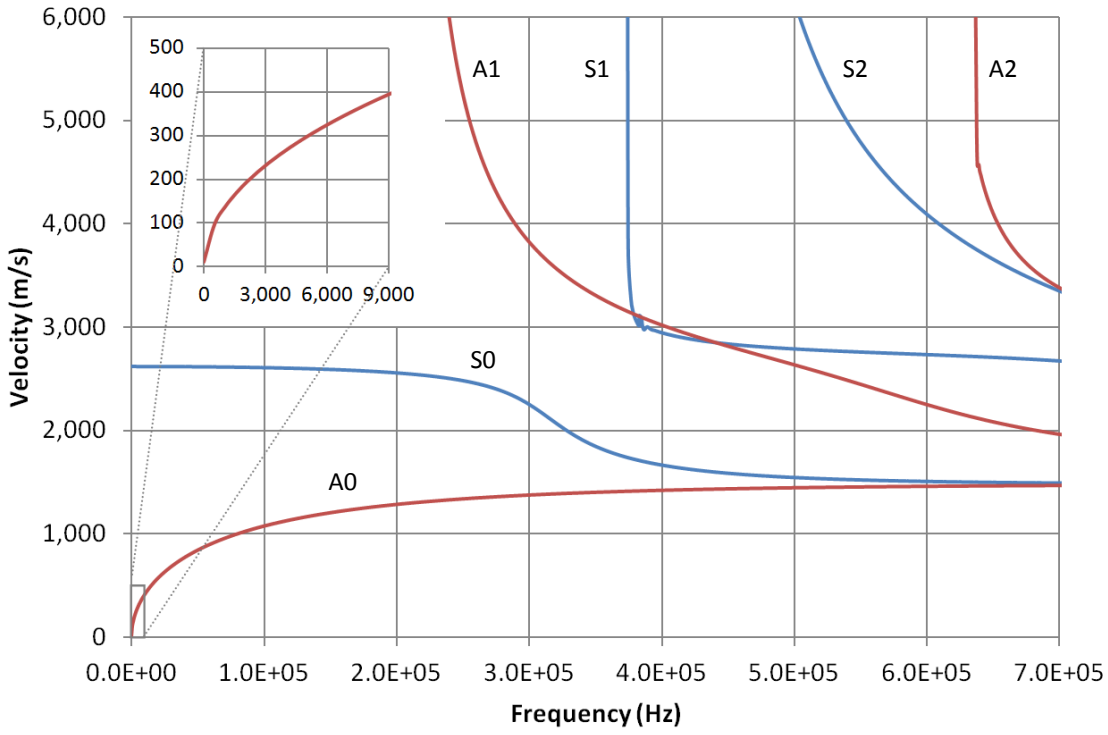


*Figure 6.11: Dispersion curves of the skull material used in the Stage 1 model, for an infinite two-dimensional plate of thickness 3.81 mm. The speed of the first three symmetric and anti-symmetric wave modes are plotted against frequency.*

It is reasonable to assume that the frequency of the flexural wave which transports the dynamic intracranial pressure transients from the coup to the contrecoup is equal to the forcing frequency of the disturbance, i.e. the "frequency of impact" ($1 / T_p$) mentioned in Section 6.1.1. For impact Case 1.10 this yields a frequency of 2907 Hz, which gives a predicted wave speed of 237 m/s for the flexural wave mode (see inset plot in Figure 6.11). While this predicted value is 28.18% less than the observed wave speed of 330 m/s, it is substantially closer to this observed speed than any of the other possible waves (the two possible bulk waves, dilatational and distortional, or the "extensional" symmetric Lamb wave). This underestimation of the predicted speed compared to the observed flexural wave speed was almost certainly due to the curvature inherent in the spherical shell[10], which could not be taken into account during the dispersion curve calculations in Waveform Revealer. The curvature of a domed surface acts to increase its radial stiffness over that of a flat plate, which would suggest an increased wave speed. Lamb waves in spherically curved plates have been addressed in the literature, and the speed of the various wave modes has been found to increase with the amount of curvature, i.e. with a decrease in the radius of curvature (Jiangong et al., 2007; Überall et al., 2000).

The solution to Lamb waves in spherical shells is complex and beyond the scope of this project; nevertheless the above analysis allowed the deduction of the wave mode responsible for the transport of dynamic pressures to the contrecoup, and provided an approximate speed for this wave, which was of the same order as the observed speed. Considering now the most complex model, used in Stage 3, the pressure-time histories captured in the short duration impact cases (the golf ball and light mass impacts) revealed delays of 0.801 and 0.809 ms respectively, between when the dynamic pressure transients were experienced by the coup and when they arrived at the contrecoup. From this the speed of the flexural wave through the skull could be back-inferred: for the light mass impact for example, this gave 315 m/s. This is close to the wave speed observed in the Stage 1 model, but slightly slower, presumably due to the biofidelic head model's use of a reduced skull elastic modulus.

---

[10] A further consideration was the fact that the skull is in contact with the CSF. The dispersion curve calculations were repeated in the PACshare Dispersion Curves software (Physical Acoustics Corp.), which allowed one surface of the plate to be modelled as the boundary of an infinite expanse of water. This was found to have no noticeable effect on the resulting wave speeds.

Finally, occasionally in the preceding chapters it was noted that the underlying transients which dominate a particular pressure-time history curve may be coloured by the inclusion of noise and small pressure fluctuations due to the excitation of higher order modes. A small amount of noise is inevitable and inherent in the numerical process used, but the moderate use of filtering where required (see Section 2.4.3.3) should have all but removed this numerical noise from the results. However, in both short and long duration impacts, small non-spurious periodic pressure fluctuations were frequently visible superimposed onto the dominant transients within the recorded pressure-time histories. These were particularly evident when examining quasi-static pressure-time histories (see for example Figures 3.3 or 4.2), due to the simple nature of the underlying signal which is known to be a single smooth sinusoidal "pulse".

While it was proven that excitation of the skull's longitudinal n=2 mode is not the cause of the dynamic pressure magnification response, the impacts were still likely to excite this mode to a greater or lesser degree. This introduces pressure fluctuations at the coup and contrecoup with a period equal to the period of this mode, $T_{\Omega}$. For example, the small pressure fluctuations superimposed onto the quasi-static response in Figure 4.2 have a period of $T_{\Omega}$, indicating excitation of this mode. Furthermore, when the contact duration $T_p$ is similar to $T_{\Omega}$ resonance of this mode can be expected to be far more pronounced: pressure fluctuations with a period close to $T_{\Omega}$ are distinctly visible in Figure 4.6, and were commented on throughout Section 4.2.2.3. The important point is, however, that in impacts where resonance of the skull does occur, it is separate from the local skull bending which causes the dynamic pressure magnification response, and tends to develop only after these larger dynamic pressure transients have ceased. In addition, while the Fourier analysis conducted above (Figure 6.1) suggests a certain amount of skull resonance did occur during the Stage 3 short duration impacts (the golf ball and light mass impact cases), there is little evidence of pressure fluctuations with a period of $T_{\Omega}$ visible in the pressure-time histories captured during these cases. Resonance of the skull appeared to have a negligible effect on the intracranial pressures in the biofidelic head model compared to the simpler models; this was perhaps due to the damping and attenuation of mechanical waves that could be expected from the introduction of a viscoelastic brain and the coating of soft scalp material that envelops the skull.

Lastly, the Fourier analysis presented at the outset of this chapter (Figure 6.1) clearly indicates, for the two short duration impact cases, the presence of a significant amount of high frequency content greater than the natural frequency of the skull's longitudinal n=2

mode ($1 / T_{\Omega}$). It is reasonable to assume that this is true in all three of the head models used. This high frequency content would inevitably lead to small fluctuations of pressure, oscillating with a short period. Indeed, such pressure fluctuations are visible throughout the Stage 1 results, and evident, although to a lesser degree, superimposed on pressure-time histories captured in Stage 2. These are presumably caused by the excitation of one of the many higher order modes that exist in the skull. For example, there are quite prominent fluctuations of pressure that occur in some of the Stage 1 pressure-time histories (particularly in Figures 3.5 and 3.6) that have a period of roughly 0.140 ms: however, this corresponds to a frequency of 7143 Hz which was beyond the frequency range investigated in the modal analyses.

Together, this and the previous section (Sections 6.1.2.1 and 6.1.2.2) provide a complete theoretical description of the mechanical processes that give rise to the dynamic "magnification" of intracranial pressures in short duration head impacts. These are initially brought about by local skull deformation at the coup, and communicated to the contrecoup by means of flexural waves.

### *6.1.3 Re-evaluating the threshold between quasi-static and dynamic intracranial behaviour*

It has been demonstrated throughout the preceding chapters, and in work by Young & Morfey (1998), Johnson (2005), and Johnson & Young (2005), that the duration of a given head impact is an excellent predictor of the system's response. In Young & Morfey's (1998) original research, it was noted that the results of their parametric studies on head impact could be collapsed onto the non-dimensional ratio of impact duration to the period of the first equivoluminal mode of the system, $T_p / T_{\Omega}$. Collapsing the results in this manner allowed a critical value of non-dimensional impact duration to be identified, $T_p / T_{\Omega} = 2$, which determines whether the intracranial response will be either quasi-static ($T_p / T_{\Omega} > 2$) or dynamic ($T_p / T_{\Omega} < 2$). The effectiveness of this criterion in predicting the nature of the pressure response has also been validated in this study, and an equal critical value was found. Furthermore, for the reasons discussed in Section 6.1.2.1, since this criterion is a function of impact duration $T_p$, in the dynamic regime it will reflect the amount of pressure "magnification" which occurs. A non-dimensional criterion such as this is useful since it is independent of the dimensions and properties of the head system; any critical values identified will apply equally to different head models or different patients.

The critical impact duration was ascertained empirically in this study, and in the previous related research, and was consistently found to be equal to twice the period of the first natural mode of the skull ($T_p = 2T_\Omega$). Therefore, it appears that the critical impact duration is dependent on the vibrational properties of the system, despite the fact that the dynamic "magnification" of intracranial pressures has been shown to be independent of the resonance of any of the skull's natural modes.

The quasi-static response is the result of rigid-body acceleration of the head, and the transition to the dynamic pressure response is only achieved when the impact duration becomes short, such that the load is no longer able to overcome the inertia of the system, so producing very little global head acceleration. In this case, the energy must be dissipated locally in the form of contact phenomena (local skull deflection) and the formation of mechanical waves. Considering loading in terms of frequency rather than time, it can be said that any arbitrary unsupported excitable structure subjected to an external periodic force with frequency below its lowest natural mode will behave as a rigid-body; this has been demonstrated also for the human skull (McKnight, 2012; Reinfeldt et al., 2013). Therefore, the limit of rigid-body motion is the lowest resonant frequency of the system: in response to an excitation at this frequency, or above, the skull does not behave as a purely rigid-body, rather its behaviour will be composed of different amounts of rigid-body motion, resonance of skull modes, and local (non-resonant) deformations.

Therefore, it could be expected that the critical impact duration be equal to the period of the skull's first mode ($T_p = T_\Omega$); however, the dynamic intracranial response has been observed in impacts with duration greater than this period. In the Stage 1 model for example, modal analysis revealed the period of this first mode $T_\Omega$ to be 0.514 ms, which implies a critical impact duration of about 1.028 ms. The force-time history of head impact tends to be approximated well by a simple Hanning function [Equation 6.10] (P. G. Young, 2003). Figure 6.12, below, depicts the Fourier transform of a Hanning function with duration $T_p$ of 1.028 ms. Also shown is the "frequency of impact", a single frequency that describes a sinusoidal function with period $T_p$ (used here as a simple representation of the impact's duration in terms of frequency), and the natural frequency of the Stage 1 model's first equivoluminal mode. Examining the Hanning function in the frequency domain revealed that the limit of this function's high frequency content lies at approximately twice the "frequency of impact". In this case, which represents an impact of critical duration, the frequency spectrum carries a small amount of high frequency content that coincides with

the natural frequency of the skull's first mode; which explains why dynamic pressure magnification still occurs even when the impact duration is up to twice $T_\Omega$.

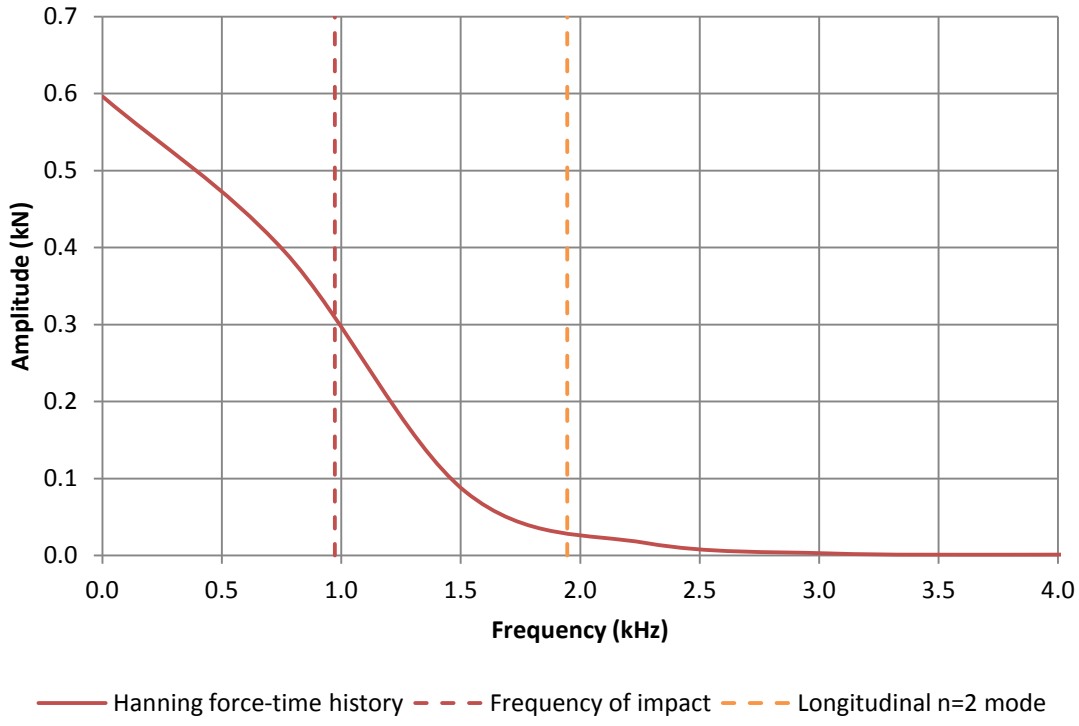


*Figure 6.12: Fourier transform of a Hanning force-time history representing a "critical" impact, with duration $T_p$ given by twice the period of the skull's first equivoluminal mode (for the Stage 1 head model $T_\Omega$ = 0.514 ms, so $T_p$ = 1.028 ms). The corresponding "frequency of impact" (1 / 1.028 ms), and the frequency of the skull's first mode (1 / 0.514 ms), are marked by vertical lines.*

## 6.2 Comparisons with previous work

### *6.2.1 Head impact investigations focussed on the dynamic pressure magnification response*

Despite the fact that related research by Young & Morfey (1998) and Johnson (2005), and the three stages of investigation in this study, have all used different numerical and physical head models of varying levels of complexity, the threshold between quasi-static and dynamic intracranial pressure behaviour was repeatedly found to be $T_p$ / $T_\Omega$ = 2. When impact duration is less than this critical value, large dynamic pressure transients were observed at the coup and contrecoup of the brain. These transients were of alternating sign and produced both positive and negative pressures much larger than those predicted by the

quasi-static solution [Equation 1.5]; the nature of these dynamic pressure transients agrees well with those reported in Young & Morfey's (1998) original paper.

Two relevant analytical models have been developed by Young. The first pertains to the calculation of the period of the first equivoluminal mode of a fluid-filled sphere $T_{\Omega}$ (P. G. Young, 2002). The accuracy of this analytical expression [Equation 1.6], and its applicability to both spherical and non-spherical skull models, was validated by comparison to numerical modal analyses performed in each of the three stages of this study. Despite a tendency to overestimate the period $T_{\Omega}$ compared to the numerically computed values, the analytical model performed remarkably well, exaggerating this period by only 4.86%, 11.21%, and 4.91%, for the Stage 1-3 head models respectively.

The second analytical model developed by Young is in the form of a set of expressions which allow the prediction of global impact characteristics such as impact duration $T_p$, peak impact force $F_{max}$, and the Head Injury Criterion (HIC) [Equations 1.12, 1.14, and 1.15] (P. G. Young, 2003). Work by Johnson (2005) and Johnson & Young (2005) is concerned mainly with the experimental validation of the accuracy of this second analytical model, by comparison to three physical representations of the head. Johnson (2005) notes that the analytical model performs excellently in regard to the first physical head model used: a simple water-filled polymer spherical shell. However, when attempting to predict these characteristics ($T_p$, $F_{max}$, HIC) resulting from impact experiments involving a rapid prototyped model of the skull filled with water, the accuracy of the predictions varied depending on the location of impact. Out of the four impact sites investigated, the analytical predictions agreed best with experimental results obtained from impacts to the occipital and parietal bones, presumably due to the simple domed surface of the skull in these regions. For these, the predictions of impact duration $T_p$ and peak impact force $F_{max}$ showed remarkable agreement with the experiments, while the estimated HIC values were even more robust, agreeing well with the experimental data irrespective of impact site. Finally, in Johnson's (2005) third trial, impacts were performed on the occipital bone of a cadaveric skull filled with water. The additional complexity introduced in this third investigation had a noticeable effect on the analytical model's performance, and the resulting predictions had significant errors. Across all three stages of Johnson's investigation, the HIC predictions tended to be most accurate, followed by the impact duration $T_p$, while the peak impact force $F_{max}$ values were least precise. The accuracy of the analytical model's predictions of $T_p$ and $F_{max}$ were also monitored in this study, for impacts to the occipital bone only. These were found to perform similarly well, having only minor

errors in the majority of cases. The errors became more significant when studying the high energy impacts in Stage 2, and the more realistic Stage 3 head model. Overall, work by Johnson (2005) and Johnson & Young (2005), and findings presented here, demonstrate that this analytical model shows excellent agreement with head impact experiments in the majority of cases, on both spherical and realistic skull geometries, so long as the site of impact can be approximated well by a domed surface. In addition, the introduction of complexities which deviate strongly from the simple approximations used in the derivation of this analytical model, such as the soft non-linear scalp layer in the Stage 3 biofidelic head model, will lead the analytical predictions to deviate more significantly from the experimental observations.

### *6.2.2 Other head impact investigations below 1 ms*

Stated in terms of time, rather than non-dimensional ratio $T_p$ / $T_\Omega$, the critical impact durations for each of the three head models used in this study were 1.028, 0.874, and 1.222 ms respectively. Other than the work discussed above that was specifically aimed at exploring the dynamic pressure magnification response, there exists only a small number of studies which explore head impacts of the order of 1 ms duration or less. As such, head impact literature is mostly limited to the quasi-static pressure behaviour of the brain. This is presumably because these studies are often concerned with head collisions involving heavy or stationary objects, which tend to produce comparatively long duration impacts.

A significant body of work by Goldsmith et al. is an exception to this rule. In work by Kenner & Goldsmith (1972) the human head is approximated by an aluminium sphere, which was studied both *in vacuo* and filled with water. Two impacts, of duration 0.06 and 0.5 ms, were performed via a pendulum-mass system. Fluid pressures were recorded by means of seven transducers placed along the central axis of the model, and were also predicted using an analytical model based on thin shell theory. The analytically predicted pressures showed good agreement with the experimental results. Both impact cases performed by Kenner & Goldsmith had very short contact durations, and so understandably appear to have produced, what has been described in this current study as, the dynamic pressure magnification response. Large fluctuating pressure transients were recorded at the coup and contrecoup, generating peaks of both positive and negative pressure. Understandably also, this effect was substantially more severe in the shorter duration impact, despite both having similar peak impact forces. In the authors' own words: "A negative pressure of nearly the same magnitude as that of the compressive peak is transmitted immediately following the initial disturbance. This is attributed to snapback

of the shell and is relatively more prominent for the shorter duration loadings." Hence, the authors propose that the formation of these negative pressure transients is likely due to "snapback" of the skull; this agrees with conclusions made in this investigation regarding the causation of these dynamic pressure transients by local acceleration of the skull at the impact site (Section 6.1.2.1). Kenner & Goldsmith also note that these transients are not transmitted to the contrecoup ("antipole") by means of bulk waves in the fluid. The authors do not separately consider the arrival time of the large pressure transients at the contrecoup (attributed here to flexural waves through the skull: see Section 6.1.2.2), but do comment on the arrival of the smaller pressures which precede these larger transients; these were accredited to the propagation of extensional waves through the skull: "The extensional disturbance travelling via the shell reaches the antipole in a shorter time than the compressive transient travelling through the water. Shell out-bending occurring at the time of arrival of the extensional disturbance causes a rarefaction in the fluid to be transmitted back toward the impact point." This original research was extended in an additional paper by the same authors (Kenner & Goldsmith, 1973), in which equivalent impacts are performed on a water-filled acrylic sphere to similar effect.

Landkof, Goldsmith, & Sackman (1976) expanded on the above work by attaching the previously used water-filled acrylic sphere to an articulated neck replica made from segmented neoprene and aluminium discs, developed by General Motors Corp. A longer duration impact, lasting 2.5 ms, was found to produce intracranial pressure behaviour which could be described as quasi-static: "...pressure histories indicate that the peak negative pressures in the fluid are observed mainly in the distal hemisphere during the impact period, while positive pressures develop concurrently in the frontal hemisphere." Lubock & Goldsmith (1980) investigate the possibility of intracranial cavitation by means of the head-neck model developed by Landkof et al. (1976), and an additional head-neck model in which the acrylic sphere is replaced by a fluid-filled cadaveric skull. These were subjected to two sets of impacts, of either approximately 2.12 ms or 0.02 ms in duration, using the aforementioned pendulum-mass system or by firing steel projectiles from a pneumatic gun respectively. The spherical model was filled with various fluids including distilled water, artificial CSF, and glycerine; while the skull model was filled with either distilled water, or gelatin. In the distilled water experiments for example, the pendulum-mass impacts on the acrylic sphere model induced peak negative pressures of roughly -0.60 MPa at the coup, and -0.40 MPa at the contrecoup, while for the shorter projectile impacts these were greater, being approximately -1.00 MPa at the coup, and -1.33 MPa at the contrecoup. The skull model was subject only to the shorter projectile impacts, and

experienced peak negative pressures of -0.02 MPa at the coup, and -0.08 MPa at the contrecoup. Three types of cavitation were observed in the acrylic sphere impacts, irrespective of the fluid used; these were coup, contrecoup, and "resonating contrecoup" cavitation. Coup and contrecoup cavitation involved the formation and subsequent collapse of voids in the fluid local to these respective regions, while the "resonating" type cavitation was defined as the manifestation of small clusters of voids which form repeatedly and collapse for about 5-6 cycles. For the skull model impacts, only contrecoup cavitation was observed in those tests using distilled water, and no cavitation occurred in the gelatin filled model. Here Lubock & Goldsmith are employing the terminology first used by Gross (1958) in his theoretical description of the mechanisms which could induce negative pressure, and therefore possible cavitation, in the cranial contents. Gross suggested three mechanisms by which this may occur: (1) contrecoup cavitation, wherein negative pressures are generated at the contrecoup due to rigid-body acceleration of the head, (2) coup cavitation, caused by "snapback" of the skull at the impact site, and (3) "resonance cavitation". This latter cavitation type was proposed to explain diffuse brain injuries: the violent collapse of cavities at either the coup or contrecoup may induce cycles of expansion and contraction of the skull, resulting in the formation of cavities distributed throughout the entire cranial vault. The first and second negative pressure mechanisms mentioned by Gross have been confirmed in the current study, where they were termed the quasi-static, and dynamic pressure magnification response respectively. Lubock & Goldsmith (1980) report a phenomenon similar to the "resonance cavitation" proposed by Gross, but this was restricted to the contrecoup region. In the current study, the preceding chapters demonstrate that long duration impacts ($T_p$ / $T_\Omega$ > 2) restrict the formation of large negative pressures to the contrecoup, while short duration impacts ($T_p$ / $T_\Omega$ < 2) appear to restrict large negative pressures to the coup, the contrecoup, and the brain-skull boundary; thus no evidence of a possible diffuse "resonance cavitation" was observed.

Lastly, the head-neck model which utilised the cadaveric skull, developed by Lubock & Goldsmith (1980), was redesigned by Kabo & Goldsmith (1983) who introduced more realistic resin vertebrae, and artificial rubber muscles and ligaments. A large set of pendulum-mass impacts were performed, ranging from 0.40 to 10.40 ms, however this study was less focussed on the intracranial pressure response or cavitation.

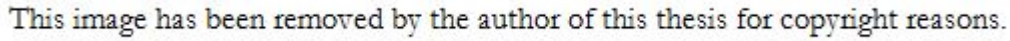


*Figure 6.13: Diagram depicting skull "snapback" as a mechanism of localised coup cavitation, as first hypothesised by Gross: "(a) Impact to top of skull causes local deformation of the skull inward. (b) Cessation of the impacting force leaves the skull locally deformed in a highly stressed condition. (c) Snap-back of the deformed skull to its normal position results in localized cavitation. (d) Collapse of the cavities formed produces the punctate contusions associated with coup injury." (Gross, 1958)*

To this author's knowledge, the only other investigation which considers impacts of the order of 1 ms or less was numerical work by Wahi & Merchant (1977). Five impacts were simulated on several one-dimensional and two-dimensional finite-difference models of the head, down to very short durations (0.06 ms). This work did not examine the intracranial response in terms of pressure, but large dynamic stress transients, both compressive and tensile in nature, were reported in response to these short duration impacts.

The above work represents the limited published research which probes head impacts of the order of 1 ms or less. These studies broadly agree with the findings presented in the preceding chapters, in that, in response to short duration impacts, large peaks of positive and negative pressure are frequently reported at both the coup and contrecoup.

## 6.3 Conclusions

Three finite element head models of differing complexity were used to investigate the intracranial pressure response to a wide variety of head impacts. Two of these models employed image-based meshing techniques, and eventually a highly complex biofidelic model of the head and neck was constructed and validated against experimental data. One of the aims of this investigation was to verify that the dynamic "magnification" of

intracranial pressures was not an artefact of the large simplifications used in some of the previous models in which this effect had been recorded. This phenomenon was demonstrated in all three models employed in this study, including the highly biofidelic head model. Furthermore, the dynamic pressure magnification response has been shown not to lie outside the window of authentic head injury scenarios, as demonstrated by a number of case studies with reasonable impact characteristics. This provides compelling evidence that this potentially severe trauma mechanism can arise in the true human head.

The second principal aim of this work was to arrive at a deeper understanding of the mechanics involved in the generation of these large dynamic pressures. This was achieved by means of Fourier analysis and through the derivation of an approximate analytical model that, together with expressions developed by Young (2003), allows the prediction of dynamic coup pressures in the brain resulting from short duration impacts ($T_p$ / $T_\Omega$ < 2). It was concluded that the dynamic pressure magnification response is a consequence of the local deflection and acceleration of the skull at the impact site, which is then communicated to the contrecoup by flexural waves in the skull.

Other than the obvious potential hazard of the greatly magnified intracranial pressures produced by this mechanism, it is noted that negative pressures also develop at the coup, whereas in the more widely investigated quasi-static response they are confined to the contrecoup. It has been suggested that the formation of negative pressures in the cranial contents may be particularly deleterious due to cavitation; the findings here suggest that cavitation may also develop beneath the point of impact, which provides a possible explanation of the peculiar distribution of trauma characteristic of coup-contrecoup injuries. While knowledge of the conditions and pressures which mark the threshold at which *in vivo* cavitation may occur is still limited, cavitation is regarded by many to be a likely brain injury mechanism. The results indicate the importance of considering the inflated prospect of injury from short duration impacts. These findings may have implications for injury preventative design and forensic investigation of blunt head trauma.

## 6.4 Future work

Some suggestions for avenues of further enquiry are provided:

- The problem of modelling the geometry of complex biological structures can all but be removed by use of image-based meshing. The accuracy of image-based finite element head models is therefore limited primarily by the number of anatomical

structures which are included and their material models. The current biofidelic head model could be improved by the introduction of the following structures: the falx and tentorium, bridging veins, and addition of pre-stressed muscles and ligaments to more accurately represent the constraints imposed by the neck. Since the dynamic pressure magnification response is strongly dependant on the properties of the skull, it is recommended also that an updated skull differentiates between the cortical and cancellous bone layers and assigns different material properties to these, or employs properties based on the greyscale intensity of the image.

- Inclusion of material models which allow plastic deformation and material failure: the biofidelic head model could then be used to extend the investigation of the intracranial response to penetrating head injuries.
- Further validation of the dynamic pressure magnification phenomenon by comparisons with clinical data, perhaps from blunt head trauma autopsies. This could be in the form of a post-trauma MRI scan, leading to a patient-specific finite element head model and simulated recreation of the injury incident. This may further our understanding of injury producing mechanisms as well as provide useful forensic evidence, or (in a non-fatal case) aid diagnosis and inform treatment.
- Simulation of blunt impact to different locations of the head, and investigation of the influence of these various locations on the intracranial response.
- This study did not aim to provide an absolute measure of the severity of the injuries which may result from the simulated head impacts, but was chiefly concerned with qualitatively exploring intracranial pressure behaviour. Experiments aimed at obtaining information on positive and negative pressure tolerance limits, and knowledge of an *in vivo* cavitation threshold for intracranial fluids, are required in order to allow quantitative predictions regarding the severity of trauma.
- While the current work has focussed on human head impact, the dynamic "magnification" mechanism that has been explored has been shown to be remarkably robust in the face of large material and geometric changes to the model. This provides confidence that this mechanism is applicable to a wide variety of fluid-filled containers. For example, it would be interesting to apply Young's (2003) analytical model of impact to a fluid-filled sphere, and analysis techniques similar to those used here, to the problem of the Earth being struck by a meteorite.

Crowe, C. T., Elger, D. F., & Roberson, J. A. (2005). *Engineering Fluid Mechanics* (8th ed.). John Wiley & Sons, Inc.

Giurgiutiu, V. (2000). *Asymmetric Lamb Wave video*. University of South Carolina, College of Engineering and Computing. Retrieved from http://www.me.sc.edu/Research/lamss/research/Waves/sld004.htm

Gross, A. G. (1958). A new theory on the dynamics of brain concussion and brain injury. *Journal of Neurosurgery*, *15*, 548–561.

Hapsara, M., & Iliescu, D. (2012). A Study of Ultrasonic-Lamb-Waves Interaction with a Notch in a Bovine Cortical Tibia using Scanning Laser Vibrometry. *International Journal of Engineering Science and Technology*, *4*(06), 2926–2935.

Jiangong, Y., Bin, W., Hongli, H., & Cunfu, H. (2007). Characteristics of guided waves in anisotropic spherical curved plates. *Wave Motion*, *44*(4), 271–281.

Johnson, E. (2005). *The response of the human head to blunt impact: experimental validation of an analytical model. Thesis*. University of Exeter. Retrieved from http://ethos.bl.uk/OrderDetails.do?uin=uk.bl.ethos.421650

Johnson, E., & Young, P. G. (2005). On the use of a patient-specific rapid-prototyped model to simulate the response of the human head to impact and comparison with analytical and finite element models. *Journal of Biomechanics*, *38*(1), 39–45.

Kabo, J., & Goldsmith, W. (1983). Response of a human head-neck model to transient saggital plane loading. *Journal of Biomechanics*, *16*(5), 313–321.

Kenner, V. H., & Goldsmith, W. (1972). Dynamic loading of a fluid-filled spherical shell. *International Journal of Mechanical Sciences*, *14*(9), 557–568.

Kenner, V. H., & Goldsmith, W. (1973). Impact on a simple physical model of the head. *Journal of Biomechanics*, *6*(I), 1–11.

Laboratory for Adaptive Materials and Smart Structures. (2012). Waveform Revealer 3.0. University of South Carolina, College of Engineering and Computing. Retrieved from http://www.me.sc.edu/research/lamss/html/software.html

Lamb, H. (1917). On waves in an elastic plate. *Proceedings of the Royal Society A*, *93*, 114–128.

Landkof, B., Goldsmith, W., & Sackman, J. L. (1976). Impact on a head-neck structure. *Journal of Biomechanics*, *9*, 141–151.

Lubock, P., & Goldsmith, W. (1980). Experimental cavitation studies in a model head-neck system. *Journal of Biomechanics*, *13*(12), 1041–1047.

McKnight, C. L. (2012). *Vibratory response of dry human skulls*. Dalhousie University, Halifax, Nova Scotia. Retrieved from http://dalspace.library.dal.ca/bitstream/handle/10222/14618/McKnight, Carmen, MASc, MECH, March 2012.pdf

Porges, G. (1979). *Applied Acoustics*. Edward Arnold Ltd.

Reinfeldt, S., Stenfelt, S., & Håkansson, B. (2013). Estimation of bone conduction skull transmission by hearing thresholds and ear-canal sound pressure. *Hearing Research*, *299*, 19–28.

Rose, J. L. (2003). Dispersion curves in guided wave testing. *Materials Evaluation*.

Rossing, T. D., & Fletcher, N. H. (2004). *Principles of Vibration and Sound* (2nd ed.). Springer Verlag.

Shull, P. J. (2002). *Nondestructive evaluation: theory, techniques, and applications*. Marcel Dekker Inc.

Überall, H., Bjørnø, I. K., & Bjørnø, L. (2000). Dispersion of circumferential waves on evacuated, water-loaded spherical steel shells. *Ultrasonics*, *37*(10), 673–5.

Wahi, K. K., & Merchant, H. C. (1977). Mechanical response of a head injury model with viscoelastic brain tissue. *Annals of Biomedical Engineering*, *5*(4), 303–21.

Young, P. G. (2002). A parametric study on the axisymmetric modes of vibration of multi-layered spherical shells with liquid cores of relevance to head impact modelling. *Journal of Sound and Vibration*, *256*(4), 665–680.

Young, P. G. (2003). An analytical model to predict the response of fluid-filled shells to impact - a model for blunt head impacts. *Journal of Sound and Vibration*, *267*(5), 1107–1126.

Young, P. G., & Morfey, C. L. (1998). Intracranial pressure transients caused by head impacts. *International Research Council on the Biomechanics of Impact (IRCOBI) Conference Proceedings* (pp. 391–403). Göteborg, Sweden.

Young, W., & Budynas, R. (2002). *Roark's formulas for stress and strain* (7th ed.). McGraw-Hill.

# Bibliography


Anzelius, A. (1943). The effect of an impact on a spherical liquid mass. *Acta Pathologica Microbiologia Scandanavia*, *48*, 153–159.

Bala, S. (2006). Overview of Mass-Scaling in LS-DYNA. *LS-DYNA and d3VIEW Blog*. Retrieved November 27, 2012, from http://blog2.d3view.com/overview-of-mass-scaling

Bandak, F. A. (1996). Biomechanics of impact traumatic brain injury. *NATO Advanced Studies Institute: Crashworthiness of Transportation Systems*, *1*.

Barber, T., Brockway, J. A., & Higgins, L. S. (1970). The density of tissues in and about the head. *Acta Neurologica Scandinavica*, *46*(1), 85–92.

Belingardi, G., Chiandussi, G., & Gaviglio, I. (2005). Development and validation of a new finite element model of human head. *Proceedings of the 19th International Technical Conference on the Enhanced Safety of Vehicles* (Vol. 38, pp. 3766–76). Washington, D.C.

Benzley, S., Perry, E., Merkley, K., & Clark, B. (1995). A comparison of all hexagonal and all tetrahedral finite element meshes for elastic and elasto-plastic analysis. *Proceedings of the 4th International Meshing Roundtable* (pp. 179–191). Sandia National Laboratories, Albuquerque.

Bradshaw, D., & Morfey, C. L. (2001). Pressure and shear responses in brain injury models. *Proceedings of the 17th International Technical Conference on the Enhanced Safety of Vehicles* (pp. 1–10). Amsterdam, The Netherlands.

Brennen, C. (2003). Cavitation in biological and bioengineering contexts. *Proceedings of the 5th International Symposium on Cavitation*. Osaka, Japan.

Bui Xuan, V. (2008). *Development of a pre-processing environment for 3D image based finite element mesh generation. Thesis*. University of Exeter.

Chen, Y., & Ostoja-Starzewski, M. (2010). MRI-based finite element modeling of head trauma: spherically focusing shear waves. *Acta Mechanica*, *213*(1-2), 155–167.

Cheng, L. Y., Rifai, S., Khatua, T., & Piziali, R. L. (1990). Finite element analysis of diffuse axonal injury. *Proceedings of the 34th STAPP Car Crash Conference* (pp. 141–154).

Christ, A. F., Franze, K., Gautier, H., Moshayedi, P., Fawcett, J., Franklin, R. J. M., Karadottir, R. T., et al. (2010). Mechanical difference between white and gray matter in the rat cerebellum measured by scanning force microscopy. *Journal of Biomechanics*.

Cifu, D. X., & Caruso, D. (2010). *Traumatic brain injury*. Demos Medical, New York.

Claessens, M. H. A. (1994). Anatomical description of the human head. *Technical report*. Retrieved from http://alexandria.tue.nl/repository/books/642185.pdf

Cory, C., & Jones, M. D. (2006). Development of a simulation system for performing in situ surface tests to assess the potential severity of head impacts from alleged childhood short falls. *Forensic Science International*, *163*(1-2), 102–14.

Cory, C., Jones, M. D., & James, D. (2001). The potential and limitations of utilising head impact injury models to assess the likelihood of significant head injury in infants after a fall. *Forensic Science International*, *123*, 89–106.

Cramer, G. D., Ross, J. K., Raju, P. K., Cambron, J. A., Dexheimer, J. M., Bora, P., McKinnis, R., et al. (2011). Distribution of cavitations as identified with accelerometry during lumbar spinal manipulation. *Journal of Manipulative and Physiological Therapeutics*, *34*(9), 572–83.

Crowe, C. T., Elger, D. F., & Roberson, J. A. (2005). *Engineering Fluid Mechanics* (8th ed.). John Wiley & Sons, Inc.

Dawson, S. L., Hirsch, C. S., Lucas, F. V., & Sebek, B. A. (1980). The contrecoup phenomenon: Reappraisal of a classic problem. *Human Pathology*, *11*(2), 155–166.

Deck, C., & Willinger, R. (2009). The current state of human head finite element modelling. *International Journal of Vehicle Safety*, *4*(2), 85–112.

Department of Health. (2005). *The national service framework for long term conditions. BMJ (Clinical research ed.)* (Vol. 330). doi:10.1136/bmj.330.7503.1280

DiMasi, F., Marcus, J., & Eppinger, R. (1991). 3-d anatomic brain model for relating cortical strains to automobile crash loading. *Proceedings of the 13th International Conference on Experimental Safety Vehicles* (pp. 916–924). Washington, D.C.

Drew, L. B., & Drew, W. E. (2004). The contrecoup–coup phenomenon: a new understanding of the mechanism of closed head injury. *Neurocritical Care*, *1*, 385–390.

Edberg, S., Rieker, J., & Angrist, A. (1963). Study of impact pressure and acceleration in plastic skull models. *Laboratory Investigation*, *12*(12), 1305–1311.

El Sayed, T., Mota, A., Fraternali, F., & Ortiz, M. (2008). Biomechanics of traumatic brain injury. *Computer Methods in Applied Mechanics and Engineering*, *197*(51-52), 4692–4701.

Engin, A. E. (1969). The axisymmetric response of a fluid-filled spherical shell to a local radial impulse – a model for head injury. *Journal of Biomechanics*, *2*(3), 325–341.

Engin, A. E., & Liu, Y. K. (1970). Axisymmetric response of a fluid-filled spherical shell in free vibrations. *Journal of Biomechanics*, *3*(1), 11–16.

Engin, A. E., & Wang, H. C. (1970). A mathematical model to determine viscoelastic behavior of in vivo primate brain. *Journal of Biomechanics*, *3*(3), 283–96.

Ewing, C. L., & Thomas, D. J. (1972). *Human Head and Neck Response to Impact Acceleration*. Pensacola, FL. Retrieved from http://oai.dtic.mil/oai/oai?verb=getRecord&metadataPrefix=html&identifier=AD0747988

Fasanella, E. L., & Jackson, K. E. (2002). *Best practices for crash modeling and simulation. NASA technical report*. Retrieved from http://citeseerx.ist.psu.edu/viewdoc/download?doi=10.1.1.6.8863&rep=rep1&type=pdf

Federal Motor Carrier Safety Administration. (2013). Standard No. 208; Occupant crash protection. Retrieved April 30, 2013, from http://www.fmcsa.dot.gov/rules-regulations/administration/fmcsr/fmcsrruletext.aspx?reg=r49CFR571.208

Flint, E. B., & Suslick, K. S. (1991). The temperature of cavitation. *Science*, *253*(5026), 1397–9.

Gadd, C. W. (1966). The use of a weighted-impulse criterion for estimating injury hazard. *Proceedings of the 10th STAPP Car Crash Conference* (pp. 164–174).

Gadd, C. W., Nahum, A. M., Schneider, D. C., & Madeira, R. G. (1970). Tolerance and properties of superficial soft tissues in situ. *Proceedings of the 14th STAPP Car Crash Conference* (pp. 356–368).

Galbraith, C. G., & Tong, P. (1988). Boundary conditions in head injury finite element modeling. *16th Annual International Workshop on Human Subjects for Biomechanical Research*, 179–193.

Galford, J., & McElhaney, J. H. (1970). A viscoelastic study of scalp, brain, and dura. *Journal of Biomechanics*.

Gibson, L. J., & Ashby, M. F. (1999). Cancellous bone. *Cellular solids: Structure and Properties - 2nd edition* (pp. 429–452). Cambridge University Press.

Giurgiutiu, V. (2000). *Asymmetric Lamb Wave video*. University of South Carolina, College of Engineering and Computing. Retrieved from http://www.me.sc.edu/Research/lamss/research/Waves/sld004.htm

Goldsmith, W. (1972). Biomechanics of head injury. In Y. C. Fung, N. Perrone, & M. Anliker (Eds.), *Biomechanics: Its Foundations and Objectives*. Prentice-Hall, Englewood Cliffs, NJ.

Goldsmith, W. (1981). Current controversies in the stipulation of head injury criteria. *Journal of Biomechanics*, *14*(12), 883.

Gong, S., Lee, H. P., & Lu, C. (2008). Computational simulation of the human head response to non-contact impact. *Computers & Structures*, *86*(7-8), 758–770.

Gross, A. G. (1958). A new theory on the dynamics of brain concussion and brain injury. *Journal of Neurosurgery*, *15*, 548–561.

Gurdjian, E. S. (1975). *Impact head injury: mechanistic, clinical, and preventive correlations*. Charles C Thomas.

Güttinger, W. (1950). Der Stoßeffekt auf eine Flüssigkeitskugel als Grundlage einer Physikalischen Theorie der Entstehung von Gehirnverletzungen. *Zeitschrift für Naturforschung*, *5a*, 622–628.

Hallquist, J. (2006). *LS-DYNA Theory Manual*. Retrieved from http://www.lstc.com/download/manuals

Hapsara, M., & Iliescu, D. (2012). A Study of Ultrasonic-Lamb-Waves Interaction with a Notch in a Bovine Cortical Tibia using Scanning Laser Vibrometry. *International Journal of Engineering Science and Technology*, *4*(06), 2926–2935.

Hardy, W. N., Foster, C., Mason, M., Yang, K. H., & King, A. I. (2001). Investigation of Head Injury Mechanisms Using Neutral Density Technology and High-Speed Biplanar X-ray. *Stapp Car Crash Journal*, *45*, 337–368.

Hardy, W. N., Khalil, T. B., & King, A. I. (1994). Literature review of head injury biomechanics. *International Journal of Impact Engineering*, 561–586.

Harewood, F. J., & McHugh, P. E. (2007). Comparison of the implicit and explicit finite element methods using crystal plasticity. *Computational Materials Science*, *39*(2), 481–494.

Ho, J. (2008). *Generation of patient specific finite element head models. Thesis*. Royal Institute of Technology, Stockholm. Retrieved from http://ntnu.diva-portal.org/smash/get/diva2:126650/FULLTEXT01

Holbourn, A. H. S. (1943). Mechanics of head injuries. *Lancet*, *2*, 438–441.

Holbourn, A. H. S. (1945). The mechanics of brain injuries. *British Medical Bulletin*, *3*, 147–149.

Holland, C. K., & Apfel, R. E. (1990). Thresholds for transient cavitation produced by pulsed ultrasound in a controlled nuclei environment. *The Journal of the Acoustical Society of America*, 2059–2069.

Horgan, T., & Gilchrist, M. D. (2004). Influence of FE model variability in predicting brain motion and intracranial pressure changes in head impact simulations. *International Journal of Crashworthiness*, *9*(4), 401–418.

Huang, H. M., Lee, M. C., Lee, S. Y., Chiu, W. T., Pan, L. C., & Chen, C. T. (2000). Finite element analysis of brain contusion: an indirect impact study. *Medical & Biological Engineering & Computing*, *38*(3), 253–9.

Hubbard, R. P. (1971). Flexure of layered cranial bone. *Journal of Biomechanics*, *4*(4), 251–263.

Ivarsson, J., Viano, D. C., Lövsund, P., & Aldman, B. (2000). Strain relief from the cerebral ventricles during head impact: experimental studies on natural protection of the brain. *Journal of Biomechanics*, *33*(2), 181–9.

Jenkins, L. W., Moszynski, K., Lyeth, B. G., Lewelt, W., DeWitt, D. S., Allen, A., Dixon, C. E., et al. (1989). Increased vulnerability of the mildly traumatized rat brain to cerebral ischemia: the use of controlled secondary ischemia as a research tool to identify common or different mechanisms contributing to mechanical and ischemic brain injury. *Brain Research*, *477*(1-2), 211–224.

Jiang, H., Young, P. G., & Dickinson, S. (1996). Natural frequencies of vibration of layered hollow spheres using exact three-dimensional elasticity equations. *Journal of Sound and Vibration*, *195*(1), 155–162.

Jiangong, Y., Bin, W., Hongli, H., & Cunfu, H. (2007). Characteristics of guided waves in anisotropic spherical curved plates. *Wave Motion*, *44*(4), 271–281.

Johnsen, E., Colonius, T., & Cleveland, R. (2009). Damage potential of the shock-induced collapse of a gas bubble. *Proceedings of the 7th International Symposium on Cavitation*. Michigan, USA.

Johnson, E. (2005). *The response of the human head to blunt impact: experimental validation of an analytical model. Thesis*. University of Exeter. Retrieved from http://ethos.bl.uk/OrderDetails.do?uin=uk.bl.ethos.421650

Johnson, E., & Young, P. G. (2005). On the use of a patient-specific rapid-prototyped model to simulate the response of the human head to impact and comparison with analytical and finite element models. *Journal of Biomechanics*, *38*(1), 39–45.

Johnson, K. L. (2003). *Contact Mechanics* (9th ed.). Cambridge University Press.

Kabo, J., & Goldsmith, W. (1983). Response of a human head-neck model to transient saggital plane loading. *Journal of Biomechanics*, *16*(5), 313–321.

Kane, M. J., Angoa-Pérez, M., Briggs, D. I., Viano, D. C., Kreipke, C. W., & Kuhn, D. M. (2012). A mouse model of human repetitive mild traumatic brain injury. *Journal of Neuroscience Methods*, *203*(1), 41–9.

Kenner, V. H., & Goldsmith, W. (1972). Dynamic loading of a fluid-filled spherical shell. *International Journal of Mechanical Sciences*, *14*(9), 557–568.

Kenner, V. H., & Goldsmith, W. (1973). Impact on a simple physical model of the head. *Journal of Biomechanics*, *6*(I), 1–11.

Khalil, T. B., & Hubbard, R. P. (1977). Parametric study of head response by finite element modeling. *Journal of Biomechanics*, *10*(2), 119–32.

Kharatishvili, I., Sierra, A., Immonen, R. J., Gröhn, O. H. J., & Pitkänen, A. (2009). Quantitative T2 mapping as a potential marker for the initial assessment of the severity of damage after traumatic brain injury in rat. *Experimental Neurology*, *217*(1), 154–64.

Kleiven, S. (2006). Evaluation of head injury criteria using a finite element model validated against experiments on localized brain motion, intracerebral acceleration, and intracranial pressure. *International Journal of Crashworthiness*, *11*(1), 65–79.

Kleiven, S., & Von Holst, H. (2002). Consequences of head size following trauma to the human head. *Journal of Biomechanics*, *35*(2), 153–60.

Kuijpers, A., Claessens, M. H. A., & Sauren, A. (1996). A two-dimensional FEM analysis of the response of the human head to impact: the importance of boundary conditions. *Computer Methods in Biomechanics and Biomedical Engineering*, 207–216.

Laboratory for Adaptive Materials and Smart Structures. (2012). Waveform Revealer 3.0. University of South Carolina, College of Engineering and Computing. Retrieved from http://www.me.sc.edu/research/lamss/html/software.html

Lamb, H. (1917). On waves in an elastic plate. *Proceedings of the Royal Society A*, *93*, 114–128.

Landkof, B., Goldsmith, W., & Sackman, J. L. (1976). Impact on a head-neck structure. *Journal of Biomechanics*, *9*, 141–151.

Lee, E. S. (1990). *A large-strain, transient-dynamic analysis of head-injury problems by the finite element method. Thesis*. Retrieved from http://smartech.gatech.edu/handle/1853/20753

Lindenberg, R., & Freytag, E. (1960). The mechanism of cerebral contusions. *Archives of Pathology*, *69*, 440. Not first source. Paper unavailable, out of print. Information is as stated in (Dawson et al., 1980; Drew & Drew, 2004; Hardy et al., 1994).

LSTC Inc. (2007). *LS-DYNA Keyword Users Manual: Volume 1* (Vol. I). Retrieved from http://www.lstc.com/download/manuals

LSTC Inc and DYNAmore GmbH. (2003). Contact: SOFT option. *LS-DYNA Support*. Retrieved November 2, 2012, from http://www.dynasupport.com/howtos/contact/soft-option

LSTC Inc and DYNAmore GmbH. (2010). Selective mass scaling (SMS). *LS-DYNA Support*. Retrieved November 28, 2012, from http://www.dynasupport.com/howtos/general/selective-mass-scaling-sms-2

LSTC Inc and DYNAmore GmbH. (2012). Hourglass. *LS-DYNA Support*. Retrieved November 27, 2012, from http://www.dynasupport.com/howtos/element/hourglass

Lubock, P., & Goldsmith, W. (1980). Experimental cavitation studies in a model head-neck system. *Journal of Biomechanics*, *13*(12), 1041–1047.

Marik, P., Varon, J., & Trask, T. (2002). Management of Head Trauma. *Chest*, *122*(2), 699–711.

Marjoux, D., Baumgartner, D., Deck, C., & Willinger, R. (2008). Head injury prediction capability of the HIC, HIP, SIMon and ULP criteria. *Accident; Analysis and Prevention*, *40*(3), 1135–48.

Maruoka, K., Sakagami, S., Yamada, K., Nakagawa, N., & Sekiguti, Y. (2001). Dynamic impact characteristics of golf ball materials. *Materials and Science in Sports Symposium* (Vol. 7514, pp. 145–149).

McElhaney, J. H., Fogle, J. L., Melvin, J. W., Haynes, R. R., Roberts, V. L., & Alem, N. M. (1970). Mechanical properties of cranial bone. *Journal of Biomechanics*, *3*(5), 495–512.

McIntosh, T. K., Vink, R., Noble, L., Yamakami, I., Fernyak, S., Soarest, H., & Faden, A. L. (1989). Traumatic brain injury in the rat: characterization of a lateral fluid-percussion model. *Neuroscience*, *28*(1), 233–244.

McKnight, C. L. (2012). *Vibratory response of dry human skulls*. Dalhousie University, Halifax, Nova Scotia. Retrieved from http://dalspace.library.dal.ca/bitstream/handle/10222/14618/McKnight, Carmen, MASc, MECH, March 2012.pdf

Mehta, B. V, Rajani, S., & Sinha, G. (1997). Comparison of image processing techniques (magnetic resonance imaging, computed tomography scan and ultrasound) for 3D modeling and analysis of the human bones. *Journal of Digital Imaging*, *10*(3 Suppl 1), 203–6.

Melvin, J. W., McElhaney, J. H., & Roberts, V. L. (1970). Development of a Mechanical Model of the Human Head- Determination of Tissue Properties and Synthetic Substitute Materials. *Proceedings of the 14th STAPP Car Crash Conference* (pp. 221–240).

Mertz, H. J., Prasad, P., & Irwin, A. L. (1997). Injury risk curves for children and adults in frontal and rear collisions. *Proceedings of the 41st STAPP Car Crash Conference* (pp. 13–30). Retrieved from http://www.snellfoundation.org/docs/articles/hics

Meulman, J. (1996). An experimental investigation to the constitutive behaviour of brain tissue. *Technical report*, *80*(10), 289–302. Retrieved from http://www.narcis.nl/publication/RecordID/oai:library.tue.nl:461975/Language/en

Misra, J., & Chakravarty, S. (1985). Dynamic response of a head-neck system to an impulsive load. *Mathematical Modelling*, *6*(2), 83–96.

Morales, D. M., Marklund, N., Lebold, D., Thompson, H. J., Pitkanen, A., Maxwell, W. L., Longhi, L., et al. (2005). Experimental models of traumatic brain injury: do we really need to build a better mousetrap? *Neuroscience*, *136*(4), 971–89.

Motherway, J., Doorly, M. C., Curtis, M., & Gilchrist, M. D. (2009). Head impact biomechanics simulations: a forensic tool for reconstructing head injury? *Legal Medicine*, *11 Suppl 1*, S220–2.

MSC Software Corporation. (2005). *Explicit transient dynamic analysis. MSC.Dytran Seminar Notes* (pp. 1–14). Retrieved from ftp://ftp.mscsoftware.com.tw/download/training/dytran_basic/chapter_2.ppt

Nahum, A. M., Smith, R., & Ward, C. C. (1977). *Intracranial pressure dynamics during head impact. Proceedings of the 21st STAPP Car Crash Conference*. New Orleans, LA, USA.

NASA. (1995). Volume 1, Section 3: Anthropometry and biomechanics. *Man-system integration standards*. Retrieved November 5, 2012, from http://msis.jsc.nasa.gov/sections/section03.htm

Newman, J., Barr, C., Beusenberg, M., Fournier, E., Shewchenko, N., Welbourne, E., & Withnall, C. (2000). A new biomechanical assessment of mild traumatic brain injury, II: results and conclusions. *International Research Council on the Biomechanics of Impact (IRCOBI) Conference Proceedings* (pp. 223–233). Retrieved from http://www.smf.org/docs/articles/hic/Newman_NFL.pdf

Nusholtz, G., Glascoe, L., & Wylie, E. (1996). Modeling cavitation during head impact. *NATO/AGARD, Head Impact Conference, Paper 6*.

O'Connor, W. T., Smyth, A., & Gilchrist, M. D. (2011). Animal models of traumatic brain injury : A critical evaluation. *Pharmacology and Therapeutics*, *130*(2), 106–113.

Oasys Ltd. (2009). *T/HIS Manual, Version 9.4*.

Oasys Ltd. (2010). *Information provided on the "Introductory training course" 18th to 19th Jan 2010. Oasys LS-DYNA training courses*. Solihull, West Midlands, UK.

Ommaya, A. K. (1968). Mechanical properties of tissues of the nervous system. *Journal of Biomechanics*, *1*(2), 127–136.

Ommaya, A. K., & Hirsch, A. E. (1971). Tolerances for cerebral concussion from head impact and whiplash in primates. *Journal of Biomechanics*, *4*, 13–21.

Ommaya, A. K., Hirsch, A. E., Yarnell, P., & Harris, E. H. (1967). *Scaling of experimental data on cerebral concussion in sub-human primates to concussion threshold for man*. Washington, D.C. Retrieved from http://www.dtic.mil/dtic/tr/fulltext/u2/666837.pdf

Ommaya, A. K., Thibault, L., & Bandak, F. A. (1994). Mechanisms of impact head injury. *International Journal of Impact Engineering*, *15*(4), 535–560.

Pelosi, G., Proietti, R., Morte, F. Della, Magalini, S. I., & Bondoli, A. (1981). Decompression sickness: a medical emergency. *Resuscitation*, *9*, 201–209.

Peterson, J., & Dechow, P. C. (2003). Material properties of the human cranial vault and zygoma. *The anatomical record. Part A, Discoveries in molecular, cellular, and evolutionary biology*, *274A*(1), 785–797.

Pinnoji, P. K., & Mahajan, P. (2008). Two wheeler helmets with ventilation and metal foam. *Defence Science Journal*, *58*(2), 304–311.

Pishchalnikov, Y. A., Sapozhnikov, O. A., Bailey, M. R., Williams, J. C., Cleveland, R. O., Colonius, T., Crum, L. A., et al. (2003). Cavitation bubble cluster activity in the breakage of kidney stones by lithotripter shockwaves. *Journal of Endourology*, *17*(7), 435–446.

Porges, G. (1979). *Applied Acoustics*. Edward Arnold Ltd.

Prange, M. T., & Margulies, S. S. (2002). Regional, Directional, and Age-Dependent Properties of the Brain Undergoing Large Deformation. *Journal of Biomechanical Engineering*, *124*(2), 244.

Prange, M. T., Meaney, D. F., & Margulies, S. S. (2000). Defining brain mechanical properties: effects of region, direction, and species. *Stapp Car Crash Journal*, *44*, 205.

R&A Rules Ltd. (2008). Initial velocity test procedure. Retrieved February 25, 2013, from http://www.randa.org/Equipment/Protocols-and-Procedures/Balls/Initial-Velocity.aspx

Rao, A. A., & Dumas, G. A. (1991). Influence of material properties on the mechanical behaviour of the L5-S1 intervertebral disc in compression: a nonlinear finite element study. *Journal of Biomedical Engineering*, *13*(2), 139–151.

Raposio, E., & Nordström, R. E. A. (1998). Biomechanical properties of scalp flaps and their correlations to reconstructive and aesthetic surgery procedures. *Skin Research and Technology*, *4*(2), 94–98.

Raul, J.-S., Baumgartner, D., Willinger, R., & Ludes, B. (2006). Finite element modelling of human head injuries caused by a fall. *International Journal of Legal Medicine*, *120*(4), 212–8.

Raul, J.-S., Deck, C., Willinger, R., & Ludes, B. (2008). Finite-element models of the human head and their applications in forensic practice. *International Journal of Legal Medicine*, *122*(5), 359–66.

Reinfeldt, S., Stenfelt, S., & Håkansson, B. (2013). Estimation of bone conduction skull transmission by hearing thresholds and ear-canal sound pressure. *Hearing Research*, *299*, 19–28.

Rho, J., Hobatho, M., & Ashman, R. (1995). Relations of mechanical properties to density and CT numbers in human bone. *Medical Engineering & Physics*, *17*(5), 347–355.

Roberts, J., Jones, R., & Rothberg, S. (2001). Measurement of contact time in short duration sports ball impacts: an experimental method and correlation with the perceptions of elite golfers. *Sports Engineering*, *4*, 191–203.

Rose, J. L. (2003). Dispersion curves in guided wave testing. *Materials Evaluation*.

Rossing, T. D., & Fletcher, N. H. (2004). *Principles of Vibration and Sound* (2nd ed.). Springer Verlag.

Roth, S., Raul, J.-S., & Willinger, R. (2009). Finite element modelling of paediatric head impact: Global validation against experimental data. *Computer Methods and Programs in Biomedicine*, *99*(1), 25–33.

Ruan, J. S., Khalil, T. B., & King, A. I. (1994). Dynamic response of the human head to impact by three-dimensional finite element analysis. *Journal of Biomechanical Engineering*, *116*, 44.

Saha, S., & Hayes, W. (1976). Tensile impact properties of human compact bone. *Journal of Biomechanics*, *9*(4), 243–244.

Santiago, L., Oh, B., Dash, P., Holcomb, J., & Wade, C. (2012). A clinical comparison of penetrating and blunt traumatic brain injuries. *Brain Injury*, *26*(2), 107–125.

Sauren, A., & Claessens, M. H. A. (1993). Finite element modeling of head impact: The second decade. *International Research Council on the Biomechanics of Impact (IRCOBI) Conference Proceedings* (pp. 241–254). Eindhoven, Netherlands.

Shearer, P. M. (2009). *Introduction to Seismology* (2nd ed.). Cambridge University Press.

Shull, P. J. (2002). *Nondestructive evaluation: theory, techniques, and applications*. Marcel Dekker Inc.

Simpleware Ltd. (2012). *ScanIP, +FE and +CAD Reference Guide*.

Snyder, R. G. (1963). Human survivability of extreme impacts in free-fall. *34th Annual Aerospace Medical Association*. Los Angeles.

Stålhammar, D. (1975). Experimental brain damage from fluid pressures due to impact acceleration. (Parts 1, 2 and 3). *Acta Neurologica Scandinavica*, *52*(1), 7–55.

Stålhammar, D. (1986). Experimental models of head injury. *Acta Neurochirurgica. Supplementum*, *36*, 33.

Steiner, L. A., & Andrews, P. J. D. (2006). Monitoring the injured brain: ICP and CBF. *British Journal of Anaesthesia*, *97*(1), 26–38. Retrieved from http://bja.oxfordjournals.org/content/97/1/26.full

Stronge, W. J. (2000). *Impact Mechanics* (1st ed.). Cambridge University Press.

Suh, C., Kim, S., & Oh, S. (2005). Analysis of Traumatic Brain Injury Using a Finite Element Model. *Journal Of Mechanical Science And Technology*, *19*(7), 1424–1431.

Tanner, J. M., Whitehouse, R. H., & Takaishi, M. (1966). Standards from Birth to Maturity for Height, Weight, Height Velocity, and Weight Velocity: British Children, 1965. *Archives of Disease in Childhood*, 454–471.

Thomas, L. M., Roberts, V. L., & Gurdjian, E. S. (1967). Impact-induced pressure gradients along three orthogonal axes in the human skull. *Journal of Neurosurgery*, *26*, 316–321.

Thomson, W. T. (1993). *Theory of Vibration with Applications* (4th ed.). Chapman & Hall.

Tong, P., DiMasi, F., Carr, G., Eppinger, R., Marcus, J., & Galbraith, C. G. (1989). Finite element modeling of head injury caused by inertial loading. *Proceedings of the 12th International Conference on Experimental Safety Vehicles* (pp. 617–626).

Trosseille, X., Tarriere, C., Lavaste, F., Guillon, F., & Domont, A. (1992). Development of a F. E. M. of the Human Head According to a Specific Test Protocol. *Proceedings of the 30th STAPP Car Crash Conference*.

Tutt, B. A., & Taylor, A. P. (2004). The use of LS-DYNA to simulate the water landing characteristics of space vehicles. *8th International LS-DYNA Users Conference* (pp. 1–14).

Überall, H., Bjørnø, I. K., & Bjørnø, L. (2000). Dispersion of circumferential waves on evacuated, water-loaded spherical steel shells. *Ultrasonics*, *37*(10), 673–5.

Unterharnscheidt, F., & Higgins, L. S. (1969). Pathomorphology of experimental head injury due to rotational acceleration. *Acta Neuropathologica*, *12*, 200–204.

US Centre for Disease Control and Prevention. (2010a). Get the stats on traumatic brain injury in the United States. Retrieved June 17, 2012, from http://www.cdc.gov/traumaticbraininjury/pdf/BlueBook_factsheet-a.pdf (updated 17th March 2010)

US Centre for Disease Control and Prevention. (2010b). What are the leading causes of TBI? Retrieved June 17, 2012, from http://www.cdc.gov/TraumaticBrainInjury/causes.html

US Department of Veterans Affairs. (n.d.). *Traumatic brain injury: a guide for patients*. Retrieved from http://www.mentalhealth.va.gov/docs/tbi.pdf

Van De Graaff, K. M., & Fox, S. I. (1995). *Concepts of human anatomy and physiology*. McGraw-Hill Education.

Van Dommelen, J. A. W., Van der Sande, T. P. J., Hrapko, M., & Peters, G. W. M. (2010). Mechanical properties of brain tissue by indentation: interregional variation. *Journal of the Mechanical Behavior of Biomedical Materials*, *3*(2), 158–66.

Versace, J. (1971). A review of the severity index. *Proceedings of the 15th STAPP Car Crash Conference* (pp. 771–796). Retrieved from http://www.snellfoundation.org/docs/articles/hics

Vincent, J. F. V. (1990). The functional design of bone. *Structural biomaterials* (pp. 179–196). Princeton University Press.

Voo, K., Kumaresan, S., Pintar, F. A., Yoganandan, N., & Sances, A. (1996). Finite-element models of the human head. *Medical & Biological Engineering & Computing*, *34*(5), 375–81.

Wahi, K. K., & Merchant, H. C. (1977). Mechanical response of a head injury model with viscoelastic brain tissue. *Annals of Biomedical Engineering*, *5*(4), 303–21.

Wang, F., Lee, H. P., & Lu, C. (2007). Effects of head size and morphology on dynamic responses to impact loading. *Medical & Biological Engineering & Computing*, *45*(8), 747–57.

Ward, C. C., Chan, M., & Nahum, A. M. (1980). Intracranial Pressure–A Brain Injury Criterion. *Proceedings of the 24th STAPP Car Crash Conference*.

Ward, J. W., Montgomery, L. H., & Clark, S. L. (1948). A mechanism of concussion: A theory. *Science*, *107*, 349–353.

Wardlaw, A., & Goeller, J. (2010). Cavitation as a Possible Traumatic Brain Injury (TBI) Damage Mechanism. *26th Southern Biomedical Engineering Conference SBEC 2010 April 30-May 2, 2010 College Park, Maryland, USA* (p. 34). Springer Verlag.

Watkins, L., & Thomas, D. G. T. (2003). Traumatic injuries of the head. *Oxford Textbook of Medicine (4th ed.)* (pp. 1108–10). Oxford University Press.

Weber, I., & Young, P. G. (2003). Automating the generation of 3D finite element models based on medical imaging data: application to head impact. *3D Modelling Paris, France* (Vol. 44, pp. 23–24).

Willinger, R., Kang, H. S., & Diaw, B. (1999). Three-dimensional human head finite-element model validation against two experimental impacts. *Annals of Biomedical Engineering*, *27*(3), 403–10.

Wittek, A., & Omori, K. (2003). Parametric study of effects of brain-skull boundary conditions and brain material properties on responses of simplified finite element brain model under angular acceleration impulse in sagittal plane. *JSME International Journal Series C*, *46*(4), 1388–1399.

Wood, J. L. (1971). Dynamic response of human cranial bone. *Journal of Biomechanics*, *4*(1), 1–12.

Yanagida, Y., Fujiwara, S., & Mizoi, Y. (1989). Differences in the intracranial pressure caused by a "blow" and/or a "fall" - An experimental study using physical models of the head and neck. *Forensic Science International*, *41*, 135–145.

Yao, J., Turteltaub, S. R., & Ducheyne, P. (2006). A three-dimensional nonlinear finite element analysis of the mechanical behavior of tissue engineered intervertebral discs under complex loads. *Biomaterials*, *27*(3), 377–387.

Young, P. G. (2002). A parametric study on the axisymmetric modes of vibration of multi-layered spherical shells with liquid cores of relevance to head impact modelling. *Journal of Sound and Vibration*, *256*(4), 665–680.

Young, P. G. (2003). An analytical model to predict the response of fluid-filled shells to impact - a model for blunt head impacts. *Journal of Sound and Vibration*, *267*(5), 1107–1126.

Young, P. G., Beresford-West, T., Coward, S., Notarberardino, B., Walker, B., & Abdul-Aziz, A. (2008). An efficient approach to converting three-dimensional image data into highly accurate computational models. *Philosophical Transactions of the Royal Society A: Mathematical, Physical and Engineering Sciences*, *366*(1878), 3155.

Young, P. G., & Morfey, C. L. (1998). Intracranial pressure transients caused by head impacts. *International Research Council on the Biomechanics of Impact (IRCOBI) Conference Proceedings* (pp. 391–403). Göteborg, Sweden.

Young, W., & Budynas, R. (2002). *Roark's formulas for stress and strain* (7th ed.). McGraw-Hill.

Zhang, L., Yang, K. H., & King, A. I. (2001). Biomechanics of neurotrauma. *Neurological Research*, *23*, 144–156.

Zioupos, P., & Currey, J. (1998). Changes in the stiffness, strength, and toughness of human cortical bone with age. *Bone*, *22*(1), 57–66.

Zong, Z., Lee, H. P., & Lu, C. (2006). A three-dimensional human head finite element model and power flow in a human head subject to impact loading. *Journal of Biomechanics*, *39*(2), 284–92.